Search for Supersymmetry in charm quark final states with the ATLAS detector

Dissertation
zur Erlangung des Grades
„Doktor der Naturwissenschaften“

am Fachbereich Physik, Mathematik und Informatik
der Johannes Gutenberg-Universität Mainz

Jan Schäffer

geb. in Bad Nauheim

Mainz, Januar 2018

Mündliche Prüfung: 26.09.2018

Abstract

This thesis presents a search for Supersymmetry in final states with charm jets and missing transverse energy. The signal models assume direct pair production of scalar top or scalar charm quarks, each decaying with a branching ratio of 100% into a charm quark and the lightest neutralino as $\tilde{t}_1 \rightarrow c + \tilde{\chi}_1^0$ and $\tilde{c} \rightarrow c + \tilde{\chi}_1^0$, respectively. Charm tagging techniques are used in order to reduce backgrounds and are an integral part of the analysis. A special focus is set on the data driven background estimation and the signal region optimization. The analyzed data was recorded with the ATLAS detector in the years 2015 and 2016 in proton-proton collisions at a center of mass energy of 13 TeV and corresponds to a total integrated luminosity of 36.1 fb^{-1}.

No deviation between the number of data events and Standard Model prediction was observed, so exclusion limits were set. For mass differences $\Delta m = m_{\tilde{q}} - m_{\tilde{\chi}_1^0}$ of ~80 GeV both scalar quarks could be excluded up to masses of 500 GeV, while scalar charm quarks could be excluded up to 845 GeV for higher Δm. Furthermore, model independent limits on the visible cross sections of 0.33 fb were set.

Kurzfassung

In dieser Arbeit wird eine Suche nach Supersymmetrie mit Charm Jets und fehlender Transversalenergie vorgestellt. Als Signalmodelle dienen die direkten Paarproduktionen von skalaren Top und skalaren Charm Quarks, sowie deren Zerfall mit einem Verzweigungsverhältnis von 100% in jeweils ein Charm Quark und das leichteste Neutralino, $\tilde{t}_1 \rightarrow c + \tilde{\chi}_1^0$ bzw. $\tilde{c} \rightarrow c + \tilde{\chi}_1^0$. Ein zentraler Bestandteil der Analyse ist die Rekonstruktion und Identifikation von Jets aus Charm Quarks, mit deren Hilfe Untergründe unterdrückt werden können. Im Fokus stehen die damit zusammenhängende datenbasierte Untergrundabschätzung, sowie die Optimierung der Signalregionen. Die analysierten Daten wurden mit dem ATLAS Detektor in den Jahren 2015 und 2016 in Proton-Proton-Kollisionen bei einer Schwerpunktsenergie von 13 TeV aufgenommen und entsprechen einer gesamten integrierten Luminosität von 36.1 fb^{-1}.

Keine Abweichung zwischen den Daten und der Standardmodellerwartung wurde festgestellt und daher Ausschlussgrenzen gesetzt. Für Massendifferenzen $\Delta m = m_{\tilde{q}} - m_{\tilde{\chi}_1^0}$ von ~80 GeV konnten beide skalare Quarks mit Massen bis zu 500 GeV ausgeschlossen werden, während skalare Charm Quarks darüber hinaus für größere Δm bis zu Massen von 845 GeV ausgeschlossen werden konnten. Weiterhin wurden modellunabhängige Grenzen von 0.33 fb auf den sichtbaren Wirkungsquerschnitt gesetzt.

Contents

1. Introduction

The pursuit of knowledge is one of the driving forces of mankind, as it leads to a deeper understanding of what holds the world together at its core. For centuries scientists have conducted experiments that lead to the discovery of the four fundamental interactions we know today: gravity is visible on macroscopic levels and is responsible for the dynamics of celestial bodies, as well as apples falling down from a tree. Electromagnetism describes the interaction between electrically charged objects, for example nuclei and the surrounding electrons. The strong force is responsible for binding protons and neutrons inside the nuclei, while the weak force handles their radioactive decays.

The Standard Model of Particle Physics was developed in the 1960s and describes all these interactions, except for gravity, in the framework of a relativistic quantum field theory. It is one of the most successful and well tested theories and predicted the existence of the W boson[1], the top quark[2] and the Higgs boson[3]. However, it is known to be incomplete. Aside the missing description of gravity, it has intrinsic issues in form of free parameters that can not be predicted and can only be determined through experiments. Furthermore, it has no Dark Matter candidate that matches the cosmological observations such as the Cosmic Microwave Background or the Bullet Cluster.

A possible and well motivated extension of the Standard Model is Supersymmetry, which stands at the center of this thesis. It introduces a symmetry between fermions and bosons, and postulates supersymmetric partners for each existing Standard Model particle. While it adds even more free parameters, many problems of the Standard Model are solved automatically. For example, Dark Matter candidates appear naturally and the new particles' contributions to the Higgs mass solve the hierarchy problem.

Supersymmetry must be broken, as the postulated particles' masses would otherwise be identical to that of their partners, and they would have been discovered already. The masses are free parameters of the theory with a drastic influence on the phenomenology, leading to countless possible production and decay channels. If realized in nature, supersymmetric particles could be produced in proton-proton collisions at the Large Hadron Collider (LHC) at CERN. The LHC was operated with center of mass energies of up to 13 TeV, delivering total integrated luminosities of over 100 fb^{-1} to its experiments (state December 2017). Numerous searches for Supersymmetry have been performed without finding evidence of its existence, thus pushing the exclusion limits of many particle masses towards or even beyond 1 TeV.

The top squark - the supersymmetric partner of the top quark - is expected to be among the lightest undiscovered particles, as its mass should be close to that of the top quark. Its decay mode is highly dependent on the overall mass hierarchy and can decay into a charm quark and an invisible particle. The Run1 ATLAS exclusion limit for this decay reaches top squark masses of around 300 GeV, leaving an uncovered and well motivated phase space. A similar situation can be found for the charm squark - the supersymmetric partner of the charm quark - which can decay in the same way.

[1] Discovery in 1983 by the UA1 [1] and UA2 [2] collaborations.
[2] Discovery in 1995 by the CDF [3] and D0 [4] collaborations.
[3] Discovery in 2012 by the ATLAS [5] and CMS [6] collaborations.

This thesis describes the search for Supersymmetry with charm quarks and missing transverse momentum in its final states, using a total integrated luminosity of 36.1 fb^{-1} recorded with the ATLAS detector in the years 2015 and 2016 in proton-proton collisions at a center of mass energy of 13 TeV. A focus is set on the data driven background estimation and the signal region optimization.
It is structured as follows: The fundamental theoretical principles of the Standard Model of Particle Physics and its possible extension through Supersymmetry are introduced in chapter 2, including a brief discussion of solutions for unresolved issues within the Standard Model. Chapter 3 describes the phenomenology of Supersymmetry at the LHC with a focus on the signatures of interest and their current limits, before the experimental setup of the ATLAS experiment is discussed in chapter 4. The analyzed data set and Monte Carlo simulations are introduced in chapter 5, with the object reconstructions and definitions being described in chapter 6. An overview of the analysis is given in chapter 7, motivating the data driven background estimation and the fit setup, which are described in chapters 8 and 9, respectively. Chapter 10 discusses the systematic uncertainties considered in this analysis, before the signal region optimization is described in chapter 11 and the final results are presented in chapter 12. Finally, chapters 13 and 14 summarize the thesis and give an outlook to possible improvements in future searches.

2. Theoretical background

This section contains the theoretical background required for the analysis presented in this thesis. The Standard Model of Particle Physics will be introduced briefly, before motivating Supersymmetry as a possible extension. Finally some open questions of the Standard Model and their solutions through Supersymmetry will be discussed.

2.1. The Standard Model of Particle Physics

The Standard Model of Particle Physics (SM) is a quantum field theory that describes three out of four known fundamental forces[1]. It contains all required particles and their interactions to make very precise predictions for high energy physics and satisfies important characteristics, such as being relativistic and renormalizable [7]. The latter guarantees that observables are always finite, while the first one ensures a predefined transformation behavior of the fields, depending on their spins' respective Lorentz group representation.

The SM is described by a locally gauge invariant Lagrangian density $\mathcal{L}_{SM}$ with the gauge group

$$SU(3)_c \otimes SU(2)_L \otimes U(1)_Y. \tag{2.1}$$

$SU(3)_c$ is the gauge group of the strong force with c (color) standing for its charge. $SU(2)_L \otimes U(1)_Y$ is the gauge group of the electroweak interaction[2], where Y stands for the weak hypercharge and L indicates the weak interaction's dependency on the particles' helicities. The gauge group of the SM is actually spontaneously broken to

$$SU(3)_c \otimes U(1)_{EM}, \tag{2.2}$$

which is an essential part of the SM and will be discussed in section 2.1.4.

The theory is required to satisfy local gauge invariance, resulting in gauge fields that can be identified with the mediators of their respective forces. The interactions and their Lagrangians will be discussed in more detail in sections 2.1.2 and 2.1.3.

2.1.1. Particle content

The SM particles can be classified as bosons (integer spin) and fermions (half integer spin). SM bosons either carry spin 1 (interaction mediators) or spin 0 (Higgs boson), while all fermions carry spin $1/2$.

Fermions can be subdivided into quarks and leptons, depending on the interactions they participate in. Quarks take part in all three interactions described by the SM. They can be arranged in three families, each containing one up and one down type quark, with an electromagnetic charge of $+2/3$ and $-1/3$, respectively. All leptons take part in the weak, but not in the strong interaction, while only those carrying the corresponding charge participate

[1] The SM contains the strong, weak and electromagnetic force, but does not include gravity.
[2] The electromagnetic and weak interaction can be unified into a single interaction, called electroweak.

in the electromagnetic interaction. They can be arranged in families, too, with each family containing one left-handed weak isospin doublet $(\ell \ \ \nu_\ell)_L$ and a right-handed singlet ℓ_R (see also section 2.1.3).

Bosons with spin 1 are the gauge fields resulting from the gauge groups of $\mathcal{L}_{SM}$ and act as mediators of the corresponding interactions. The only spin 0 particle in the SM is the Higgs boson. It is essential, since the theory's gauge invariance forbids explicit mass terms for the particles. In section 2.1.4 it is discussed, how the particles gain non-zero masses via the so called *Higgs mechanism*. The Higgs boson was predicted by the Standard Model and was finally observed by ATLAS and CMS in 2012 [5, 6]. It was the last undiscovered particle of the SM.

Some important characteristics of all SM particles are shown in tables 2.1, 2.2 and 2.3. It should be noted that all particles, except for the electromagnetic neutral bosons, have antiparticles with the same quantum numbers, except for the electromagnetic charge, which is flipped.

Quarks					
Name	Symbol	Spin	Em. Charge	Color	Mass
Down	d	$1/2$	$-1/3$	r, b, g	$4.7^{+0.5}_{-0.4}$ MeV
Up	u	$1/2$	$+2/3$	r, b, g	$2.2^{+0.6}_{-0.4}$ MeV
Strange	s	$1/2$	$-1/3$	r, b, g	96^{+8}_{-4} MeV
Charm	c	$1/2$	$+2/3$	r, b, g	1.27 ± 0.03 GeV
Bottom	b	$1/2$	$-1/3$	r, b, g	$4.18^{+0.04}_{-0.03}$ GeV
Top	t	$1/2$	$+2/3$	r, b, g	$173.21 \pm 0.51 \pm 0.71$ GeV

Table 2.1: Experimentally measured spins, charges and masses of the SM quarks [8]. Natural units $c = \hbar = 1$ are used.

Leptons					
Name	Symbol	Spin	Em. Charge	Color	Mass
Electron	e	$1/2$	-1	-	0.51 MeV
Electron neutrino	ν_e	$1/2$	0	-	< 2 eV
Muon	μ	$1/2$	-1	-	105.65 MeV
Muon neutrino	ν_μ	$1/2$	0	-	< 0.19 MeV
Tau	τ	$1/2$	-1	-	1776.86 ± 0.12 MeV
Tau neutrino	ν_τ	$1/2$	0	-	< 18.2 MeV

Table 2.2: Experimentally measured spins, charges and masses of the SM leptons [8]. Natural units $c = \hbar = 1$ are used. Uncertainties much lower than the percent level are omitted.

Bosons					
Name	Symbol	Spin	Em. Charge	Color	Mass
Photon	γ	1	0		0
Z boson	Z^0	1	0		91.1876 ± 0.0021 GeV
W boson	$W^\pm$	1	± 1		80.386 ± 0.015 GeV
Gluon	g	1	0	yes	0
Higgs boson	H	0	0		$125.09 \pm 0.21 \pm 0.11$ GeV

Table 2.3: Experimentally measured spins, charges and masses of the SM bosons [8]. Natural units $c = \hbar = 1$ are used.

2.1.2. Strong interaction

The strong interaction is described by Quantum Chromo Dynamics (QCD). Its Lagrangian can be written as

$$\mathcal{L}_{QCD} = -g\,(\bar{q}\gamma^\mu T_a q)\,G^a_\mu - \frac{1}{4} G^a_{\mu\nu} G^{\mu\nu}_a \tag{2.3}$$

$$\text{with } G^a_{\mu\nu} = \partial_\mu G^a_\nu - \partial_\nu G^a_\mu - g f^a_{bc} G^b_\mu G^c_\nu. \tag{2.4}$$

All indices for spin, color, etc, are omitted in this representation. $G^a_{\mu\nu}$ is the field strength tensor of the gluons, g is the coupling strength of the strong force and T_a are the generators of $SU(3)_C$. Mass terms for the gauge fields would break the symmetry, so gluons are massless. The first term describes the interactions between the quark fields q and gluon fields G^a_μ, while the second describes the gluons' kinematics.

The non-abelian nature of $SU(3)_C$ leads to $G^a_{\mu\nu}$ having the term $-g f^a_{bc} G^b_\mu G^c_\mu$, which implies that the gluons carry color charge themselves and results in their self-interaction in form of three and four gluon vertices. The strong interaction has another unique characteristic, the so called *Confinement*: the potential energy between two quarks increases with their distance, up to a point where real quark-antiquark pairs are created in order to go to a lower energy level. Therefore free quarks do not exist and hadrons, bound states of several quarks, are always color neutral. The QCD has a running coupling constant α_s, which decreases for increasing energy transfer Q^2. Since high Q^2 are equivalent to small distances, color charged particles that are very close to each other can move almost without any interaction. This effect is called *Asymptotic Freedom*.

2.1.3. Electroweak interaction

The electromagnetic and weak interactions are unified within the electroweak theory. Its Lagrangian can be written as

$$\mathcal{L}_{EW} = \mathcal{L}_{Gauge} + \mathcal{L}_{Fermion}. \tag{2.5}$$

$\mathcal{L}_{Gauge}$ describes the kinematics of the gauge bosons and reads as

$$\mathcal{L}_{Gauge} = -\frac{1}{4} B_{\mu\nu} B^{\mu\nu} - \frac{1}{4} W^a_{\mu\nu} W^{\mu\nu}_a \tag{2.6}$$

$$\text{with } B_{\mu\nu} = \partial_\mu B_\nu - \partial_\nu B_\mu \tag{2.7}$$

$$\text{and } W^a_{\mu\nu} = \partial_\mu W^a_\nu - \partial_\nu W^a_\mu - g\epsilon^a_{bc} W^b_\mu W^c_\nu. \tag{2.8}$$

g is the coupling constant, $B_{\mu\nu}$ is the field strength tensor corresponding to the $U(1)_Y$ and $W^a_{\mu\nu}$ denotes the tensor of $SU(2)_L$. ϵ_{abc} is the Levi-Civita symbol. The non-commutating nature of $SU(2)_L$ results in the term $-g\epsilon^a_{bc} W^b_\mu W^c_\nu$, which leads to self interaction of the W_μ fields.

The second term of the Lagrangian can be written as

$$\mathcal{L}_{Fermion} = \bar{R}\left(iD^R_\mu \gamma^\mu\right) R + \bar{L}\left(iD^L_\mu \gamma^\mu\right) L \tag{2.9}$$

$$\text{with } D^R_\mu = \partial_\mu + ig' B_\mu Y \tag{2.10}$$

$$\text{and } D^L_\mu = \partial_\mu + ig' B_\mu Y + igW^a_\mu T_a \tag{2.11}$$

where D^R_μ and D^L_μ are the covariant derivatives, which ensure local gauge invariance. Y is the generator of $U(1)_Y$ and T^a are the generators of $SU(2)_L$. R (L) denotes the right (left) handed components of the fermion fields, which behave differently. The chirality of a particle is defined using its helicity

$$H = \frac{\hat{s} \cdot \vec{p}}{|\hat{s}| \cdot |\vec{p}|} \tag{2.12}$$

with the spin $\hat{s}$ and the momentum $\vec{p}$ of the particle. Left handed particles have $H = -1$ while right handed particles have $H = +1$. The charged bosons couple only to left (right) handed (anti-) fermions and parity is violated in the maximal way. Neutrinos are massless within the SM, so they can not flip their helicity, and only left (right) handed (anti-)neutrinos exist[3] (see table 2.4).

					Isospin I	I_3
Left handed	Leptons	ν_e	ν_μ	ν_τ	1/2	+1/2
		e	μ	τ		−1/2
	Quarks	u	c	t	1/2	+1/2
		d	s	b		−1/2
Right handed	Leptons	e	μ	τ	0	0
	Quarks	u	c	t	0	0
		d	s	b		

Table 2.4: Fermions and their Weak Isospin I in the SM[8]. The quantum number I was introduced, after no interactions between right handed particles and charged currents of the weak interaction were observed.

[3] This is known to be incorrect from experimental observations like neutrino oszillations, which require non-zero neutrino masses [9, 10].

The gauge eigenstates B_μ and W_μ^a mix to the mass eigenstates A_μ^0, Z_μ^0 and $W_\mu^\pm$ like

$$W_\mu^\pm = \frac{1}{\sqrt{2}}\left(W_\mu^1 \mp W_\mu^2\right) \tag{2.13}$$

$$Z_\mu^0 = -B_\mu \sin\Theta_W + W_\mu^0 \cos\Theta_W \tag{2.14}$$

$$A_\mu^0 = B_\mu \cos\Theta_W + W_\mu^0 \sin\Theta_W \tag{2.15}$$

where A^0can be identified with the photon field and $\Theta_W \approx 0.23$ is the *Weinberg angle* [11].

2.1.4. The Higgs mechanism

As explicit mass terms for the boson fields of the electroweak interaction would break the symmetry, an additional mechanism is needed to explain the non-zero masses of the mass eigenstates $W^\pm$ and Z (see table 2.3).

The solution comes in form of the Higgs mechanism: the term

$$\mathcal{L}_{Higgs} = \left(D_\nu^L H\right)^\dagger \left(D^{L\nu} H\right) + V(\Phi) \tag{2.16}$$

is added to the SM Lagrangian. D_ν^L is the covariant derivative introduced in 2.11 and H is the complex Higgs field doublet

$$H = \begin{pmatrix} H^+ \\ H^0 \end{pmatrix}. \tag{2.17}$$

Thus the term describes the interaction of the Higgs field with the gauge bosons of the weak interaction. $V(\Phi)$ is the Higgs potential

$$V(\Phi) = \mu^2 H^\dagger H + \lambda\left(H^\dagger H\right)^2 \tag{2.18}$$

with the Higgs coupling $\lambda > 0$ and $\mu^2 < 0$. It has a non-vanishing vacuum expectation value

$$\langle H \rangle = \begin{pmatrix} 0 \\ v \end{pmatrix} \qquad \text{with} \qquad v = m/\sqrt{\lambda} \tag{2.19}$$

where m is the mass of the Higgs particle.

Expanding the Higgs potential around the vacuum state breaks the gauge group of the SM spontaneously

$$SU(3)_c \otimes SU(2)_L \otimes U(1)_Y \qquad \Rightarrow \qquad SU(3)_c \otimes U(1)_{EM} \tag{2.20}$$

which leaves the photon massless, while giving masses to the weak gauge bosons

$$M_W = \frac{1}{\sqrt{2}} g v \qquad \text{and} \qquad M_Z = M_W / \cos\Theta_W \tag{2.21}$$

Breaking the symmetry also adds a neutral Goldstone boson, the so called Higgs boson.

The fermionic matter fields gain their masses in a similar way via Yukawa interactions with the Higgs field through an additional term to the Lagrangian density:

$$\mathcal{L}_{Yukawa} = -G\left(\bar{L}HR + \bar{R}H^{\dagger}L\right) \tag{2.22}$$

L and R stand for the left and right handed fermion fields, G denotes their Yukawa couplings to the Higgs field.

All masses of the SM particles, including the Higgs boson, are free parameters of the SM and have to be determined through experiments.

In 2012 the ATLAS and CMS Collaborations announced the discovery of a new Higgs-like particle [5, 6]. It has a mass of $125.09 \pm 0.21 \pm 0.11$ GeV [8] and is seen as the last puzzle piece of the SM.

2.2. Supersymmetry

The Standard Model of Particle Physics evolves around symmetries, implementing all but one non-trivial space-time symmetries possible, as shown by the Haag-Lopuszanski-Sohnius extension of the Coleman-Mandula theorem [12, 13]. The missing symmetry connects bosons and fermions and is called Supersymmetry (SUSY) [14, 15]. While it is possible to construct a theory with N SUSY partners per SM particle, this section will focus on the $N = 1$ case as other scenarios are not considered in this thesis.

$$Q|\text{boson}\rangle = |\text{fermion}\rangle \qquad \text{and} \qquad Q|\text{fermion}\rangle = |\text{boson}\rangle \tag{2.23}$$

All indices are suppressed in this representation. Q is an anti-commutating fermionic operator that carries spin 1/2. Particle states of a SUSY theory fall into irreducible representations of the SUSY algebra, called supermultiplet, each containing the same amount of fermionic and bosonic degrees of freedom. Particles within these supermultiplets are called superpartners and have the exact same quantum numbers, except for the spin, which differs by 1/2. It is impossible to fill these supermultiplets solely with SM particles, since it would result in lepton number non-conservation and a mass for at least one of the neutrinos, that is much higher than what is observed. Instead SUSY doubles the SM particle spectrum by postulating a superpartner for each SM particle and also adds one additional Higgs supermultiplet, which is required to fix a gauge anomaly of the electroweak symmetry. This results in a total of five Higgs bosons of which three are neutral (h^0, H^0 and A^0) and two charged (H^+ and H^-). This is the smallest possible supersymmetric extension of the Standard Model and is called the Minimal Supersymmetric Standard Model (MSSM).

The nomenclature for the new particles depend on their spin: scalar partners of fermionic SM particles use the same name with a prefixed *s*, e.g. the partner of the top quark is called *stop*. Fermionic partners of bosonic particles receive *ino* as affix, so the partners of the gluons are called *gluinos*. An overview of the superpartners can be found in table 2.5.

The mass operator P^2 commutates with Q and $Q^{\dagger}$, so the superpartners are required to have equal masses. However no SUSY particle has been observed, yet, thus SUSY must be broken. There are several possible breaking mechanisms (e.g. gauge mediated symmetry breaking) each leading to a set of additional free parameters for the theory. The breaking mechanism itself is not important for this thesis and will not be discussed further.

Names	Spin 0	Spin 1/2	Spin 1
squarks, quarks	$(\tilde{u}_L\ \tilde{d}_L)$	$(u_L\ d_L)$	
(×3 families)	$\tilde{u}_R^*$	$u_R^\dagger$	
	$\tilde{d}_R^*$	$d_R^\dagger$	
sleptons, leptons	$(\tilde{\nu}\ \tilde{e}_L)$	$(\nu\ e_L)$	
(×3 families)	$\tilde{e}_R^*$	$e_R^\dagger$	
Higgs, Higgsinos	$(H_u^+\ H_u^0)$	$(\tilde{H}_u^+\ \tilde{H}_u^0)$	
	$(H_d^0\ H_d^-)$	$(\tilde{H}_d^0\ \tilde{H}_d^-)$	
gluino, gluon		$\tilde{g}$	g
Winos, W bosons		$\tilde{W}^\pm\ \tilde{W}^0$	$W^\pm\ W^0$
Bino, B boson		$\tilde{B}^0$	B^0

Table 2.5: Supermultiplets in the MSSM.

After electroweak and SUSY breaking, the particles' mass eigenstates can be mixed from states that have the same quantum numbers. Higgsinos, Winos and Binos mix to four neutralinos ($\tilde{\chi}_i^0$, $i \in [1,4]$, electromagnetic charge 0) and four charginos ($\tilde{\chi}_j^\pm$, $j \in [1,2]$, electromagnetic charge ± 1), while the various sets of squarks, sleptons and Higgs scalars can mix within their sets.

R-Parity

The SUSY Lagrangian in its most general form contains terms that violate baryon and lepton number conservation, which lead e.g. to proton decays. While it is possible to build the theory in a way that the proton lifetime is increased to the current experimental limits ($\gtrsim 10^{34}$ years [16]), the problem can also be solved by introducing *R-Parity* conservation. It is multiplicative for all particles and is defined as

$$P_R = (-1)^{3(B-L)+2s} = \begin{cases} +1 & \text{for SM particles} \\ -1 & \text{for SUSY particles} \end{cases} \tag{2.24}$$

where B is the baryon number, L the lepton number and s the spin of the particle.

This constrain not only fixes the proton lifetime, but also implicates additional characteristics for the theory:

- Every interaction vertex contains an even number of SUSY particles. This means that SUSY particles are always produced in pairs and decay into an odd number of other SUSY particles.
- The lightest SUSY particle (LSP) is stable and can not decay further into SM particles. Heavier SUSY particles will always decay via cascades into final states that include the LSP.

2.3. Problems of the SM and their solutions through SUSY

SUSY can be motivated simply because it is the last space-time symmetry possible. However, if it was realized in nature, it would automatically solve many of the SM's problems in a simple and elegant way. This section will present some of these problems and their solutions.

Unification of coupling constants

In quantum field theories the forces' coupling strengths are not constant but *running*. Grand Unifying Theories (GUTs) assume that all strengths were equal in the early universe and that there must be an energy scale at which this is the case, too. For the SM extrapolations to high energies show no convergence, while the MSSM's new particles influence the couplings to unify at $M_U \approx 1.5 \times 10^{16}$ GeV (see figure 2.1).

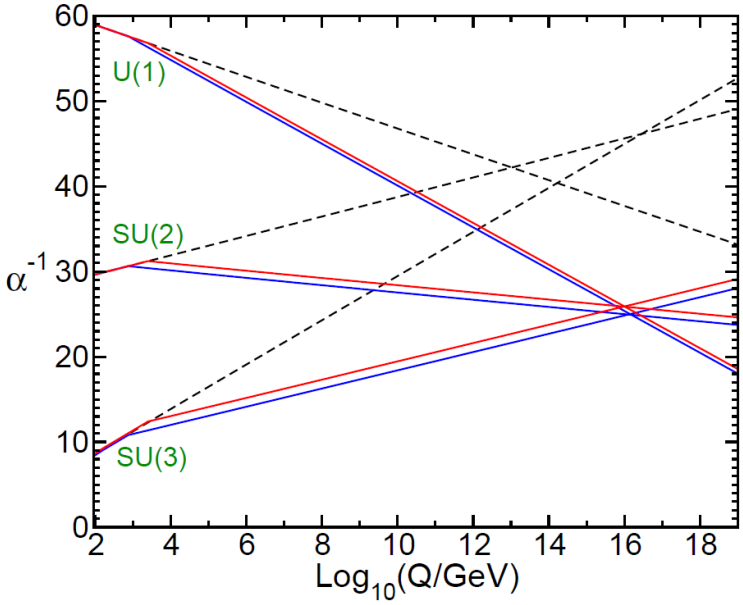

Figure 2.1: Two-loop renormalization group evolution of the inverse gauge couplings $\alpha_i^{-1}(Q)$ in the SM (dashed lines) and in the MSSM (solid lines) with their respective errors [14]. The SUSY particles' influence start at their masses (here varied between 750 GeV and 2.5 TeV).

Dark Matter

There are several observations pointing towards the existence a stable heavy particle that interacts via gravity and possibly weakly. The SM does not contain a candidate for such a *Dark Matter* (DM).

The Bullet Cluster is the collision of two galaxy clusters. The particles within the galaxies interact with each other, mainly via electromagnetic interaction, slowing down their movement. While this behavior can be observed for the visible mass[4], the gravitational centers[5] are not slowed down (see figure 2.2). This observation can be seen as a direct confirmation of the existence of DM. Baryonic matter can not explain this phenomenon, thus new unknown particles must be responsible. These unknown particles have to interact via gravity and might interact weakly.

The Millennium Simulation [18] simulates the formation and clustering of the universe. It starts with a homogeneous distribution of particles that interact with each other. Inserting only SM particles or *Hot Dark Matter*[6] does not lead to a structure that resembles today's

[4]Baryonic mass can be detected via its radiation.
[5]Detected via gravitational lense effects.
[6]Relativistic particles, $v \approx c$

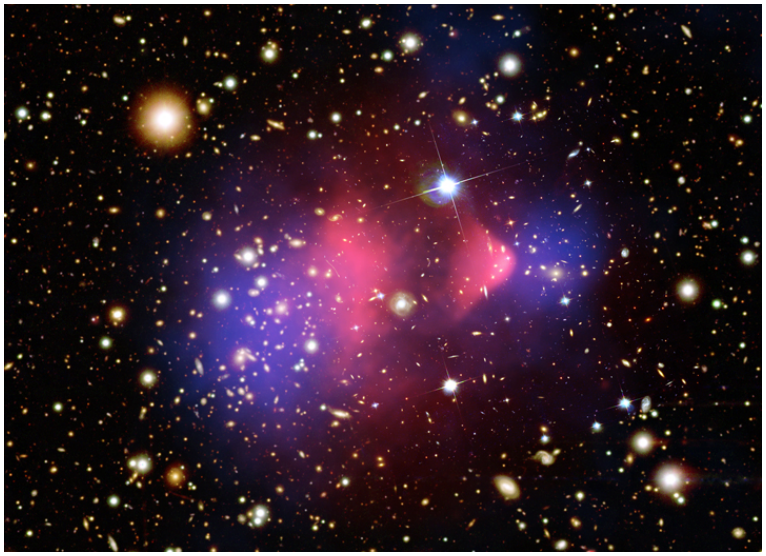

Figure 2.2: Bullet Cluster with its visible matter (pink) and dark matter (blue) [17].

universe. *Cold Dark Matter* particles[7] on the other hand gravitate towards each other and also attract baryonic matter that starts clustering. For particles with a mass $\mathcal{O}(100)$ GeV that interact only weakly and via gravitation a structure similar to our universe emerges.

There are more indicators for DM (e.g. rotation speeds of galaxies [19] or the Cosmic Microwave Background [20, 21]) that will not be discussed here. Many of them point towards a Weakly Interacting Massive Particle (WIMP) with mass below 1 TeV. While the SM does not have a candidate for such a particle, R-Parity conserving SUSY models automatically have a stable LSP that fits the requirements perfectly. Depending on the model the LSP is usually the gravitino[8] or the lightest neutralino.

Hierarchy problem

The observable mass of a particle is determined through its mass parameter in the Lagrangian density and quantum loop diagrams, connecting the particle with others. For the Higgs boson, this is of utmost importance, as it couples to all massive particles and is not protected against huge corrections, unlike the fermions and gauge bosons. As the Higgs boson's coupling to other particles increases with their mass, the top quark yields the highest correction of all SM particles. Its loop correction is that of a fermion coupling to the Higgs field with $-\lambda_f H \bar{f} f$ (see figure 2.3) and can be written as

$$\Delta m_H^2 = -\frac{|\lambda_f|^2}{8\pi^2}\Lambda_{\mathrm{UV}}^2 + ... \tag{2.25}$$

where Λ_{UV} is the ultraviolet momentum cutoff used to regulate the loop integral. It is the scale at which new physics begin to impact the experiment, thus ending the SM's validity[9]. Yet, after including these corrections that can extent several orders of magnitude, the final result must be the observed Higgs mass of approximately 125 GeV. This can only be achieved

[7] Non-relativistic particles $v \ll c$

[8] The supersymmetric partner of a hypothetical graviton.

[9] $\Lambda_{\mathrm{UV}} \leq M_P = (8\pi G_{\mathrm{Newton}})^{-\frac{1}{2}} = 2.4 \times 10^{18}$ GeV, also known as the Planck Scale.

Figure 2.3: One-loop quantum corrections to the Higgs squared mass parameter m_h^2, due to a fermion f (left) and a scalar S (right). [14]

through incredible fine tuning or through additional particles that cancel the SM particles' contributions.

SUSY adds such particles in form of the superpartners. In case of the top quark two new scalar fields are added[10] each coupling to the Higgs as $-\lambda_S|H|^2|S|^2$ (see figure 2.3), thus each adding a contribution

$$\Delta m_H^2 = \frac{\lambda_S}{16\pi^2}\left[\Lambda_{\mathrm{UV}}^2 - 2m_S^2 \ln(\Lambda_{\mathrm{UV}}/m_S)\right] + ... \tag{2.26}$$

Notably the sign of the Λ_{UV}^2 term is the opposite of the fermion's contribution. The terms cancel as $\lambda_S = |\lambda_f|^2$ by construction of SUSY and two scalar fields are added. For unbroken SUSY this cancellation persists through all higher order corrections and also for bosonic particles and their fermionic partners [14, 15, 22].

However SUSY is broken, thus terms depending on the particles' masses will not cancel completely. In order to not being forced to reintroduce fine tuning, the superpartners' masses should not be too far from their SM counterparts. This is especially the case for the scalar top quark, as the top quark has the strongest Yukawa coupling and therefore leads to the biggest corrections.

[10] One for each helicity state.

3. Phenomenology

SUSY particles have the same couplings as their superpartners, so, if realized in nature, they could be produced in collider experiments like the LHC (see section 4). However, even the most simple supersymmetric extension of the SM has around 100 free parameters [23]. The production and decay of SUSY particles can therefore vary a lot, depending for example on the mass hierarchy or R-Parity violating couplings (see figure 3.1). Many searches use simplified models [24, 25] to reduce the number of parameters that need to be tested in their analysis. These simplified models usually assume that only a few particles are sufficiently light to be produced and the other particles do not have any effect on their production. Additionally the branching ratio of a specific decay is often set to 100%.

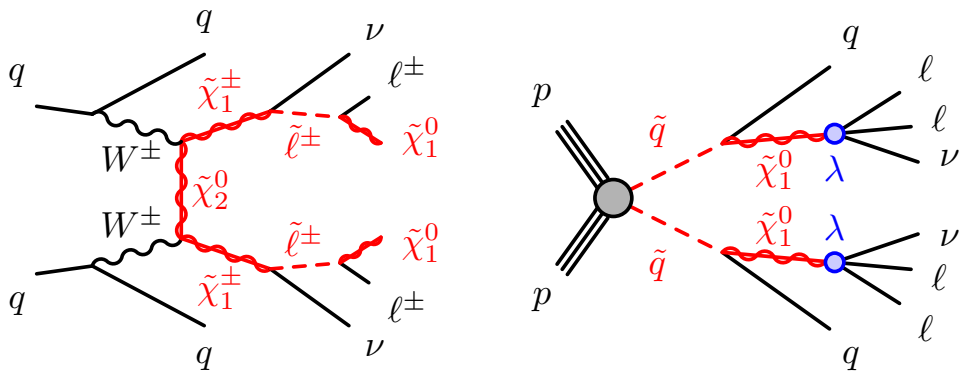

Figure 3.1: Examples for the production of SUSY particles at the LHC [26]. Left: Production of two charginos $\tilde{\chi}_1^\pm$ in a R-Parity conserving model through the exchange of the second lightest neutralino $\tilde{\chi}_2^0$. They decay via sleptons $\tilde{\ell}^\pm$ into the LSP $\tilde{\chi}_1^0$. Right: Production of two squarks $\tilde{q}$ in a R-Parity violating model. The squarks decay into LSPs, which further decay into leptons and neutrinos via the R-Parity violating coupling λ.

3.1. Scalar top and scalar charm quarks in simplified models

The analysis presented in this thesis uses two simplified models that relate to a R-Parity conserving version of the MSSM. The details of the SUSY breaking are not important, however the Lagrangian must not contain any terms that introduce flavor mixing or CP violation of the types that are restricted by experiments. No mixing between the different squark families is allowed, so the mass eigenstate $\tilde{q}_{1/2}$ are mixtures of their left and right handed fields $\tilde{q}_{L/R}$[1]. The light squark flavors ($\tilde{u}$, $\tilde{d}$, $\tilde{s}$, $\tilde{c}$) have nearly degenerate, unmixed mass eigenstates, while the sbottom and stop pairs can have high mixing and very different masses [14].

The models differ only in the mass hierarchies where the second lightest particle (NLSP) is

[1] Left and right handed indicates that these are the super partners of the left and right handed components of the SM fermions.

either the lightest scalar top quark (stop, $\tilde{t}_1$) or the scalar charm quark (scharm, $\tilde{c}$)[2], while the lightest neutralino ($\tilde{\chi}_1^0$) is the LSP in both cases. All other SUSY particles are too heavy to be produced. As the LSP is stable and cannot be detected, signal events will always have missing transverse momentum ($E_{\mathrm{T}}^{\mathrm{miss}}$, see section 6.7).

The only remaining free parameters are the masses of the squarks $m_{\tilde{q}}$ and the neutralinos $m_{\tilde{\chi}_1^0}$[3]. While the scharm will always decay into a charm quark and a neutralino (see figure 3.2, left), the decays of the stop are highly dependent on the mass difference $\Delta m = m_{\tilde{t}_1} - m_{\tilde{\chi}_1^0}$:

$\Delta m > m_t$
: The stop decays into a top quark and a neutralino: $\tilde{t}_1 \to t\tilde{\chi}_1^0$. The top will then decay either hadronically or leptonically, allowing for searches targeting 0, 1 or 2 leptons in the final state.

$m_W + m_b < \Delta m < m_t$
: It is not possible for the stop to decay into an on-shell top, so the dominant process is a three body decay: $\tilde{t}_1 \to Wb\tilde{\chi}_1^0$.

$\Delta m < m_W + m_b$
: In order to keep the *top-like* decay, the W also needs to be virtual, resulting in a four body decay: $\tilde{t}_1 \to bf\bar{f}\tilde{\chi}_1^0$. This decay mode is highly suppressed, though, and another two body decay is possible: $\tilde{t}_1 \to c\tilde{\chi}_1^0$. The stop decays via a flavor changing loop that contains a virtual chargino into a charm quark and a neutralino[4] (see figure 3.2, right). In the simplified model used in this thesis, the two body decay's branching ratio is set to 100%[5].

The analysis focuses on decays with charm quarks, thus the stop model is limited to $\Delta m < m_W + m_b$, while the scharm model is not restricted. For a given $m_{\tilde{q}}$-$m_{\tilde{\chi}_1^0}$ pair the two processes have the exact same kinematics and cross sections, so in the following both will be discussed as a single model, simply referring to squarks $\tilde{q}$. The mass restriction of the stop is always implied.

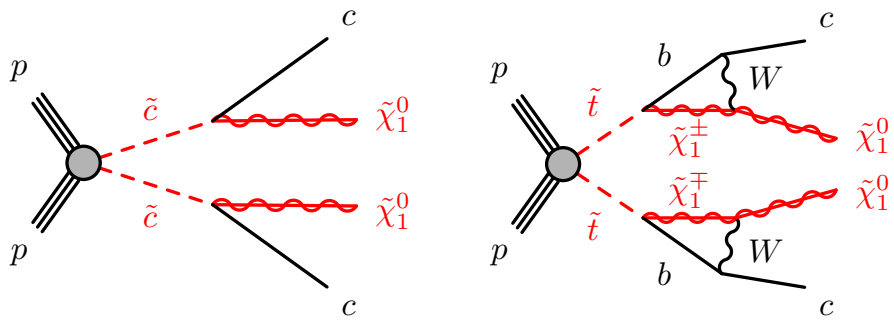

Figure 3.2: Signal processes of interest in this analysis. Direct production of charm squarks (left) and top squarks (right) and their decay into a charm quark and a neutralino [26].

[2]It should be noted that only one scharm state is taken into account. Using both states would effectively double the cross section.
[3]The SUSY particles' couplings are given through the SM couplings, so the cross sections depend only on $m_{\tilde{q}}$.
[4]The branching ratio is only suppressed by the loop itself, as the chargino's mass appears only inside the loop's integral.
[5]In a model with squark mixing across families, $\tilde{t}_1$ could contain components of $\tilde{c}_{L/R}$ thus allowing a direct decay without the loop. This could also lead to non-zero branching ratios for this decay at higher Δm.

3.2. Signal characteristics

The signal's final state contains only charm quarks and neutralinos, which result in jets and missing transverse momentum, respectively. The number of free parameters in each model has been reduced to two ($m_{\tilde{q}}$ and $m_{\tilde{\chi}_1^0}$), yet, varying these masses leads to vastly different event kinematics. While an increase in squark mass mainly reduces the cross section of the process, varying the mass difference Δm has a huge impact on the squarks' decay products (see figure 3.3).

In scenarios with almost degenerate squark and neutralino masses $\Delta m \lesssim 3$ GeV, the squarks gain a non-negligible life time and can even leave the detector before decaying. These scenarios will not be covered in this thesis.

Mass hierarchies with $\Delta m \lesssim 10$ GeV lead to very low momenta for the charm quarks and the neutralinos. The emerging jets are too soft to be reconstructed, while the $E_{\mathrm{T}}^{\mathrm{miss}}$ from the neutralinos is very low. If additional gluons or quarks are radiated in the initial state (Initial State Radiation, ISR), the squark system and its decay products are boosted. The charm quarks are already highly relativistic before the boost ($m_c = 1.28 \pm 0.03$ GeV [8]), thus its impact on the total momentum is only minor. The neutralinos are much more massive ($m_{\tilde{\chi}_1^0} \gtrsim 275$ GeV, see section 3.3) so they are almost at rest before the boost, which in return has a huge impact. This leads to the so-called *Monojet* signature with high $E_{\mathrm{T}}^{\mathrm{miss}}$ and a low number of (ISR) jets.

At mass differences $\Delta m \approx 50$ GeV the charm quarks gain sufficient momentum from the decay that their jets can be reconstructed. The neutralinos' momenta also increase, reducing the boost's impact. This effect gets stronger with growing mass differences, such that the boost has only minor influences for very high Δm.

This effect is also shown in figure 3.4. The left plot shows the inclusive[6] $E_{\mathrm{T}}^{\mathrm{miss}}$ distribution for several benchmark signals. The mass differences $\Delta m = 5/80$ GeV have much lower $E_{\mathrm{T}}^{\mathrm{miss}}$ values than $\Delta m \approx 600/800$ GeV. After requiring at least one jet with a transverse momentum (p_{T}, see section 4.2) of at least 250 GeV, the low Δm curves shift to higher values, while the high Δm distributions are almost unchanged (right plot). The p_{T} requirement adds a boost to the low Δm points, as the jets from the charm quarks don't have the required momentum and the hard jet must be ISR. For high Δm the decay products are usually sufficiently energetic, so no additional ISR jet is required to pass the cut.

This thesis focuses on the region where the charm quarks' jets can be reconstructed, as the low Δm area is already covered by the Monojet analysis [27] (see section 3.3). Each signal event should have two jets from charm quarks, which is rare for SM processes, so *charm tagging* will be used in order to separate the signal from SM backgrounds (see section 6).

[6] The only requirement is a generator level filter of $E_{\mathrm{T}}^{\mathrm{miss,truth}} > 100$ GeV.

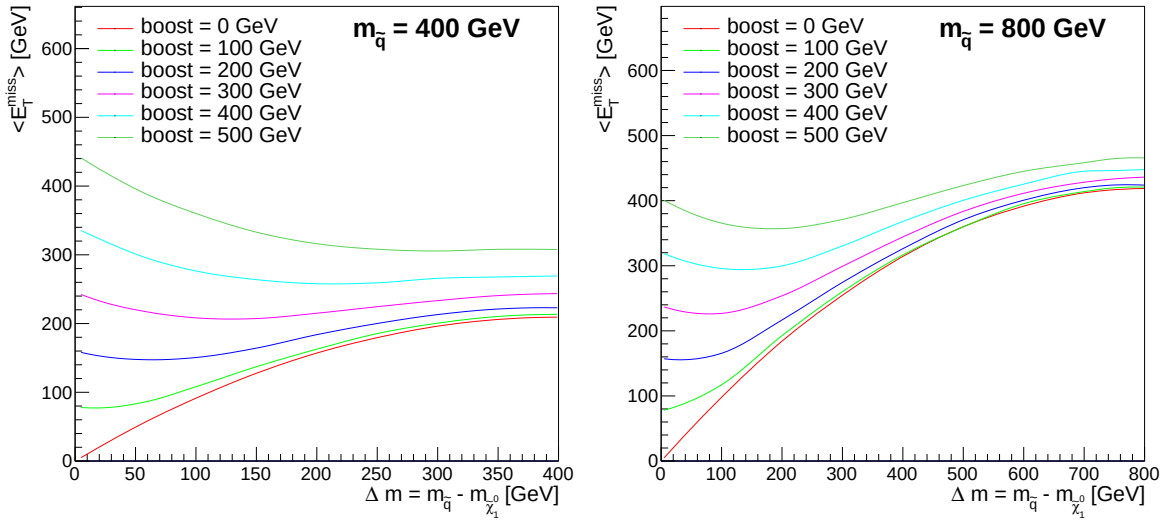

Figure 3.3: Average missing transverse momentum $<E_{\mathrm{T}}^{\mathrm{miss}}>$ against the mass difference Δm for $m_{\tilde{q}} = 400$ GeV (left) and $m_{\tilde{q}} = 800$ GeV (right). The colored lines show varying boosts of the squark system. While $<E_{\mathrm{T}}^{\mathrm{miss}}>$ is very dependent on the boost for small Δm, there is almost no influence for high Δm.

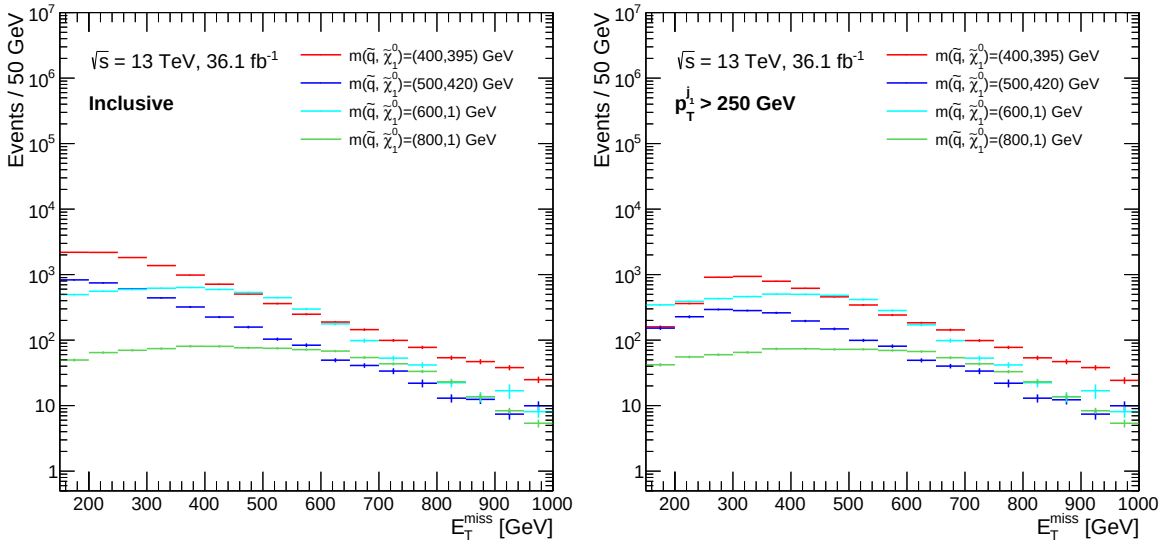

Figure 3.4: $E_{\mathrm{T}}^{\mathrm{miss}}$ distributions of several benchmark models at the inclusive stage (left) and after requiring one jet with at least 250 GeV p_{T} (right). *Inclusive* applies no event selection, except a generator level requirement of $E_{\mathrm{T}}^{\mathrm{miss,truth}} > 100$ GeV.

3.3. Current exclusion limits

At the time of writing, no SUSY particles have been observed. Many of the diverse models are being tested in experiments, having their parameter space restricted. The strongest limits on Supersymmetry are currently set by the ATLAS [28] and CMS [29] collaborations. This chapter focuses on the stop and scharm limits, but a full list of results can be found on the experiments' public results web pages [30][31]. More information on limit setting can be found in section 9.

An overview of the stop decay channels introduced in section 3.1, as well as a zoom into the $\tilde{t}_1 \to c + \tilde{\chi}_1^0$ region with the latest ATLAS Monojet analysis, is shown in figure 3.5. In general scalar top quarks are excluded up to ~1 TeV for high mass differences, while the reach decreases for smaller Δm.

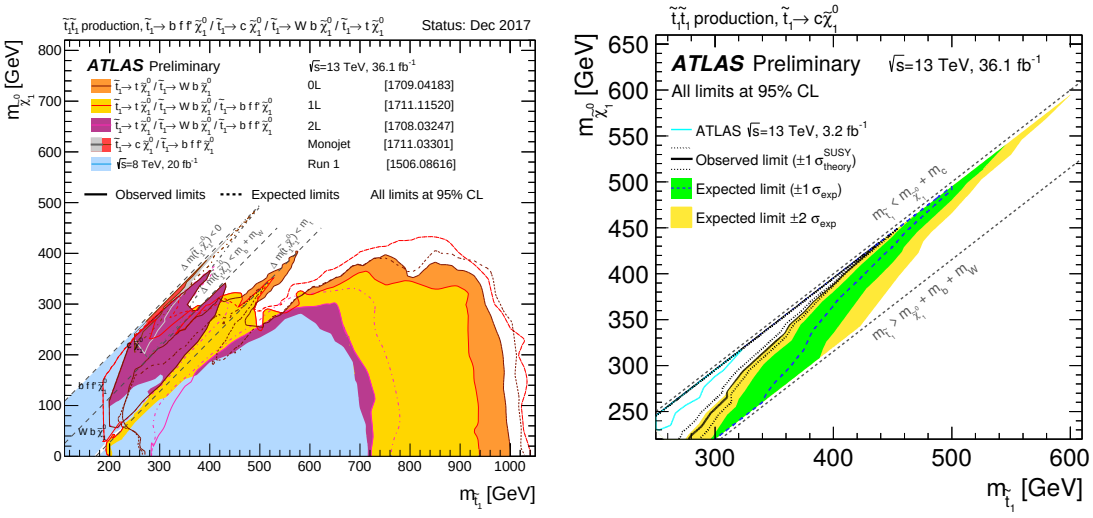

Figure 3.5: Left: ATLAS overview plot of current scalar top quark mass limits [30]. The plot overlays contours belonging to different stop decay channels, different mass hierarchies, and simplified decay scenarios, so care must be taken when interpreting them. Right: Zoom into the $\Delta m < m_W + m_b$ region, showing the $\tilde{t}_1 \to c + \tilde{\chi}_1^0$ interpretation of the ATLAS Monojet *Run2* analysis [27].

The best limits for $\tilde{t}_1 \to c + \tilde{\chi}_1^0$ outside of the Monojet region are shown in figure 3.6. The ATLAS Run2 limits are the result of this thesis, so the Run1 limits are presented, reaching up to $m_{\tilde{t}_1} \approx 280$ GeV. CMS has an expected limit on $m_{\tilde{t}_1} \approx 475$ GeV, while the observed limit is at $m_{\tilde{t}_1} \approx 550$ GeV due to a negative excess in data.

Figure 3.7 shows the limits for $\tilde{c} \to c + \tilde{\chi}_1^0$ (again only the Run1 results for ATLAS). The comparable scharm limit in the CMS plot is labeled *'one light $\tilde{q}$'*. Scharm masses up to ~ 1050 GeV can be excluded for very high mass differences, while the reach goes down to ~ 550 GeV for small Δm.

Both CMS plots should be taken with a grain of salt, as it is not clear whether the signal model is the same as described in this thesis and used in ATLAS. The CMS analysis' highest sensitivity is seen in kinematic regions, where almost no signal is expected for the ATLAS model (see appendix A).

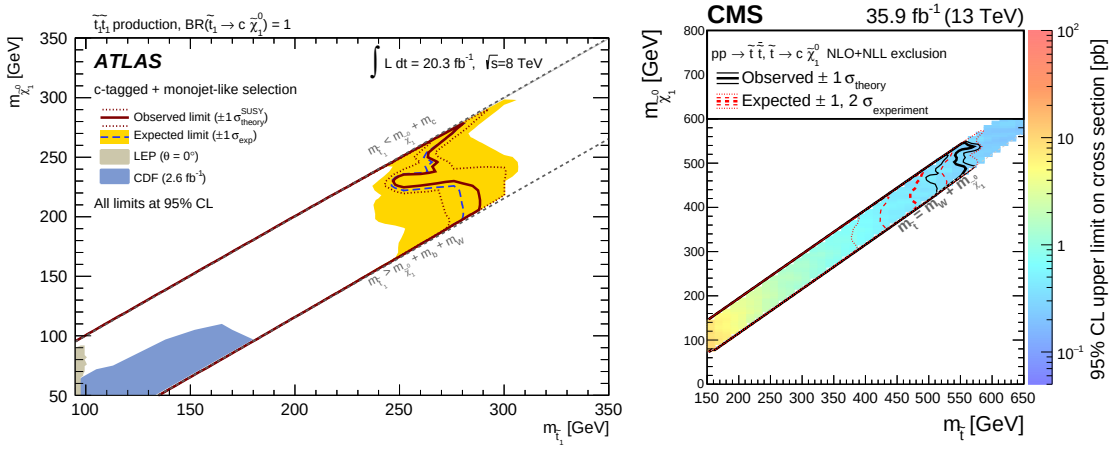

Figure 3.6: Left: *Run1* limits of the ATLAS $\tilde{t}_1 \to c + \tilde{\chi}_1^0$ analysis [32]. Right: $\tilde{t}_1 \to c + \tilde{\chi}_1^0$ interpretation of the CMS m_{T2} *Run2* analysis [33].

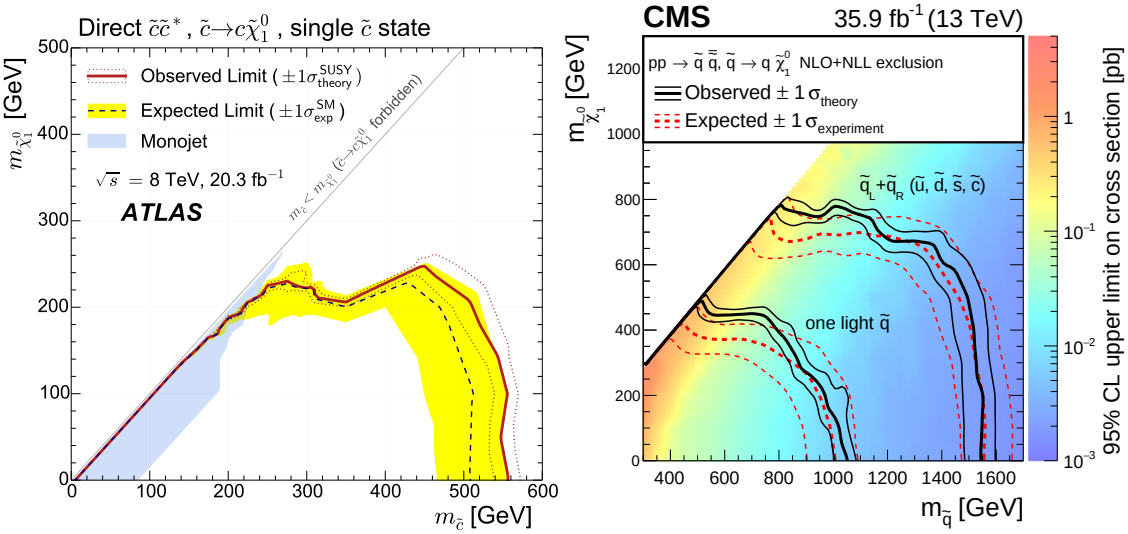

Figure 3.7: Left: *Run1* limits of the ATLAS $\tilde{c} \to c + \tilde{\chi}_1^0$ analysis [34]. Right: Limits on light flavored squarks if the CMS m_{T2} *Run2* analysis [33]. The contour labeled '*one light* $\tilde{q}$' can be interpreted for the direct $\tilde{c}$ production.

4. Experimental Setup

4.1. The Large Hadron Collider

The Large Hadron Collider (LHC) at the European Organization for Nuclear Research CERN[1] is so far the largest and most powerful particle accelerator in the world. It was designed to perform proton-proton collisions every 25 ns at a center of mass energy $\sqrt{s}$= 14 TeV, reaching an instantaneous luminosity of $\mathcal{L} = 10^{34}\text{cm}^{-2}\text{s}^{-1}$. Since an incident during the first weeks of operation [35], the accelerator has been running at lower energies, though. During *Run1* the center of mass energy has been $\sqrt{s}$= 7 TeV (2010-2011) and $\sqrt{s}$= 8 TeV (2012), and was increased to $\sqrt{s}$= 13 TeV in 2015 for the start of *Run2* [36]. Since then the LHC operates at this energy (state December 2017).

Before being injected into the LHC, the protons are accelerated in several steps (see figure 4.1): The ionized Hydrogen atoms start at the linear accelerator LINAC2 and are transferred to the Booster (1.4 GeV), before being accelerated by the Proton Synchrotron (PS, 25 GeV) and the Super Proton Synchrotron (SPS, 450 GeV). The beam is then divided and inserted into the LHC in opposite directions, where the protons are accelerated to their final energy (6.5 TeV).

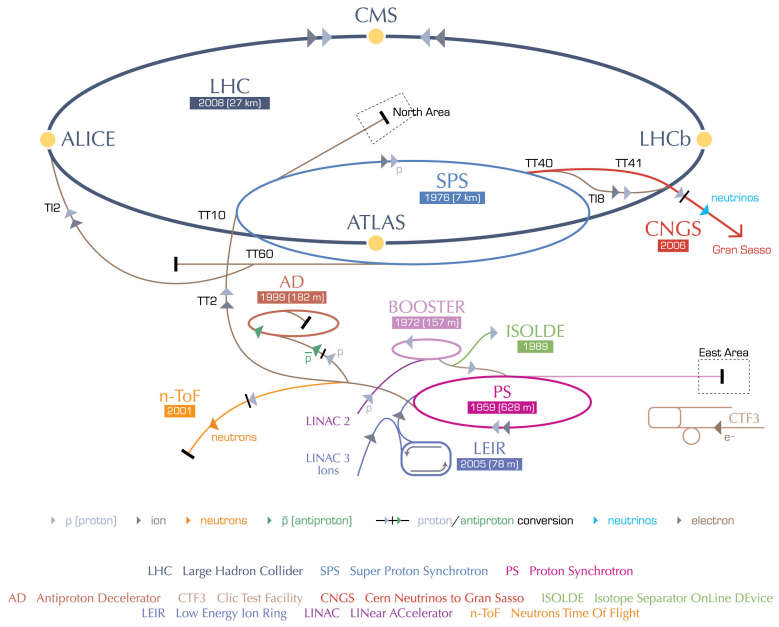

Figure 4.1: Schematic layout of the CERN accelerator complex [37].

[1] **C**onseil **E**uropéen pour la **R**echerche **N**ucléaire

4.2. Proton-Proton collisions

The LHC beams are not continuous, but instead consist of bunches with $\sim 10^{11}$ protons each, and are further arranged in *bunch trains*. They are brought to collision in the four main LHC experiments[2] at a frequency of 25 ns. Each *bunch crossing* leads to multiple interactions, with the average number of interactions defined as $<\mu>$. This number is not constant, but depends on the collider's parameters like the center of mass energy or the beam focusing (see figure 4.2). Only very few interactions lead to physics processes that are not simple proton scatterings. In order to identify the individual interactions and to distinguish between interesting events and the so called *pile up*, a highly precise detector, as well as a good trigger system is required. As the Monte Carlo simulations for the background and signal events are usually produced before the final pile up profile is known, a reweighting is applied to correct for differences.

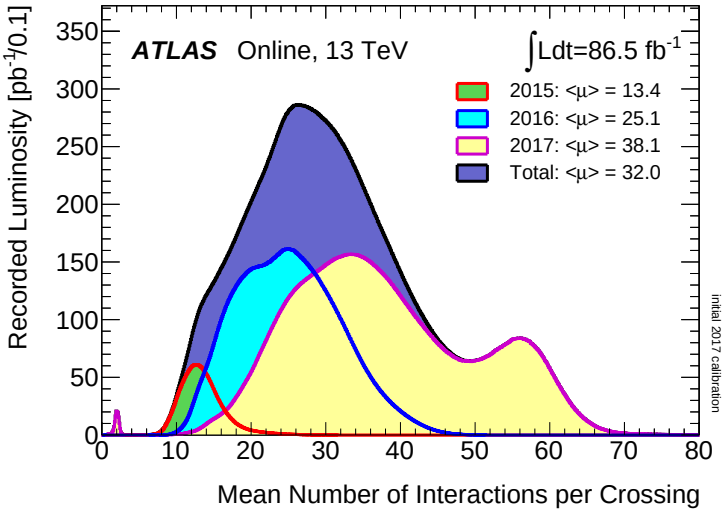

Figure 4.2: Average number of interactions per bunch crossing $<\mu>$ in the ATLAS detector during the data taking periods of Run2 (state December 2017) [40].

The instantaneous luminosity for collider experiments is defined as

$$\mathcal{L} = \frac{N_p^2 n_b f}{A} F = n_b \frac{<\mu> f}{\sigma_{\text{inel}}}$$

where N_p is the number of protons per bunch, n_b the number of bunches, f the revolution frequency, A the transverse beam size at the interaction point and F a geometrical factor correcting for losses due to the crossing angle [11]. The alternative definition uses the average number of interactions per bunch crossing $<\mu>$ and the total inelastic pp cross section σ_{inel} [41]. The integrated luminosity is defined as the integral over time of the instantaneous luminosity, which can be used to calculate the number of expected events for a specific physics process like

$$N_X = \sigma_{pp\to X} \cdot \int \mathcal{L} dt$$

where $\sigma_{pp\to X}$ is the cross section.

[2] ATLAS [28], CMS [29], ALICE [38] and LHCb [39]

During inelastic proton-proton scatterings, it's not actually the hadrons themselves that collide, but the *partons*[3] they consist of. Each parton carries a fraction x of the total proton energy, called Bjorken scale [11], depending on their Parton Distribution Functions (PDF, see figure 4.3). PDFs can not be derived by theory, but can be measured for example in electron-proton collisions at low energies and extrapolated to LHC levels. As there are not only different ways to extract PDFs, but also different data sets and groups, various PDF sets are available[4]. The "correct" PDFs are unknown, therefore most analyses introduce uncertainties based on these sets (see section 10.2).

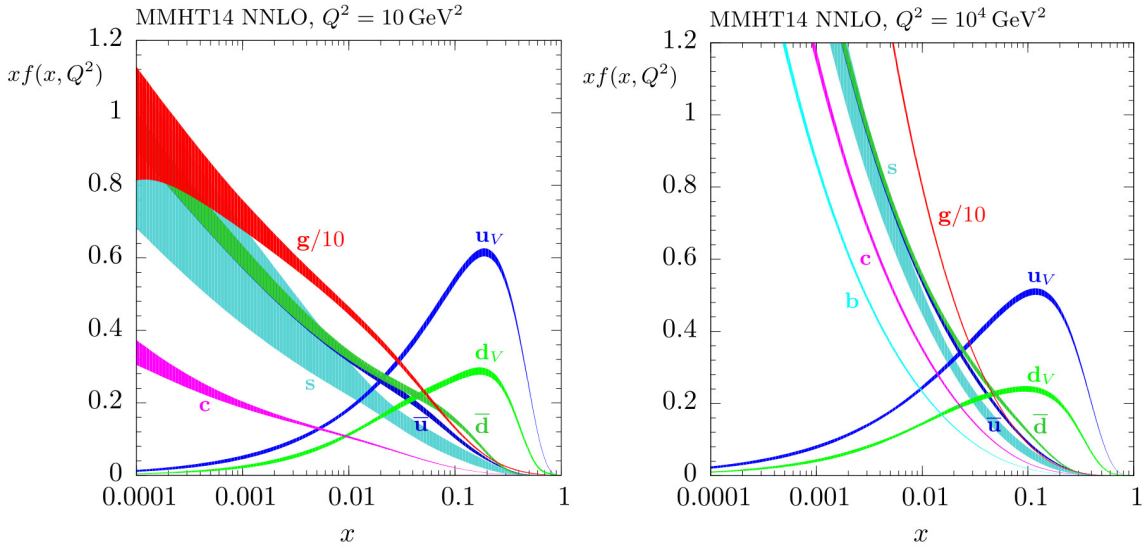

Figure 4.3: MMHT2014 NNLO Particle Distribution Functions of quarks and gluons at $Q^2 = 10$ GeV^2 and $Q^2 = 10^4$ GeV^2 [42]. The band widths indicate the 68% confidence level uncertainties.

PDFs influence the total cross section of a given physics process, as the effective center of mass energy depends on them. The individual components factorize and the cross section can be written as

$$\sigma_{pp\to X} = \sum_{a,b} \int dx_a dx_b \cdot f_a(x_a) \cdot f_b(x_b) \cdot \hat{\sigma}_{ab}(x_a, x_b, s)$$

where a and b are all parton pairs for which the parton level cross section $\hat{\sigma}_{ab}$ is non-zero, s is the total center of mass energy, $x_{a/b}$ are the Bjorken scales and $f_{a/b}$ their corresponding PDFs.

4.3. The ATLAS detector

ATLAS[5] [45] is a general purpose particle detector at the LHC with a length of 44 m and a diameter of 25 m (see figure 4.4). It allows for precision measurements and reconstructions of particle tracks, momenta and energies and is therefore suitable for the search for new physics like SUSY.

[3] Valence and sea quarks, as well as gluons.
[4] MMHT PDF [42], NNPDF [43], CT10 [44] and others.
[5] **A** **T**oroidal **L**HC **A**pparatu**S**

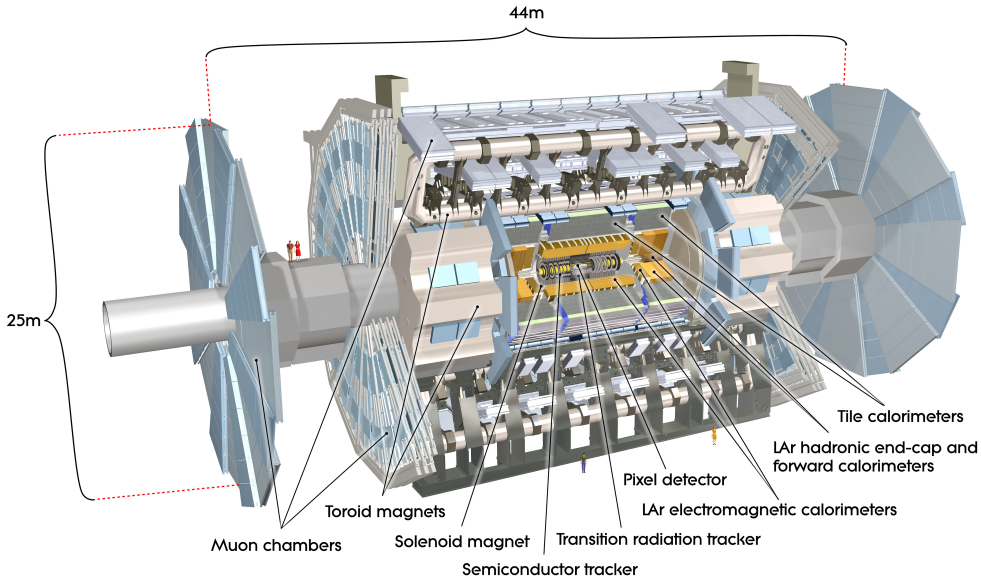

Figure 4.4: Computer generated image of the whole ATLAS detector [46].

The detector consists of several subsystems, namely the inner detector, the electromagnetic and hadronic calorimeters, and the muon system. After introducing the coordinate system, these detector components will be briefly described in this section.

4.3.1. Coordinate System

Given that the partons' Bjorken scales are not constant, the final states can have unknown boosts along the beam axis in the laboratory frame. If the detector had a perfect 4π coverage, the initial state could be derived from measuring the proton-remains. However, this is not possible, as the beam pipe needs to be free. It is therefore the norm to introduce special coordinates and variables that reduce the boost's effect:
The base is a right handed Cartesian coordinate system with its origin at the interaction point. Its x-axis points towards the center of the LHC ring, while the y-axis points upwards. The z-axis is therefore aligned with the beam axis counter clockwise. For the description of objects, one uses modified spherical coordinates. The azimuth angle ϕ is in the x-y-plane, but instead of using the polar angle θ, the pseudo rapidity

$$\eta = -\ln \tan \frac{\theta}{2}$$

is introduced. It is a good approximation[6] for the rapidity

$$y = \frac{1}{2} \ln \frac{E + p_z}{E - p_z}.$$

As rapidity differences $\Delta y = y_1 - y_2$ are invariant under Lorentz boosts along the z-axis, so are differences of the pseudo rapidity $\Delta\eta$ (in good approximation), and both are indifferent to

[6] $E \gg m$, which is usually the case at the LHC.

the unknown boost along the beam axis. The distance between objects can then be defined as

$$\Delta R = \sqrt{\Delta\phi^2 + \Delta\eta^2}.$$

An object's momentum is also biased by the unknown boost, so the variable of interest is usually the transverse momentum

$$p_{\mathrm{T}} = \sqrt{p_{\mathrm{x}}^2 + p_{\mathrm{y}}^2}.$$

Each interaction must conserve momentum in the transverse plane[7], so imbalances point towards particles that cannot be detected, like neutrinos or neutralinos. Thus the total transverse momentum of the invisible particles, missing transverse momentum $\vec{p}_{\mathrm{T}}^{\,\mathrm{miss}}$, can be obtained by be the negative vectorial sum of all visible contributions. Its module is referred to as $E_{\mathrm{T}}^{\mathrm{miss}}$:

$$\begin{aligned} E_{\mathrm{T}}^{\mathrm{miss}} &= |\vec{p}_{\mathrm{T}}^{\,\mathrm{miss}}| \\ \text{with } \vec{p}_{\mathrm{T}}^{\,\mathrm{miss}} &= -\sum_{i \in \text{visible}} \vec{p}_{\mathrm{T}}^{\,i}. \end{aligned}$$

4.3.2. Inner Detector

The Inner Detector is the subsystem closest to the interaction point and reconstructs tracks of charged particles with high precision in an area up to $|\eta| < 2.5$. It is surrounded by the Central Solenoid Magnet (2 Tesla, parallel to beam axis) and consists of the Pixel Detector, the Semiconductor Tracker (SCT) and the Transition Radiation Tracker (TRT) (see figure 4.5).

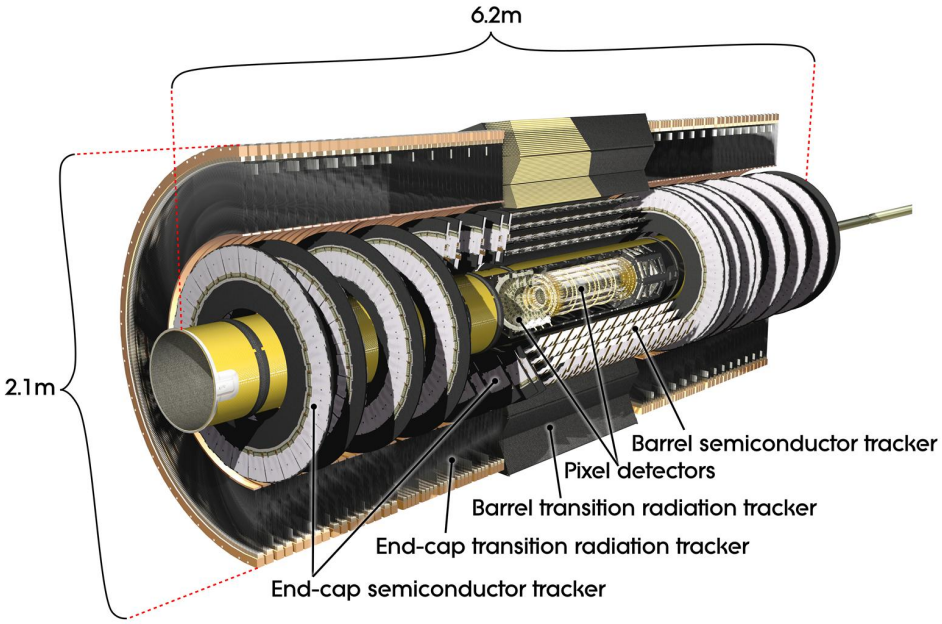

Figure 4.5: Computer generated image of the ATLAS inner detector [47].

[7]The conservation is also satisfied as a whole, but the z-component is unknown.

The Pixel Detector drives the reconstruction of interaction vertices as well as secondary vertices (see section 6.1), which can arise from long lived particles like B- or D-hadrons[8] and are of high importance for *heavy flavor tagging* (see section 6.5). It consists of three layers of silicon sensors, plus the Insertable B-Layer (IBL [48]) which was added at the beginning of *Run2* as a new innermost layer. The three layers contain roughly 80 million pixels with a size of 50 x 400 µm^2, while the IBL adds roughly 6 million pixels of 50 x 250 µm^2. The smaller radius and reduced pixel size improves the performance significantly.

The SCT is a silicon micro strip detector which consists of four barrels and 18 end cap discs, holding a total of 4088 modules. Each module contains two layers of silicon strips (80 µm x 12 cm, roughly 6 million in total) which are slightly rotated relative to each other in order to provide a two-dimensional position measurement.

The TRT is the outermost part of Inner Detector, however it covers only areas up to $|\eta| < 2$. It consists of gas filled straw tubes with 4 mm diameter and a wire at the center which serves as the electrode. They are aligned with the beam axis in the barrel region and radially in the end caps, so that only information in $R - \phi$ can be extracted. Polypropylene is used as transition radiation material between the tubes, prompting charged particles to emit radiation proportional to their Lorentz factor $\gamma = E/m$. This allows to separate between different types of particles like electrons and hadrons.

The tracks are reconstructed by combining information from all three subsystems [45]. The magnetic field forces charged particles on curved tracks which are used for the momentum measurement. As increasing momenta lead to smaller curvatures, the resolution also increases like

$$\frac{\sigma_{p_\mathrm{T}}}{p_\mathrm{T}} \approx \frac{0.05\% \cdot p_\mathrm{T}}{\mathrm{GeV}} \oplus 1\%.$$

4.3.3. Calorimeters

The ATLAS calorimeter (see figure 4.6) is a sampling calorimeter, meaning that passive and active layers appear alternately. Particles interact with the dense passive material, leading to electromagnetic or hadronic showers, whose energy depositions are measured in the active layers.

As the two shower types differ, there is a calorimeter for each of them. Electromagnetic showers originate from bremsstrahlung producing electron-positron pairs, which again radiate photons, thus leading to cascades of particles[9]. Bremsstrahlung decreases for higher particle masses, so only electrons and photons can be detected. Muons deposit almost no energy in the calorimeters, so an additional muon system is required (see section 4.3.4). Hadronic showers arise from strong interactions with the passive material and are typically longer and broader than electromagnetic showers. Therefore the electromagnetic calorimeter is built around the Central Solenoid Magnet and is surrounded by the hadronic calorimeter.

The electromagnetic calorimeter uses Liquid Argon (LAr) as active and lead as passive material, with the latter being arranged in an accordion like structure. The barrel ($|\eta| < 1.475$) is 0.53 m thick, corresponding to at least 22 radiation lengths X_0[10]. The end-caps ($1.375 < |\eta| < 3.2$, 0.632 m) have a small overlap with the barrel in η.

The hadronic calorimeter's barrel ($|\eta| < 1.7$) is a tile calorimeter containing ~500000 plastic scintillator tiles for detection and steel as absorber material. As for the electromagnetic

[8] Mesons containing Bottom or Charm quarks.
[9] Photons start by creating electron-positron pairs.
[10] X_0 is the mean distance over which an electron drops to $1/e$ of its former energy through bremsstrahlung.

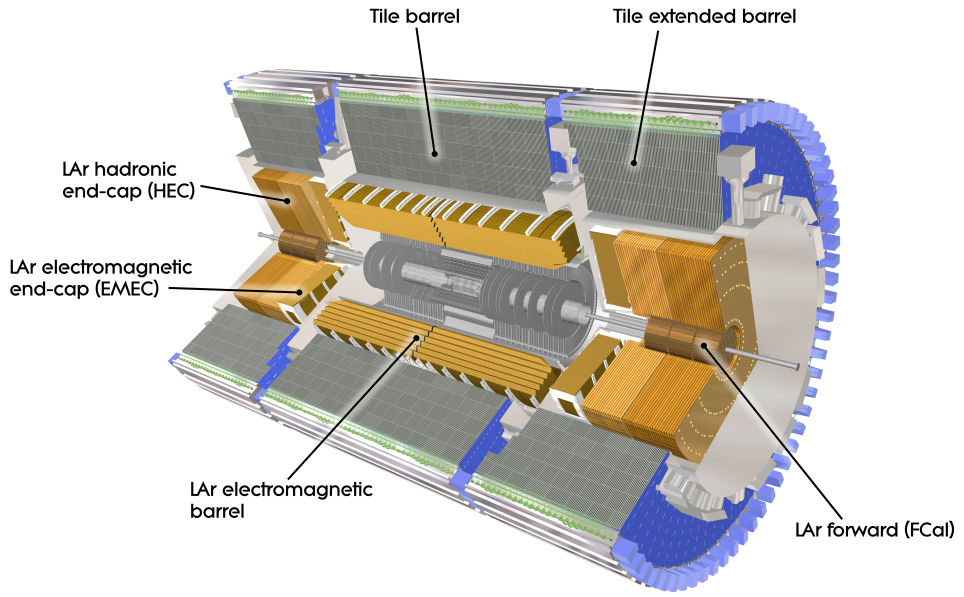

Figure 4.6: Computer Generated image of the ATLAS calorimeter [49].

calorimeter, the end-caps ($1.5 < |\eta| < 3.2$) use LAr as active material. The thickness corresponds to at least 10 nuclear interaction lengths λ_I.

The forward calorimeter (FCal) covers regions even closer to the beam pipe ($3.1 < |\eta| < 4.9$) and consists of three modules with a radius of 0.455 m and a thickness of 0.45 m each. LAr is used as the active material and both, electromagnetic and hadronic, showers are detected.

The ATLAS calorimeters are non-compensating, meaning that energy depositions are always measured at the electromagnetic scale. For hadronic showers calibration coefficients have to be applied in order to gain an equal response for hadrons as for electrons at the same energy. This can be done for example with the local cluster weight (LCW) algorithm. [50, 51, 52].

The overall resolution of the calorimeter improves with increasing particle energy E and can be written as

$$\frac{\sigma_E}{E} = \frac{N}{E} \oplus \frac{S}{\sqrt{E}} \oplus C,$$

where N is the noise term, S the stochastic term and C the constant term [45, 53]. N describes electronic and detector noise as well as pile up contributions. It is η dependend and increases from ~0.5 GeV in the barrel to ~1.5 GeV in the end-caps, and dominates at energies below ~30 GeV. At high energies (> 400 GeV) C is the dominant term. It includes fluctuations that are a constant fraction of the particle energy, like signal losses in passive materials, and is ~3% globally. In intermediate regions the statistical fluctuations of the energy measurement described by S are most relevant, as they reach ~60%$\sqrt{\text{GeV}}$. However there are correlations between these terms and they can not be disentangled entirely.

4.3.4. Muon system

As discussed before, muons can not be stopped by the calorimeters, as they emit almost no bremsstrahlung and do not interact strongly. They are, besides neutrinos that interact only weakly and can not be detected at all, the only SM particles that pass the other detector systems, and reach the muon system which is installed as the outermost detector part[11] (see figure 4.7). It contains the eponymous toroidal magnet which creates an inhomogeneous field of approximately 0.5 T, bending the muons orthogonal to the transverse detector plane. The muon system's precision measurements of the muons' momenta and trajectories are done in monitored drift tubes and cathode strip chambers. Thin-gap and resistive-plate chambers are used for triggering and additional precision on the track reconstruction. The muon system's measurements are later combined with track information from the inner detector.

A transverse momentum resolution of ~3% is reached in most of the $\eta - \phi$ plane, however it is degradet to ~5% at $|\eta| = 0.2$, 0.3 and 0.7 due to support structures of the magnet coils [45]. Another reduction of the resolution to ~5% in $1.1 < |\eta| < 1.7$ is due to the transition between the barrel and end-cap regions [45].

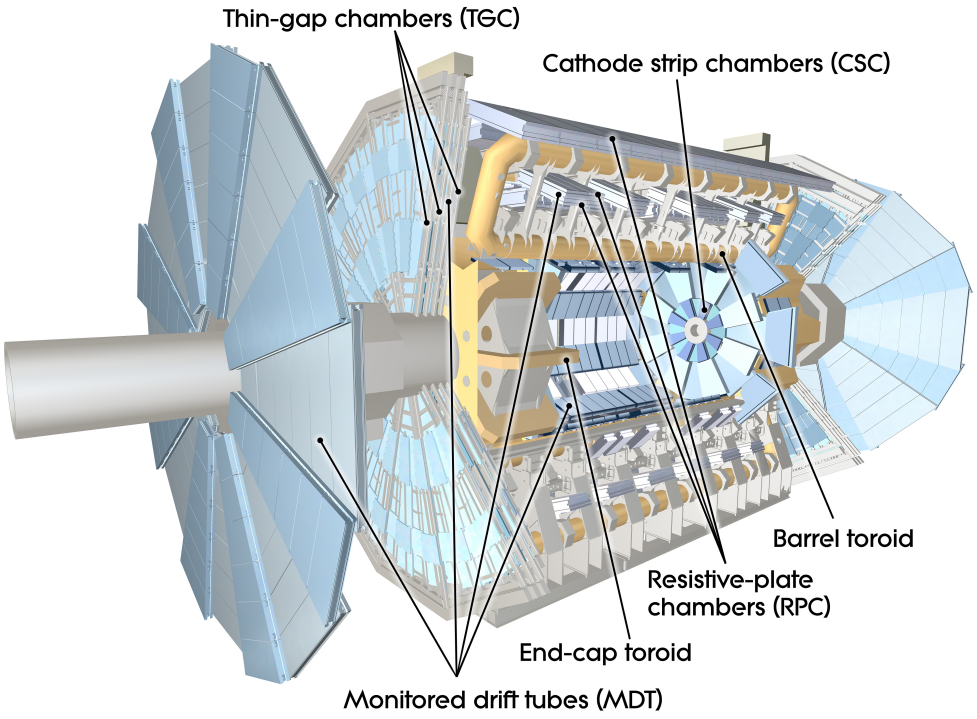

Figure 4.7: Computer generated image of the ATLAS Muons subsystem [54].

4.3.5. Trigger system

The LHC provides proton-proton collisions with a frequency of 40 MHz inside the ATLAS detector, which in return generates several Terabyte of data per second worth of measurements [55]. It is not possible to store all data at this rate, so *interesting* events need to be identified

[11] It should be noted that very high energetic jets can punch through the calorimeters and also reach the mon system.

and selected very fast and efficiently. This is achieved through a two-step trigger system, consisting of the Level 1 (L1) and the High-Level Trigger (HLT)[12].

L1 is purely hardware based and has access to calorimeter and muon data, but no tracking information. It is therefore, and also because of the limited time frame, not possible to perform the same object reconstruction as in offline analyses, meaning that the object definitions differ. By triggering on jets, electrons and muons, as well as variables calculated through simple algorithms like $E_{\mathrm{T}}^{\mathrm{miss}}$, the event rate is reduced to a maximum of 100 kHz[13]. L1 also marks certain $\eta - \phi$ ranges as Regions of Interest (RoI), which can be further investigated later on.

The software based HLT has on-demand data readout, meaning that it can utilize information from all detector parts in the RoIs. It implements object definitions closer to those in the analyses and uses more complex algorithms than L1. The event rate is brought down to ~1 kHz.

As mentioned before, trigger and analysis objects differ, therefore impacting the final event selection. Figure 4.8 shows the efficiency of L1 and HLT triggers versus offline $E_{\mathrm{T}}^{\mathrm{miss}}$. These *turn on curves* start at the nominal value of the L1 trigger, yet are not fully efficient until ~200 GeV offline $E_{\mathrm{T}}^{\mathrm{miss}}$. There are different algorithms in use that can improve the HLT performance, but the turn on is always driven by the L1 performance.

Selecting events before a trigger reaches its full efficiency is possible, but requires good modeling of the turn on curves and introduces systematic uncertainties.

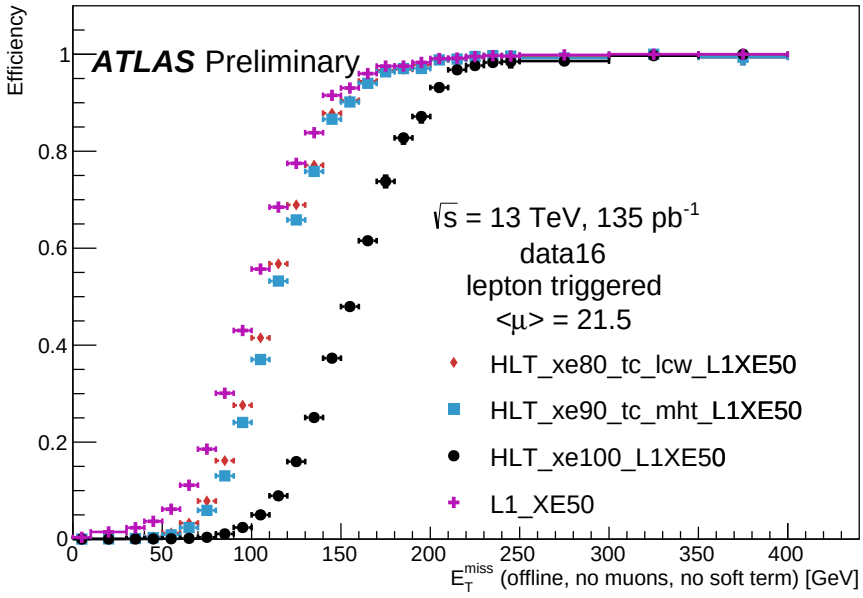

Figure 4.8: Turn-on curves for several $E_{\mathrm{T}}^{\mathrm{miss}}$ triggers. The performance of a L1 trigger and its combination with HLT triggers are shown [57].

[12] At the start of Run2 the before existing Level 2 trigger was merged with the former third step *Event Filter* into the HLT.

[13] During *Run2* a topological trigger has been added that allows the use of more complex algorithms like invariant mass calculations or pile up corrections for the $E_{\mathrm{T}}^{\mathrm{miss}}$ calculation [56].

4.3.6. Luminosity measurement

The precise knowledge of instantaneous and integrated luminosity is highly important for most physics analyses, as they determine the number of observed events. The ATLAS main luminometers are BCM[14] and LUCID[15], with other detectors (e.g. ALFA [58]) and methods (using inner detector tracks [41]) used additionally.

The BCM [59] consists of eight diamond sensors and provides bunch-by-bunch luminosities. The sensors are arranged in a cross pattern around the beam pipe at $z = \pm 1.84$ m of the interaction point. The horizontal and vertical sensors are read out separately, leading to two independent measurements that can be combined later on.

LUCID [45] is a Cherenkov detector consisting of 16 aluminum tubes that surrounds the beam pipe in a distance of 17 m from the interaction point. If hit by protons, Cherenkov photons are emitted and detected by photomultipliers. A single hit in one of the tubes records the bunch crossing.

While the relative instantaneous luminosity is being measured constantly, the absolute value needs to be derived in so called *van der Meer* scans [41]: during special runs, the beams are dislocated in the x-y plane and afterwards brought to collision by moving them along the axis. The luminometers then measure the luminosity as a function of the beam positions.

[14] **B**eam **C**onditions **M**onitor
[15] **LU**minosity measurement using a **C**herenkov **I**ntegrating **D**etector

5. Data set and Monte Carlo simulations

5.1. Data set and trigger

During the 2015 and 2016 data taking the LHC's center of mass energy was constant at $\sqrt{s} = 13$ TeV, so the combined data set can be used. The recorded integrated luminosities of these periods are shown in figure 5.1, however for data to be accepted as *good for physics*, the whole detector must be in a working state. The data taking is split into short time periods[1] called *luminosity blocks*, that are listed and marked as suitable in *Good Run Lists* (GRL). For this analysis the GRLs

`data15_13TeV.periodAllYear_DetStatus-v79-repro20-02_`
`DQDefects-00-02-02_PHYS_StandardGRL_All_Good_25ns.xml`
and
`data16_13TeV.periodAllYear_DetStatus-v88-pro20-21_`
`DQDefects-00-02-04_PHYS_StandardGRL_All_Good_25ns.xml`

are used, leaving a total integrated luminosity of $\int \mathcal{L}dt = 36.1$ fb^{-1}. It was derived following a methodology similar to that detailed in [41], from a calibration of the luminosity scale using x-y beam-separation scans performed in August 2015 and May 2016. The final uncertainty using these measurements is 2.1%. The average number of interactions per bunch crossing $<\mu>$ was 13.5 during the 2015 data taking and 24.9 in 2016.

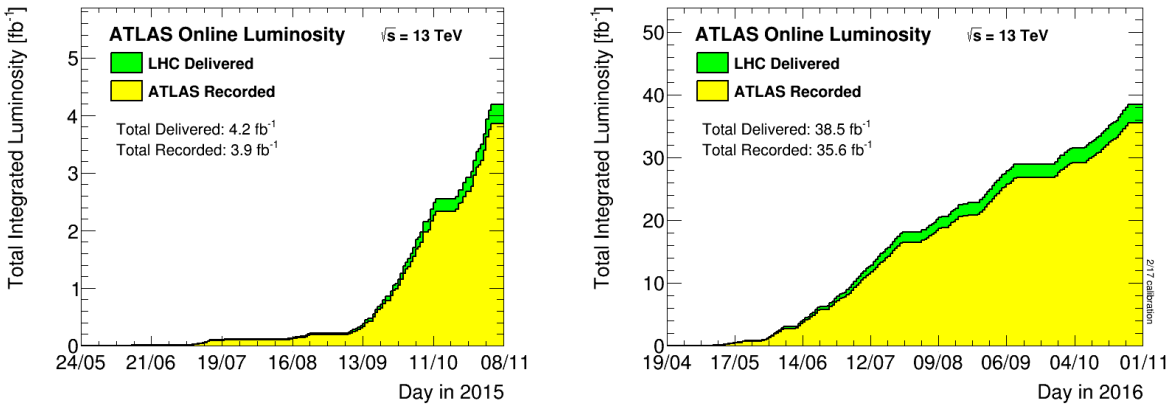

Figure 5.1: LHC's delivered and ATLAS' recorded integrated luminosities during the years 2015 (left [60]) and 2016 (right [61]).

As the LHC run conditions can change between fills (e.g. changes to the beam focusing), so can the instantaneous luminosity and therefore the trigger rate. In order to keep the output manageable, it is necessary to *prescale* triggers with low thresholds, meaning that they accept only a fraction of events that would otherwise pass them[2]. As prescaling effectively reduces

[1] Roughly one minute.
[2] This fraction can vary from relatively high probabilities to $< 10^{-6}$% for low p_{T} jet triggers.

luminosity, this analysis uses the lowest unprescaled triggers available for each time period. As a result different triggers are in use for the 2015 and 2016 data taking, and the $E_{\mathrm{T}}^{\mathrm{miss}}$ triggers were also changed during 2016 (see table 5.1). To select events with electrons or muons, a combination of several single lepton triggers are used, as their efficiency can drop at values high above their threshold. The details of the trigger algorithms (as indicated in the trigger names) are not important for this analysis and will not be discussed further.

Year	$E_{\mathrm{T}}^{\mathrm{miss}}$	Single electron	Single muon
2015	xe70	e24_lhmedium_L1EM20VH OR e60_lhmedium OR e120_lhloose	mu20_iloose_L1MU15 OR mu50
2016	xe80_tc_lcw_L1XE50 xe90_mht_L1XE50 xe100_mht_L1XE50 xe110_mht_L1XE50	e26_lhtight_nod0_ivarloose OR e60_lhmedium_nod0 OR e60_medium OR e140_lhloose_nod0 OR e300_etcut	mu26_ivarmedium OR mu50

Table 5.1: List of triggers used in this analysis. Their names indicate the algorithms used, as well as the corresponding thresholds in HLT and (in many cases) L1.

Examples for triggers and their turn on curves are shown in figures 4.8 ($E_{\mathrm{T}}^{\mathrm{miss}}$) and 5.2 (single lepton). To avoid selecting events before reaching the trigger plateau, the offline requirements must be chosen accordingly. Events that pass the $E_{\mathrm{T}}^{\mathrm{miss}}$ trigger also need to satsify $E_{\mathrm{T}}^{\mathrm{miss}} > 250$ GeV. For the single lepton triggers it is required that a reconstructed lepton of the same flavor fired one of them and satisfies $p_{\mathrm{T}} > 2\ \mathrm{GeV} + p_{\mathrm{T}}^{\mathrm{thresh}}$ with $p_{\mathrm{T}}^{\mathrm{thresh}}$ being the HLT Trigger threshold.

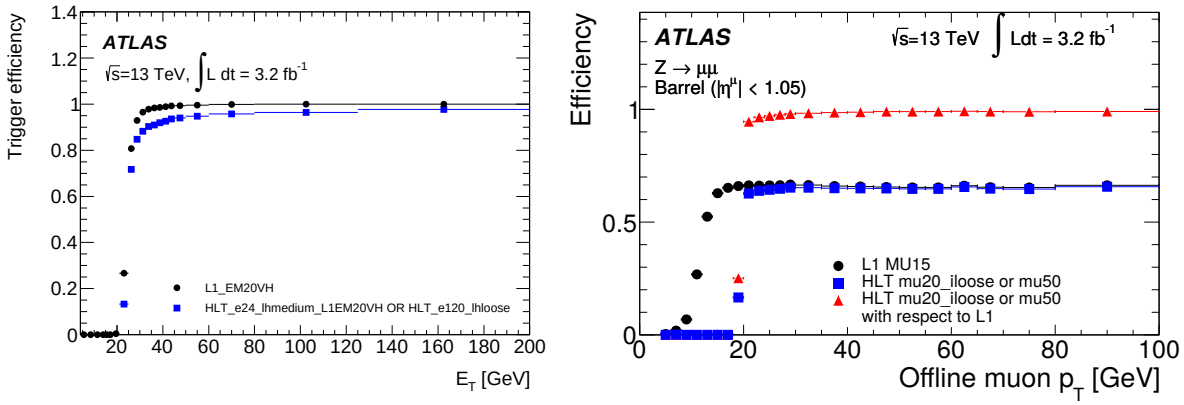

Figure 5.2: Examples for turn on curves of single electron (left) and single muon (right) triggers. [62]

5.2. Event cleaning

The GRLs remove whole luminosity blocks, if the overall detector performance was not sufficient. However, single events that pass these requirements can be flawed, so to further increase the data quality any event with one of the following criteria is discarded:

Primary vertex Events are required to have a reconstructed primary vertex (see section 6.1).

Bad jets *Baseline* jets surviving the overlap removal (see section 6.6) must pass the *Loose Bad* requirement, and also *Tight Bad* in case of the p_{T} leading jet (see section 6.5).

Bad muons Events are rejected if they contain *baseline* muons (see section 6.3) with $\frac{\sigma_{q/p}}{|q/p|} > 0.2$. q is the charge, p the momentum and σ the uncertainty. This can happen for high p_{T} muons with low curvature and can severely influence the $E_{\mathrm{T}}^{\mathrm{miss}}$ calculation.

Incomplete events After restarting parts of the trigger system, it is possible that information is not read out properly from the detector.

Subdetector error Subsystems like the SCT, Tile or LAr calorimeters can temporarily see huge noise bursts or produce errors during the readout, falsifying the energy measurement.

5.3. Monte Carlo Simulations

In order to analyze the collected data, theoretical predictions for signal and background processes need to be simulated in the most precise way possible. Monte Carlo (MC) generators simulate collision events by calculating matrix elements (ME) of the hard scatter processes and the subsequent *parton shower* and *hadronization*. Afterwards an *underlying event* is added and the the detector's response is simulated.

The ME describes the transition amplitudes between the initial and the final states, taking into account all allowed particle quantities like flavor, spin and color, as well as the proton substructure in form of PDFs (see section 4.2). It is calculated at a certain order in perturbation theory and can contain additional radiation of quarks and gluons. Not all radiation can be included, though, and a so called *matching* parameter $\mathcal{O}(10\ \mathrm{GeV})$ is defined, above which jets must be calculated in the ME, if the perturbation order is sufficiently high. The matching parameter and procedure depends on the generators used. In this analysis samples generated with Madgraph+Pythia use the *MLM* matching scheme [63], while Sherpa uses the *ckkw* [64] and Powheg the *hdamp* parameters [65]. The threshold's impact on the analysis needs to be investigated and is a source of systematic uncertainties.

Softer radiation is added in the parton shower step, which follows non-perturbative QCD and is usually described with empirical models. It has lower precision, but no limit on the particle multiplicity. All color charged particles are unbound after this step and are interacting with each other. The hadronization describes their formation of color neutral hadrons, which lead to jets.

Finally, the detector simulation is applied using the GEANT4 [66] based Athena framework [67, 68]. The detector's response to the formerly generated events, as well as the presence of additional pile up collisions, is simulated. The results are stored in a format similar to that of the recorded data[3], which allows the usage of the same object reconstruction algorithms on data and simulated events.

[3] It contains additional *truth* information on all particles from matrix element level to the final objects in the detector.

The detector simulation and reconstruction of objects are very time-consuming[4], so *filters* are applied on generator level to reduce the number of events in a certain phase space. As the analysis needs to be independent from the filtering, it must implement even tighter requirements, that would reject the missing events anyway. For example, an analysis has a requirement on the reconstructed $E_{\mathrm{T}}^{\mathrm{miss}}$, so a filter on the sum of all invisible particles' transverse momenta can be used. However, at generator level no detector and pile-up effects can be taken into account, so the filtered variable is not the same as in the analysis and the threshold needs to be chosen carefully.

Generator filters also allow to increase the MC statistic in certain phase spaces, like the tails of $E_{\mathrm{T}}^{\mathrm{miss}}$ or jet p_{T} distributions. A sample can be split into orthogonal *slices* of the particular variable, allowing to freely choose their number of events. Due to the orthogonality, the final prediction can be derived by simply adding the individual parts.

Background simulations

Many different MC generators are used for the background simulations, including Sherpa [64], Madgraph [63], Pythia [69, 70], Herwig [71, 72], Alpgen [73] and Powheg [65, 74]. The generators differ not only by their tuning, but also the fact that some of them are leading order (LO, e.g. Pythia) and others are next to leading order generators (NLO, e.g. Powheg). As a result, different generators yield different predictions at different accuracy. For each background process one generator is chosen as the nominal samples, later systematic uncertainties will be added to account for differences between the generators (see section 10.2).

Independent from the generators' precisions, the overall normalizations for each process are calculated using higher order cross sections (see table 5.2).

Process	Generator	Filter & slicing	Cross section
W/Z+jets	Sherpa 2.2.1	decay mode, boson p_{T}, ISR flavor	NNLO
Diboson	Sherpa 2.2.1	decay mode, ISR flavor	NLO
$t\bar{t}$	Powheg + Pythia6	decay mode, $E_{\mathrm{T}}^{\mathrm{miss}}$	NNLO+NNLL
Single top	Powheg + Pythia6	decay mode, $E_{\mathrm{T}}^{\mathrm{miss}}$	NLO
$t\bar{t}Z$, $t\bar{t}W(W)$	Madgraph + Pythia8	decay mode	NLO+NNLL
3/4 top	Madgraph + Pythia8		NLO

Table 5.2: MC generators used for the nominal background predictions.

Signal simulations

As discussed in section 3, the signal models used in this analysis have $m_{\tilde{q}}$ and $m_{\tilde{\chi}_1^0}$ as free parameters, therefore all allowed combinations need to be tested. This is clearly not possible, so a grid of points in the $m_{\tilde{q}}$-$m_{\tilde{\chi}_1^0}$-plane is defined to cover the parameter space (see figure 5.3). In most of the plane ($\Delta m > m_W + m_b$) the step size in both parameters is 50 GeV. The remaining grid has a step size of 25 GeV in $m_{\tilde{q}}$ with each four points at varying Δm. The increased density is required as the signal kinematics change much more with respect to Δm in this region than for higher mass differences. In order to reduce the number of generated events, several points were removed if no change in signal characteristics is expected with respect to adjacent points

[4] Up to several minutes per event.

As the squark mass drives the cross section, the number of expected events varies and can go up to ~750000 for a single point. It is not feasible to generate that many events, so a generator filter of $E_{\mathrm{T}}^{\text{miss, generator}} > 100$ GeV is applied. The event selection will require events to satisfy reconstructed $E_{\mathrm{T}}^{\text{miss}} > 250$ GeV, so the threshold is sufficiently low, yet, results in filter efficiencies down to ~5%. Samples with $\Delta m < m_W + m_b$ are additionally split at $E_{\mathrm{T}}^{\text{miss, generator}} = 250$ GeV to further increase the statistics in the tails. Using these filters, it is possible to generate events with an equivalent luminosity of ~100 fb^{-1} for all points except those at $m_{\tilde{q}} \leq 300$ GeV, which have an equivalent of ~50 fb^{-1}.

All signal events are generated using Madgraph for the matrix element calculation with up to two additional ISR jets, and Pythia8 for the showering. The cross section is calculated at NLO+NLL precision [75, 76, 77, 78].

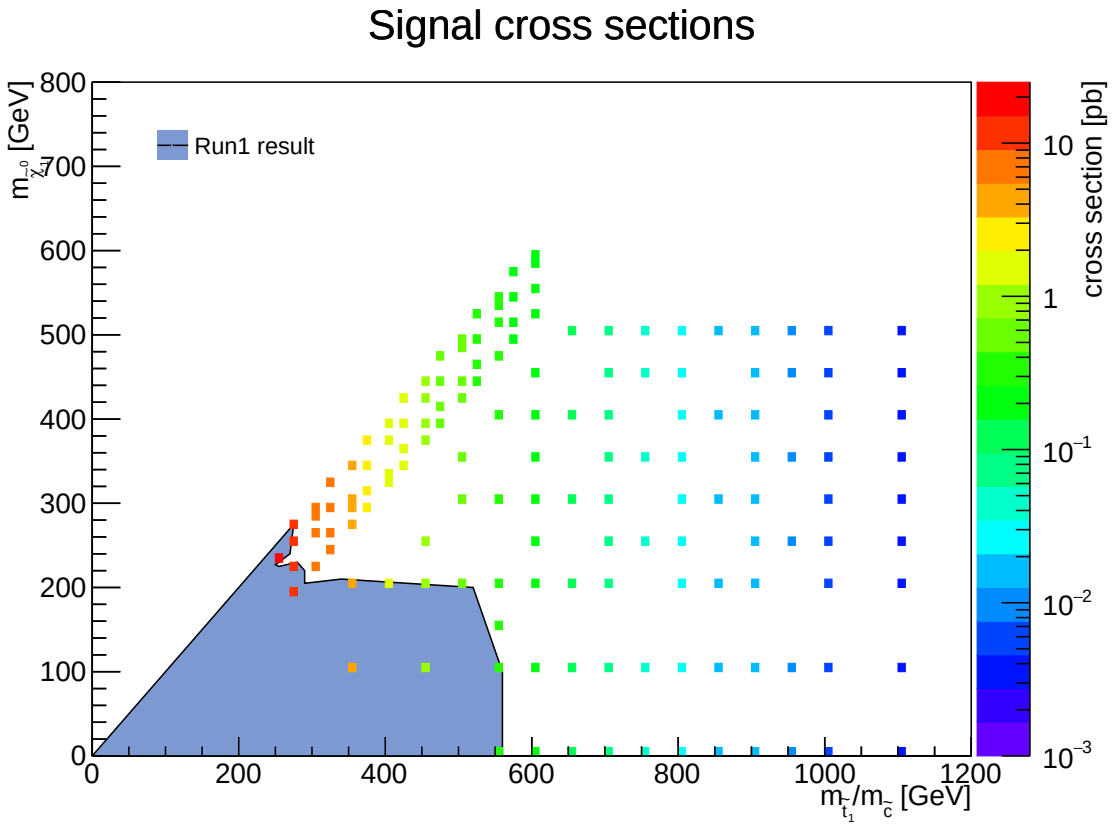

Figure 5.3: Overview of the signal grid and the cross sections for each point.

6. Object definitions

In order to perform physics analyses, the information recorded by the detector needs to be identified with physical objects. This chapter describes the definitions of reconstructed objects with a special attention on the identification of jets from charm quarks.

6.1. Vertices

As discussed before, each bunch crossing leads to a number of interactions between protons. The collision positions are called *vertices*, as all scattered and produced particles' paths emerge from there. They can not be directly measured, but their position can be reconstructed using the detector's track information, for which at least two tracks are required. The *primary vertex* is defined as having the highest sum of squared transverse track momenta $\sum p_{\mathrm{T}}^2$, while all other vertices along the beam axis are labeled *pile up vertices* [79].

When reconstructing objects, they are often required to originate in the primary vertex, to reduce the influence of pile up collisions. The *transverse* and *longitudinal impact parameters* (IP, d_0 and z_0) are defined in the point of closest approach (PCA) of the track to a reference point on the beam axis $\vec{r}$. d_0 is the distance in the transverse plane and identical for each interaction vertex. Often its significance $d_0/\sigma_{d_0}$is used, with σ_{d_0} being the uncertainty. z_0 is the distance in longitudinal direction and can be used to calculate the corresponding value for a given vertex position $\vec{p}$ via $\Delta z_0 = z_0 + r_z - p_z$. To avoid rejecting jets from the forward region, which have a larger uncertainty on z_0, $\Delta z_0 \sin\theta$ can be used, where θ is the track's polar angle. This parameter's significance can also be calculated for an even tighter constrain.

Particles with a travel distance of $\mathcal{O}(10\ \mu\mathrm{m})$ before decaying, like taus or B-hadrons, can lead to *secondary vertices*, that are displaced from the primary vertex. These differ from interaction vertices in a sense that they originate from a single particle instead of a collision, but their decay products' tracks will emerge from their position. The impact parameters of secondary vertices are crucial for heavy flavor tagging, as they are neither produced by light quarks nor gluons (see section 6.5).

6.2. Electrons

Electrons and positrons, in the following collectively referred to as electrons, create tracks in the inner detector and deposit their energy in the electromagnetic calorimeter. Their reconstruction proceeds in several steps [80]. A sliding window algorithm with a size of 3×5 calorimeter cells (in $\eta \times \phi$) searches for so called *cluster seeds* with a total energy above 2.5 GeV, which are used as input for clustering algorithms [81]. Tracks are chosen using special pattern recognition[1] and are matched to the clusters. If several tracks can be matched, the *primary* track is chosen via the distance ΔR to the cluster seed. An electron candidate's total energy is taken from the calorimeters, while its direction corresponds to the primary track.

[1] The opposing pattern recognition is used for pions and accounts for less energy loss due to bremsstrahlung. For more information see [82].

Electron candidates are classified into three categories using quantities related to their calorimeter shower shapes, track-cluster matching, track properties, number of hits in the IBL and bremsstrahlung effects (for more information see [80]). The identification (ID) categories are called *Loose*, *Medium* and *Tight*[2] and differ in signal efficiency and background rejection (see figure 6.1). To further reduce the background, *isolation* can be required on top of any ID, meaning that no further calorimeter activity close to the the candidate's cluster is allowed.

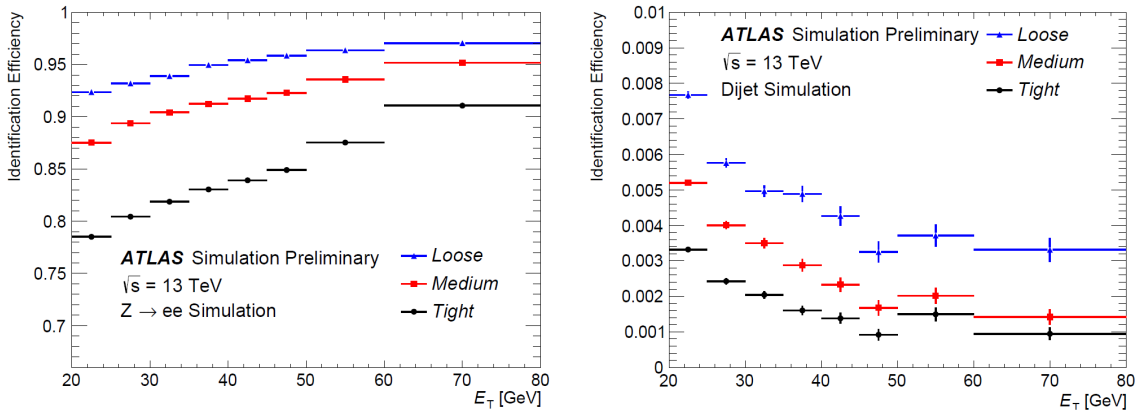

Figure 6.1: Identification efficiencies for electrons (left) and for jets (right) for *Loose*, *Medium* and *Tight* electron identification criteria [80].

p_{T} and η dependent efficiencies have been measured in data and simulations for all working points using the *tag-and-probe* method[3] in $J/\Psi \to ee$ and $Z \to ee$ events. These result in correction factors for the simulations, as well as uncertainties through varying the selection and ID criteria.

In this analysis, a further specification for the electrons candidates is applied. *Baseline electrons* are required to pass the *Loose* ID and satisfy $p_{\mathrm{T}} > 7$ GeV and $|\eta|<2.47$. They are used in regions vetoing electrons, like those enriched with the signal processes (see section 3.2). The softest available ID proves to be most suitable, because the gain from vetoing more events with electron candidates is higher than the rejection of signal events due to misidentification, which happens rarely. *Signal electrons* are defined to be isolated baseline electrons that pass the *Medium* ID, originate from the primary vertex ($d_0/\sigma_{d_0} < 5$ and $\Delta z_0 \sin\theta < 0.5$ mm) and satisfy $p_{\mathrm{T}} > 25$ GeV. This definition is used in regions requiring at least one electron.

6.3. Muons

Muon candidates are reconstructed by combining tracks from the inner detector and the muon system [83]. The inner detector tracks are selected in a similar way as described for electrons. For tracks in the muon system, hits aligned on a trajectory are searched by fitting track segments in the subdetectors.

Depending on the tracks found in the inner detector and the muon system, different combination types are used. In case of overlapping candidates, the method with better performance is chosen (the list is sorted from high to low).

[2] These correspond to the likelihood based definitions in [80].

[3] A *tag* electron with a tight selection and a loose *probe* electron are selected, and are required to satisfy another criterion, like an invariant mass close to m_Z. The probe can then be used to measure the efficiency. The tag selection is not necessarily the *Tight* selection discussed before.

1. **Combined** Tracks in the inner detector as well as multiple segments are available, and are fitted to one trajectory. The best performance is achieved by this method.

2. **Segment tagged** Only one segment is found in the muon system for a given inner detector track. Acceptance can be extended to muons that pass only one layer of the muon system because of low p_{T} or detector architecture.

3. **Calorimeter tagged** An inner detector track can be matched to energy depositions in the calorimeter that is compatible with a minimum-ionizing particle. The purity is very low but this method regains acceptance in regions where no muon spectrometer is instrumented because of cabling (e.g. $|\eta| < 0.1$).

4. **Extrapolated** No inner detector track is available and the trajectory is reconstructed based only on the muon system information. This method extends the muon reconstruction to areas outside of the inner detector coverage ($2.5 < |\eta| < 2.7$).

The muon candidates are classified as *Loose*, *Medium*, *Tight* and *High-p_T* depending on their number of hits in the muon system, quality of tracks and combination type. *Medium* accepts only *combined* and *extrapolated* ($2.5 < |\eta| < 2.7$) muons with at least three hits in the detector. Additionally the momentum measurements from the inner detector and the muon systems must be compatible. The *Loose* classification extends *Medium* by allowing all combination types in the $|\eta| < 0.1$ region. Efficiencies are measured in data and simulations in order to obtain correction factors, as well as their uncertainties (see figure 6.2).

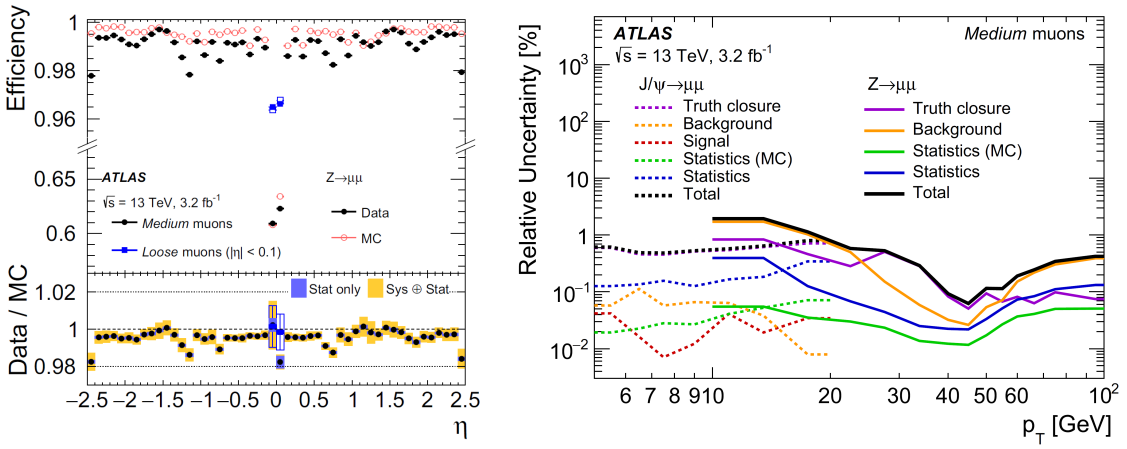

Figure 6.2: Identification efficiencies for the *Loose* and *Medium* muon IDs as a function of η (left) and relative uncertainties of the efficiency scale factors for the *Medium* muon ID as a function of p_{T} (right). [83]

An isolation criterion can be defined by requiring low calorimeter activity close to the reconstructed trajectory. This rejects most muons originating from hadron decays, as they are usually embedded in jets.

As for electrons, two types of muons are used. *Baseline muons* must pass the *Loose* requirement and satisfy $p_{\mathrm{T}} > 7$ GeV and $|\eta|<2.7$. *Signal muons* additionally need to be isolated, have $p_{\mathrm{T}} > 25$ GeV and originate from the primary vertex ($d_0/\sigma_{d_0} < 3$ and $\Delta z_0 \sin\theta < 0.5$ mm). They are used in analogy to their electron counterparts.

6.4. Taus

Taus can decay either hadronically or leptonically, with both containing at least one neutrino that leads to missing transverse momentum. The leptonic decay produces electrons or muons that are reconstructed as described before. The hadronic channel on the other hand forms jets that are often identified as originating from a secondary vertex due to the tau's lifetime [8], leading to a high mistag probability and an enhanced selection efficiency when applying charm tagging (see section 6.5).

It is possible to define tau IDs to reject these events, however the efficiency is lower and the uncertainties are higher than for electrons and muons [84]. It was found that most events with mistagged tau jets can also be rejected by a simple cut on the transverse mass of these jets and $\vec{p}_{\mathrm{T}}^{\,\mathrm{miss}}$ (see section 7.1), such that a special tau reconstruction and identification is not necessary. In the following *leptons* will refer only to electrons and muons excluding taus, if not noted otherwise.

6.5. Jets

Quarks and gluons, that were scattered or produced in collisions, hadronize while passing the detector. The hadrons leave tracks in the inner detector (if they are charged) and create hadronic showers in the calorimeters. Topologically connected calorimeter cells with sufficient energy depositions are combined to three dimensional *topological clusters*, that serve as input for the anti-k_t algorithm [85], an infrared and collinear safe[4] jet finding algorithm. Starting with the most energetic cluster, all cells above the noise threshold are merged into jets with a radius parameter of $R = 0.4$. In order to associate the jets with inner detector tracks, the latter are added to the algorithm with infinitesimal p_{T}. This does not bias the calorimeter-based result, but shows which tracks belong to each jet [86].

Jets need to be calibrated in several steps to improve their energy resolution (JER) and scale (JES) [52, 87] (see figure 6.3).

First the jet origin is changed to match the primary vertex instead of the nominal interaction point. As the longitudinal beam spot size is ~5 cm this has a huge impact on the η resolution. The second step is to correct for pile up effects by subtracting the pile-up energy density (depending on the number of pile up vertices N_{PV}) from the jet areas [86, 88] and a residual correction for in-time[5] and out-of-time[6] pile up. Afterwards a purely simulation based correction is applied, to bring the detector response closer to the true energy of the jets. Additionally a correction for the difference of quark and gluon jets, as well as a *punch-through*[7] correction are used. Finally, for data in-situ calibration techniques are applied, that use reference objects (photons, Z bosons or other jets) recoiling against the jets in the transverse plane.

The jet energy measurement has more than 70 independent uncertainties [87], resulting from the various calibration and correction methods. The total and the most important ones are shown in figure 6.4. However it is possible to combine these parameters to a reduced set with minimal loss of correlations, resulting in 18 variations. More information on these uncertainties can be found in section 10.

[4] It is almost unchanged by the emission of gluons under a small angle or with low energies.
[5] Energy depositions from collisions in the same bunch crossing, depending on N_{PV}.
[6] Energy depositions from previous and following bunch crossings, depending on $<\mu>$.
[7] Jets with very high energies can have showers that extend the calorimeters and punch through into the muon system. Their energy will therefore not be fully deposited in the calorimeters.

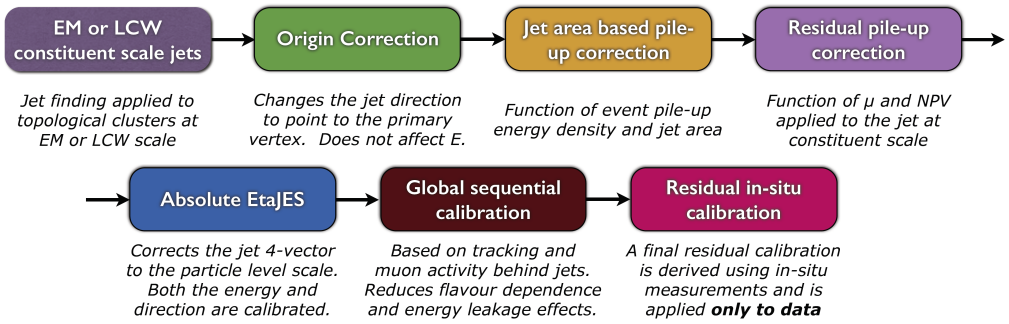

Figure 6.3: Schematic overview of the jet calibration [52].

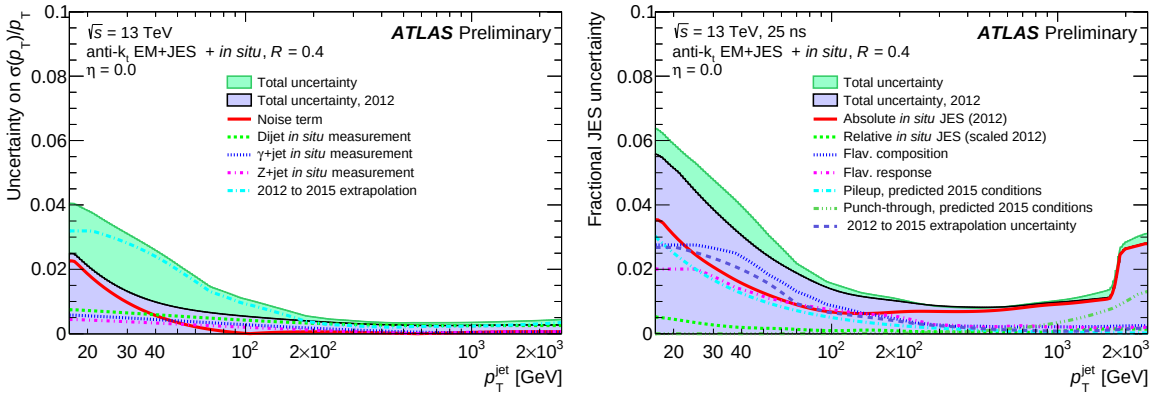

Figure 6.4: Uncertainties on the jet energy resolution (left) and jet energy scale (right) as a function of jet p_{T}. [87]

When selecting jets in the analysis, only those from the hard scattering process should be taken into account, so pile up jets need to be rejected. This is done using a two dimensional likelihood called *jet vertex tagger* (JVT) [89]. Its first input is the charged fraction of a jet

$$R_{p_{\mathrm{T}}} = \frac{\sum_k p_{\mathrm{T}}^{\mathrm{track}_k}}{p_{\mathrm{T}}^{\mathrm{jet}}}$$

where $p_{\mathrm{T}}^{\mathrm{track}_k}$ is the transverse momentum of a track that belongs to the jet and originates from the primary vertex. $p_{\mathrm{T}}^{\mathrm{jet}}$ is the total jet transverse momentum based on calorimeter measurements. The second input is a modified version of the *jet vertex fraction* (JVF, see figure 6.5 left). The JVF is a measure for the fraction of transverse track momenta from the primary vertex over the sum of the tracks from all vertices in the jet. Figure 6.5 (right) shows the JVT's separation power. The working point is chosen to yield a 90% signal efficiency and a fake rate of 1%[8].

In order to remove jets with bad quality (e.g. jet candidates from electrons), additional cleaning criteria are applied. Among other variables, these criteria are based on $R_{p_{\mathrm{T}}}$, measures for the calorimeter noise, and the energy fractions deposited in the electromagnetic and hadronic calorimeters. Two working points called *Loose Bad* and *Tight Bad* are defined as described in [90]. In this analysis all jets are required to not be marked as *Loose Bad*, while the p_{T} leading jet must also not be marked as *Tight Bad*. If any bad jet persists after the overlap removal (see section 6.6), the whole event is vetoed.

[8] This definition corresponds to the medium working point in [89].

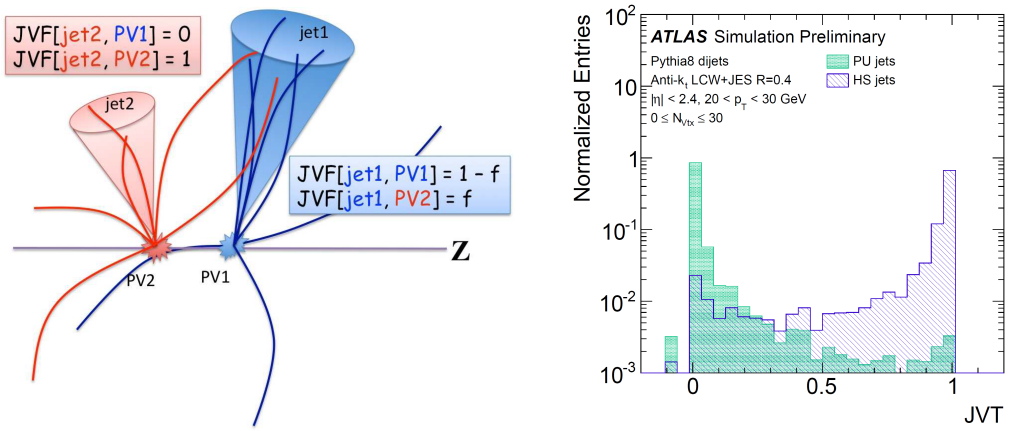

Figure 6.5: Left: Schematic representation of the Jet Vertex Fraction [86]. Right: JVT distribution for pile up and hard scattering jets [89].

In this analysis two types of jets are defined. *Baseline Jets* have to pass the JVT criterion, and satisfy $p_{\mathrm{T}} > 20$ GeV and $|\eta| < 2.8$. They are used only for the recalculation of $E_{\mathrm{T}}^{\mathrm{miss}}$ (see section 6.7) and during the overlap removal procedure.

Signal Jets are tightened to $p_{\mathrm{T}} > 30$ GeV and $|\eta| < 2.5$. The latter is required, as the jets are candidates for charm tagging, which requires the full inner detector information. In the following signal jets will be simply referred to as jets if not noted otherwise.

Charm tagging

The identification of jets from charm quarks, in the following referred to as *charm tagging*, is crucial to reject background events in this analysis. This chapter follows the descriptions in [91], as the corresponding charm tagging note is not published at the time of writing. The procedure is the same, except that the *boosted decision tree* (BDT) is trained with different signal and background compositions.

Heavy flavor tagging in general tries to separate jets from different quark flavors. It is mainly based on the hadron lifetimes from heavy (bottom and charm) quarks, and the secondary vertices that can be reconstructed from their decays. The current methods were developed for bottom tagging, but can be used for charm tagging as well. The algorithms use inner detector track and vertex information to produce variables suitable to differentiate between jets from charm quarks (charm jets), bottom quarks (bottom jets), and light quark flavors and gluons (light or light-flavored jets). However the resulting efficiencies and background rejections are worse for charm tagging, as the main variables have less separation power from the backgrounds (mainly light jets) than for bottom tagging.

Impact parameter based algorithm The algorithms *IP2D* and *IP3D* [92] are based on the *signed* IP significances of a jet's tracks. These significances are calculated as described in section 6.1 and are defined to be negative, if a track's PCA to the primary vertex points in the opposite jet direction. The distributions (see figure 6.6) are interpreted as probability density functions and used to calculate likelihoods (P_{b}, P_{c}, P_{light}) for each jet flavor. The final outputs are logarithmic ratios of these probabilities for each jet, for example $\log(P_{\mathrm{c}}/P_{\mathrm{light}})$.

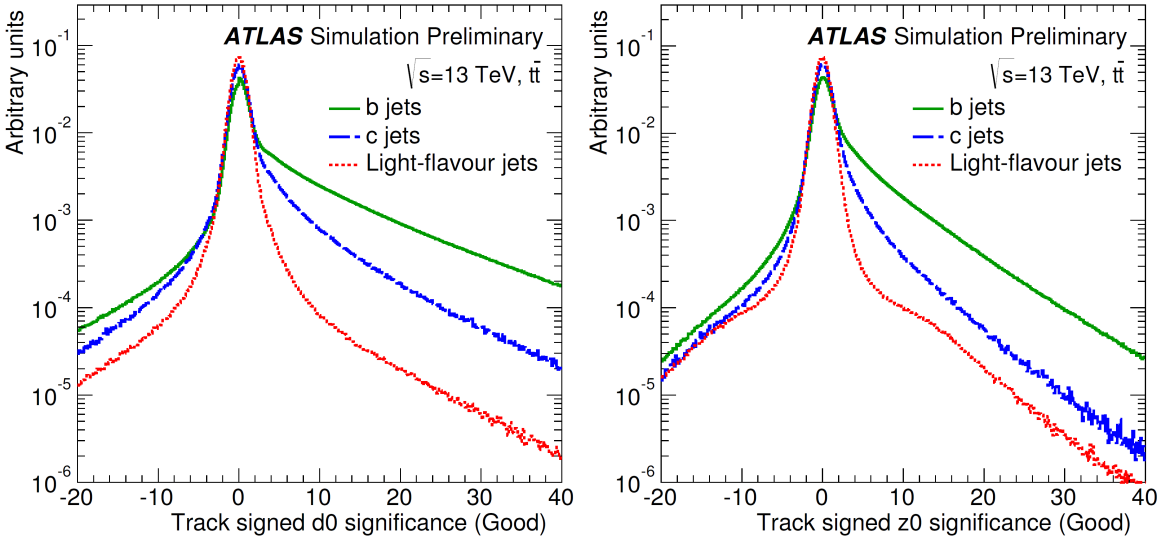

Figure 6.6: Transverse (left) and longitudinal (right) signed impact parameter significance for tracks in b, c and light-flavored jets. *Good* denotes the track selection as described in [91].

Secondary vertex finding algorithm The algorithm *SV* [92] tries to reconstruct secondary vertices within jets. In a first step tracks are selected by forming vertices from track-pairs and rejecting the tracks, if they are likely to be originating from the decay of long-lived particles (e.g. K_S or Λ), photon conversions or hadronic interactions with the detector material. The remaining tracks are used to reconstruct a single secondary vertex, removing outlier tracks in the process. The efficiency of finding secondary vertices depends heavily on the jet flavor and is a factor ~2.5 lower for charm jets than for bottom jets (see figure 6.7 left). For the reconstructed secondary vertices different properties can be measured (see figure 6.7 center and right): $N_{TrkAtVtx}$ is the track multiplicity and shows a much worse separation between charm and light jets, than between charm and bottom jets. f_E is the ratio of the track energy from the secondary vertex and the total energy of the jet. It shows a separation of charm jets mainly from light jets and is one of the driving variables for the rejection of this background.

Decay chain multi-vertex algorithm The *JetFitter* algorithm [93, 94, 95] also reconstructs secondary vertices. However it exploits the topological structure of weak b- and c-hadron decays inside the jet. It is assumed that the primary and secondary vertices are aligned on a *flight line* from which single tracks emerge. These tracks are then clustered into individual secondary (or higher order) vertices, thus resulting in the full decay chain. *JetFitter* is capable of reconstructing secondary vertices with only one reconstructed track, which leads to a higher reconstruction efficiency than requiring vertices to have at least two tracks or using *SV* (see figure 6.8 left). However, the relative gain of allowing single track vertices is higher for light jets (~1.5) than for bottom jets (~1.2) and charm jets (~1.4). The secondary vertices' properties again can be used to separate the jet flavors (see figure 6.8 right).

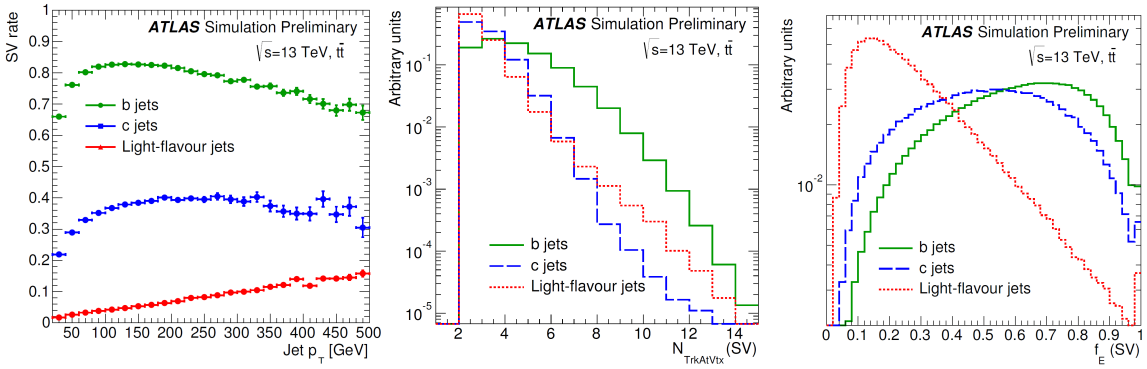

Figure 6.7: Left: *SV* reconstruction efficiency of secondary vertices. Center: *SV* Track multiplicity of secondary vertices. Right: *SV* Fraction of the energy from secondary vertex tracks compared to the total energy of the jet. All plots from [91].

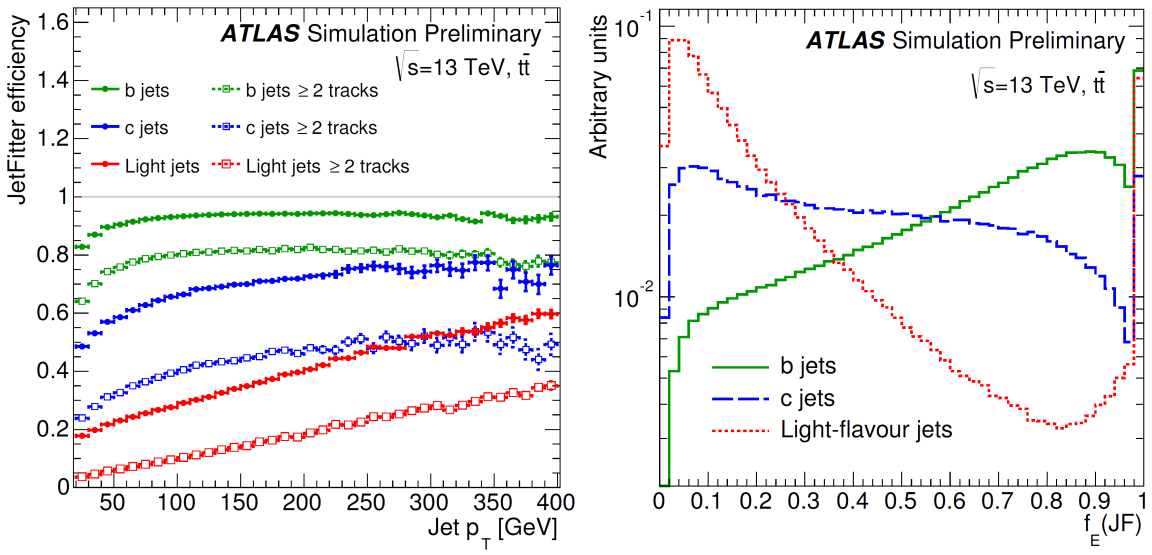

Figure 6.8: Left: *JetFitter* reconstruction efficiency of secondary vertices with at least one or two tracks. Right: *JetFitter* Fraction of the energy from secondary vertex tracks compared to the total energy of the jet. [91].

The algorithms' outputs are used to train two boosted decision trees (BDT). The first one is called MV2c100 and uses bottom jets as signal and charm jets as background[9], while MV2cl100 defines the charm jets as signal and light jets as background. The responses for both BDTs are shown in figure 6.9 for all jet flavors. Bottom jets are mostly accumulated in the upper right corner (high MV2c100 and high MV2cl100) and light jets tend to be in the lower left (low MV2c100 and low MV2cl100). Charm jets are more spread out and can be found in the upper left (low MV2c100 and high MV2cl100) and lower left areas. Still, most light jets can be rejected by selecting the upper left corner, at the cost of a significant efficiency loss for charm jets. Tau jets on the other hand have an even higher overlap with charm jets and can not efficiently be rejected, which is a result of them being not considered during the training. However, in the end this mistag rate has only a minor influence, as most effected events can be rejected using kinematic cuts (see section 7.1).

The working point was chosen to keep the *Run1* charm jet efficiency of roughly 20% [32], while improving all other flavors' rejections. In *Run1* events with top quarks (see section 7.2) were among the main backgrounds and sources of uncertainties, thus the rejection of bottom jets was focused over that of light jets.

A jet is defined to be *charm tagged* if it satisfies MV2cl100 > 0.7 and MV2c100 < -0.3 simultaneously. The average charm jet efficiency is ~18%, while reaching rejections for bottom and light jets of around 20 (8 in *Run1*) and 200 (200 in *Run1*), respectively. The working point and its average efficiencies are shown again in table 6.1.

MV2cl100	MV2c100	ϵ_c	$1/\epsilon_\mathrm{b}$	$1/\epsilon_\mathrm{light}$	$1/\epsilon_\tau$
> 0.7	< -0.3	0.18	20	200	6

Table 6.1: Definition of a charm tagged jet and the average efficiencies for the different jet flavors.

The tagging efficiency is not constant, though, and is instead highly dependent on the jet p_T (see figure 6.10). It peaks between ~100-150 GeV and drops rapidly for higher values. This will negatively impact the sensitivity of signal events with both low and high mass differences, as the jets' momenta directly depend on Δm.

Charm tagging needs to be calibrated in order to remove discrepancies between data and simulations. Several different approaches are used for the calibrations of light [96], bottom [97], and charm jets [98], resulting in correction factors (and corresponding uncertainties) depending on jet flavor, transverse momentum and pseudorapidity. The values range between ~1.4-1.8 for light flavor jets, ~0.85-0.95 for charm jets, and ~0.82-0.88 for bottom jets[10]. The systematic uncertainties are $\sim 25\%$ for each flavor, which could lead to huge total uncertainties for the analysis. Therefore the control region strategy is chosen such, that the uncertainties on the transfer factor cancel (see section 8).

[9] The result is the same as with switched roles, except for a sign of the BDT discriminant.

[10] At the time of writing no public documentation of the charm tagging calibration and the resulting uncertainties was available.

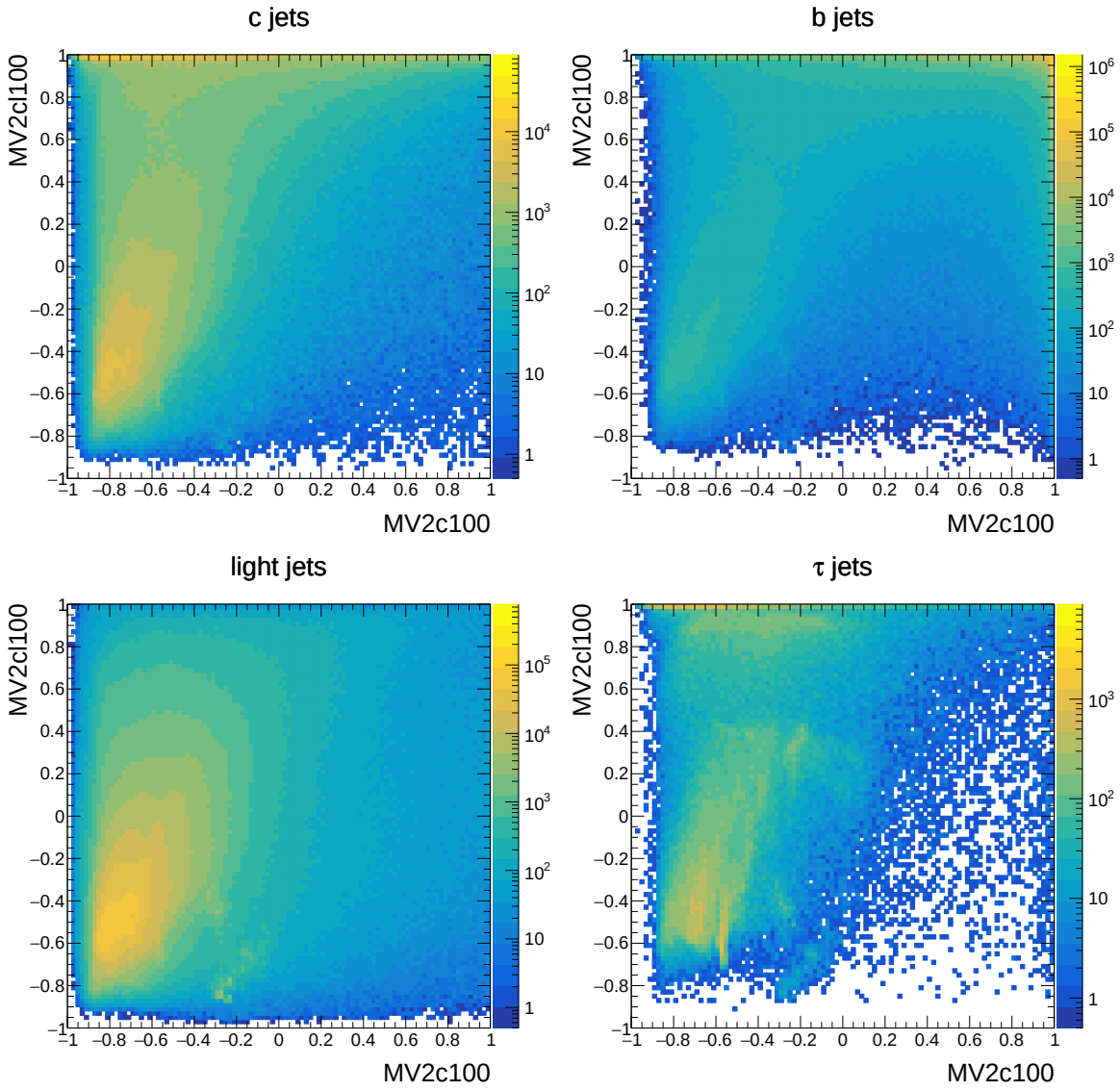

Figure 6.9: Scatter plots of MV2c100 and MV2cl100 for jets of different flavors.

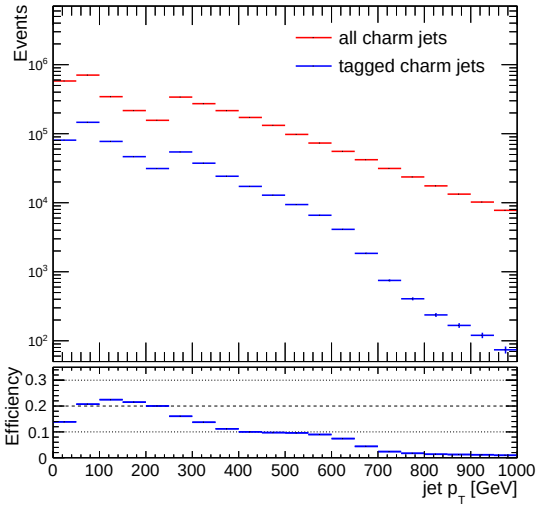

Figure 6.10: Jet p_{T} dependent tagging efficiency for charm jets. The dip at 250 GeV is due to a cut on the leading jet in the event selection used for this plot.

6.6. Overlap removal

The described object definitions are non-exclusive, meaning that a single physical object can be identified as two different types of reconstructed objects. The identification criteria limit these effects to only a few combinations, though. For example, each electron will also lead to a jet candidate in its vicinity, as tracks and energy depositions in the calorimeters are found. However jets from neutral hadrons do not leave tracks, thus it's not possible for them to be reconstructed as an electron. The *overlap removal* procedure searches for these problematic object pairs and rejects which ever is less likely.

Electron-Muon overlap Calorimeter-tagged muons are of very low purity, and are removed if they share inner detector tracks with an electron. All other muon types require hits in the muon system, which is usually not reached by electrons. As such electrons are removed if they share tracks with them.

Electron-Jet overlap Jets can be reconstructed from electromagnetic showers and are therefore removed if they are overlapping with an electron in $\Delta R < 0.2$. Hadronic showers also have electromagnetic components which can lead to reconstructed electrons. Thus electrons are rejected if they are within $\Delta R < 0.4$ to a jet.

Muon-Jet overlap Jets with less than 3 tracks are removed if they overlap with a muon within $\Delta R < 0.2$ or if they are associated with tracks from the muon. The remaining muons are removed if they are within $\Delta R < 0.04 + 10\ \text{GeV}\ /p_{\text{T}}^{\mu}$ of a jet.

There are other, usually more complex, possibilities to remove overlapping objects, for example by introducing a p_{T} dependent ΔR requirement for the Electron-Jet part, too. A study has been performed and found negligible influence on the sensitivity, so the most simple procedure was chosen. It would also be possible to include tagging information in the procedure, for example by not rejecting tagged jets at all. However, this was not done for the tagging calibration and can not be used here, as it would introduce an unknown bias.

In the following it is implied that all objects discussed pass the overlap removal, if not stated otherwise. Also all objects are sorted by their transverse momentum, so the *leading* jet always denotes the jet with the highest p_{T}.

6.7. Missing transverse momentum

As discussed before, particles that interact only weakly leave the detector without any energy depositions, thus seemingly leading to imbalances in the energy momentum conservation (see section 4.2). The missing transverse momentum $\vec{p}_{\text{T}}^{\,\text{miss}}$ is calculated using the negative sum of all transverse momenta of the *baseline* objects and the so called *soft term* [99]. The soft term contains detector responses which are not associated with any reconstructed objects and can be calculated either by summing up the remaining energy depositions in calorimeter cells (Cluster-based Soft Term, CST), or the remaining inner detector tracks from the primary vertex (Track-based Soft Term, TST). As comparison, $E_{\text{T}}^{\text{miss}}$ can also be calculated using a purely track based method, which does not take any reconstructed objects into account, but is completely pile up independent. CST does not cover muons as they don't deposit energy in the calorimeters and therefore reduces the resolution (see figure 6.11 left). The purely track based method ignores neutral particles and shows a bad performance for events with high jet multiplicities (see figure 6.11 right). TST shows the overall best performance and is therefore used.

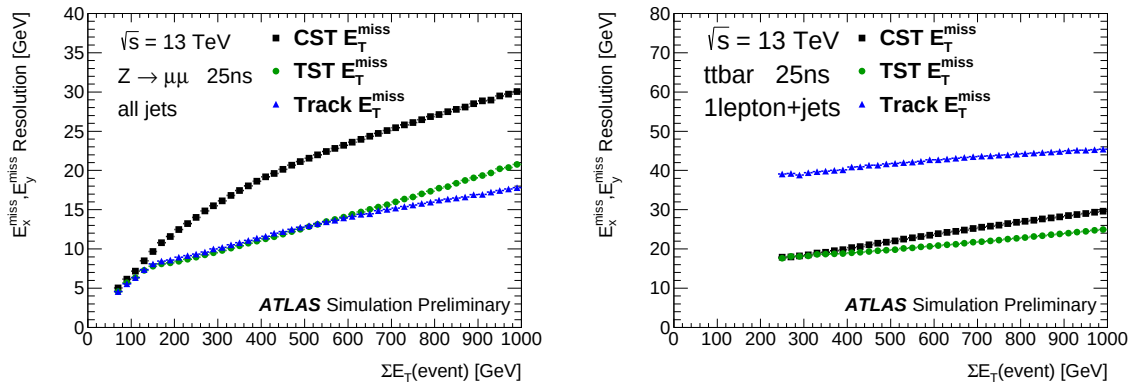

Figure 6.11: Resolution of the missing transverse energy in terms of the root mean square of its x and y components as a function of the energy sum $\sum E_{\mathrm{T}}$ in $Z \to \mu\mu$ (left) and $t\bar{t}$ events (right). [99]

7. Analysis overview

The search for $\tilde{t}_1 \to c + \tilde{\chi}_1^0$ and $\tilde{c} \to c + \tilde{\chi}_1^0$ is performed as a cut and count analysis. It uses various kinds of selections called Signal Regions (SR), Control Regions (CR) and Validation Regions (VR), each serving a special purpose.

SRs are designed to be sensitive to the physics process of interest. Cuts are applied to reduce the backgrounds as much as possible, while keeping a high signal acceptance. These regions are usually blinded during the analysis optimisation, meaning that no data is shown in order to not be biased towards a possible signal.

The most relevant backgrounds in the SRs need to be well understood. This is done with the help of CRs that are each dedicated to a single backround process. They must be as pure as possible while being kinematically close, yet orthogonal to the SR. In this analysis orthogonality is reached by changing the lepton requirement, which rejects almost all signal events. MC simulations are used for the background predictions in the CRs and are fitted to the observed data, resulting in normalization factors. These are then applied in all other regions in order to achieve realistic background estimations.

Before unblinding the SRs, the background estimation strategy needs to be validated. Therefore the extracted normalization factors are applied in the VRs, which are also kinematically close to the SRs, yet have as low signal contamination as possible. They remain orthogonal by inverting cuts on variables known to enhance signal sensitivity. If the background predictions in the VRs match the observed data, the estimation method is seen as validated.

The final step of the analysis is to unblind the SRs and compare the observed yields with the background predictions. Depending on their compatibility, exclusion limits or discovery sensitivities are calculated.

7.1. Preselection

A *Preselection* is defined as foundation for the signal region optimization and is used to search for variables suitable to separate signal from background events. These variables need to be selected on a rather inclusive stage in order to avoid cutting into statistical fluctuations without any physical motivation.

As discussed in section 3.2, signal events have jets, missing transverse energy and no leptons. Thus events are required to pass $E_{\mathrm{T}}^{\mathrm{miss}}$ triggers and are on the plateau at $E_{\mathrm{T}}^{\mathrm{miss}} > 250$ GeV (see section 5.1). Additionally, events with any baseline leptons are vetoed, while at least two signal jets are required, with the leading jet satisfying $p_{\mathrm{T}} > 250$ GeV. The number of multi jet events passing these cuts is very high, even though they have no invisible particles that would lead to $E_{\mathrm{T}}^{\mathrm{miss}}$. The missing transverse momentum appears solely due to mismeasurements of the jets and is therefore usually aligned with one of them in the ϕ-plane (see figure 7.1, left). By requiring $\Delta\phi_{\mathrm{min}}(\vec{p}_{\mathrm{T}}^{\,\mathrm{jets}}, \vec{p}_{\mathrm{T}}^{\,\mathrm{miss}}) > 0.4$ the number of these events can be reduced to a negligible level and will not be considered anymore [1].

[1] A dedicated study using jet smearing techniques has been performed to estimate the amount of multi jet events in the final signal regions and was found to be negligible. [100]

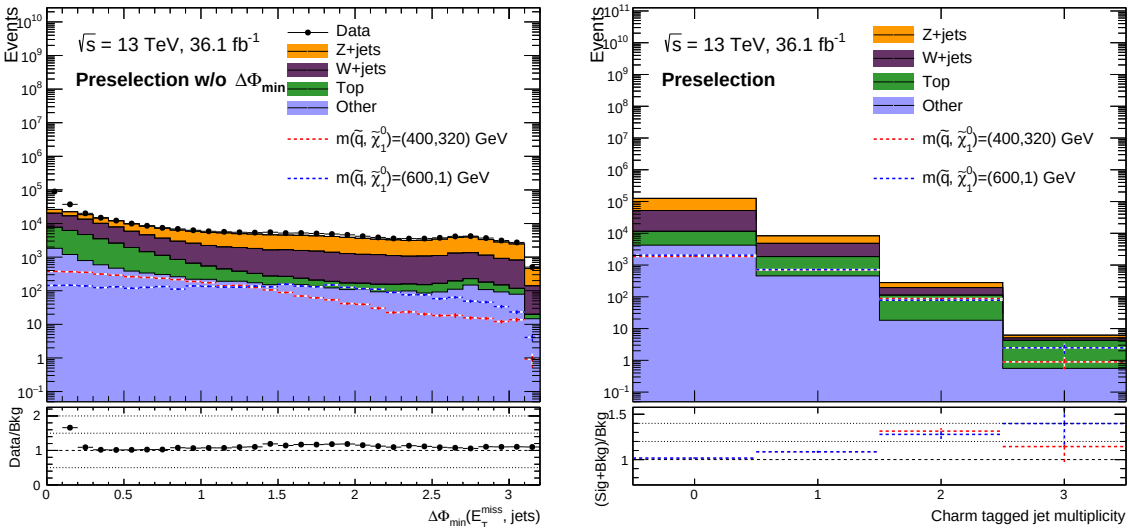

Figure 7.1: Left: Minimum angle $\Delta\phi$ between jets and $\vec{p}_{\mathrm{T}}^{\,\mathrm{miss}}$ in the Preselection without the $\Delta\phi$ requirement. No multi jet simulation is used, so the disagreement between data and MC at low values is solely due to these events. Right: Charm tagged jet multiplicity in the Preselection. Only statistical uncertainties are shown.

Signal events usually have jets from charm quarks, which is much rarer for background processes. As a result the charm tagged jet multiplicity is an efficient discriminant (see figure 7.1, right) and the *Preselection c-tag* is defined with the additional requirement of at least one charm tagged jet. Selecting events with at least two charm tagged jet would further improve the signal to background ratio, however it will turn out that the control regions, which should use the same charm tagging requirements, would run out of statistics.

The charm tagging requirement not only enhances the signal, but also certain types of background events. Those with jets from charm quarks (charm quark ISR or from W decays) have a higher chance of passing the cut, but also backgrounds with either bottom or tau jets, due to the relatively high mistag rate.

At this stage, $W \to \tau\nu$ is one of the leading backgrounds, however most of it can be rejected with a very simple cut: the W boson decay products need to satisfy $m_W^2 = (p_\tau + p_{\nu_\tau})^2$, which can not be fully reconstructed, as only the transverse component for the invisible neutrino is known[2]. Therefore a transverse mass is defined in analogy to the definition often used in one lepton selections:

$$m_{\mathrm{T}}^{c} = \min_{j \in \text{ c-tagged jets}} \sqrt{2 \cdot E_{\mathrm{T}}^{\mathrm{miss}} E_{\mathrm{T}}^{c_j} \cdot (1 - \cos\Delta\phi(\vec{p}_{\mathrm{T}}^{\,\mathrm{miss}}, \vec{p}_{\mathrm{T}}^{\,c_j}))}$$

where $E_{\mathrm{T}}^{c_j}$ is the charm jet's energy and $\vec{p}_{\mathrm{T}}^{\,c_j}$ its transverse momentum. In case there are several charm tagged jets the minimum is used, as jets not originating from the W decay will usually lead to higher values. The resulting distribution is shown in figure 7.2. $W \to \tau\nu$ events are split into a *fake* and an *ISR* component. The former contains events with mistagged tau jets, while the latter contains only charm tagged jets that originated from ISR (not necessarily charm quarks). A veto against the mistagged tau jets is applied by requiring $m_{\mathrm{T}}^{c} > 120$ GeV.

Table 7.1 shows an overview of all preselection cuts and table 7.2 shows their expected

[2]The hadronic tau decay also contains a neutrino, but its influence on the final variable is small.

event yields. The main backgrounds are $Z \to \nu\nu$ and $W \to \tau\nu$ with charm tagged ISR jets, followed by events with top quarks or two vector bosons. They will be discussed in more detail in the next section.

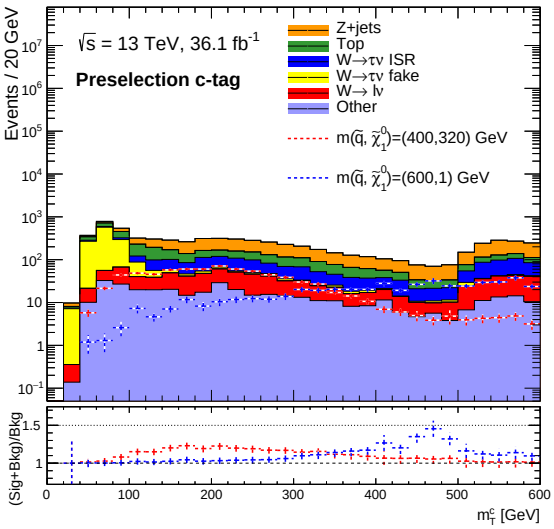

Figure 7.2: m_{T}^{c} distribution after the charm tagged Preselection. Only statistical uncertainties are shown.

Selection	Variable	Value
Preselection	Trigger	$E_{\mathrm{T}}^{\mathrm{miss}}$ (see section 5.1)
	$E_{\mathrm{T}}^{\mathrm{miss}}$	> 250 GeV
	jet multiplicity	≥ 2
	$p_{\mathrm{T}}^{j_1}$	> 250 GeV
	$\Delta\phi_{\mathrm{min}}(\vec{p}_{\mathrm{T}}^{\,\mathrm{jets}}, \vec{p}_{\mathrm{T}}^{\,\mathrm{miss}})$	> 0.4
	N_e,N_μ	$= 0$
Preselection c-tag	charm tagged jet multiplicity	≥ 1
Preselection τ veto	m_{T}^{c}	> 120 GeV

Table 7.1: Cuts applied in the three Preselection stages. Each selection includes all looser definitions listed above.

	Preselection	Preselection c-tag	Preselection τ veto
$W \to e\nu$	6994.2 ± 75.8	361.5 ± 15.8	296.4 ± 14.2
$W \to \mu\nu$	8056.4 ± 76.2	350.4 ± 13.3	319.5 ± 12.8
$W \to \tau\nu$ ISR	27422.3 ± 144.9	1233.9 ± 24.9	1132.1 ± 24.1
$W \to \tau\nu$ fake	1274.9 ± 33.9	1120.6 ± 29.9	73.3 ± 11.7
$Z \to ee$	0.1 ± 0	0 ± 0	0 ± 0
$Z \to \mu\mu$	143.4 ± 5.7	5.4 ± 1	5 ± 0.9
$Z \to \nu\nu$	75981.7 ± 174.9	3595.6 ± 34.4	3331.7 ± 33.6
$t\bar{t}$	7283.7 ± 24.9	1271.8 ± 10.4	920.3 ± 8.7
single top	1551.5 ± 19.9	220.1 ± 8	146.7 ± 5.7
Diboson	4280.5 ± 44.1	415.7 ± 13.4	341.6 ± 12.2
Other	426.3 ± 14.6	59.2 ± 3.1	43.6 ± 2.5
Total background	133415 ± 259.8	8634.3 ± 59.1	6610.2 ± 49.7
$m(\tilde{q}, \tilde{\chi}_1^0) = (400, 320)$ GeV	2668.6 ± 28.5	793.4 ± 14.5	673.8 ± 13.5
$m(\tilde{q}, \tilde{\chi}_1^0) = (500, 200)$ GeV	4193.4 ± 47.8	1325.9 ± 26.1	1294.6 ± 25.8
$m(\tilde{q}, \tilde{\chi}_1^0) = (600, 1)$ GeV	2859.3 ± 37.2	801.4 ± 18.9	789.1 ± 18.8

Table 7.2: Expected event yields in the three preselection stages for the individual background components and some benchmark signals. Only statistical uncertainties are shown.

7.2. Standard Model backgrounds

Preselection τ veto serves as base for the signal region optimization. The main backgrounds for this analysis will be discussed in this section.

Z boson production

Z bosons can be produced in association with jets, as shown for some examples in figure 7.3. They can decay with varying branching ratios (in brackets [8]) either in a pair of quarks ($q\bar{q}$, total ~ 69.9 %), leptons (e^+e^-, $\mu^+\mu^-$, $\tau^+\tau^-$, each $\sim 3.3\%$) or neutrinos ($\nu_\ell\bar{\nu}_\ell$, total $\sim 20\%$).

The hadronic decays could contain charm quarks, however no invisible particles are present and the events usually do not reach the required missing transverse momentum. Events with mismeasured jets will be removed by the $\Delta\phi_{\min}(\vec{p}_{\mathrm{T}}^{\,\mathrm{jets}}, \vec{p}_{\mathrm{T}}^{\,\mathrm{miss}})$ requirement.

Decays into electrons and muons face the same problem and are additionally very likely to be rejected by the lepton veto. While not important for the signal regions, they will be used for the control region definitions.

$Z \to \tau\tau$ events can be fully hadronic, include invisible particles and have a significant mistag rate for tau jets. However, the branching ratio for this process is small and it plays only a minor role.

Decays with neutrinos are the main background, as they always contain $E_{\mathrm{T}}^{\mathrm{miss}}$ and can be produced with additional jets from ISR, that can pass the charm tagging requirements. Its topology is very similar to the signals and is the only truly irreducible background of this analysis.

In the following events with electrons or muons will be labeled $Z \to \ell\ell$, while those with neutrinos are called $Z \to \nu\nu$. $Z \to \tau\tau$ events are combined with more small backgrounds in *Other*.

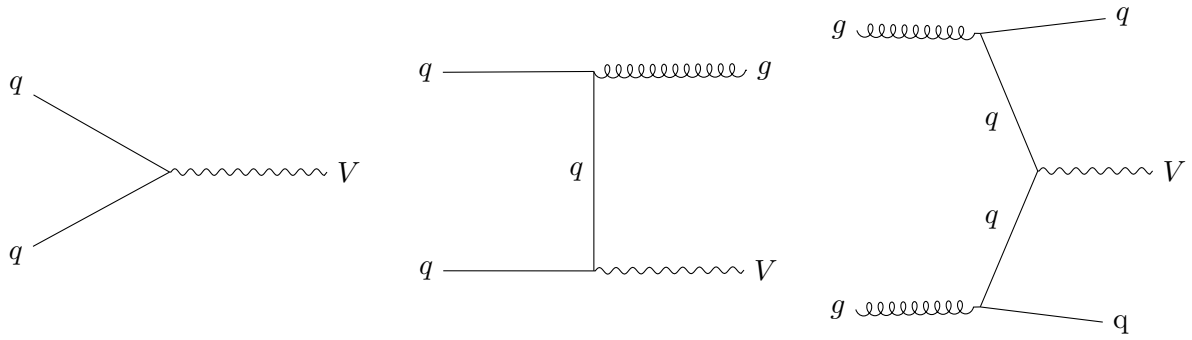

Figure 7.3: Examples for the production of vector boson ($V = W, Z$) events with zero, one or two additional jets from ISR. Quark flavors are suppressed and no distinction between particles and antiparticles is done.

W boson production

W bosons can be produced in association with jets in similar way as Z bosons (see figure 7.3), but they can not decay completely invisible. The hadronic decay ($q\bar{q}'$) does not reach the required values of $E_{\mathrm{T}}^{\mathrm{miss}}$, while most decays with electrons and muons ($e\nu_e$, $\mu\nu_\mu$, and leptonic tau decays) are rejected by the lepton veto.

Decays into hadronic taus on the other hand have invisible particles and jets. The increased mistag rate of the tau jets is almost nullified by the cut on m_{T}^{c}, so that almost exclusively events with tagged ISR jets remain. Similar to $Z \to \nu\nu$, these events have a topology close to the signal, but the rate is much lower.

In the following direct decays into electrons and muons will be labeled $W \to \ell\nu$, while those with taus will be split into $W \to \tau\nu$ *fake* and $W \to \tau\nu$ *ISR* using the formerly introduced definitions. No separation between hadronic and leptonic taus is used, however the latter is rare. Similar to Z+jets, events with electrons and muons will be used for the control region definitions.

Top quark production

Top quarks can be produced either in pairs or in so called single top events (see figure 7.4). They will each decay into a bottom quark and a W boson, which will further decay as described before. The final states can have various amounts of jets, taus, electrons and muons. Fully hadronic decays do not reach the required $E_{\mathrm{T}}^{\mathrm{miss}}$ values, while decays with electrons and muons are usually vetoed. Events passing the Preselection τ veto requirements generally have at least one hadronic tau, as well as bottom jets, both with a relatively high charm mistag rate. The hadronic W decays can also contain charm quarks, further increasing the acceptance.

In the following these events will be collectively referred to as *top* events.

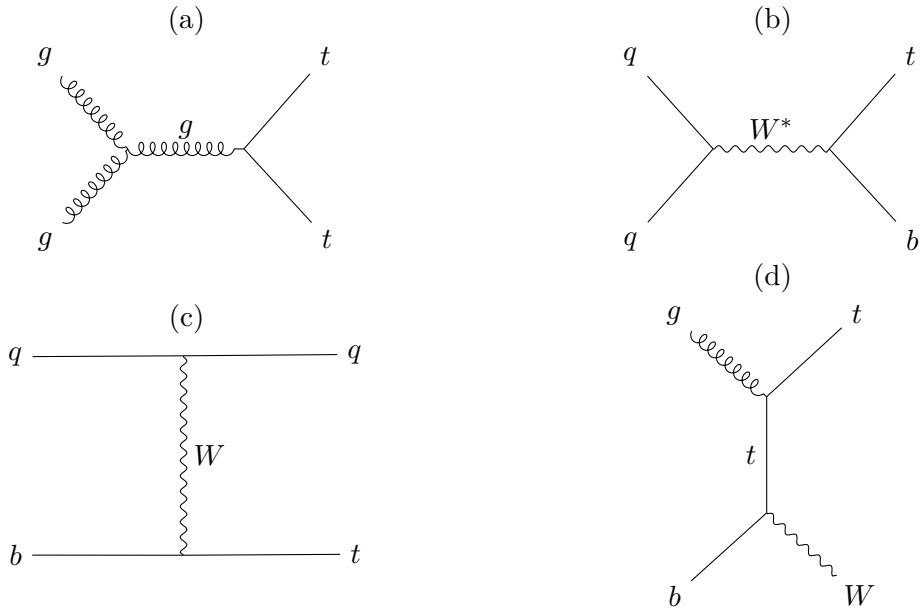

Figure 7.4: Examples of top pair (a) and single top production via the s- (b), t- (c), and w-t-channel (d). q denotes only up, down, charm and strange quarks, no distinction between particles and antiparticles is done.

Diboson production

W and Z bosons can be produced in pairs (see figure 7.5), however the rate is drastically reduced compared to the single production modes. As the bosons decay as described before, it is possible to reach final states with invisible particles and no electrons or muons. The most important ones are $VZ \to qq\ \nu\nu$, $VW \to qq\ \tau\nu$ and $WZ \to \tau\nu\ \nu\nu$, where V is either W or

Z and q denotes quarks. As the rates for these processes are quite low, it is currently not possible to define dedicated control regions for these backgrounds. For example a possible CR for $VZ \to qq\,\nu\nu$, where $VZ \to qq\,\ell\ell$ events would be selected instead, is completely dominated by $Z \to \ell\ell$ events.

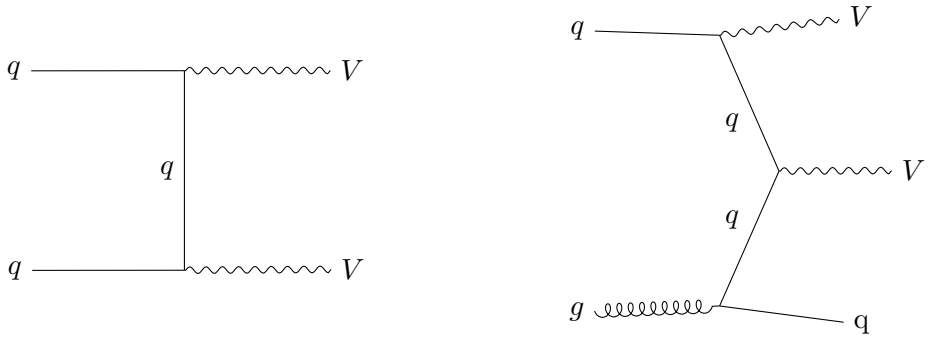

Figure 7.5: Examples for the production of diboson events. Quark flavors are suppressed and no distinction between particles and antiparticles is done.

Other backgrounds

There are more SM backgrounds passing the preselection cuts, however their rates are lower than for the processes listed above. The reasons for them to be small are low cross sections and low acceptances. These minor backgrounds include among others the production of three or four top quarks, top quark pair production in association with vector bosons, and multi jet events.

7.3. Differences between signal and backgrounds

To prepare for the optimization process, signal and background distributions for various variables need to be compared to check for discrimination power. As the signal event characteristics vary depending on the mass difference $\Delta m = m_{\tilde{q}} - m_{\tilde{\chi}_1^0}$, not all variables show equal separation power for the whole parameter space. All variables discussed in this section will be used during the optimization process, but are not necessarily part of the final selections.

$E_{\mathrm{T}}^{\mathrm{miss}}$ and m_{T}^{c} show promising separation power between all signals and the background (see figure 7.6, upper). While the signals' $E_{\mathrm{T}}^{\mathrm{miss}}$ distributions always have long tails, m_{T}^{c} is more Δm dependent and increases for higher mass differences. The dip in the background distribution for m_{T}^{c} is due to the interplay of the $E_{\mathrm{T}}^{\mathrm{miss}}$ cut at 250 GeV and the fact that the leading jets ($p_{\mathrm{T}}^{j_1} > 250$ GeV) can be charm tagged. The jet multiplicity peaks at 3 for all signals, however it is much more pronounced for low Δm, as an additional ISR jet is required (see figure 7.6, lower left). The leading jet's transverse momentum shows tails for signals of all mass differences, however it is highly correlated with $E_{\mathrm{T}}^{\mathrm{miss}}$(see figure 7.6, lower right).

The subleading jets can also give additional separation power, as their momenta peak at low values for small Δm signals, while the distributions shift to higher values for increased Δm (see figure 7.7, upper). A similar behavior can be observed for the transverse momentum of the leading charm tagged jet (see figure 7.7, lower left). The kink at $p_{\mathrm{T}}^{c_1}$ is a result of the

$p_{\mathrm{T}}^{j_1} > 250$ GeV requirement. The probability for the leading jet to be charm tagged decreases for lower Δm as it usually is from ISR (see figure 7.7, lower right).

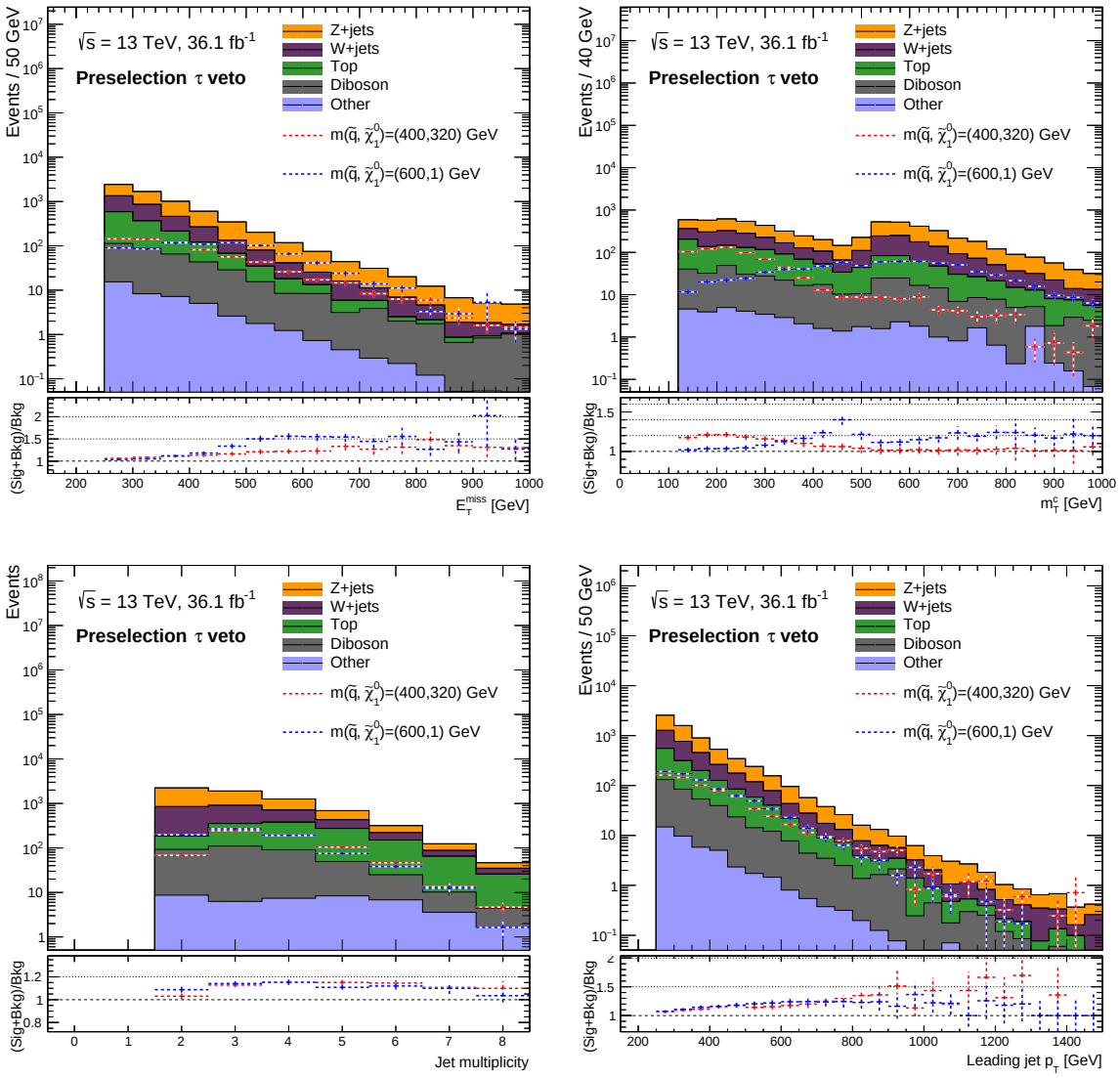

Figure 7.6: $E_{\mathrm{T}}^{\mathrm{miss}}$ (upper left), m_{T}^{c} (upper right), jet multiplicity (lower left) and leading jet p_{T} (lower right) in Preselection τ veto. Only statistical uncertainties are shown.

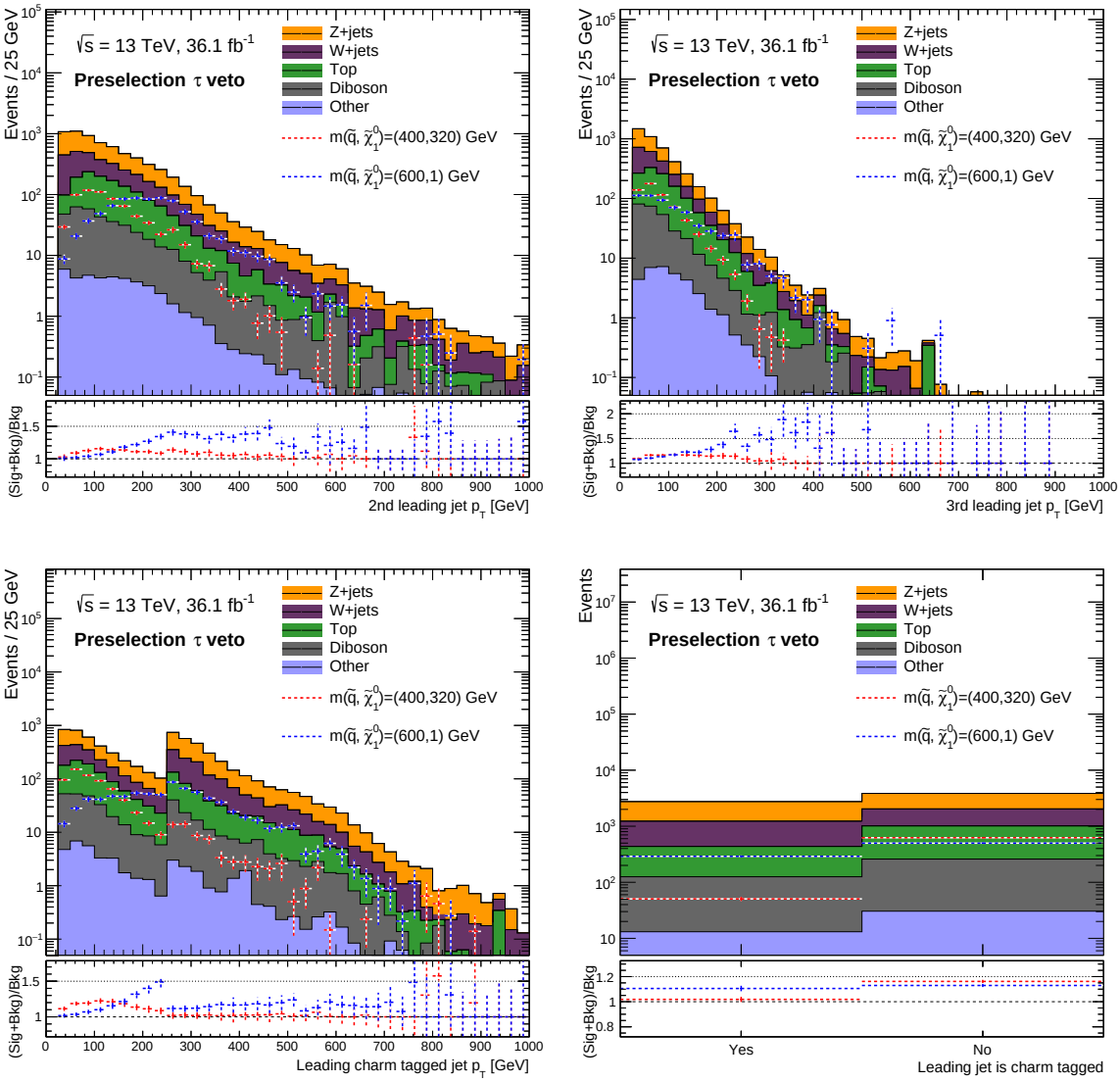

Figure 7.7: Transverse momenta of the second and third leading jets (upper), transverse momentum of the leading charm tagged jet (lower left), and the probability for the leading jet to be charm tagged (lower right) in Preselection τ veto. Only statistical uncertainties are shown.

7.4. Signal region optimization strategy

The signal region optimization should result in a small set of regions that maximizes the sensitivity in the $m_{\tilde{q}}$-$m_{\tilde{\chi}_1^0}$ parameter space. However, each signal point's distributions are unique, so the highest possible sensitivity would be achieved by defining dedicated signal regions for each of them. This is clearly not feasible, so signal points with similar mass differences and therefore comparable characteristics are combined. Signal region candidates are then tested for these groups and the best performing ones are selected.

Usually the optimization is done using purely MC based signal and background estimates, as well as a constant value for the total systematic uncertainty. This approach is not usable for this analysis, though, and the optimization would most likely result in suboptimal regions for two reasons:

V+HF normalization As discussed before, events with W and Z bosons contain exclusively ISR jets, which are favored to originate from heavy flavor (charm or bottom) quarks when applying charm tagging requirements[3]. While the inclusive cross sections for the W/Z+jets processes are very well known, their heavy flavor fraction is not and has uncertainties of up to ~50% on the fiducial cross sections [101, 102]. The MC based estimation of these backgrounds are therefore very likely to be incorrect and could lead to vastly different optimization results. Additionally, the expected and observed sensitivities might not be in agreement, as the main backgrounds could differ greatly after the fit.

Charm tagging uncertainties The background predictions have significant uncertainties due to charm tagging (~25% for each jet flavor, see section 6.5), so an initial estimation for the total systematic uncertainty would be huge. Yet, the actual impact is smaller when using CRs, as the uncertainties will partially cancel due to the transfer factor approach (see section 9.1). The reduction depends heavily on the exact definitions of the signal and control regions, so the total uncertainty is not constant for all candidates.

A data driven background estimation needs to be applied during the optimization process, including sensible control regions and a technique valid for all possible SR candidates. Ideally one would apply the exact same cuts in the CRs (except for the lepton requirements), extract normalization factors for the backgrounds and use the improved SR estimations (including the reduced systematics) for the sensitivity calculation. However, this is not possible and more sophisticated methods are required, which will be described in section 8. The next step is the sensitivity calculation for which the statistical basics will be introduced in section 9, and which includes the systematic uncertainties that will be described in section 10. Finally, the optimization's evaluation and the resulting signal and control regions will be discussed in section 11.

[3] This class of events will be called *V+HF* in the following, where V stands for the vector bosons W and Z.

8. Data driven background estimation

The data driven background estimation is required during the optimization process and must therefore follow a method that yields sensible results for all signal region candidates. It is required at least for the main backgrounds $Z \to \nu\nu$ and $W \to \tau\nu$, because of the heavy flavor mismodeling, and is also performed for $t\bar{t}$. Diboson events will also play a non-negligible role in the signal regions, however it is currently not possible to define dedicated control regions because of the low cross section.

The seemingly easiest approach would be to define the CRs by changing the lepton requirements (for orthogonality) and apply the same kinematic cuts as in the SR. However, the only possibility for a Z+jets control region is to select $Z \to \ell\ell$ events, which have almost no missing transverse momentum and will not pass the corresponding cuts. A similar situation exists for W and top events, which mainly contain hadronic taus in the SRs, but electrons and muons in possible CRs. Replacements for the leptons will be performed in both cases, which will lead to topologies close to those of the SRs and are described in sections 8.1 and 8.2. Afterwards the kinematic cuts of the signal region candidates can be applied, which will be discussed in section 8.3.

8.1. Dilepton control regions

The main background of this analysis is $Z \to \nu\nu$ with additional jet radiation. It is an irreducible background for this analysis, so it is impossible to define a suitable control region without high signal contamination. However, leptonic Z boson decays have the exact same kinematics and only differ by the fact that the leptons can be reconstructed. They usually do not pass the $E_{\mathrm{T}}^{\mathrm{miss}}$ trigger, so single lepton triggers are used instead. On top of that, exactly two same flavor opposite sign leptons are required, with an invariant mass close to the Z mass $|m_{\ell\ell} - m_Z| < 15$ GeV (see figure 8.1). This cut not only removes other backgrounds like dileptonic $t\bar{t}$ and increases the region's purity, but also selects on-shell Z events with properly reconstructed leptons which would otherwise not result in the correct invariant mass.

The invisible decay of the Z is simulated by adding the leptons' transverse momenta vectorially to $\vec{p}_{\mathrm{T}}^{\,\mathrm{miss}}$, and recalculating $\Delta\phi_{\mathrm{min}}(\vec{p}_{\mathrm{T}}^{\,\mathrm{jets}}, \vec{p}_{\mathrm{T}}^{\,\mathrm{miss}})$ and m_{T}^{c} to reflect the corrected value. The recalculated variables are not renamed, to simplify the nomenclature. Generally a very good agreement between $Z \to \nu\nu$ and the corrected $Z \to \ell\ell$ variables can be observed for the τ veto preselection and the corresponding control regions (see figure 8.2).

Using the corrected variables, the kinematic preselection cuts as defined in section 7.1 can be applied. The names for these regions are the same as before, simply replacing *Preselection* by *CR Z*. In CR Z a disagreement between data and MC can be observed in the charm tagged jet multiplicity, which is due to the formerly mentioned MC mismodeling of Z+HF events (see figure 8.3, left). This effect can also be seen very well in CR Z τ veto, where the non-replaced (original) $E_{\mathrm{T}}^{\mathrm{miss}}$ distribution shows an excess in the Z dominated region only (see figure 8.3, right). While the purity in this region is already very high, it can be further increased by requiring $E_{\mathrm{T}}^{\mathrm{miss,original}} < 75$ GeV, which will be added to all dilepton selections.

Requiring a second charm tagged jet reduces the number of events to ~20, which is not

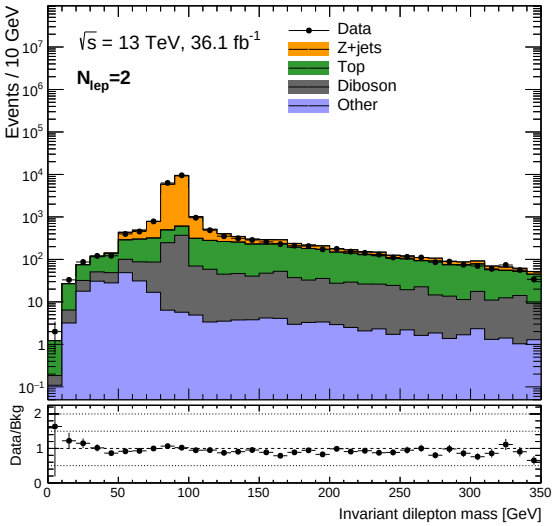

Figure 8.1: Invariant dilepton mass $m_{\ell\ell}$ for events with two leptons. Events without a same flavor opposite sign lepton pair and $m_{\ell\ell} < 50$ GeV are removed from this selection. Only statistical uncertainties are shown.

sufficient to constrain any background. In order to correct for the mismodeling of the heavy flavor composition, the charm tagging requirements should be the same in signal and control regions. The signal regions therefore cannot require a second charm tagged jet.

An overview of the dilepton regions can be found in table 8.1. CR Z implements the requirements discussed above, while CR Z c-tag adds the requirement of at least one charm tagged jet. CR Z τ-veto also requires $m_{\mathrm{T}}^{c} > 120$ GeV, which is not needed to reject events with hadronic taus in the control region, but is used to be closer to the signal region selections.

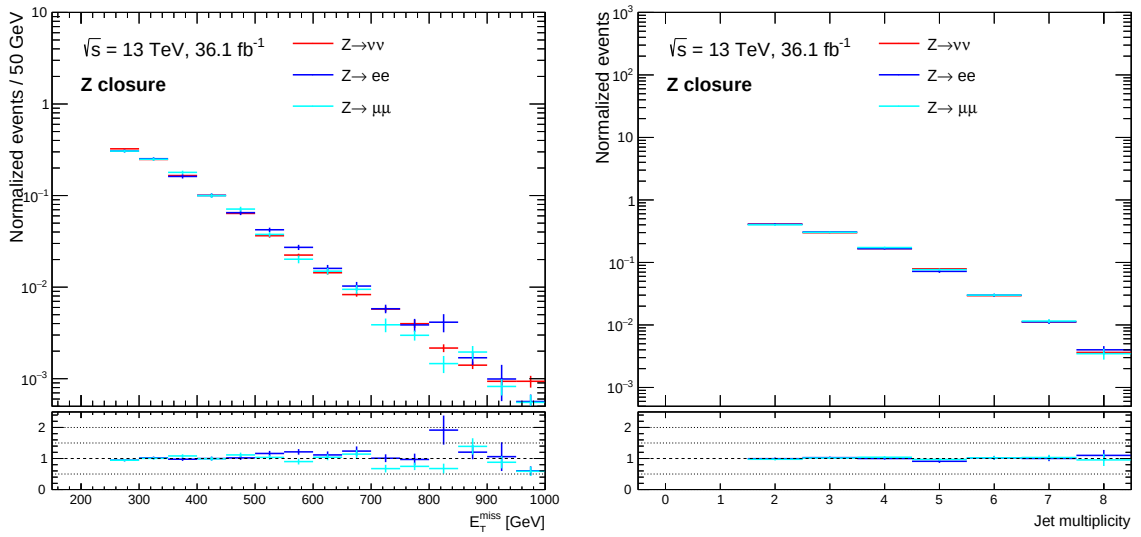

Figure 8.2: Closure tests of the replacement in the dilepton region for $E_{\mathrm{T}}^{\mathrm{miss}}$ (left) and jet multiplicity (right): $Z \to \nu\nu$ events in Preselection τ veto are shown in red, while $Z \to ee$ and $Z \to \mu\mu$ events in the corresponding control region are shown in blue and teal, respectively. Only statistical uncertainties are shown.

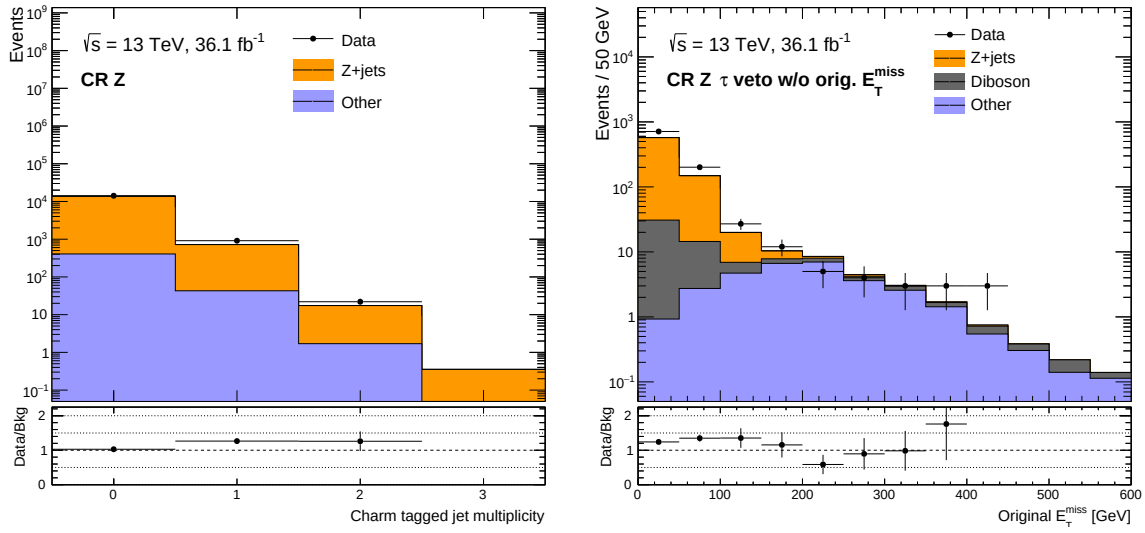

Figure 8.3: Charm tagged jet multiplicity in CR Z (left) and original $E_{\mathrm{T}}^{\mathrm{miss}}$ in CR Z τ veto without the requirement on $E_{\mathrm{T}}^{\mathrm{miss,original}}$. Only statistical uncertainties are shown.

Selection	Variable	Value
CR Z	Trigger	single lepton (see section 5.1)
	Lepton selection	$N_\ell^{\text{Baseline}} = 2$
		$N_\ell^{\text{Signal}} = 2$
		Same flavor
		Opposite sign
		$\lvert m_{\ell\ell} - m_Z \rvert < 15$ GeV
	$E_{\text{T}}^{\text{miss,original}}$	< 75 GeV
	$E_{\text{T}}^{\text{miss}}$	> 250 GeV
	jet multiplicity	≥ 2
	$p_{\text{T}}^{j_1}$	> 250 GeV
	$\Delta\phi_{\text{min}}(\vec{p}_{\text{T}}^{\text{jets}}, \vec{p}_{\text{T}}^{\text{miss}})$	> 0.4
CR Z c-tag	charm tagged jet multiplicity	≥ 1
CR Z τ veto	m_{T}^c	> 120 GeV

Table 8.1: Cuts applied in the three dileptonic preselection stages. Each selection includes all looser definitions listed above.

Significantly more data events are observed in CR Z τ veto than predicted by MC (see table 8.2), however the ratio is flat within statistical uncertainties for all kinematic distributions (see figures 8.4 and 8.5). This means that only the overall normalization of the background prediction is wrong, while the kinematic distributions are modeled correctly. A global normalization factor is sufficient to fix this offset and also to yield a correct background estimation in the SRs, assuming that the same mismodeling occurs.

The disagreement between data and MC in the CRs, and therefore the extracted normalization factor, is highly dependent on the fraction of heavy flavor jets. As these jets can only appear in this region as ISR in Z+HF events, they always suffer from the MC mismodelling. Mistagged light flavor jets on the other hand are usually from events containing no heavy flavor jets at all and therefore do not suffer from the MC mismodelling. The correction factor is thus only valid for a specific jet flavor composition, and needs to be similar in the CRs and the SRs. As shown in figure 8.6, this is indeed the case for Preselection τ veto and CR Z τ veto.

	CR Z	CR Z c-tag	CR Z τ veto
$Z \to ee$	7289.7 ± 36.7	363.9 ± 7.3	342.2 ± 7.1
$Z \to \mu\mu$	6809.5 ± 38.5	330.8 ± 6.5	305.6 ± 6.3
$t\bar{t}$	10.6 ± 1.9	2.1 ± 0.9	2.1 ± 0.9
single top	4.2 ± 1	0.2 ± 0.2	0 ± 0
Diboson	433.6 ± 5.4	42.1 ± 1.6	38.8 ± 1.6
Other	1.9 ± 0.4	0.2 ± 0.1	0.2 ± 0.1
Total background	14551.0 ± 53.6	739.4 ± 10	688.9 ± 9.7
Data	15137 ± 123	935 ± 30.6	859 ± 29.3
Data/Bkg	1.04	1.26	1.25

Table 8.2: Expected event yields and observed data in the three dilepton preselection stages. Statistical uncertainties are shown in brackets.

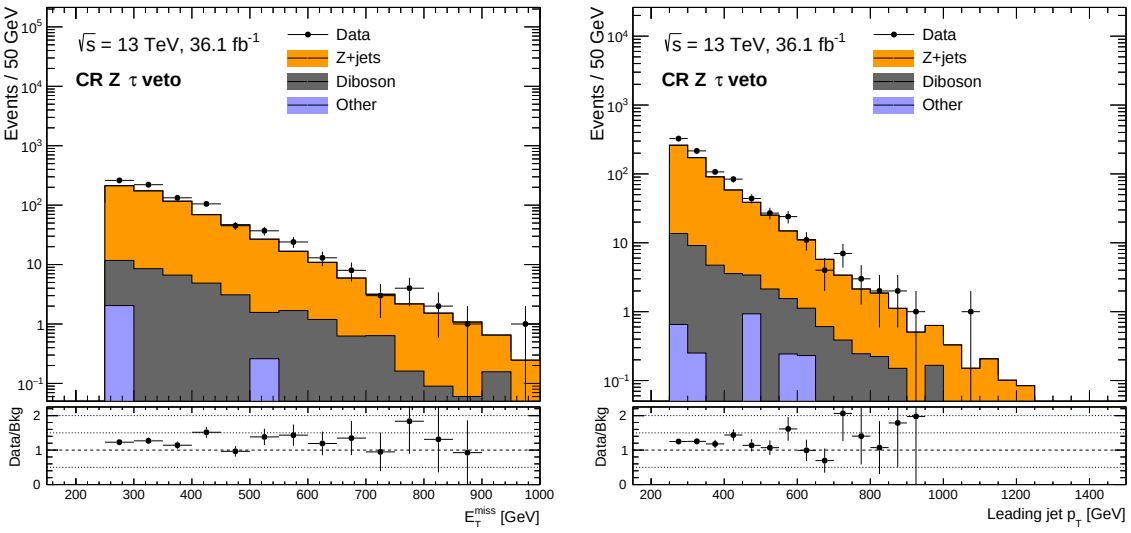

Figure 8.4: $E_{\mathrm{T}}^{\mathrm{miss}}$ and leading jet p_{T} in CR Z τ veto. Only statistical uncertainties are shown.

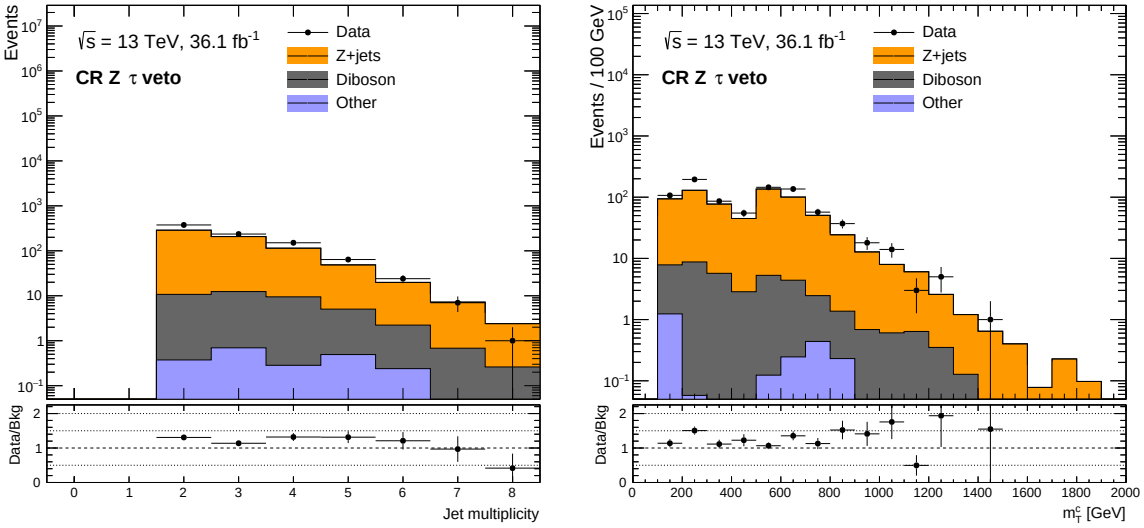

Figure 8.5: Jet multiplicity and m_{T}^{c} in CR Z τ veto. Only statistical uncertainties are shown.

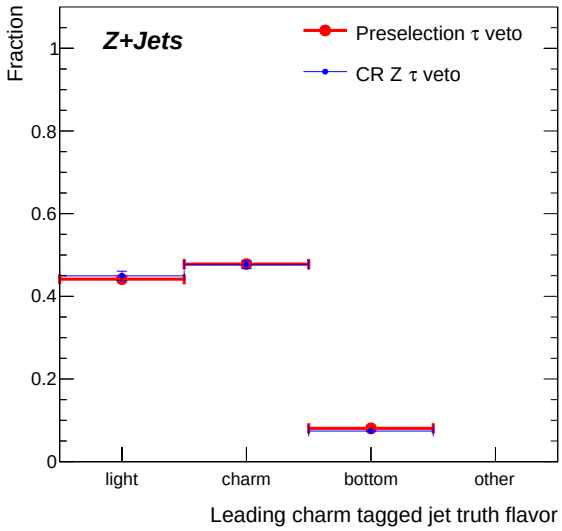

Figure 8.6: True flavor of the leading charm tagged jet of Z+jets events in Preselection τ veto and CR Z τ veto. Only statistical uncertainties are shown.

8.2. One lepton control regions

In Preselection τ veto W+jets events are dominated by $W \to \tau\nu$ with hadronic taus, while top events are dominated by semileptonic decays where the lepton is also a hadronic tau (see figure 8.7). Events with true electrons or muons can sometimes pass the lepton veto, because the objects are either reconstructed incorrectly, or are outside of the kinematic or spatial acceptance.

It is not possible to define proper control regions for W and top using events with τ leptons. However, selections with exactly one electron or muon can be used for both, as they have the same kinematics except for the W decay.

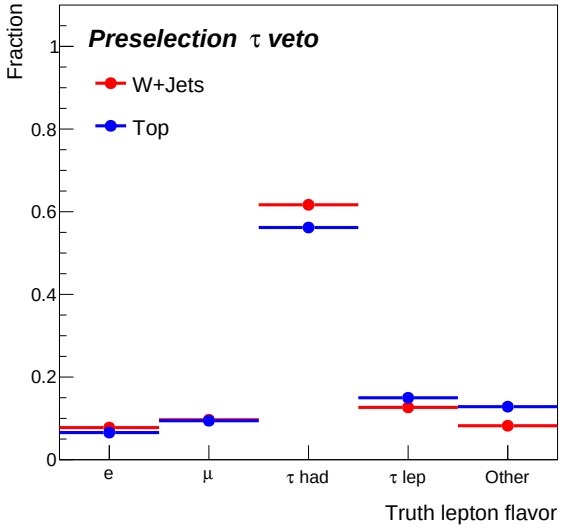

Figure 8.7: Decay modes of W+jets and top events in Preselection τ veto. *Other* contains events with two leptons (e, μ, τ) and also events where the true leptons have $p_{\mathrm{T}} < 10$ GeV, as they can not be definitely identified as decay products of the W bosons.

Even though the leptonic W decays lead to $E_{\mathrm{T}}^{\mathrm{miss}}$, single lepton triggers are used and exactly one lepton that fired the corresponding trigger is required (see section 5.1). Multi jet events can pass these requirements if jets are misidentified as electrons, so the transverse mass

$$m_{\mathrm{T}} = \sqrt{2E_{\mathrm{T}}^{\mathrm{miss}} E_{\mathrm{T}}^{\ell} \cdot (1 - \cos\Delta\phi(\vec{p}_{\mathrm{T}}^{\,\mathrm{miss}}, \vec{p}_{\mathrm{T}}^{\,\ell}))}$$

is used to reject these events by requiring $m_{\mathrm{T}} > 60$ GeV.

W+jets and top processes need to be separated in order to define independent control regions. As both gain their $E_{\mathrm{T}}^{\mathrm{miss}}$ and leptons from W decays, the leptonic variables are very similar. Instead two hadronic masses defined as follows are used:

Hadronic top mass This variable tries to calculate the hadronic top quark mass. First the jet pair whose invariant mass m_{jj} is closest to m_W is selected. Then a third jet is searched to minimize $|m_{jjj} - m_t|$, while requiring that at least one of these jets is charm tagged[1]. The invariant mass of these three jets is called m_{jjj}^{t}. For events with an insufficient jet multiplicity the value is set to 0.

[1] The charm tagged jet can either be a mistagged bottom jet from the top decay or a real charm jet from the hadronic W.

Hadronic W mass The jet pair that minimizes $|m_{jj} - m_W|$ is searched, however pairs not containing charm tagged jets are always preferred, independently of their invariant mass. This rejects events with mistagged bottom jets as they are not part of the hadronic W decay. The invariant mass of this jet pair is called m_{jj}^W.

m_{jjj}^t shows a a peak at the top mass for top events, with a tail towards higher values where not all constituents of the hadronic top decay were found (see figure 8.8, left). W events on the other hand have no peak, but are instead much more spread. The top control region therefore requires events to satisfy 50 GeV$< m_{jjj}^t <$ 220 GeV. The remaining events show a peak for m_{jj}^W at m_W, which is much more pronounced for top events (see figure 8.8, right). The W control region is defined as $m_{\mathrm{jj}}^W >$ 175 GeV.

In principle the acceptances for both regions and also the separation could be further increased by using more complicated requirements. However the current definitions yield a sufficiently high purity and jet flavor compositions close to the signal regions, which is not necessarily given for other definitions.

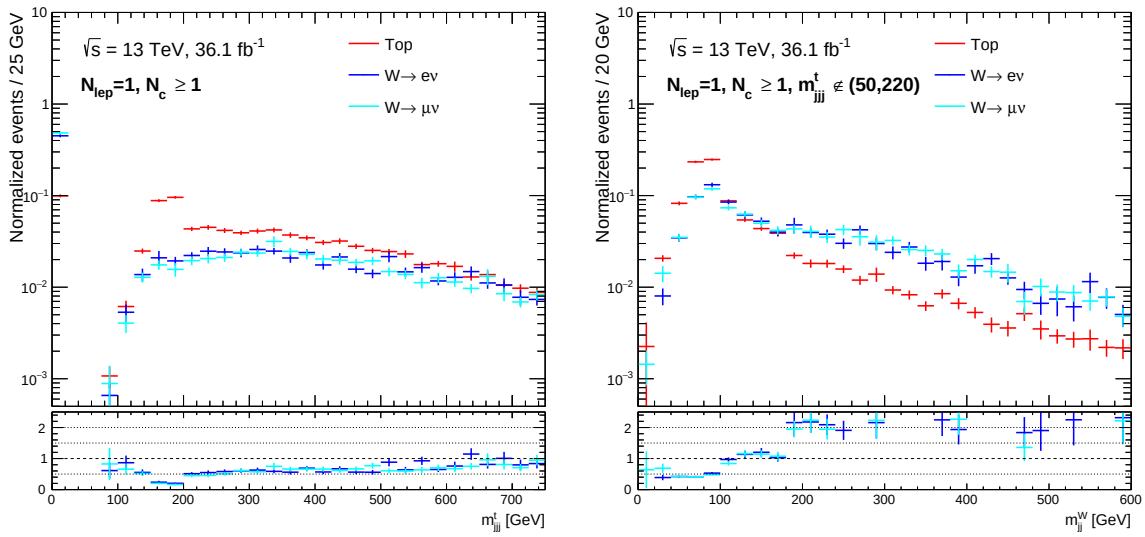

Figure 8.8: Jet mass variables used to separate top from $W \to \ell\nu$ in the one lepton control regions. Only statistical uncertainties are shown.

Hadronic tau decays result in an invisible contribution (due to the neutrino) and a jet contribution. This is currently not reflected in the control regions. A study has been performed to measure the invisible and the jet fraction, showing that in average 60% of the total transverse momentum is carried away by the neutrino [100]. In order to reproduce this in the CR, a "pseudo-hadronic" decay is added to the electrons and muons, meaning that 60% of their $\vec{p}_{\mathrm{T}}$ is added vectorially to $\vec{p}_{\mathrm{T}}^{\,\mathrm{miss}}$. Afterwards a new jet with 40% of the lepton's transverse momentum is added, in case it passes the signal jets' 30 GeV p_{T} requirement. As for CR Z, variables affected by these corrections are recalculated ($E_{\mathrm{T}}^{\mathrm{miss}}$, m_{T}^c, $\Delta\phi_{\mathrm{min}}$, jet multiplicity and momenta). The additional jets can not be charm tagged, as this class of events is mostly removed from the SRs by the τ veto. Also, m_{jjj}^t and m_{jj}^W continue to be calculated with the non-replaced variables, because the new jets are known to not originate from the hadronic top decays. Figure 8.9 shows a comparisons for W+jets and $t\bar{t}$ events, each in the τ veto preselection and in their respective control region. The jet multiplicity is different for the

top control regions, as the definition of m^t_{jjj} requires at least three jets, however the charm tagged jet multiplicity is unchanged.

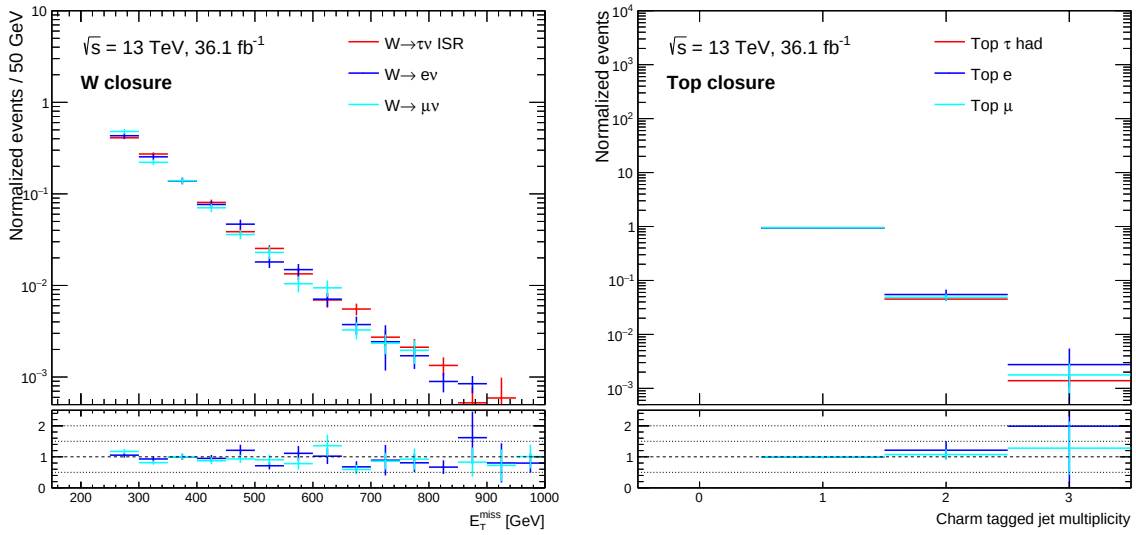

Figure 8.9: Closure test for the replacement in the one lepton control regions for W+HF events (left) and $t\bar{t}$ events (right): Events with hadronic taus in Preselection τ veto are shown in red, while events with exactly one electron or muon in the corresponding control regions are shown in blue and teal, respectively. Only statistical uncertainties are shown.

8.2.1. $W + c$ estimation

The W preselection stages are defined in the same way as before, an overview is given in table 8.3 and the expected yields are shown in table 8.4[2]. The purity is lower compared to the dilepton regions, especially after requiring charm tagged jets, but it is still sufficiently high. The charm tagged jet multiplicity shows the same mismodeling effects as before, though a normalization difference can also be seen without charm tagging (see figure 8.10). The kinematic distributions in CR W τ veto show a flat data to MC ratio with an offset, however the jet flavor composition differs slightly from Preselection τ veto (see figure 8.11). As the normalization factor is dependent on the flavor composition (as for the Z control regions), uncertainties need to be added to the signal regions if this disagreement persists (see section 10.2.5).

[2]While the W preselection itself does not require charm tagging, events vetoed by the m^t_{jjj} requirement can contain charm tagged jets.

Selection	Variable	Value
CR W	Trigger	single lepton (see section 5.1)
	Lepton selection	$N_\ell^{\text{Baseline}} = 1$ $N_\ell^{\text{Signal}} = 1$ $m_{\text{T}} > 60$ GeV
	W selection	$m_{jjj}^t \notin (50, 220)$ GeV $m_{\text{jj}}^W > 175$ GeV
	$E_{\text{T}}^{\text{miss}}$	> 250 GeV
	jet multiplicity	≥ 2
	$p_{\text{T}}^{j_1}$	> 250 GeV
	$\Delta\phi_{\text{min}}(\vec{p}_{\text{T}}^{\text{jets}}, \vec{p}_{\text{T}}^{\text{miss}})$	> 0.4
CR W c-tag	charm tagged jet multiplicity	≥ 1
CR W τ veto	m_{T}^c	> 120 GeV

Table 8.3: Cuts applied in the three W preselection stages. Each selection includes all looser definitions listed above.

	CR W	CR W c-tag	CR W τ veto
$W \to e\nu$	13612.8 ± 108.5	502.9 ± 16.7	472.2 ± 16.4
$W \to \mu\nu$	13855.8 ± 116.5	544.9 ± 18.4	507.3 ± 18
$W \to \tau\nu$ ISR	713.7 ± 25.5	24.3 ± 2.9	22.7 ± 2.9
$W \to \tau\nu$ fake	0.4 ± 0.3	0.4 ± 0.3	0.4 ± 0.1
$Z \to ee$	81 ± 10.1	3.2 ± 0.6	2.4 ± 0.6
$Z \to \mu\mu$	112.8 ± 7.3	4 ± 0.6	3.8 ± 0.6
$Z \to \nu\nu$	13 ± 0.9	0.5 ± 0.1	0.4 ± 0.1
$t\bar{t}$	971.2 ± 13.2	234.9 ± 6.6	182.4 ± 5.4
single top	544.5 ± 12.6	96 ± 5.1	75.3 ± 4
Diboson	1130.2 ± 32	97.2 ± 10.3	83.4 ± 9.7
Other	36.9 ± 2.4	5 ± 0.6	4.1 ± 0.5
Total background	31072.3 ± 165.9	1513.3 ± 28.4	1354.5 ± 27.3
Data	34574 ± 185.9	2053 ± 45.3	1900 ± 43.6
Data/Bkg	1.11	1.36	1.4

Table 8.4: Expected event yields and observed data in the three W preselection stages. Only statistical uncertainties are shown.

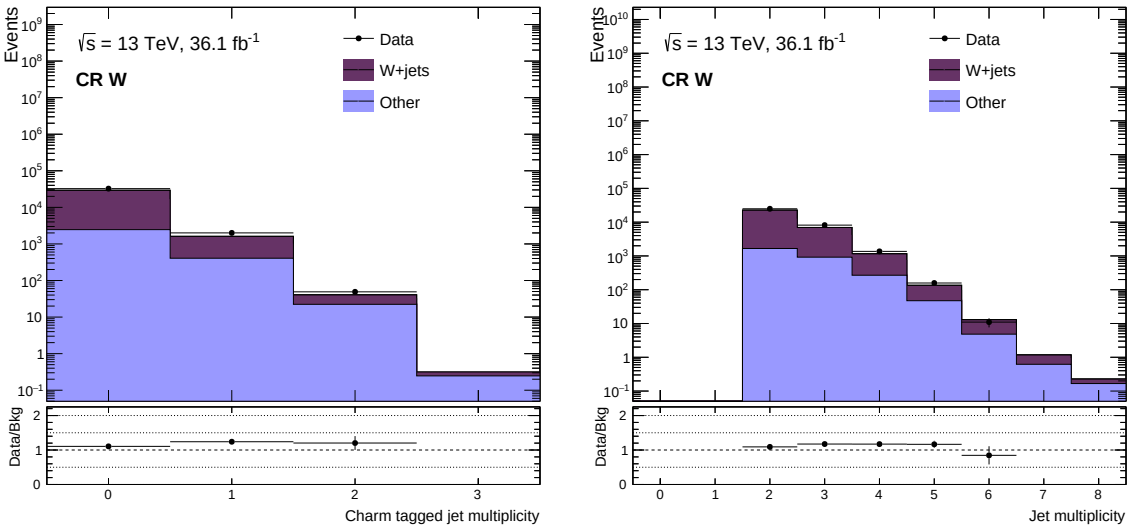

Figure 8.10: Charm tagged jet multiplicity and jet multiplicity in CR W. Only statistical uncertainties are shown.

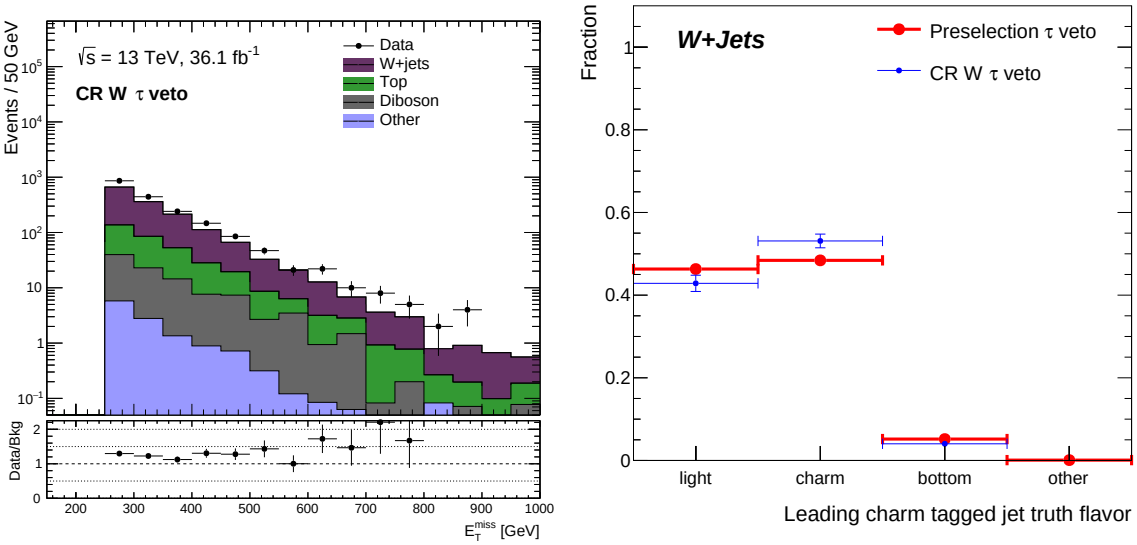

Figure 8.11: Left: $E_{\mathrm{T}}^{\mathrm{miss}}$ in the τ veto W preselection. Right: True flavor of the leading charm tagged jet of W+jets events in Preselection τ veto and CR W τ veto. Only statistical uncertainties are shown.

8.2.2. Top estimation

The top control regions are defined using m^t_{jjj}, which requires at least three jets with one of them being charm tagged, so no tagging agnostic stage can be defined. The region definitions are shown in table 8.5 and the resulting yields in table 8.6. The difference between data and MC is much smaller than for the W and Z regions, because the dominating process does not have additional heavy flavor ISR, but instead the charm tagged jets come from the top and W decays. This is also visible in the flavor composition of the leading charm tagged jet, as it has much more bottom instead of light mistags (see figure 8.12).

The flavor composition differs more than for V+jets, however it is not needed to introduce additional systematics as the normalization factor controls solely the inclusive cross section and not additional heavy flavor radiation (see also section 10.2.5). The differences between data and MC that arise from tagging different jet flavors is corrected by the charm tagging calibration, so it has no influence on the normalization factor.

The kinematic distributions show good agreement between data and MC (see figure 8.13).

Selection	Variable	Value
CR Top c-tag	Trigger	single lepton (see section 5.1)
	Lepton selection	$N_\ell^{\text{Baseline}} = 1$ $N_\ell^{\text{Signal}} = 1$ $m_{\text{T}} > 60$ GeV
	W selection	$m^t_{jjj} \in (50, 220)$ GeV
	$E_{\text{T}}^{\text{miss}}$	> 250 GeV
	jet multiplicity	≥ 3
	$p_{\text{T}}^{j_1}$	> 250 GeV
	$\Delta\phi_{\text{min}}(\vec{p}_{\text{T}}^{\text{jets}}, \vec{p}_{\text{T}}^{\text{miss}})$	> 0.4
	charm tagged jet multiplicity	≥ 1
CR Top τ veto	m^c_{T}	> 120 GeV

Table 8.5: Cuts applied in the two top preselection stages. The τ veto selection includes the c-tag requirements.

	CR Top c-tag	CR Top τ veto
$W \to e\nu$	98.3 ± 6.7	93.5 ± 6.7
$W \to \mu\nu$	87.7 ± 5.6	82.8 ± 5.5
$W \to \tau\nu$ ISR	4 ± 0.9	4 ± 0.9
$W \to \tau\nu$ fake	0.1 ± 0	0.1 ± 0
$Z \to ee$	0.4 ± 0.1	0.3 ± 0.1
$Z \to \mu\mu$	0.7 ± 0.4	0.7 ± 0.4
$Z \to \nu\nu$	0.1 ± 0	0.1 ± 0
$t\bar{t}$	375.6 ± 8.1	329.9 ± 7.7
single top	55.4 ± 2.8	51.7 ± 2.6
Diboson	20.9 ± 2.9	19 ± 2.8
Other	6.6 ± 0.3	5.9 ± 0.2
Total background	649.7 ± 12.6	587.8 ± 12.2
Data	691 ± 26.3	630 ± 25.1
Data/Bkg	1.06	1.07

Table 8.6: Expected event yields and observed data in the top preselection stages. Only statistical uncertainties are shown.

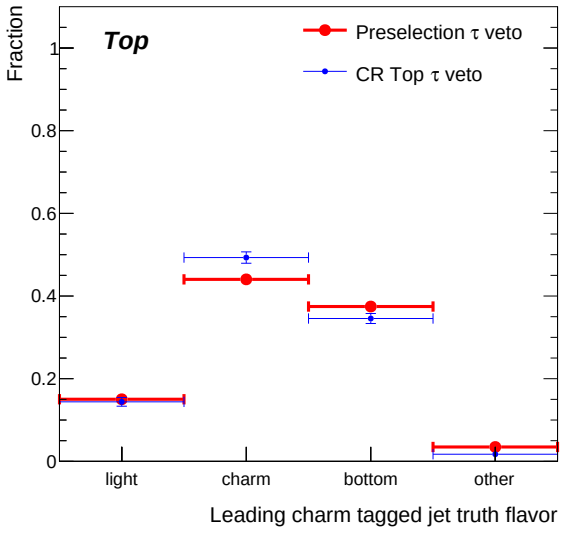

Figure 8.12: Truth flavor of the leading charm tagged jet of top events in the in Preselection τ veto and CR Top τ veto. Only statistical uncertainties are shown.

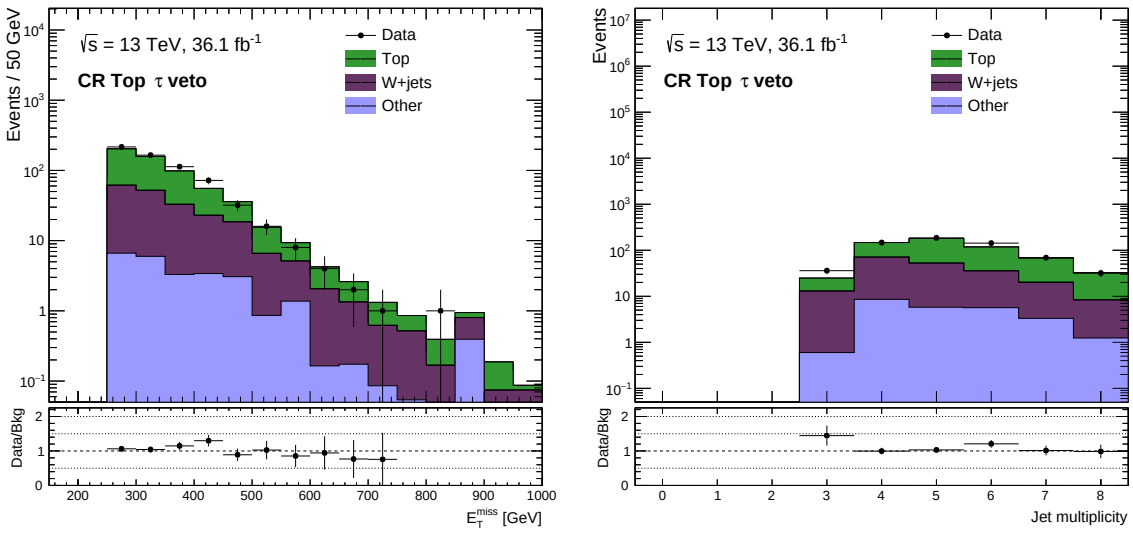

Figure 8.13: $E_{\mathrm{T}}^{\mathrm{miss}}$ and jet multiplicity in the τ veto top preselection. Only statistical uncertainties are shown.

8.3. Control regions during the optimization

In order to define sensible control regions for each signal region candidate, it is necessary to add specific cuts on top of the τ veto requirements. However, using the same cuts is impossible, as the signal region candidates could require $E_{\mathrm{T}}^{\mathrm{miss}} > 600$ GeV, for which the control regions run out of statistics (see figures 8.4, 8.11 and 8.13). Loosened kinematic cuts need to be used instead: jet multiplicity, charm tagged jet multiplicity and m_{T}^{c} requirements are identical to the SRs, as they are of utmost importance for the correct jet flavor compositions. $E_{\mathrm{T}}^{\mathrm{miss}}$ and the leading jet's transverse momentum cuts are set to > 250 GeV. The transverse momenta of the second and third leading jet, as well as the leading charm tagged jet are set to the SR values, however the tightest requirement is > 100 GeV. Table 8.7 shows an overview of the loosened definitions.

Even when using these loose definitions, the event yields in the control regions can go down to ~40 events for the tightest signal region candidates. While this is quite low and will lead to high statistical uncertainties on the normalization factors, it is considered necessary to keep the flavor compositions of signal and control region candidates close, which could otherwise introduce even higher uncertainties. The differences between signal and control regions lead to extrapolation uncertainties, which will be discussed in section 10.2.

Cut	Value in CR
jet multiplicity	same as SR
charm tagged jet multiplicity	same as SR
m_{T}^{c}	same as SR
leading jet tag veto	same as SR
$E_{\mathrm{T}}^{\mathrm{miss}}$	> 250 GeV
leading jet p_{T}	> 250 GeV
2nd and 3rd jet p_{T}	capped at > 100 GeV
leading charm tagged jet p_{T}	capped at > 100 GeV

Table 8.7: Overview of the kinematic control region cuts. "capped" means that the requirement can not be tighter than the given value, but is set to the SR value if it is softer.

9. Simultaneous fit

A fit will be performed simultaneously in signal and control regions to determine the agreement between data and simulations and to calculate sensitivities for the signals. The statistical interpretation is done using the `HistFitter` package [103], which serves as an interface for the underlying HistFactory [104] and RooStats [105] frameworks. More information on the statistical methods can be found in [106].

9.1. Maximum Likelihood Fit

A maximum likelihood fit as described in [106] is performed to estimate the background yields, systematic uncertainties and signal strengths. The likelihood can be written as

$$L(\boldsymbol{n}, \boldsymbol{\theta}^0 | \mu, B, \boldsymbol{\theta}) = \prod_{i \in \text{Regions}} P_i(n_i | \lambda_i(\mu, B)) \times P_{\text{Syst}}(\boldsymbol{\theta}^0 | \boldsymbol{\theta})$$

where P_i denotes Poisson probabilities for all regions with the observed number of events n_i at an expectation λ_i. The systematic uncertainties are reflected as nuisance parameters in the Gaussian probability density function P_{Syst} where $\boldsymbol{\theta}^0$ are the nominal values around which $\boldsymbol{\theta}$ can be varied during the fit. The expectation λ_i for a given region is defined as

$$\lambda_i = \mu \cdot s_i + \sum_{j \in \text{BGs}} c_j \cdot b_{ij}$$

where s_i and $B = (b_{ij})$ are the signal and background predictions. c_k are global normalization factors that will be fitted, with the one for the signal called its strength μ[1].

s_i and b_{ij} are directly dependent on the uncertainties, while the fit result for c_j depends indirectly on them, as it changes with s_i and b_{ij}. This definition allows systematic uncertainties to *cancel* during the fit: if a given uncertainty changes a certain background j by a factor f in the control regions, the resulting normalization factor c_j will change by $1/f$. If the uncertainty has the same effect in the signal region, the prediction is the same as before and the uncertainty effectively cancels. As this is usually not entirely the case, only a partial cancellation can be achieved. A measure for this is the so called transfer factor

$$T_{ij} = \frac{b_{\text{SR},j}}{b_{\text{i}j}}$$

from a control region i to the signal region. The cancellation is of utmost importance for this analysis, as it reduces the otherwise huge uncertainties (e.g. from charm tagging) and increases the sensitivity drastically.

[1] In the HistFitter setup the normalization factors will be called `mu_XXX`, with `XXX` indicating the process.

9.2. Profile likelihood test

After the fit is performed, the result needs to be tested against the two hypothesis of presence or absence of signal. This is done as described in [106], using the test statistics $\Lambda(\mu)$ which is calculated using the profile likelihood ratio of L and can be written as

$$\Lambda(\mu) = -2 \ln \frac{L(\boldsymbol{n}, \boldsymbol{\theta}^0 | \mu, \hat{\hat{B}}, \hat{\hat{\boldsymbol{\theta}}})}{L(\boldsymbol{n}, \boldsymbol{\theta}^0 | \hat{\mu}, \hat{B}, \hat{\boldsymbol{\theta}})}.$$

The numerator is the likelihood function's maximum for a specific signal strength μ, while the denominator is the overall maximum likelihood. $\Lambda(\mu)$ increases with incompatibility of data and hypothesis, with its minimum following approximately a χ^2 distribution. The additional constrain $0 \leq \hat{\mu} < \mu$ is added to make sure that the signal contribution is always positive and that data fluctuations higher than the signal plus background expectation are not treated as evidence against the signal.

Evaluating Λ for specific values of μ leads to the corresponding probability density functions $f(\Lambda|\mu)$[2] that can be used to quantify the disagreement between data and expectation using so called p-values

$$p_\mu = \int_{\Lambda_{\mu,\text{obs}}}^{\infty} f(\Lambda|\mu)\, d\Lambda$$

where $\Lambda_{\mu,\text{obs}}$ is the test statistics evaluated for the observed data. p_μ is the probability that the total expectation of signal and background are at least as high as the observed value. It can be translated to a significance using the quantile Φ^{-1} like

$$Z = \Phi^{-1}(1 - p_\mu).$$

For a discovery (evidence) of a signal, the background-only hypothesis $\mu = 0$ must be rejected with a significance of 5σ (3σ), while signal hypothesis are rejected at 1.64σ. However, using only the p-value for the latter is not robust for small backgrounds[3], so the the CL_s method is used instead. The likelihood ratio is replaced by

$$q \coloneqq \Lambda_{CL_s} = -2 \ln \frac{L(\boldsymbol{n}, \boldsymbol{\theta}^0 | \mu = 1, \hat{\hat{B}}_1, \hat{\hat{\boldsymbol{\theta}}}_1)}{L(\boldsymbol{n}, \boldsymbol{\theta}^0 | \mu = 0, \hat{\hat{B}}_0, \hat{\hat{\boldsymbol{\theta}}}_0)} = -2 \ln \frac{L_{s+b}}{L_b}$$

which incorporates the likelihoods of the nominal signal model L_{s+b} and the background only hypothesis L_b. The p-values (see figure 9.1)

$$p_{s+b} = \int_{q_\text{obs}}^{\infty} f(q|s+b)\, dq$$
$$1 - p_b = \int_{q_\text{obs}}^{\infty} f(q|b)\, dq$$

are then used to calculate the CL_s value

$$CL_s = \frac{p_{s+b}}{1 - p_b}.$$

Signal hypothesis with $CL_s < 0.05$ are defined to be excluded at 95% confidence level.

[2] In this analysis $f(\Lambda|\mu)$ is always obtained through Monte Carlo methods.

[3] Ignoring all systematic uncertainties, an experiment with 0 observed and 3 expected background events would reject all signal models with $s > 0$ when using only the p-value.

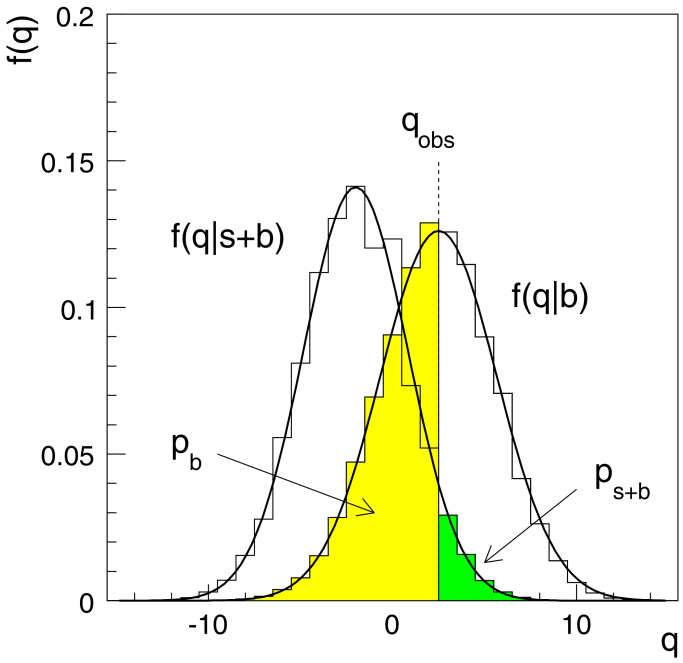

Figure 9.1: Schematic visualization of important quantities used for the CL_s calculation. [106]

The CL_s method can also be used in reverse to calculate the number of signal events S^{95}_{obs} (or S^{95}_{exp} for the expected case) that leads to $CL_s = 0.05$, and is therefore the highest number of signal events that can not be excluded. One can then calculate the limit on the visible cross section as

$$\sigma_{\text{vis}} = S^{95}_{\text{obs}} / \int \mathcal{L} dt.$$

The visible cross section satisfies $\sigma_{\text{vis}} = \sigma \cdot \epsilon \cdot A$, where σ is the total signal cross section, and ϵ and A are the selection's efficiency and acceptance for the signal. This method can be used to set model independent limits, that allow an interpretation of the results for signal models not covered in this analysis.

9.3. Fit setup

The analysis is a cut and count experiment, so every region consists only of a single bin and ignores any shape information. For validation purposes, distributions with multiple bins can be shown, however. Three different fit setups will be used:

Background-only fit A fit of the backgrounds is performed in the control regions, which are assumed to have no signal contamination ($\mu = 0$). The fit result is independent of all signal and validation regions and can therefore be used to compare the post-fit background predictions with their observed events. All post-fit yields and systematic tables shown in the following are based on this fit setup.

Exclusion fit In case of the absence of any excess in the signal regions, a signal model dependent fit is performed in the signal and control regions simultaneously. All backgrounds and

the signal are considered in each region, so the signal strength μ is fitted along the background normalization factors c_j. This procedure is repeated for the whole signal grid and the results are used to calculate exclusion limits with the CLs method.

Discovery fit This setup is defined to be independent of any assumption about the possible signal. The control regions are assumed to have no signal contamination and instead of the signal strength the total signal expectation is used as a free parameter in the signal regions[4]. The configuration can be used to measure the discovery sensitivity in case of a data excess in the signal regions, or to calculate model independent limits, if no excess was observed.

The signal region optimization procedure uses the exclusion fit and the resulting CLs values as figure of merit. However, this analysis uses a data driven background estimation during the signal region optimization process, leading to an unusual setup: the control regions are unblinded, as required for the extraction of the normalization factors, while the signal regions remain blinded. This is not intended in `HistFitter`, as it expects to be either fully blinded or fully unblinded. In the blinded case the observed values in all regions are replaced with so-called *Asimov data*, which is set to the pre-fit background expectation and is known to be too small due to the V+HF mismodeling. Running a background-only fit ignores the signal region, resulting in a proper background prediction. An exclusion fit on the other hand also includes the SR, which in return artificially reduces all background normalization factors and results in a lower background prediction. As the sensitivity is highly dependent on the background prediction, it ends up being too optimistic. This problem can be fixed by manually setting the Asimov data in the signal regions to the value predicted by the background-only fit.

[4] In analysis with multi-bin signal regions, the shape information needs to be ignored and only a single bin is used, because the signal's shape depends on the specific model.

10. Treatment of systematic uncertainties

All signal and background estimations are influenced by systematic uncertainties, as described in previous chapters, and are treated as nuisance parameters in the fit. The most important uncertainties will be discussed briefly in this section. Table 10.1 shows an overview of all experimental uncertainties.

10.1. Experimental uncertainties

Experimental uncertainties emerge for example from the reconstruction of objects (as discussed in section 6). They are correlated between all processes in all regions and many cancel to a great extent due to the transfer factor approach. Non-cancellations of uncertainties arise from differences between signal and control regions. For example the jet energy scale uncertainty is dependent on the jet momenta, which are different in CRs and SRs, so it will not cancel completely.

The nominal MC samples can be used for the estimation, with the identification criteria being varied within their specific uncertainty ranges.

Jet energy scale and resolution

Jet energy scale and resolution describe the detector response to object energies measured by the calorimeters, and were calibrated using data from the 2012 run period. However, there are a number of changes in the detector and the run conditions that lead to p_{T} and η dependent systematic uncertainties [87]. Among other differences, the IBL was added as a new subdetector and the topo clustering algorithm was optimized in terms of noise levels and pile up jet reconstruction. The different beam conditions are for example the increase of the collision frequency from 50 ns to 25 ns and the higher average number of interactions per bunch crossings $<\mu>$, leading to higher in-time and out-of-time pile up.

There are a total of 74 uncertainties on the jet energy scale and resolution, mainly from the in-situ calibrations. The uncertainties from Z+jets, γ+jets and multi jet balance calibrations can be combined, resulting in only 18 remaining nuisance parameters. Furthermore, from the jet energy scale uncertainties four sets of uncertainties with three nuisance parameters each are derived. While each set has a significant loss of correlation information, this loss affects different parts of the parameter space in each set. It was tested whether this analysis is sensitive to these correlations, which was found to not be the case. It is therefore valid to use only one of these reduced sets.

Charm tagging

The reconstruction and identification of charm jets is used in this analysis, so the corresponding systematic uncertainties need to be taken into account. The uncertainties depend on the true jet flavor, as they not only result in different detector responses, but also follow different calibration techniques [96, 97, 98]. This results in a total of 36 correlated uncertainties, that can be combined to a reduced set of 5 nuisance parameters by ignoring the correlations within

each jet flavor. The correlations are highly analysis dependent, so the reduced set could vastly overestimate the total uncertainty. However, this has been tested and the difference was found to be $< 1\%$, so the reduced set will be used.

Missing transverse momentum

The missing transverse momentum is recalculated using the baseline objects and the soft term (see section 6.7). The uncertainties of the former are propagated to $E_{\mathrm{T}}^{\mathrm{miss}}$ and the latter is varied within its scale and energy resolution.

Leptons

The lepton energy resolution and identification uncertainties are applied to baseline candidates of the corresponding flavor. As the signal regions veto events with baseline leptons, no direct impact can be observed and these uncertainties will not be listed in any systematic breakdowns. However they impact the control regions which are used to constrain the backgrounds, therefore contributing to the total uncertainty. As this influence is still small, only the most important lepton uncertainties are taken into account.

Other

Other uncertainties include the JVT selection efficiency, the pileup reweighting and the measured luminosity.

Type	Name in `SUSYTools`	Name in fit setup
Jet	JET_Grouped_NP_X, $X = 1, 2, 3$	JES_NP_X, $X = 1, 2, 3$
	JET_EtaIntercalibration_NonClosure	JET_EtaCalib
	JET_JER_SINGLE_NP	JER
Charm tagging	FT_EFF_B_Systematics	FT_B
	FT_EFF_C_Systematics	FT_C
	FT_EFF_Light_Systematics	FT_Light
	FT_EFF_extrapolation	FT_Ex
	FT_EFF_extrapolation_from_charm	FT_ExC
$E_{\mathrm{T}}^{\mathrm{miss}}$	MET_SoftTrk_ResoPara	MET_ResoPara
	MET_SoftTrk_ResoPerp	MET_ResoPerp
	MET_SoftTrk_Scale	MET_Scale
Leptons	EG_RESOLUTION_ALL	EG_Res
	EG_SCALE_ALL	EG_Scale
	MUONS_ID	MUONS_ID
	MUONS_SCALE	MUONS_Scale
Other	JET_JvtEfficiency	JVT
	PRW_DATASF	PRW
		Luminosity

Table 10.1: Overview of all experimental uncertainties used in this analysis. The right column shows the names which are used in `HistFitter` and the post-fit yields and systematics tables, as well as the correlation matrizes.

10.2. Theory uncertainties

Theory uncertainties cover effects from generator modeling and are highly dependent on the processes. As these change the event generation itself, usually new MC samples need to be generated and compared to the nominal ones. This section will introduce the general method of extracting these uncertainties before discussing them for the main backgrounds and the signal.

Backgrounds that are not listed here do not take into account any theory uncertainties, as their influence would be negligible. However, all samples without dedicated control regions have a 15% uncertainty on their cross sections because their normalization is not fitted. It is set to a value which is higher than the actual cross section uncertainty of each background in order to have a conservative estimation.

10.2.1. General strategy

Theory uncertainties are usually treated as uncertainties on the transfer factor for each background (see section 9). This means that the corresponding control regions are assumed to be correctly modeled after the fit as the background normalizations are constrained there, and only extrapolations to other regions need to be covered. This would include control regions for other processes as well, however the kinematic requirements are the same so there is no extrapolation.

The uncertainty estimation is done by selecting events in the control regions for the nominal and variation samples, and extracting a factor r_i from their ratios

$$r_i = \frac{N_{\text{nom}}^{\text{CR}}}{N_{\text{i}}^{\text{CR}}},$$

which can be used to normalize all yields to the same value[1]. Afterwards the signal region requirements are applied and the variations are scaled with r_i to reflect the information gained from the CRs:

$$n_{\text{i}} = r_i \cdot N_{\text{i}}^{SR}.$$

The resulting uncertainties are calculated by comparing the nominal yield n_{nom} to those of the variations n_{i}, using systematic dependent methods:

In case of a two sided systematic, the variations are defined as

$$v_2 = \begin{cases} \frac{n_{\text{up}} - n_{\text{nom}}}{n_{\text{nom}}} & \text{, direction up} \\ \frac{n_{\text{nom}} - n_{\text{down}}}{n_{\text{nom}}} & \text{, direction down} \end{cases}$$

where *up* and *down* denote whichever is higher or lower than the nominal value. If both variations are below or above the nominal, the uncertainty is instead defined to be symmetric with the highest possible variation

$$v_{\text{max}} = \frac{|n_{\text{X}} - n_{\text{nom}}|}{n_{\text{X}} + n_{\text{nom}}}.$$

One sided systematics are also symmetrized and use their variation

$$v_1 = \frac{|n_{\text{var}} - n_{\text{nom}}|}{n_{\text{nom}}}.$$

[1] The absolute normalization is arbitrary, as only the relative differences are of interest.

In some cases the nominal value can not be compared directly to the variations, so the reference is set to their median. The symmetrized variation is given by

$$v_{ud} = \frac{|n_{\text{up}} - n_{\text{down}}|}{n_{\text{up}} + n_{\text{down}}}.$$

Not all variation samples are available with a full detector simulation, so truth-level samples are used instead. To keep the selections as close as possible to the actual regions, the same cuts are applied to the truth based variables. Charm tagging is simulated by randomly tagging jets using the average p_{T}, η and flavor dependent tagging probabilities. As such all tagging related variables can be calculated as well.

10.2.2. V+jets

Z+jets and W+jets use Sherpa 2.2.1 [64] as nominal generator, therefore following the same strategy to determine the uncertainties, differing only in the requirements for their respective regions. The individual uncertainties are derived separately for each process, but they are treated as correlated in the fit. An overview of the uncertainties and their names in the fit setup are shown in table 10.2.

Factorization & renormalization scale The factorization scale μ_f and renormalization scale μ_r are varied to estimate the uncertainty due to missing higher order corrections. The nominal Sherpa samples contain additional weights for 6 pairwise variations of $\{\mu_f, \mu_r\}$, where $\mu_{f/r} \in \{0.5, 1, 2\}$ in all possible combinations. The total uncertainty is the *envelope* of all individual variations v_2, meaning that the maximum value is used instead of the quadratic sum. This uncertainty is not constrained in the control regions.[2]

Resummation scale The resummation scale defines the starting point of the parton shower evolution and is varied up and down by a factor $\sqrt{2}$. The corresponding samples are available only on truth level and also using Sherpa 2.2.0 as generator. While the change in generator version does not invalidate the result, the variations can not be directly compared to the nominal samples, thus v_{ud} is used.

Matching scale The matching scale determines which particles are being calculated in the matrix element and which in the parton shower (see section 5.3). The nominal value is 20 GeV and is varied to 10 GeV and 30 GeV. Like for the resummation scale, the variation samples are only available at truth level using Sherpa 2.2.0, so v_{ud} is used as well.

Strong coupling constant The strong coupling α_s drives the radiation of additional quarks and gluons. It is being varied within its experimental uncertainties and uses the two sided definition v_2.

PDF As discussed in section 4.2, different PDF sets are available and each set has intrinsic uncertainties. Therefore two uncertainties are introduced. The first one covers the difference between different PDF sets, namely *NNPDF3.0nnlo* (nominal) [43], *MMHT2014nnlo68cl* [42] and CT14nnlo [107]. The second systematic is derived from 100 internal variations of the nominal PDF using the LHAPF tool [108] to calculate a single up and down

[2] Other analyses apply this constrain, however it was decided by the ATLAS SUSY group conveners that the cancellation is too strong. This renders the uncertainty to be far more conservative.

variation. This can be done, as the uncertainties are estimated on a statistical basis, essentially leading to a single standard deviation.

The uncertainties from the α_s and PDF variations are available within the fully reconstructed samples and can as such be added to all regions. This does not change the overall size of these uncertainties in the SRs, but enables the fit to check for correlations with other parameters, thus effectively reducing the overall uncertainty.

Type	Name
Factorization & renormalization scale	V_RenormFac
Resummation scale	VJets_qsf
CKKW matching scale	VJets_ckkw
Strong coupling constant α_s	VJets_AlphaS
PDF set comparison	VJets_PDFSet
PDF internal variations	VJets_PDFInt

Table 10.2: Overview of the V+jets theory uncertainties used in this analysis.

10.2.3. Top

The Top background consists of $t\bar{t}$ and single top events, with the former being far more important. The extraction of theory uncertainties for single top would suffer from limited MC statistics, rendering a precise evaluation of the theory uncertainty impossible. As the total single top background is expected to be very small (and will turn out to be $< 2\%$ in the SRs), a very conservative flat uncertainty of 100% is assumed.

The $t\bar{t}$ nominal sample is generated using Powheg+Pythia6. All theory uncertainties considered in this analysis are listed below and the corresponding names in the fit are given in table 10.3.

Hard scattering The uncertainty on the hard scattering process needs to be evaluated by using a different event generator. The default recommendation is to use aMcAtNLO+Pythia6 as variation sample, since the showering is done by Pythia as well. However, the statistics are too low for $E_{\mathrm{T}}^{\mathrm{miss}} > 500$ GeV, so using this sample would result in $\gtrsim 100\%$ uncertainties for many regions. The Sherpa 2.2.1 sample has higher, yet, still limited statistics and is also suboptimal as it includes a different showering type (which is also done by Sherpa). The resulting uncertainties are therefore overlapping with the parton shower uncertainty (see next paragraph) and will result in higher variations. As Sherpa still yields smaller variations than aMcAtNLO, it is chosen to be the variation sample.

Parton shower The uncertainty related to the parton shower is estimated by comparing the nominal sample to Powheg+Herwig and using the one sided variation v_1.

Radiation Uncertainties due to additional initial and final state radiation are derived using specific samples. The factorization, renormalization and matching scales are varied up and down by a factor of 2. The samples are only available on truth level, so variation v_{ud} is used.

Type	Name
$t\bar{t}$ hard scattering	Ttbar_Generator
$t\bar{t}$ parton shower	Ttbar_Shower
$t\bar{t}$ radiation	Ttbar_Radiation
single top total	singletop_Theory

Table 10.3: Overview of the Top theory uncertainties used in this analysis.

10.2.4. Diboson

Diboson events are also generated using Sherpa 2.2.1, so the general approach is the same as for V+jets. The factorization, renormalization and resummation scales are taken into account in form of truth level samples and use v_{ud}, while the remaining uncertainties are omitted, as they have negligible impact.

As no dedicated control regions for the diboson backgrounds are defined, these uncertainties are not treated as extrapolations (so the variation samples' yields are not scaled with r_i), but instead use the full differences. Additionally the uncertainties need to be added not only in the signal regions, but also in all control regions of other processes.

An overview of the uncertainties is given in table 10.4.

Type	Name
Factorization scale	VV_fac
Renormalization scale	VV_renorm
Resummation scale	VV_qsf

Table 10.4: Overview of the diboson theory uncertainties used in this analysis.

10.2.5. Heavy flavor modeling

In case of mismatches in the flavor compositions between signal and control regions (see figure 10.1), an additional uncertainty needs to be added for some backgrounds.

In V+jets events all jets are ISR as the bosons don't decay hadronically and their decay products can not radiate additional jets. After applying the charm tagging requirements, most events have heavy flavor ISR jets (see figure 10.2), while the rest has mistagged light jets. The control regions are defined to measure the cross section for a given fraction of heavy flavor jets, so if this fraction is the same as in the signal region, no additional uncertainty is required. This even holds true, if the charm and bottom fractions differ, however the cancellation of the charm tagging uncertainties would be reduced. If the light fraction is different, the cross section is controlled incorrectly and an uncertainty needs to be added.

Heavy flavor jets in top events can either emerge through initial or final state radiation (top+HF), or through the top and W decays. While top+HF would add uncertainties the same way it does for V+jets, it occurs rarely and has almost no influence (see figure 10.2). Differences in the flavor composition would therefore only lead to different acceptances due to the flavor dependent tagging efficiencies.These are however already accounted for by the charm tagging calibration, so the only effect is a reduced cancellation of the charm tagging uncertainties.

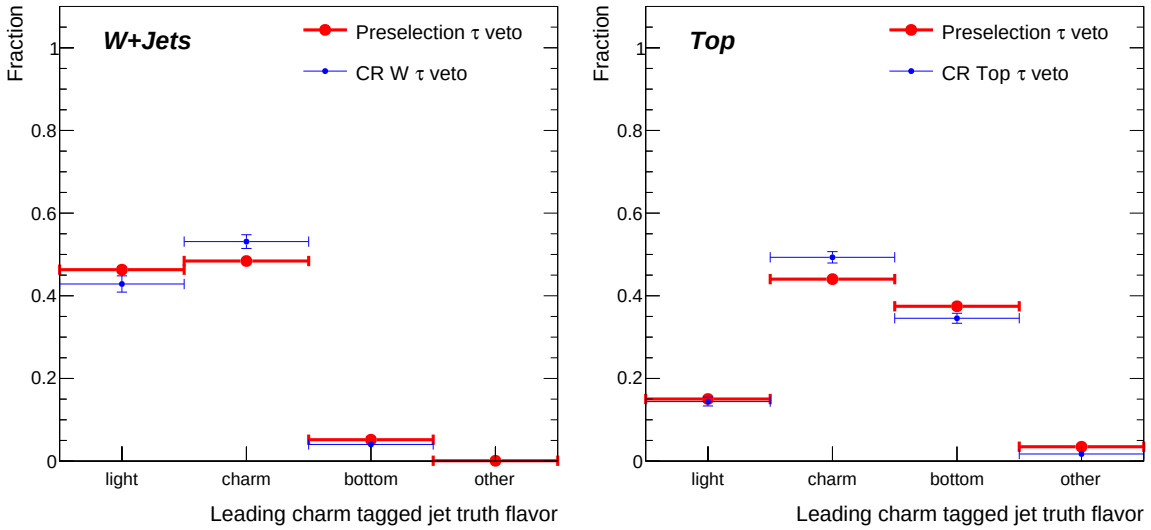

Figure 10.1: True flavor of the leading charm tagged jet of W+Jets (left) and $t\bar{t}$ (right) events in the zero lepton τ veto preselection and the corresponding control regions after the τ veto.

The uncertainty is calculated by comparing the light and heavy flavor fractions of signal and control regions, and varying the number of heavy flavor events within the cross section uncertainty. For W+HF an uncertainty of 54% [101] is used, for Z+HF 30% [102][3]. The transfer factors (see section 9.1) are then calculated for all variations and the uncertainties are extracted from the differences. As the *up* variation leads to more expected events and therefore a smaller normalization factor, its deviation is defined to be negative. Table 10.5 shows an example for arbitrary event numbers of W+jets. The uncertainty is called VJets_HF in the fit setup.

	SR			CR			Transfer factor	Uncertainty
	W+c	W+b	W+light	W+c	W+b	W+light	$T^i = \frac{n^{\mathrm{SR}}_{\mathrm{tot}}}{n^{\mathrm{CR}}_{\mathrm{tot}}}$	$u = \frac{T^{\mathrm{nom}} - T^{\mathrm{var}}}{T^{\mathrm{nom}}}$
Nominal	10	3	5	100	30	100	0.078	
Up	15.4	4.62	5	154	46.2	100	0.083	-6.5%
Down	4.6	1.38	5	46	13.8	100	0.068	12.2%

Table 10.5: Schematic example of the V+HF cross section uncertainty calculation for arbitrary numbers.

[3]Both numbers correspond to the bins with the highest relative uncertainty, so they are conservative.

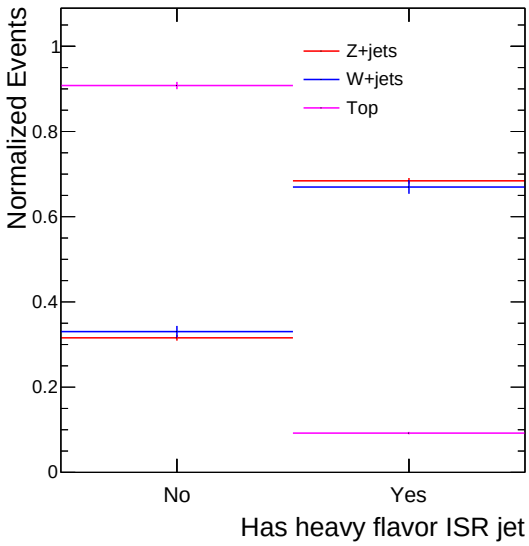

Figure 10.2: Probability of events having a heavy flavor ISR jet for W+jets, Z+jets and Top events in the τ veto preselection. ISR jets are defined to not emerge from top, W or Z decays.

10.3. Signal uncertainties

Signal events are reconstructed the same way as background events, so they also suffer from all experimental uncertainties described in section 10.1. Theory uncertainties are covered using a set of dedicated samples, that vary α_s and PDFs, as well as all scales that were discussed for the backgrounds. The samples are produced at truth level and variation v_{ud} is used. It is not feasible to generate these samples for the whole signal grid, so several benchmark points were chosen such that various squark masses and mass differences can be tested (see table 10.6). The specific uncertainties for each signal point can then be extracted via extrapolations. However, this procedure can not be easily automatized, so the exact signal theory uncertainties can not be taken into account during the optimization process. A total uncertainty of 10% is used instead, which is based on the *Run1* analysis [32]. The actual values are calculated afterwards for the final signal regions and will prove to be consistent with this initial assessment.

By definition no control regions exist for the signals, so the uncertainties are applied without any rescaling of the event yields. However, the changes to the generator parameters would in principle lead to differences in the cross sections which can vary by a factor of 2. As this would result in double counting the cross section uncertainty, all yields are scaled to the nominal NLO+NLL cross sections [75, 76, 77, 78] instead.

The signal cross section uncertainties are not taken into account in the fit directly, instead the fit is performed twice again with the increased and reduced values. The resulting limits or discovery sensitivities are labeled $\pm 1\sigma^{\text{SUSY}}_{\text{Theory}}$.

$m_{\tilde{q}}$ [GeV]	$m_{\tilde{\chi}_1^0}$ [GeV]
400	320
400	395
600	1
600	200
600	400
600	520
600	550
600	585
600	595
800	1
800	400

Table 10.6: List of squark and neutralino mass combinations for which the signal theory uncertainty variation samples were generated.

11. Signal region optimization

The signal regions are optimized by defining a set of cut combinations from the variables discussed in section 7.3, and calculating the sensitivities for each point in the signal grid. As the signals' characteristics depend on Δm, several signal regions are necessary to reach the best possible coverage. The $m_{\tilde{t}_1}$-$m_{\tilde{\chi}_1^0}$-plane is divided into Δm slices[1] and the best performing cut combination is searched for each of them.

The signal region candidates are obtained by combining all possible requirements on the parameters of interest as defined in table 11.1. The cut values can be negative, which is interpreted as an upper cut on the corresponding variable. For example, the leading charm tagged jets is expected to be soft for small mass differences, so the requirement $p_{\mathrm{T}}^{c_1} < 100$ GeV should be tested, which corresponds to the value of *-100* GeV in the scan. For high mass differences a tighter requirement of $p_{\mathrm{T}}^{c_1} > 300$ GeV could be favorable, corresponding to *300* GeV in the scan.

Combinations that invalidate each other, like a cut on the third jet p_{T} while only requiring a total of two jets, are removed as they effectively duplicate cuts.

Variable	Minimum value	Maximum value	Step size
$E_{\mathrm{T}}^{\mathrm{miss}}$ [GeV]	300	600	100
Jet multiplicity	2	4	1
leading jet p_{T} [GeV]	300	600	100
2nd leading jet p_{T} [GeV]	-200	300	100
3rd leading jet p_{T} [GeV]	-100	300	100
leading charm tagged jet p_{T} [GeV]	-100	300	100
m_{T}^{c} [GeV]	-300	500	100
leading jet charm tag veto	no	yes	

Table 11.1: Overview of the minimum and maximum values, as well as step sizes, for all variables used in the signal region scan.

As discussed before, the data driven background estimation needs to be implemented. The control regions are defined using the logic introduced in section 7.4 and are used to calculate the theory uncertainties. A background-only fit is then performed and the normalization factors extracted from the control regions are used for the signal region background estimation. The figure of merit for the optimization is the exclusion reach in terms of CL_s, so exclusion fits are performed for all signal points, using the formerly extracted background expectation as Asimov data in the signal region.

The Δm slices are defined with some overlap in order to reduce sensitivity dips between the final regions. However, when selecting the best performing cut by simply counting the number of excluded points, it is possible that a region is favored because it excludes more points in these overlaps, and which might already be covered by the neighboring regions. The probability for this to happen increases with lower masses, as the cross sections and therefore

[1] E.g. all signals with 40 GeV$\leq \Delta m \leq$ 80 GeV are combined in one slice.

the sensitivities are generally higher. Instead each excluded point is weighted with the square of its squark mass and the region with the highest weight is chosen.

As the parameter scan has fixed step sizes, the regions found to be best performing are further investigated. All variables of interest are plotted without the regions' requirement on the same (N-1 plot) and, if possible improvements are observed, variations of the cuts are tested in terms of sensitivity.

The resulting signal region definitions are shown in table 11.2 and are sorted from low (SR1) to high mass differences (SR5). While the $E_{\mathrm{T}}^{\mathrm{miss}}$ requirement is the same for all regions, especially the m_{T}^{c} and jet p_{T} requirements increase with mass differences.

The total pre-fit background yields are between 25 and 50 events (see table 11.3), with $Z \to \nu\nu$ being the main background ($\approx 50\%$), followed by $W \to \tau\nu$, Top and diboson events with varying influence.

The signal yields are highly dependent on the region and reaching their highest purity in the region targeting their mass difference. This is also visible in the expected exclusion limits (see figure 11.1) where the regions show sensitivity in their target areas. However, there is a sharp change in sensitivity between SR3 and SR4. The expected sensitivity exceeds the exclusion limits from *Run1* and goes up to squark masses of ~800 GeV for high Δm and up to ~500 GeV for the $\tilde{t}_1 \to c + \tilde{\chi}_1^0$ area. No sensitivity can be achieved for very small mass differences, which is however covered by the Monojet analysis [27]. The sensitivity of SR1 overlaps almost completely with SR2, however it reaches higher sensitivities at low mass differences and therefore reduces the gap to the Monojet region.

The individual signal regions will be discussed in more detail in sections 11.1-11.5, before discussing the corresponding control regions in section 11.6 and introducing validation regions in section 11.7.

	SR1	SR2	SR3	SR4	SR5
	Preselection τ veto				
jet multiplicity	≥ 2	≥ 3	≥ 3	≥ 3	≥ 3
leading jet tag veto	yes	yes	yes	yes	no
$E_{\mathrm{T}}^{\mathrm{miss}}$ [GeV]	> 500	> 500	> 500	> 500	> 500
$p_{\mathrm{T}}^{j_1}$ [GeV]					> 300
$p_{\mathrm{T}}^{j_2}$ [GeV]			> 100	> 140	> 200
$p_{\mathrm{T}}^{j_3}$ [GeV]			> 80	> 120	> 150
$p_{\mathrm{T}}^{c_1}$ [GeV]	< 100	> 60	> 80	> 100	> 150
m_{T}^{c}	< 250	< 250	$\in (175, 400)$	> 200	> 400

Table 11.2: Overview of all signal region definitions.

	SR1	SR2	SR3	SR4	SR5
$W \to e\nu$	0.7 ± 0.4	0.9 ± 0.3	0.6 ± 0.2	1.3 ± 0.3	1.1 ± 0.3
$W \to \mu\nu$	1.8 ± 0.5	0.6 ± 0.2	0.7 ± 0.2	1.9 ± 0.6	0.7 ± 0.2
$W \to \tau\nu$ ISR	5.8 ± 1.0	2.4 ± 0.5	3.2 ± 0.5	6.3 ± 0.8	2.8 ± 0.4
$W \to \tau\nu$ fake	1.7 ± 0.5	1.8 ± 0.5	0.8 ± 0.2	0.5 ± 0.2	0 ± 0
$Z \to \nu\nu$	27.4 ± 1.7	12.5 ± 1.0	14.2 ± 0.8	26.3 ± 1.0	15.4 ± 0.7
$t\bar{t}$	3.8 ± 0.2	4.3 ± 0.2	1.9 ± 0.1	3.3 ± 0.2	1.2 ± 0.1
single top	0.9 ± 0.2	0.1 ± 0.3	0.3 ± 0.1	0.6 ± 0.1	0.5 ± 0.2
Diboson	6.3 ± 1.3	2.7 ± 0.5	2.4 ± 0.4	5.9 ± 1.0	3.2 ± 0.7
Other	0.6 ± 0.1	0.5 ± 0.1	0.5 ± 0.1	1.0 ± 0.1	0.3 ± 0
Total background	49.0 ± 2.5	25.8 ± 1.4	24.7 ± 1.1	47.2 ± 1.8	25.1 ± 1.1
$m(\tilde{q}, \tilde{\chi}_1^0) = (400, 370)$ GeV	43.8 ± 3.1	20.9 ± 2.0	6.6 ± 1.1	2.8 ± 0.9	0.5 ± 0.4
$m(\tilde{q}, \tilde{\chi}_1^0) = (450, 425)$ GeV	22.5 ± 2.1	9.1 ± 1.8	1.6 ± 0.8	1.8 ± 0.6	0.5 ± 0.3
$m(\tilde{q}, \tilde{\chi}_1^0) = (475, 415)$ GeV	20.4 ± 1.7	19.3 ± 1.7	11.3 ± 1.6	5.4 ± 0.9	0.4 ± 0.3
$m(\tilde{q}, \tilde{\chi}_1^0) = (500, 420)$ GeV	18.4 ± 2.5	19.7 ± 2.9	15.3 ± 2.4	8.0 ± 1.4	1.3 ± 0.6
$m(\tilde{q}, \tilde{\chi}_1^0) = (500, 350)$ GeV	5.4 ± 1.4	11.6 ± 1.9	26.0 ± 3.6	18.7 ± 3.3	3.0 ± 1.0
$m(\tilde{q}, \tilde{\chi}_1^0) = (550, 400)$ GeV	4.6 ± 1.0	9.1 ± 2.1	15.2 ± 2.8	14.3 ± 2.3	5.7 ± 1.5
$m(\tilde{q}, \tilde{\chi}_1^0) = (600, 350)$ GeV	1.9 ± 0.8	3.2 ± 0.9	10.5 ± 1.9	24.0 ± 3.6	7.0 ± 1.8
$m(\tilde{q}, \tilde{\chi}_1^0) = (700, 300)$ GeV	1.4 ± 0.7	4.1 ± 2.4	5.2 ± 1.4	20.3 ± 2.3	9.5 ± 1.4
$m(\tilde{q}, \tilde{\chi}_1^0) = (600, 1)$ GeV	5.7 ± 1.3	4.7 ± 1.2	10.9 ± 2.1	54.4 ± 4.3	32.1 ± 3.2
$m(\tilde{q}, \tilde{\chi}_1^0) = (850, 1)$ GeV	1.0 ± 0.3	1.5 ± 0.5	2.1 ± 0.4	16.2 ± 1.1	13.2 ± 1.0

Table 11.3: Expected event yields for backgrounds and several benchmark signals in the signal regions. Signal yields in the non-target regions are shown in gray. Only statistical uncertainties are shown.

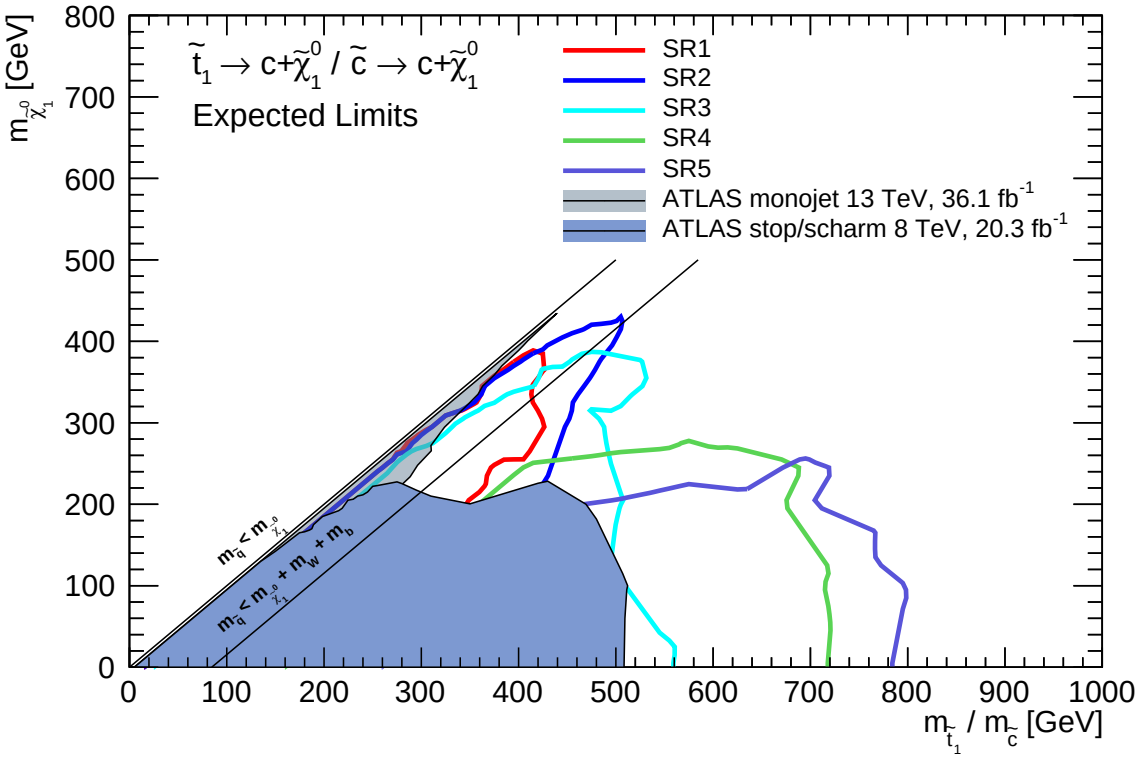

Figure 11.1: Expected exclusion sensitivity for all signal regions. The ATLAS results from *Run1* and the latest Monojet analysis are shown for comparison.

11.1. SR1

SR 1 targets signal topologies with $\Delta m \lesssim 50$ GeV. In this region a hard ISR boost is required and the jets from charm tags are not always reconstructed. Thus at least two jets are required, with the leading one not being charm tagged. The requirement on the leading jet p_{T} is not needed because of its high correlation with $E_{\mathrm{T}}^{\mathrm{miss}}$.

As expected, signals with very small mass differences $\lesssim 10$ GeV show no sensitivity because of the low probability to reconstruct and tag charm jets (see figure 11.2). $E_{\mathrm{T}}^{\mathrm{miss}}$ shows a great background reduction and reaches even higher signal purity at values above 500 GeV, however the increased extrapolation uncertainties result in an overall worse sensitivity. The signals peak at low values of m_{T}^{c} and $p_{\mathrm{T}}^{c_1}$, so an upper cut is applied.

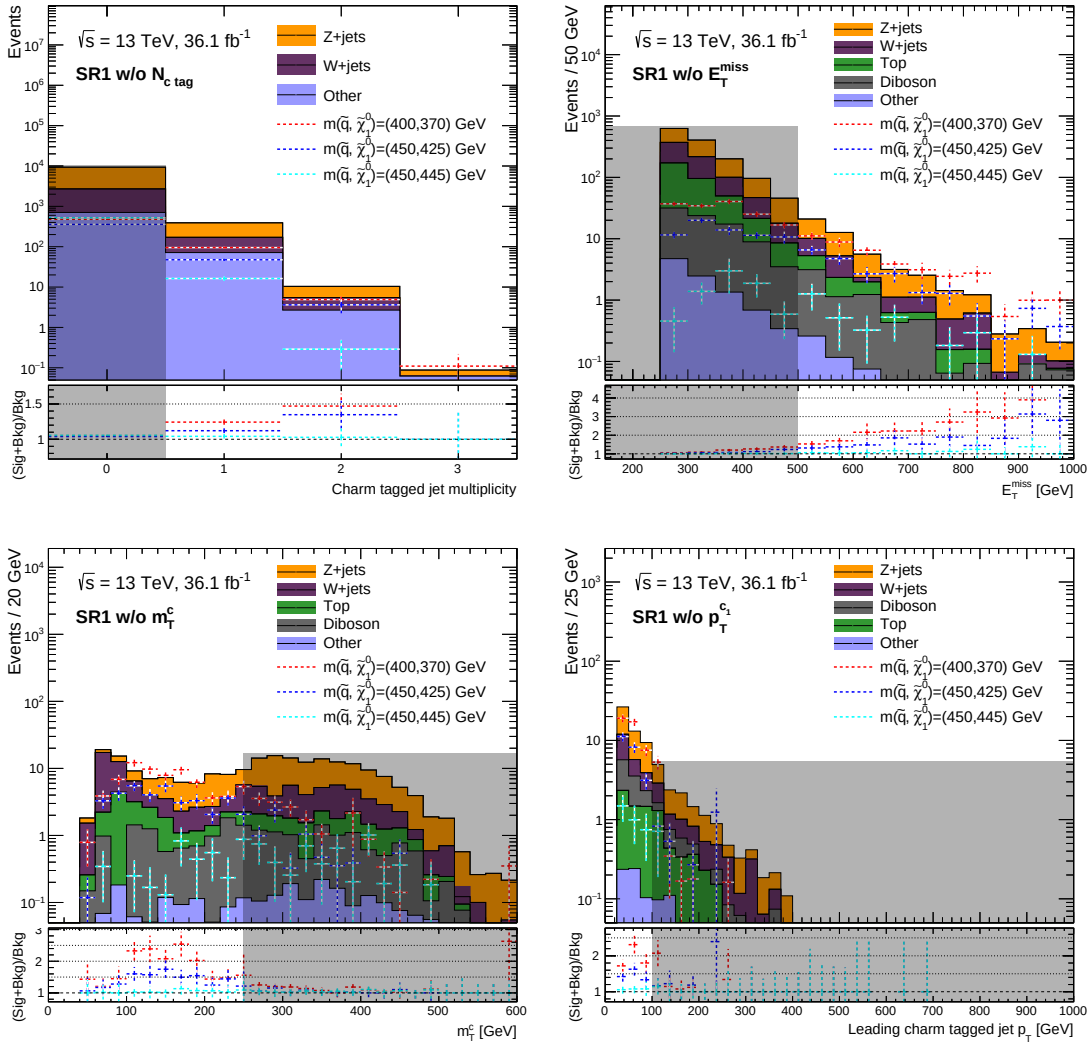

Figure 11.2: N-1 plots of SR1 showing the charm tagged jet multiplicity (upper left), $E_{\mathrm{T}}^{\mathrm{miss}}$ (upper right), m_{T}^{c} (lower left) and $p_{\mathrm{T}}^{c_1}$ (lower right) before the fit. The removed signal region requirements are indicated by the gray areas. The charm tagged jet multiplicity plot also removes requirements on the $p_{\mathrm{T}}^{c_1}$ and m_{T}^{c}. Backgrounds with less than 5% contribution are combined in *Other*. Only statistical uncertainties are shown.

11.2. SR2

SR2 is designed for signals with 40 GeV $\lesssim \Delta m \lesssim$100 GeV. An ISR boost is still required to pass the $E_{\mathrm{T}}^{\mathrm{miss}}$ requirements and the jets from charm quarks can usually be reconstructed, thus at least three jets are required (see figure 11.3). As for SR1 a tighter $E_{\mathrm{T}}^{\mathrm{miss}}$ cut could improve the signal over background ratio, but suffers from higher extrapolation uncertainties. The upper cut on m_{T}^{c} is loosened, as the signals are shifted slightly towards higher values. The signals' leading charm tagged jet p_{T} peaks at ~75 GeV, while the background is even lower, so the upper cut is replaced by a requirement of $p_{\mathrm{T}}^{c1} > 60$ GeV.

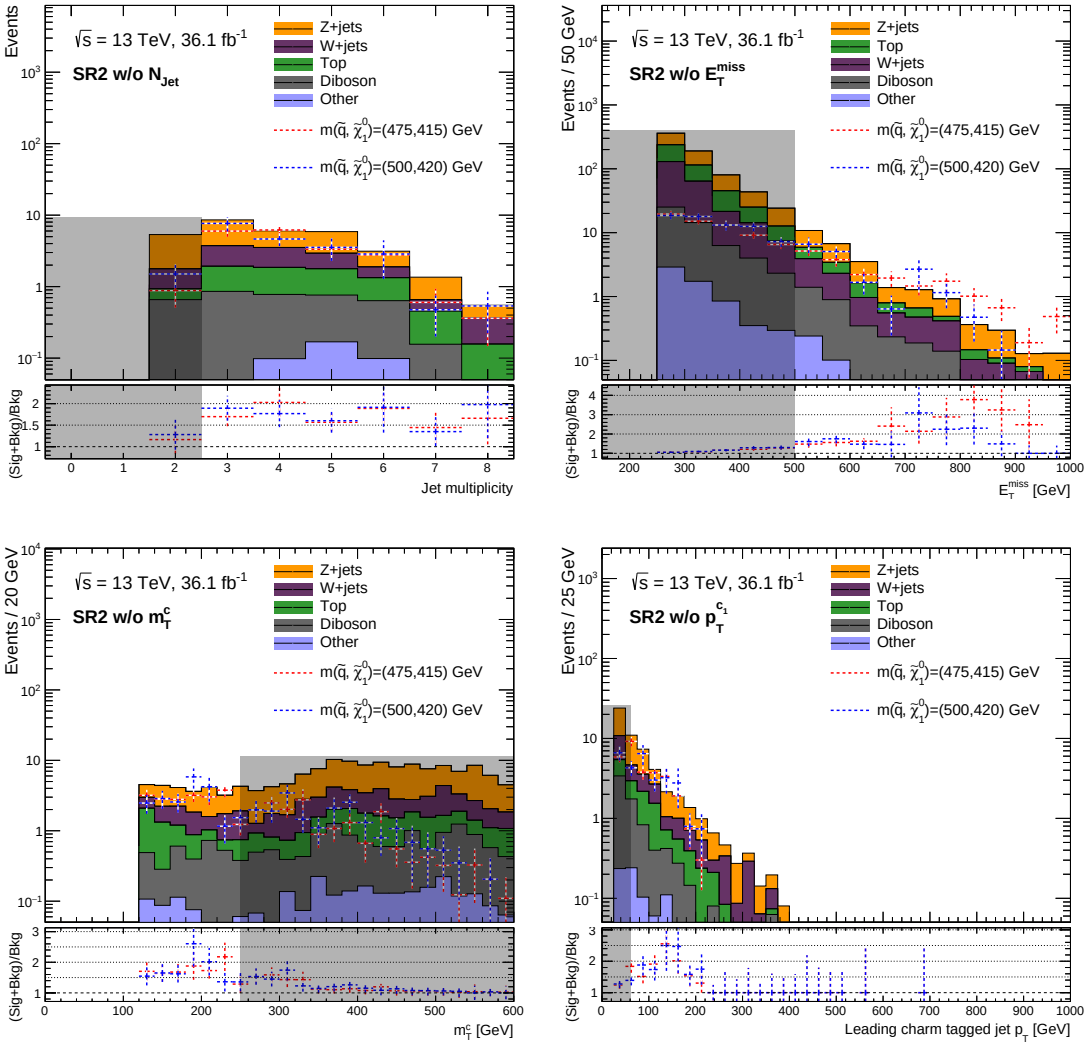

Figure 11.3: N-1 plots of SR2 showing the jet multiplicity (upper left), $E_{\mathrm{T}}^{\mathrm{miss}}$ (upper right), m_{T}^{c} (lower left) and p_{T}^{c1} (lower right) before the fit. The removed signal region requirements are indicated by the gray areas. Backgrounds with less than 5% contribution are combined in *Other*. Only statistical uncertainties are shown.

11.3. SR3

SR3 was optimized for signals with mass differences of $100-200$ GeV. They are still dominated by events with leading jets from ISR, however the subleading jets gain momentum from the increased mass differences and the requirements are tightened (see figure 11.4). The same is therefore true for the highly correlated p_{T}^{c1}, as the second or third jet are usually charm tagged.

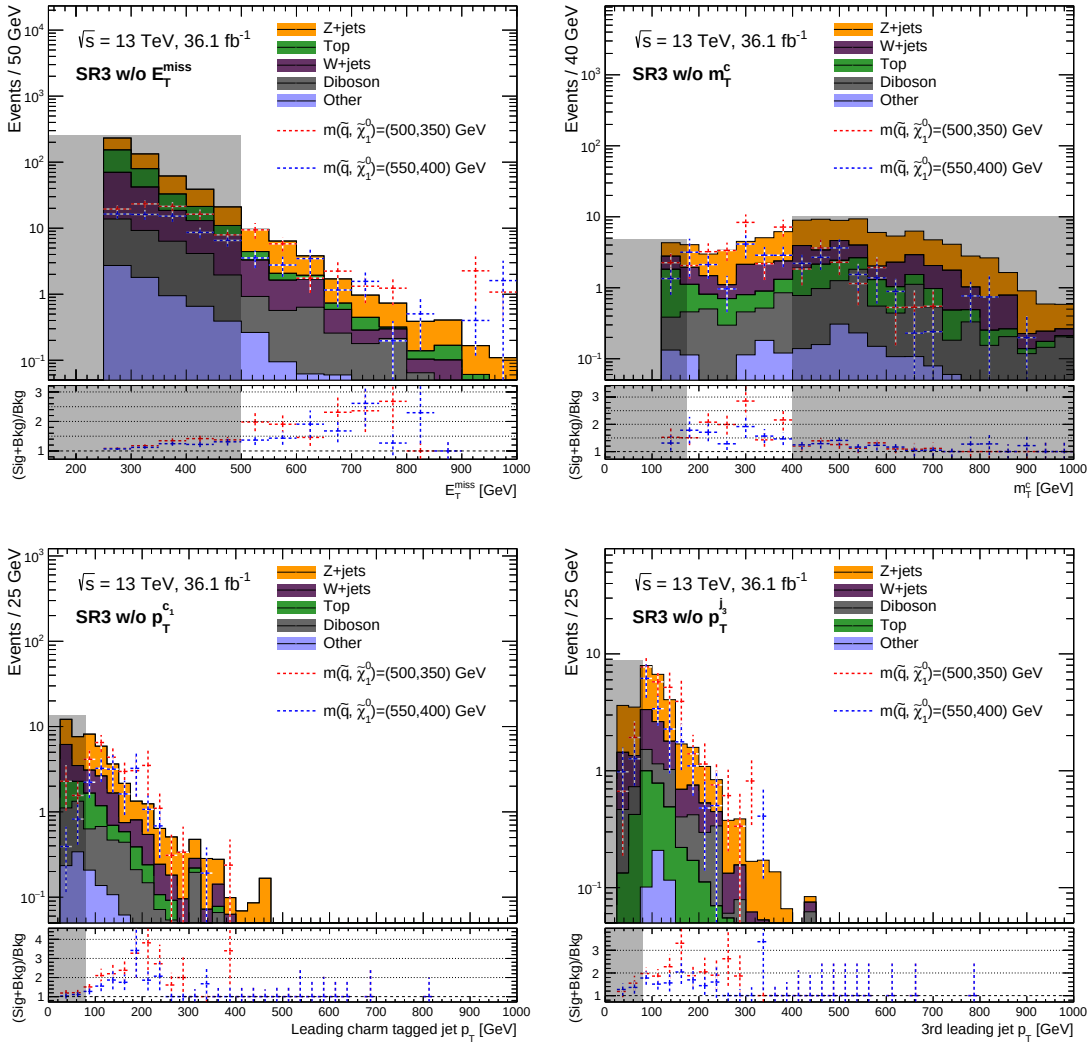

Figure 11.4: N-1 plots of SR3 showing $E_{\mathrm{T}}^{\mathrm{miss}}$ (upper left), m_{T}^{c} (upper right), p_{T}^{c1} (lower left) and the third leading jet p_{T} (lower right) before the fit. The removed signal region requirements are indicated by the gray areas. Backgrounds with less than 5% contribution are combined in *Other*. Only statistical uncertainties are shown.

11.4. SR4

SR4 targets signals with mass differences up to 400 GeV. The ISR boost's efficiency is reduced, leading to a less pronounced tail in $E_{\mathrm{T}}^{\mathrm{miss}}$ (see figure 11.5). Still, sensitivity is gained by rejecting events with charm tagged leading jets. The requirements on the momenta of the subleading jets and the leading charm tagged jet are further tightened.

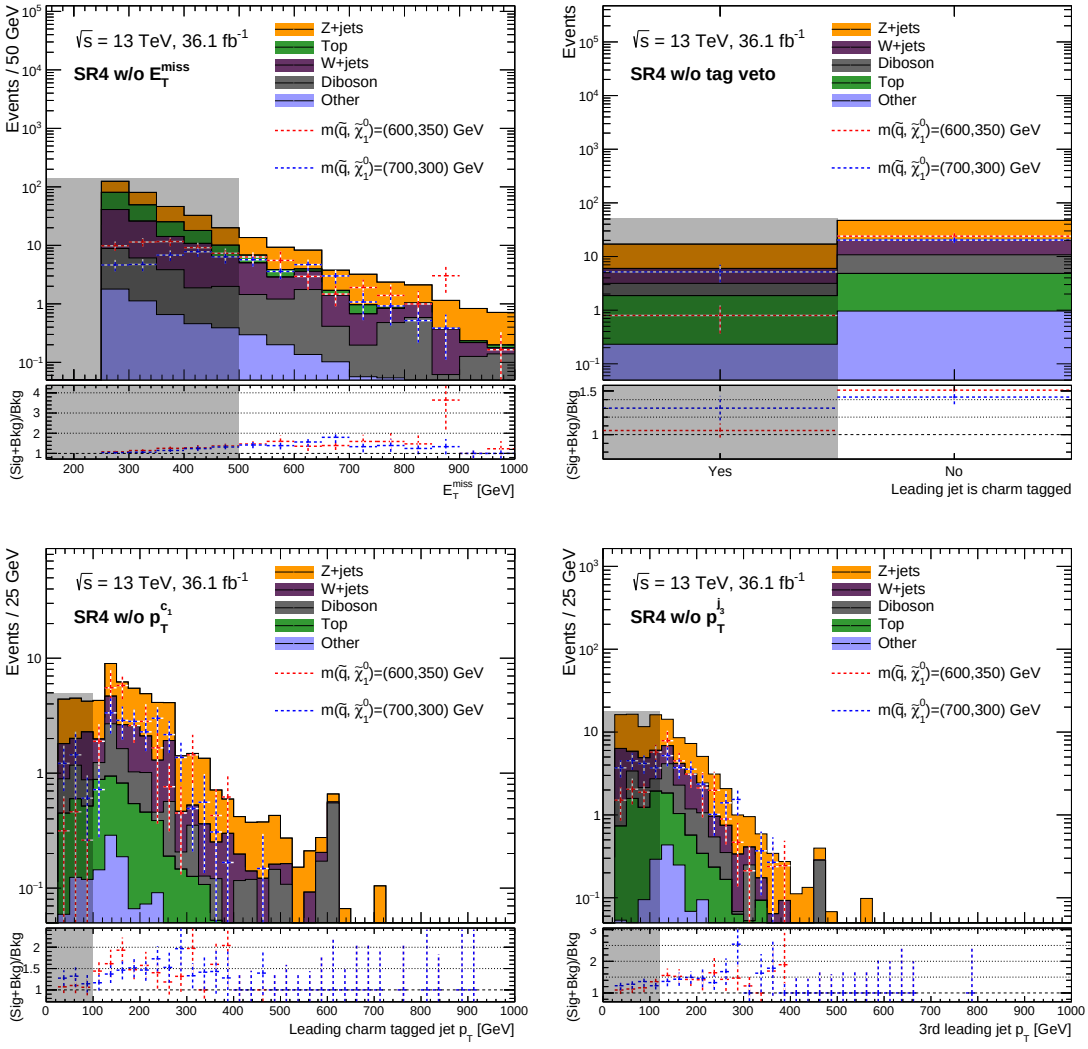

Figure 11.5: N-1 plots of SR2 showing $E_{\mathrm{T}}^{\mathrm{miss}}$ (upper left), the probability for the leading jet to be tagged (upper right), p_{T}^{c1} (lower left) and the third leading jet p_{T} (lower right) before the fit. The removed signal region requirements are indicated by the gray areas. Backgrounds with less than 5% contribution are combined in *Other*. Only statistical uncertainties are shown.

11.5. SR5

SR5 targets the largest mass differences, meaning signals with neutralino masses of 1 GeV. The missing transverse momentum originates completely in the squark decays and no additional boost is required (see figure 11.6). The signals' m_{T}^{c} distribution shifts towards even higher values and so do the subleading jet momenta. Even though no hard ISR jet is required, the possibility of additional jet radiation is high and the jet multiplicity cut remains at ≥ 3.

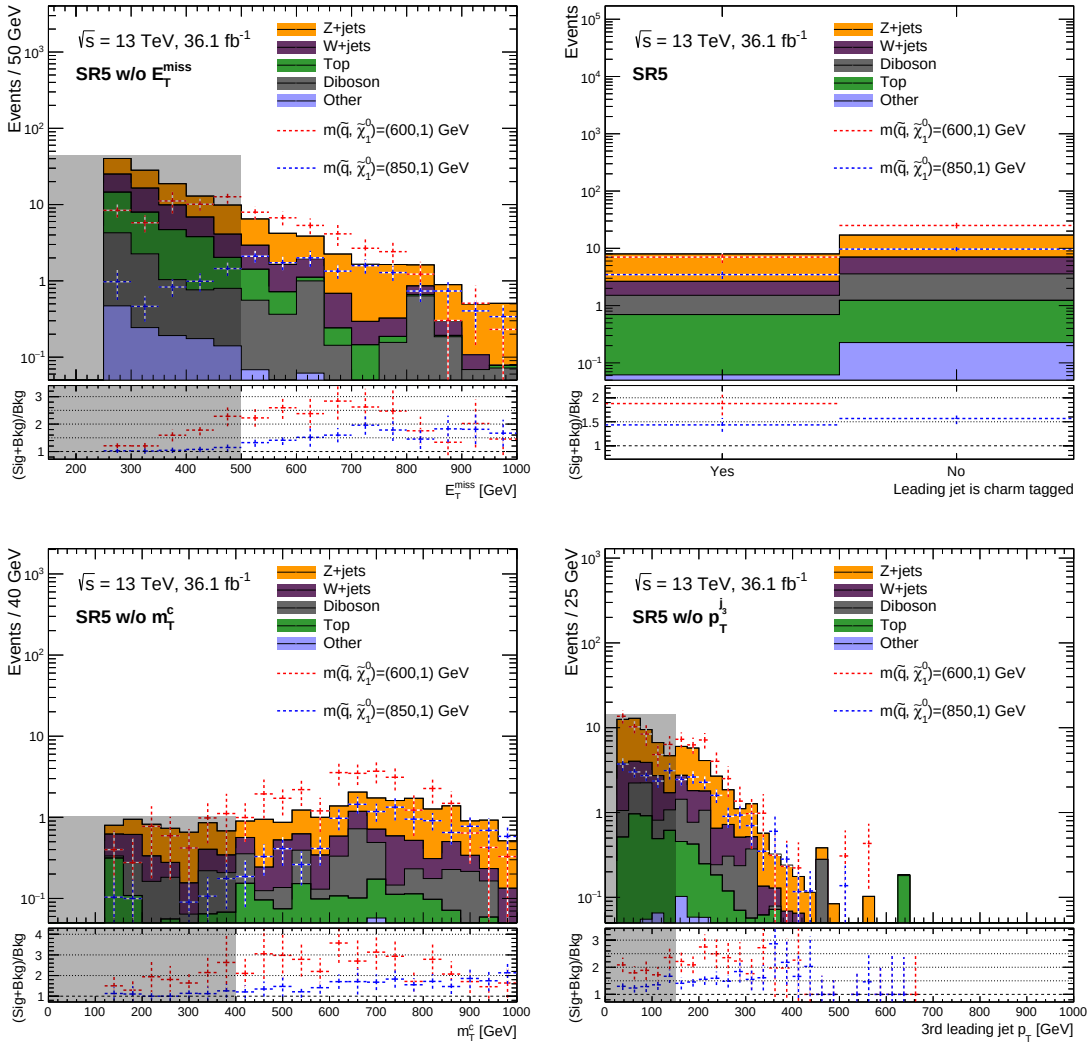

Figure 11.6: N-1 plots of SR2 showing $E_{\mathrm{T}}^{\mathrm{miss}}$ (upper left), m_{T}^{c} (upper right), $p_{\mathrm{T}}^{c_1}$ (lower left) and the third leading jet p_{T} (lower right) before the fit. The removed signal region requirements are indicated by the gray areas. Backgrounds with less than 5% contribution are combined in *Other*. Only statistical uncertainties are shown.

11.6. Control regions

The control region definitions follow the logic for kinematic requirements introduced in section 7.4 and the lepton selections and replacements described in section 8. Each region is denoted *CRX,* with $X = 1, ..., 5$ corresponding to the signal regions, plus an indicator for the specific process. For example CR3 Z is the Z+jets control region of SR3. It applies the requirements of CRZ τ veto and adds the loosened signal region requirements. An overview of the control region definitions is shown in table 11.4, the individual regions will be discussed in the following. In general the control region yields are quite low[2], which is mainly due to the low charm tagging efficiency.

	CR1	CR2	CR3	CR4	CR5
	Lepton and mass selections depending on controlled process				
	Preselection τ veto				
jet multiplicity	≥ 2	≥ 3	≥ 3	≥ 3	≥ 3
leading jet tag veto	yes	yes	yes	yes	no
$p_{\mathrm{T}}^{j_2}$ [GeV]			> 100	> 100	> 100
$p_{\mathrm{T}}^{j_3}$ [GeV]			> 80	> 100	> 100
$p_{\mathrm{T}}^{c_1}$ [GeV]	< 100	> 60	> 80	> 100	> 100
m_{T}^{c}	< 250	< 250	$\in (175, 400)$	> 200	> 400

Table 11.4: Overview of the control region selections.

11.6.1. Z+jets control regions

The Z+jets control regions have a very high purity of $Z \to \ell\ell$ events, however the statistics are quite low, going down to ~40 events in CR3 Z, CR4 Z and CR5 Z. While the normalization factor will still be driven by the control regions in the exclusion fits[3], the low yields will lead to relatively high statistical uncertainties.

The MC predictions are 20-35% lower in all regions, as expected due to the heavy flavor modeling, yet, the kinematic variables show an overall good description (see figure 11.7 and more in appendix B). This again validates the approach of using only a single normalization factor for this background.

The flavor composition of the charm tagged jets is consistent between each signal and control region, such that no additional uncertainty needs to be added (see figure 11.8 and more in appendix E).

As discussed in section 10.2, theory uncertainties are extracted based on the extrapolations from signal to control regions. Figure 11.9 shows the $E_{\mathrm{T}}^{\mathrm{miss}}$ distributions of Z+jets ckkw variation samples in a control region (left) and the corresponding signal region (right). Both plots are scaled using the normalization factor r_i and the resulting uncertainty is calculated as v_{ud} using the normalization differences in the signal region. The uncertainties for all sources are listed in table 11.6.

[2]Other analyses usually have a factor 5-10 more events.
[3]The background only fit does not include the signal region and is thus automatically driven by the CRs.

	CR1 Z	CR2 Z	CR3 Z	CR4 Z	CR5 Z
$W \to e\nu$	0	0	0	0	0
$W \to \mu\nu$	0	0	0	0	0
$W \to \tau\nu$ ISR	0	0	0	0	0
$W \to \tau\nu$ fake	0	0	0	0	0
$Z \to ee$	64.6 (2.8)	21.5 (1.1)	16.8 (0.7)	20.1 (0.8)	20.6 (0.9)
$Z \to \mu\mu$	56.1 (2.8)	22.7 (1.1)	16.8 (0.7)	18.8 (0.9)	18.4 (1)
$Z \to \nu\nu$	0	0	0	0	0
$t\bar{t}$	0.3 (0.3)	1 (0.6)	0.5 (0.5)	0	0.7 (0.5)
single top	0	0	0	0	0
Diboson	7.8 (0.7)	4.4 (0.4)	3.6 (0.4)	3.7 (0.4)	3.6 (0.5)
Other	0 (0)	0 (0)	0 (0)	0 (0)	0
Total background	128.7 (4)	49.6 (1.7)	37.6 (1.2)	42.7 (1.3)	43.3 (1.5)
Data	172 (13.1)	65 (8.1)	45 (6.7)	54 (7.3)	55 (7.4)
Data/BG	1.34	1.31	1.2	1.26	1.27

Table 11.5: Pre-fit event yields in the Z control regions. Statistical uncertainties are shown in brackets.

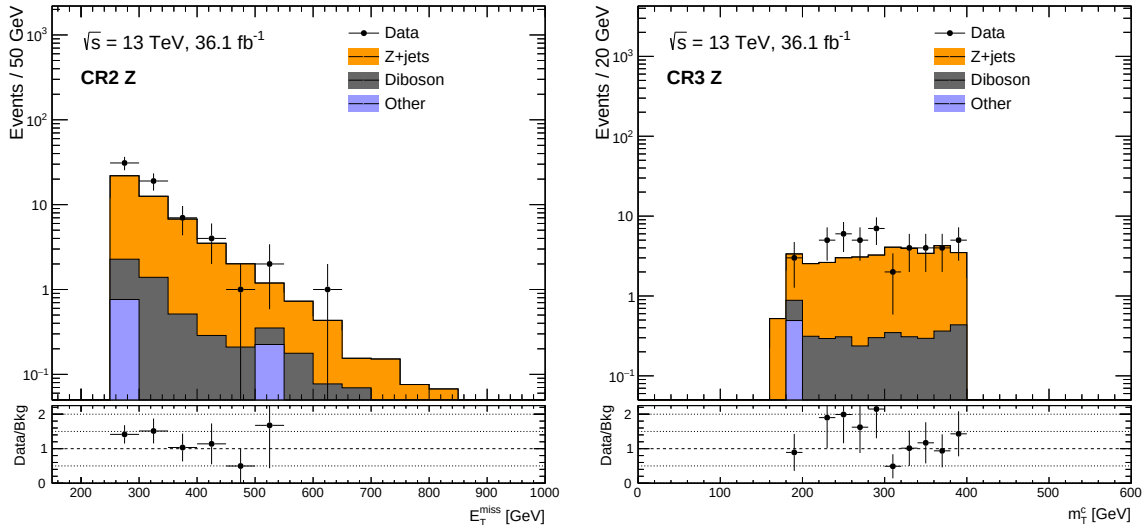

Figure 11.7: $E_{\mathrm{T}}^{\mathrm{miss}}$ in CR2 Z (left) and m_{T}^{c} in CR4 Z (right) before the fit. Only statistical uncertainties are shown.

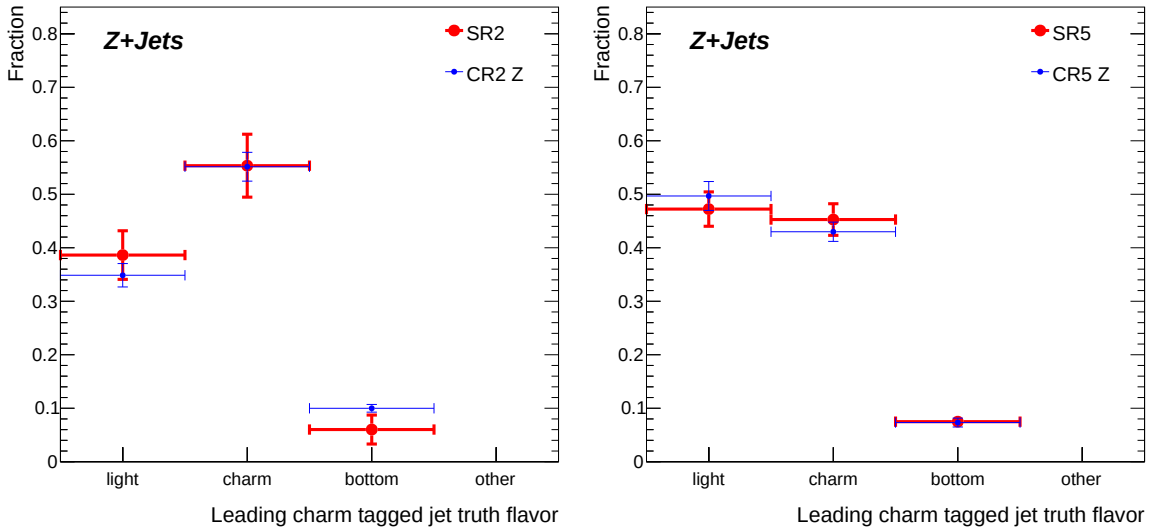

Figure 11.8: Truth flavor of the leading charm tagged jet in CR2 Z (left) and CR5 Z (right) and the corresponding signal regions. Only statistical uncertainties are shown.

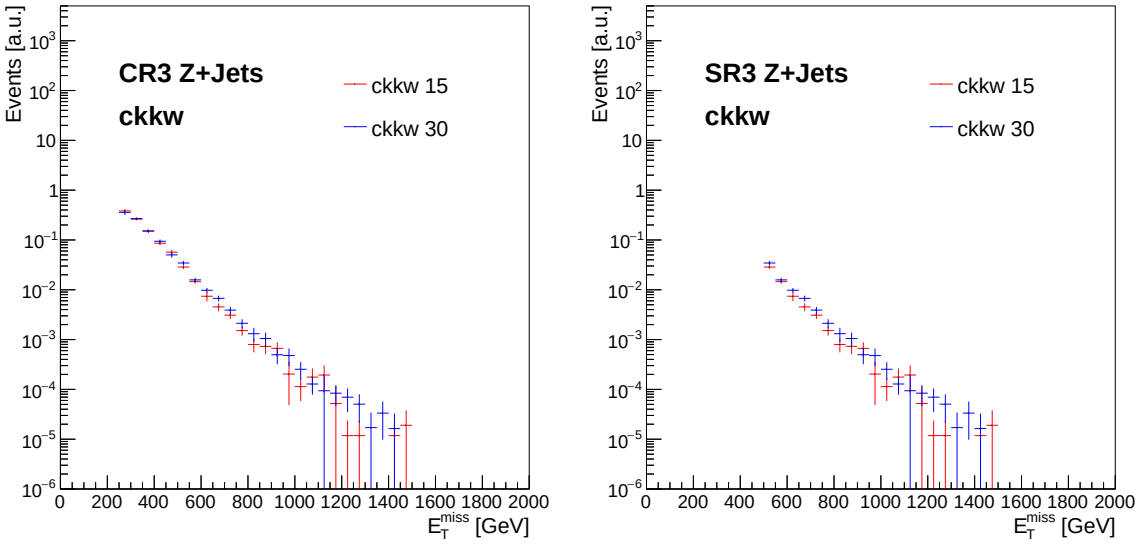

Figure 11.9: Z+jets $E_{\mathrm{T}}^{\mathrm{miss}}$ distributions in CR3 Z and SR3 used to extract the ckkw theory uncertainty. Both plots are scaled by r_i as introduced in section 10.2.

		Resummation scale	Factorization & Renormalization scales	Matching scale
SR1	Up	3.86%	11.87%	0.82%
	Down	-3.86%	-12.27%	-0.82%
SR2	Up	2.38%	5.03%	4.79%
	Down	-2.38%	-5.59%	-4.79%
SR3	Up	3.88%	6.06%	10.19%
	Down	-3.88%	-10.27%	-10.19%
SR4	Up	3.76%	6.25%	7.87%
	Down	-3.76%	-7.47%	-7.87%
SR5	Up	0.59%	5.07%	5.15%
	Down	-0.59%	-4.9%	-5.15%

Table 11.6: Overview of the theory uncertainties for Z+jets in all signal regions.

11.6.2. W+jets control regions

The W+jets control regions have higher statistics than the Z+jets regions, however the purity goes down to ~55% in CR2 W with the competing process being top. They also show an offset between data and MC predictions, which is however lower than for Z+jets in most regions due to the reduced purity (see table 11.7). The ratio between data and MC is flat in most distributions, yet shows slopes in some of them (see figure 11.10 and more in appendix C). These variables are sensitive to differences between $W \to \ell\nu$ and top events, like jet multiplicity, so there is a higher offset in the W dominated areas and a lower one where top events have the highest impact. The approach of using only a single normalization factor per process remains valid, as the slope is not the result of mismodeling one background, but instead the interference of the two processes with different normalization offsets.

The flavor compositions of the leading charm tagged jet show good agreements in all regions, except for CR4 (see figure 11.11 and more in appendix E). The uncertainty is calculated as described in section 10.2.5, resulting in $\sigma^{W}_{\mathrm{HF}} = (+16.6\%, -6.6\%)$. An overview of all theory uncertainties is shown in table 11.8.

	CR1 W	CR2 W	CR3 W	CR4 W	CR5 W
$W \to e\nu$	90 (6.8)	31.1 (2.8)	31.1 (2.5)	47.6 (2.9)	66.5 (9.8)
$W \to \mu\nu$	92 (7.9)	32.9 (4)	35.7 (2.7)	47.1 (3)	50.3 (3.3)
$W \to \tau\nu$ ISR	4.1 (1.1)	1 (0.5)	1.4 (0.8)	1.4 (0.3)	1.5 (0.4)
$W \to \tau\nu$ fake	0.2 (0.1)	0.1 (0)	0.1 (0.1)	0 (0)	0 (0)
$Z \to ee$	0.3 (0.2)	0.3 (0.1)	0.4 (0.1)	0.7 (0.2)	0.6 (0.3)
$Z \to \mu\mu$	0.6 (0.2)	0.2 (0.1)	0.4 (0.2)	0.5 (0.1)	0.5 (0.1)
$Z \to \nu\nu$	0.1 (0)	0 (0)	0 (0)	0 (0)	0.1 (0)
$t\bar{t}$	44.2 (2.9)	29.6 (2.4)	19.5 (2.2)	21.3 (1.9)	18.4 (1.8)
single top	14.2 (1.5)	8.9 (1.3)	9.6 (1.4)	11.6 (1.7)	13 (2.2)
Diboson	20.3 (4.2)	12.2 (3)	9.4 (2.8)	7.3 (2)	6.4 (2.1)
Other	0.8 (0.2)	0.6 (0.2)	1 (0.2)	0.8 (0.2)	0.7 (0.2)
Total background	266.7 (11.7)	116.9 (6.4)	108.7 (5.4)	138.4 (5.3)	157.9 (10.9)
Data	301 (17.3)	141 (11.9)	153 (12.4)	179 (13.4)	192 (13.9)
Data/BG	1.13	1.21	1.41	1.29	1.22

Table 11.7: Pre-fit event yields in the Z control regions. Statistical uncertainties are shown in brackets.

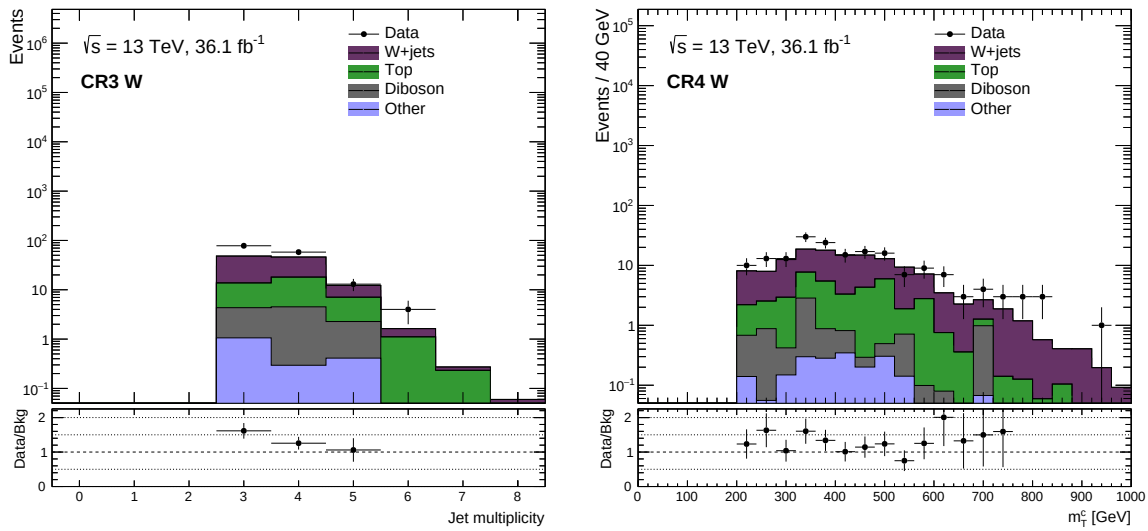

Figure 11.10: $E_{\mathrm{T}}^{\mathrm{miss}}$ in CR3 W (left) and m_{T}^{c} in CR4 W (right) before the fit. Only statistical uncertainties are shown.

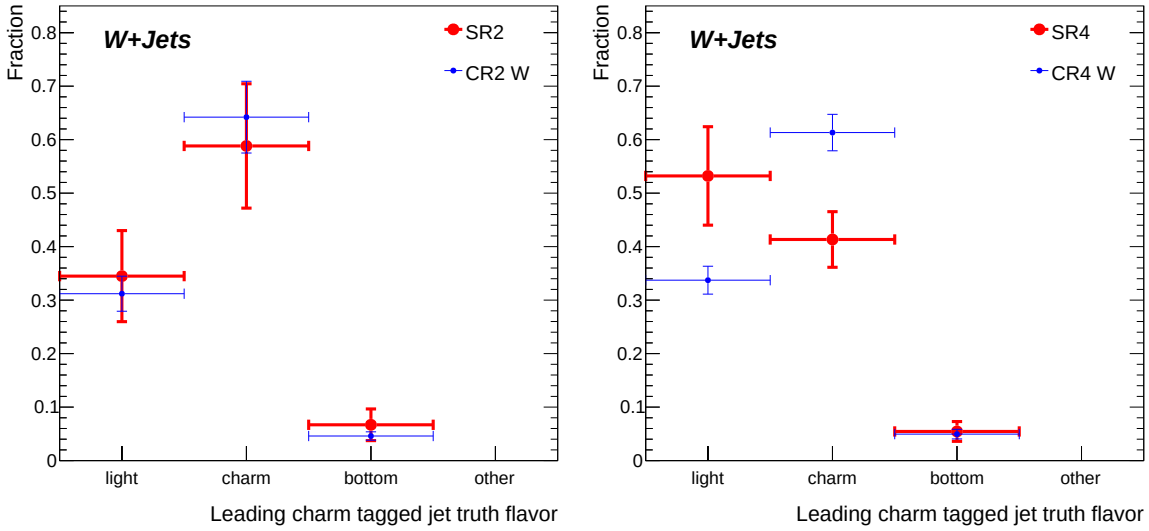

Figure 11.11: Truth flavor of the leading charm tagged jet in CR1 W (left) and CR4 W (right) and the corresponding signal regions. Only statistical uncertainties are shown.

		Resummation scale	Factorization & Renormalization scales	Matching scale	Jet Flavor Composition
SR1	Up	3.86%	11.87%	0.82%	-
	Down	-3.86%	-12.27%	-0.82%	-
SR2	Up	2.38%	5.03%	4.79%	-
	Down	-2.38%	-5.59%	-4.79%	-
SR3	Up	3.88%	6.06%	10.19%	-
	Down	-3.88%	-10.27%	-10.19%	-
SR4	Up	3.76%	6.25%	7.87%	16.6%
	Down	-3.76%	-7.47%	-7.87%	-6.6%
SR5	Up	0.59%	5.07%	5.15%	-
	Down	-0.59%	-4.9%	-5.15%	-

Table 11.8: Overview of the theory uncertainties for W+jets in all signal regions.

11.6.3. Top control regions

The Top control regions reach a purity of ~70%, competing with $W \to \ell\nu$ events. They show an overall smaller offset between data and MC predictions than the V+jets regions (see table 11.9), and have a good description of the kinematic variables (see figure 11.12 and more in appendix D).

The charm tagged jet flavor compositions show a worse agreement than for V+jets, yet are usually within 1σ statistical uncertainty. No additional uncertainties need to be added, as discussed in section 10.2.5. The other theory uncertainties are extracted as described in section 10.2, however some samples run out of statistics for high values of $E_{\mathrm{T}}^{\mathrm{miss}}$. While the samples with varied radiation show no problems, the Sherpa 2.2.1 sample used for the generator comparison has no events left in SR3 (see figure 11.14), so an uncertainty of 100% is assumed. While this is an overly conservative estimation, the $t\bar{t}$ contamination is quite low in all signal regions, so it has only a minor impact. An overview of the uncertainties is shown in table 11.10.[4]

	CR1 Top	CR2 Top	CR3 Top	CR4 Top	CR5 Top
$W \to e\nu$	28.6 (4.3)	6.2 (0.8)	12.4 (2.8)	12.6 (2.8)	7.1 (1)
$W \to \mu\nu$	27.9 (3.3)	7.6 (1.2)	6.8 (1.1)	5.9 (0.9)	6.5 (1.3)
$W \to \tau\nu$ ISR	0.9 (0.4)	0.2 (0.1)	0.3 (0.1)	0.7 (0.2)	0.6 (0.2)
$W \to \tau\nu$ fake	0.1 (0)	0 (0)	0 (0)	0	0
$Z \to ee$	0.2 (0.1)	0 (0)	0.1 (0)	0 (0)	0 (0)
$Z \to \mu\mu$	0 (0)	0.1 (0)	0 (0)	0 (0)	0.1 (0.1)
$Z \to \nu\nu$	0 (0)	0	0 (0)	0 (0)	0 (0)
$t\bar{t}$	97.9 (4.2)	34.1 (2.4)	45.4 (3.2)	41.1 (2.9)	31.5 (2.4)
single top	14.1 (1.5)	5.1 (0.8)	8.4 (1.2)	7.5 (1)	7.9 (1.1)
Diboson	5.8 (1.4)	1.2 (0.6)	2.9 (1.2)	2.5 (1)	1.1 (0.4)
Other	1.7 (0.1)	0.7 (0.1)	1.1 (0.1)	1.1 (0.1)	0.8 (0.1)
Total background	177.2 (7.2)	55.3 (3)	77.5 (4.7)	71.4 (4.4)	55.7 (3.1)
Data	202 (14.2)	69 (8.3)	84 (9.2)	71 (8.4)	60 (7.7)
Data/BG	1.14	1.25	1.08	0.99	1.08

Table 11.9: Pre-fit event yields in the Z control regions. Statistical uncertainties are shown in brackets.

	Ttbar_Radiation	Ttbar_Shower	Ttbar_Generator
SR1	±3.77%	±22.94%	±12.96%
SR2	±1.07%	±31.72%	±6.71%
SR3	±3.34%	±62.71%	±100.0%
SR4	±2.25%	±47.99%	±26.44%
SR5	±1.31%	±6.38%	±9.56%

Table 11.10: Overview of the theory uncertainties for $t\bar{t}$ in all signal regions.

[4] As discussed in section 10.2.3, the single top theory uncertainty is set to 100%.

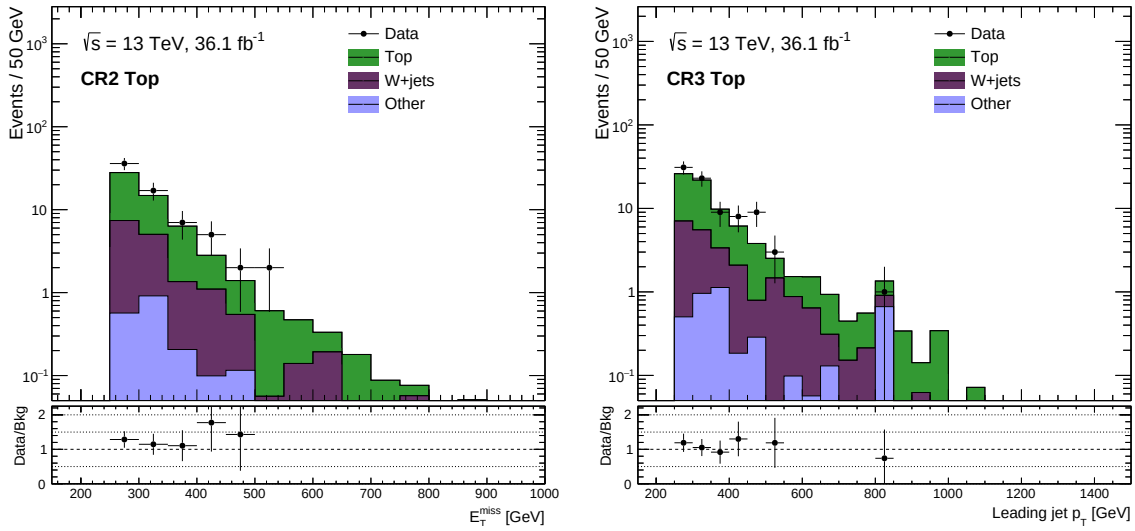

Figure 11.12: $E_{\mathrm{T}}^{\mathrm{miss}}$ in CR2 Top (left) and p_{T}^{j1} in CR3 Top (right) before the fit. Only statistical uncertainties are shown.

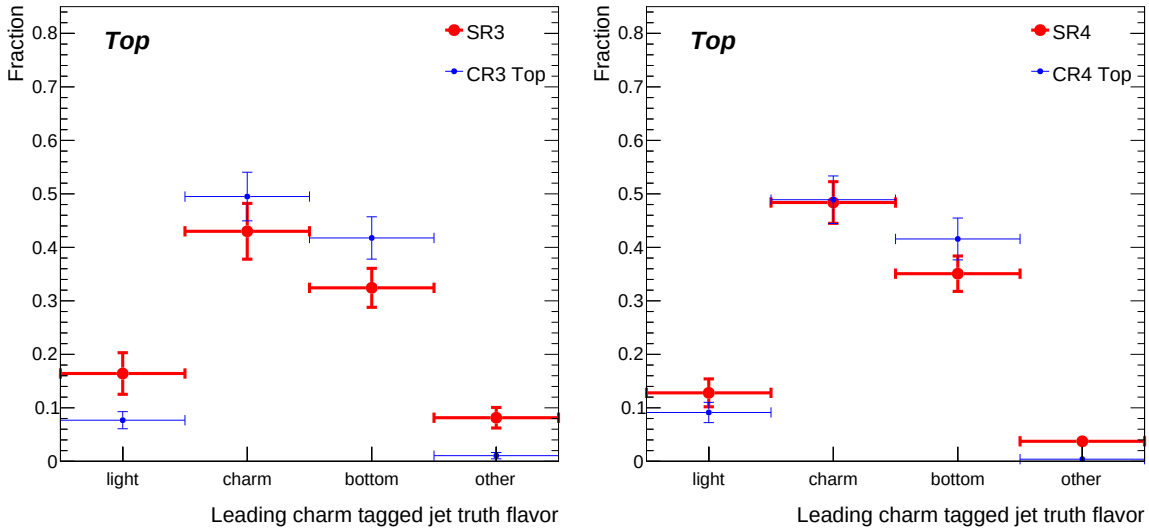

Figure 11.13: Truth flavor of the leading charm tagged jet in CR3 Top (left) and CR4 Top (right) and the corresponding signal regions. Only statistical uncertainties are shown.

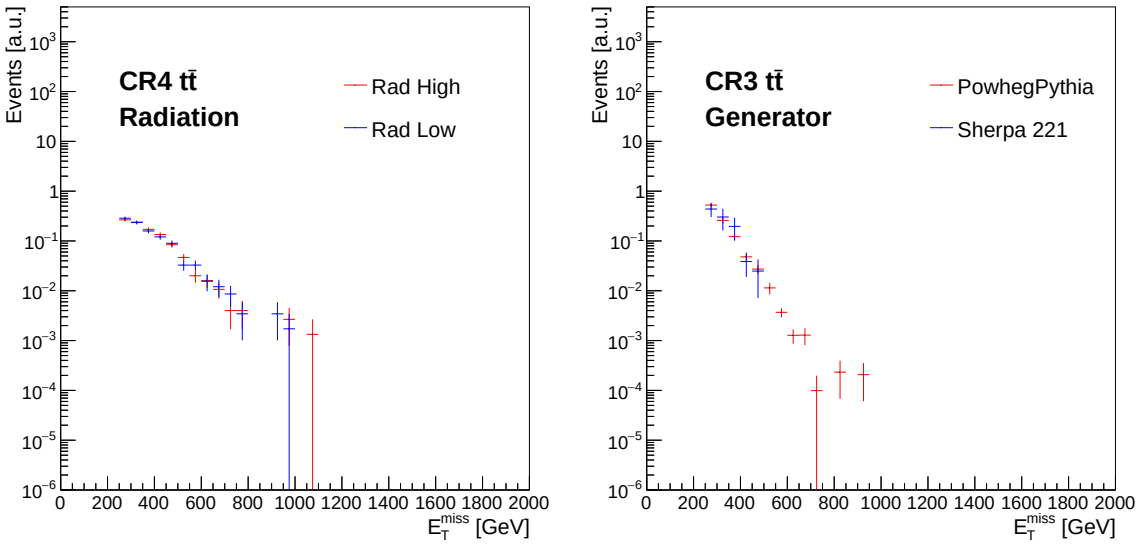

Figure 11.14: $E_{\mathrm{T}}^{\mathrm{miss}}$ distributions for $t\bar{t}$ events in CR4 Top (left) and CR3 Top (right) used to extract the radiation and generator theory uncertainties, respectively. Both plots are scaled by r_i as introduced in section 10.2.

11.6.4. Diboson events

As no control regions are defined for diboson events, the theory uncertainties must be applied not only in the signal but also in all control regions of other processes (see section 10.2.4). The kinematic requirements of the process specific control regions are identical for each signal region respectively, so the same value is used. An overview is shown in table 11.11.

	Factorization scale	Renormalization scale	Resummation scale
SR1	±6.21%	±17.82%	±16.35%
CR1	±0.95%	±18.76%	±1.03%
SR2	±29.45%	±36.78%	±22.13%
CR2	±2.72%	±25.96%	±1.63%
SR3	±8.4%	±4.36%	±13.5%
CR3	±4.07%	±11.14%	±6.9%
SR4	±17.55%	±10.28%	±26.53%
CR4	±1.71%	±0.65%	±9.35%
SR5	±5.31%	±4.24%	±46.24%
CR5	±10.08%	±0.14%	±24.29%

Table 11.11: Overview of the theory uncertainties for diboson events in all signal and control regions.

11.7. Validation regions

Before the signal regions can be unblinded, the background estimation procedure needs to be validated. Validation regions are defined to be orthogonal, yet kinematically close to the signal regions. This is achieved in three steps. First, signal enhancing cuts are modified or dropped with respect to the SR definitions. Second, a requirement of $m_{\mathrm{jj}}^{W} > 125$ GeV is applied in all regions, which was not designed for this purpose but rejects signal events without changing the jet flavor compositions[5]. Each region is then split into several selections by inverting kinematic variables to be able to validate others up to high values. For example VR1A inverts the $E_{\mathrm{T}}^{\mathrm{miss}}$ requirement such that $p_{\mathrm{T}}^{j_1}$ can be validated, while VR1B inverts $p_{\mathrm{T}}^{j_1}$ and $E_{\mathrm{T}}^{\mathrm{miss}}$ can be validated. In VR2-4 it is not sufficient to invert a single variable, so in each selection two requirements are inverted and therefore three regions (A, B and C) are defined. An overview of the validation region definitions is shown in table 11.12.

The validation regions should not be sensitive to any signal point. The eventual signal contamination was calculated and found to be at most 25% for signals with low squark masses that are close to the existing exclusion limits. As the cross section drops with increasing squark masses, this value decreases rapidly.

The leading charm tagged jet flavor compositions are in good agreement in all regions for Z+jets, and only differ in SR4 for W+jets (11.15 and more in appendix E). However, the disagreement is only between the signal and control regions, thus no uncertainty needs to be added for VR4 A-C. The top regions show more differences, but as discussed in section 10.2.5 it is not needed to introduce uncertainties.

[5]It was tested whether m_{jj}^{W} can be used to increase signal sensitivity in the signal regions, but was found to be not sufficiently sensitive.

	VR1	VR2	VR3	VR4	VR5
	Preselection + NCTag≥ 1 + τ veto				
NJet	≥ 2	≥ 3	≥ 3	≥ 3	≥ 3
lead. jet tag veto	yes	yes	yes	yes	no
$E_{\mathrm{T}}^{\mathrm{miss}}$ [GeV]	> 500	> 500	> 500	> 500	> 500
$p_{\mathrm{T}}^{j_1}$ [GeV]					> 300
$p_{\mathrm{T}}^{j_2}$ [GeV]			> 30 [> 100]	> 30 [> 140]	> 30 [> 200]
$p_{\mathrm{T}}^{j_3}$ [GeV]			> 30 [> 80]	> 30 [> 120]	> 30 [> 150]
$p_{\mathrm{T}}^{c_1}$ [GeV]	< 100	> 60	> 80	> 100	> 150
m_{T}^{c} [GeV]	> 250 [< 250]	$\in (300-450)$ [< 250]	$\in (300-400)$ [$\in (175, 400)$]	$\in (300, 500)$ [> 200]	> 400
	$m_{\mathrm{jj}}^{W} > 125.$ GeV				
VR A $E_{\mathrm{T}}^{\mathrm{miss}}$ [GeV]	< 350	< 350	< 350	< 350	< 350
VR A $p_{\mathrm{T}}^{j_2}$ [GeV]		< 175	< 200	< 200	
VR B $p_{\mathrm{T}}^{j_1}$ [GeV]	< 350	< 350	< 350	< 350	< 175
VR B $p_{\mathrm{T}}^{j_2}$ [GeV]		< 175	< 200	< 200	
VR C $E_{\mathrm{T}}^{\mathrm{miss}}$ [GeV]		< 350	< 350	< 350	
VR C $p_{\mathrm{T}}^{j_1}$ [GeV]		< 350	< 350	< 350	

Table 11.12: Definitions of all validation regions. Cuts that differ from their SR counterparts are marked in red with the SR cuts shown in brackets.

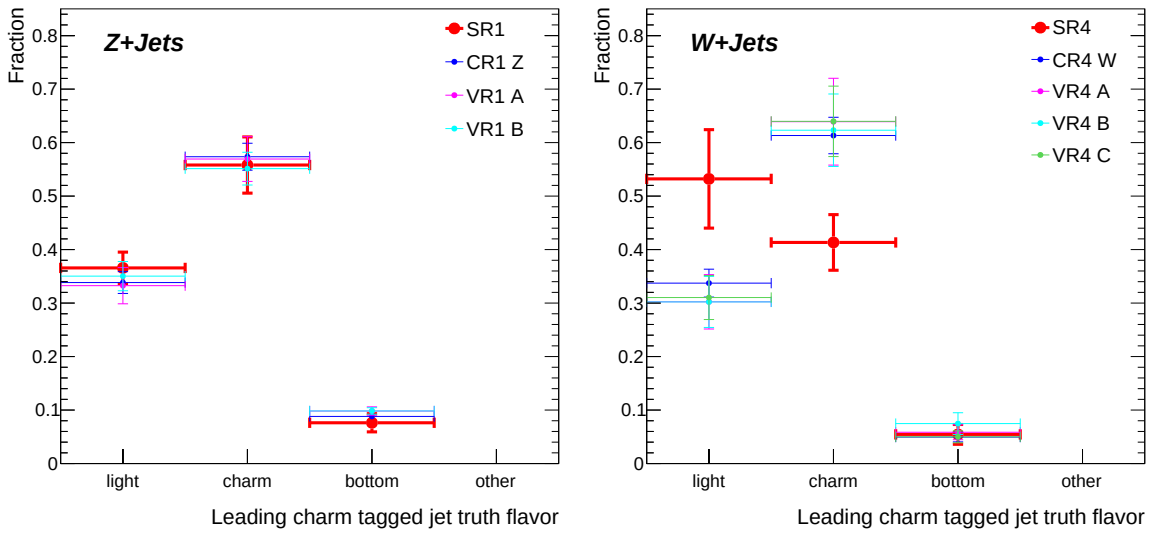

Figure 11.15: Flavor compositions of the leading charm tagged jet in signal, control and validation regions for Z+jets (left) and for W+jets (right). Only statistical uncertainties are shown.

All validation regions show a normalization difference between data and MC predictions, while no shape mismodeling is apparent (see figure 11.16). This fits the observations in the control regions, so adding normalization factors for each background is expected to fix the disagreements. The validation regions are therefore accepted to provide a proper test for the background estimation procedure.

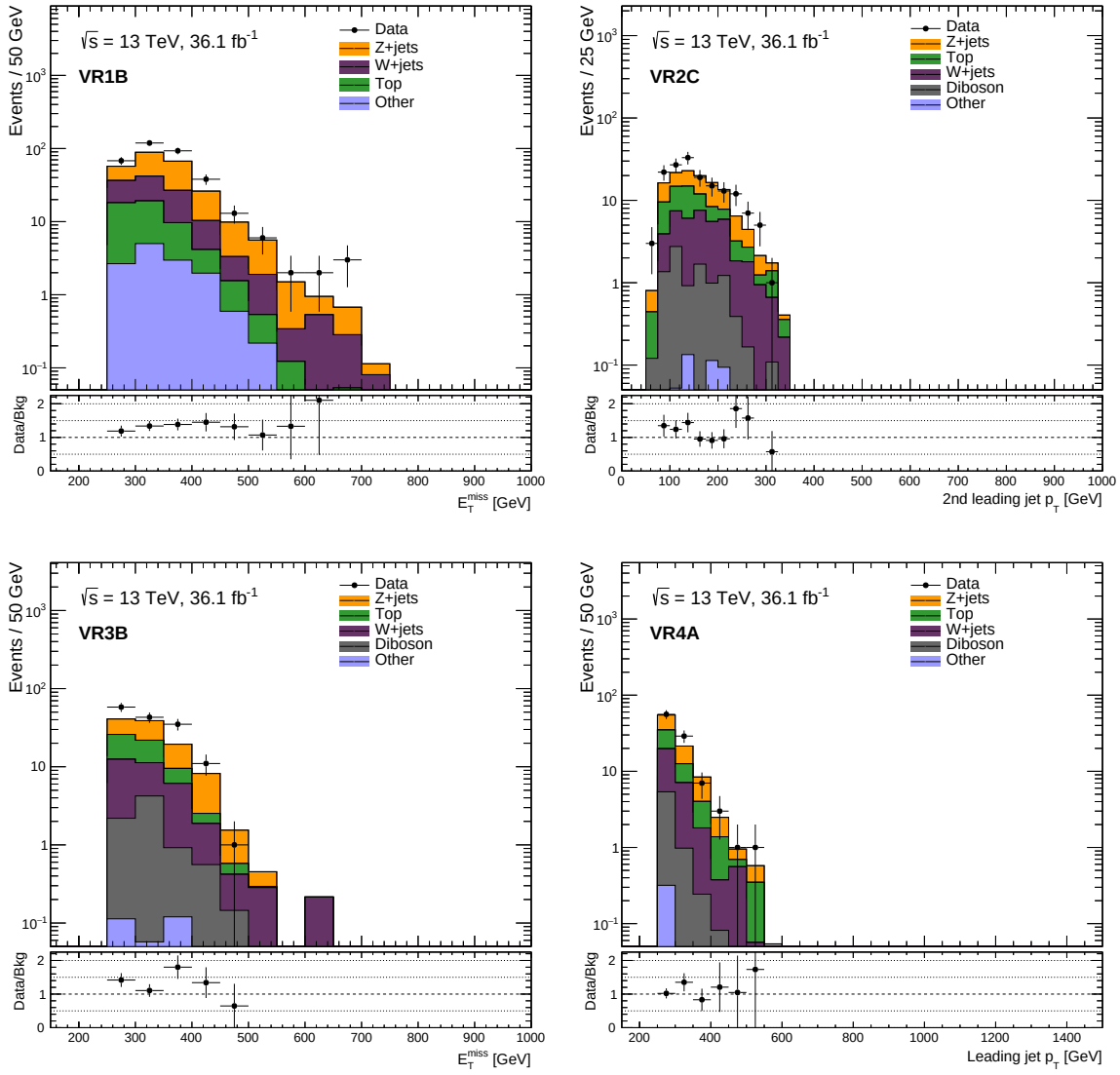

Figure 11.16: Distributions in various validation regions. $E_{\mathrm{T}}^{\mathrm{miss}}$ in VR1B (upper left), $p_{\mathrm{T}}^{j_2}$ in VR2C (upper right), $E_{\mathrm{T}}^{\mathrm{miss}}$ in VR3B (lower left) and $p_{\mathrm{T}}^{j_1}$ in VR4 A (lower right) before the fit. Only statistical uncertainties are shown.

12. Results

In order to compare the data driven background predictions with the observed data, background-only fits are performed for all regions as described in section 9.3. They use only in the control regions to estimate the normalization factors `mu_XXX` for each background process, which can then be applied in the validation regions to test the estimation procedure. If agreement is observed, the signal regions are unblinded and compared to the respective SM predictions. Depending on their agreement, the interpretation is done in form of discovery sensitivity or exclusion limits. All uncertainties described in previous chapters are included and their nuisance parameters are called `alpha_XXX` in case of experimental and theoretical uncertainties, or `gamma_XXX` in case of statistical uncertainties.

12.1. Background-only fit

Table 12.1 and figure 12.1 show the fitted background normalization factors `mu_XXX` in all signal regions after the background-only fit. As expected during the control region definition, the central values for W and Z+jets are in general higher than for Top because of the heavy flavor mismodeling. Their total uncertainties range from ~20% for mu_Z to ~40% for mu_Top, which are driven by the relatively low control region yields and, in case of mu_W and mu_Top, their high impurities. This results in anti-correlations between the regions' statistical uncertainties `gamma_XXX` and the corresponding normalization factors, as well between mu_W and mu_Top (see figure 12.2 and appendix F.1).

Additional anti-correlations can be observed between the charm tagging uncertainty `alpha_FT_C` and the normalization factors, indicating that the control region strategy of using similar charm tagging definitions was successful.

Fit parameter	SR1	SR2	SR3	SR4	SR5
mu_Wc	$1.13^{+0.20}_{-0.43}$	$1.20^{+0.44}_{-0.45}$	$1.70^{+0.45}_{-0.42}$	$1.49^{+0.37}_{-0.32}$	$1.28^{+0.33}_{-0.26}$
mu_Z	$1.35^{+0.27}_{-0.40}$	$1.34^{+0.26}_{-0.22}$	$1.22^{+0.28}_{-0.23}$	$1.29^{+0.29}_{-0.22}$	$1.30^{+0.32}_{-0.23}$
mu_Top	$1.15^{+0.38}_{-0.28}$	$1.28^{+0.54}_{-0.48}$	$0.86^{+0.33}_{-0.35}$	$0.80^{+0.34}_{-0.30}$	$1.01^{+0.45}_{-0.30}$

Table 12.1: Background-only post-fit values of the background normalization parameters. All uncertainties are included.

By definition, the overall normalization of the SM prediction matches the observed data perfectly in each control region after the background-only fit. However, only a single normalization factor is used for each process, so the kinematic distributions are not guaranteed to show agreement and can only do so, if the mismodeling was a pure normalization effect. This is indeed the case and a good agreement can be observed in all control regions (see figures 12.3-12.5 and appendix F.3). Even distributions in the W control regions that are sensitive to differences between W+jets and top, and which showed discrepancies in the shape of data and MC before the fit (e.g. jet multiplicity, see section 11.6.2) are compatible within the uncertainties after the fit.

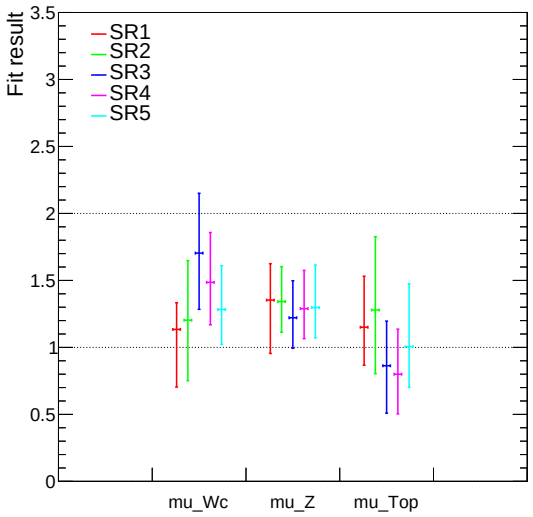

Figure 12.1: Background-only post-fit values of the background normalization parameters. All uncertainties are included.

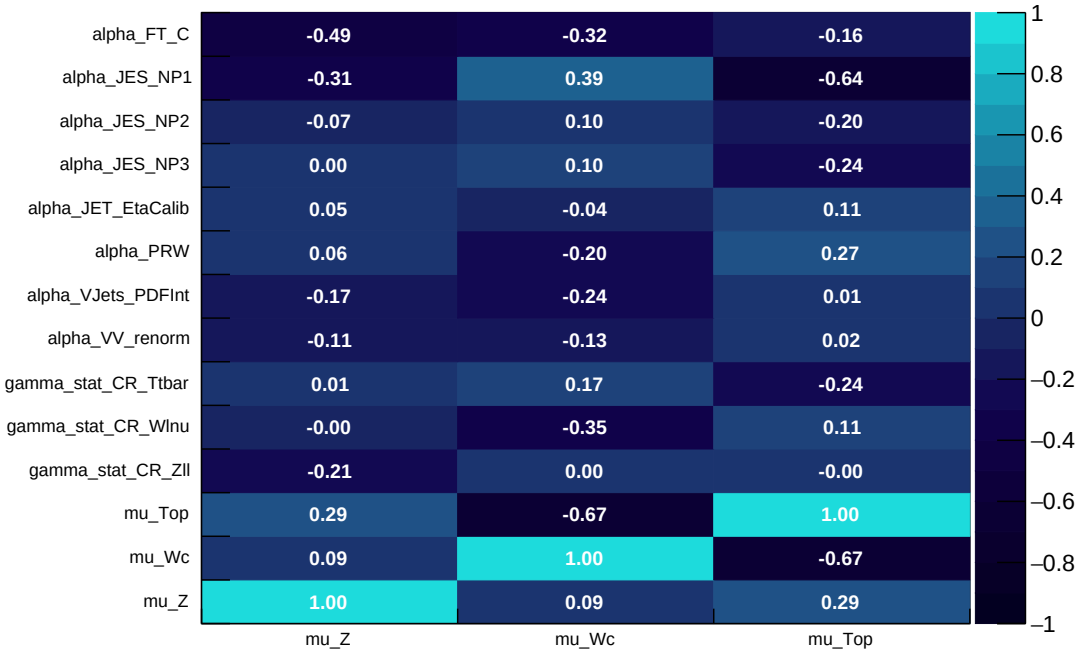

Figure 12.2: Correlation matrix of the background-only fit parameters in SR2. Only parameters that have at least one (anti-) correlation with an absolute value ≥ 0.1 are shown.

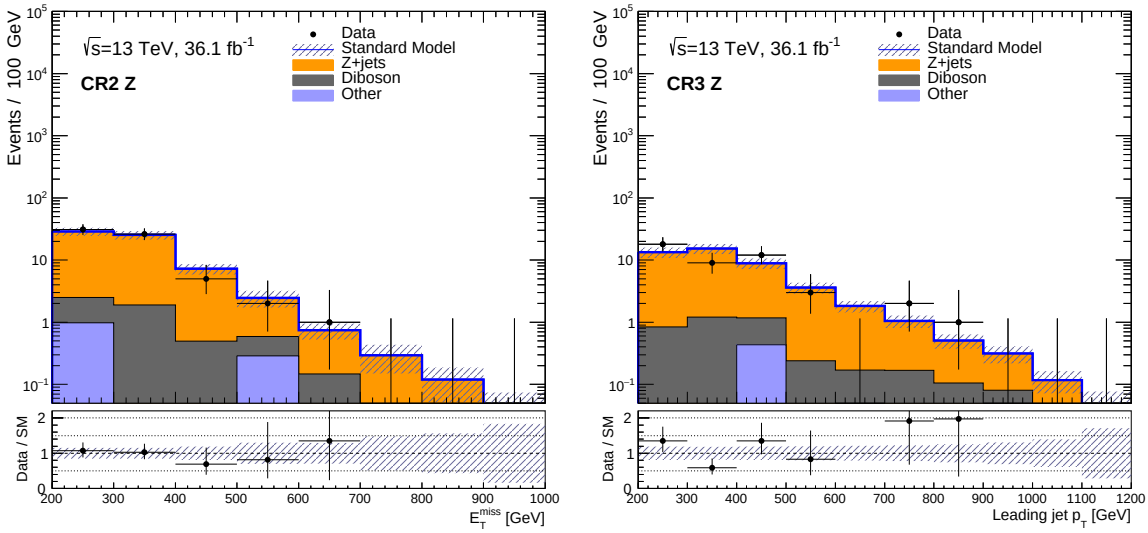

Figure 12.3: Distributions of $E_{\mathrm{T}}^{\mathrm{miss}}$ in CR2 Z and leading jet p_{T} in CR4 Z after the background-only fit. The shaded bands indicate the total uncertainty on the background prediction.

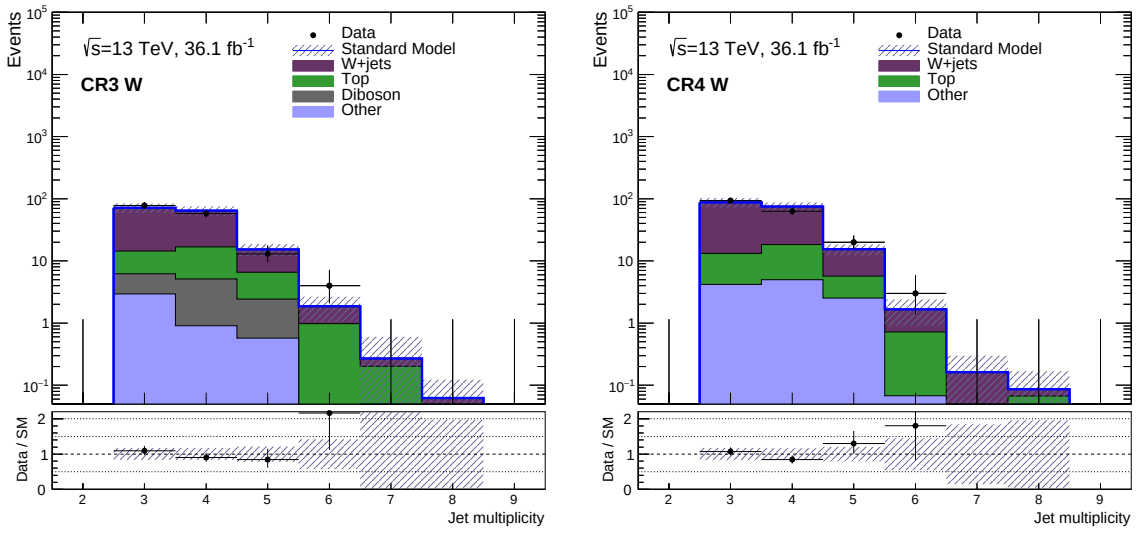

Figure 12.4: Distributions of $E_{\mathrm{T}}^{\mathrm{miss}}$ in CR2 Z and leading jet p_{T} in CR4 Z after the background-only fit. The shaded bands indicate the total uncertainty on the background prediction.

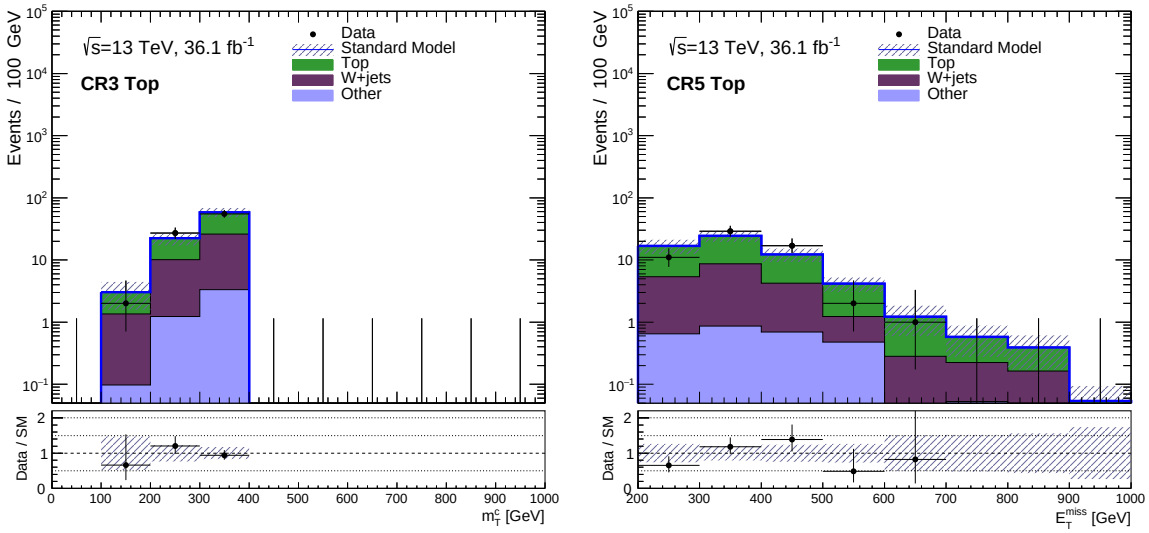

Figure 12.5: Distributions of $E_{\mathrm{T}}^{\mathrm{miss}}$ in CR2 Z and leading jet p_{T} in CR4 Z after the background-only fit. The shaded bands indicate the total uncertainty on the background prediction.

The extracted normalization factors are applied in the validation regions and a good agreement with data is observed (see figure 12.6). All deviations are below 1σ, which is not completely expected given the high number of VRs. However, the VRs are not orthogonal, thus reducing the statistical significance. Additionally, the conservative estimation of the systematic uncertainties on W+jets and top events[1] can reach up to ~50% each (see tables 12.2 and 12.3 and appendix F.2). While this has only small influences in the SRs, the contamination of these backgrounds is much higher in the VRs, increasing the overall uncertainty. The total uncertainties in the validation regions are $\sim 15 - 30\%$, with the main uncertainties varying for each region, but usually containing the background normalization factors and charm tagging calibration.

The exact yields for all processes in the control and validation regions are shown in tables 12.4-12.8.

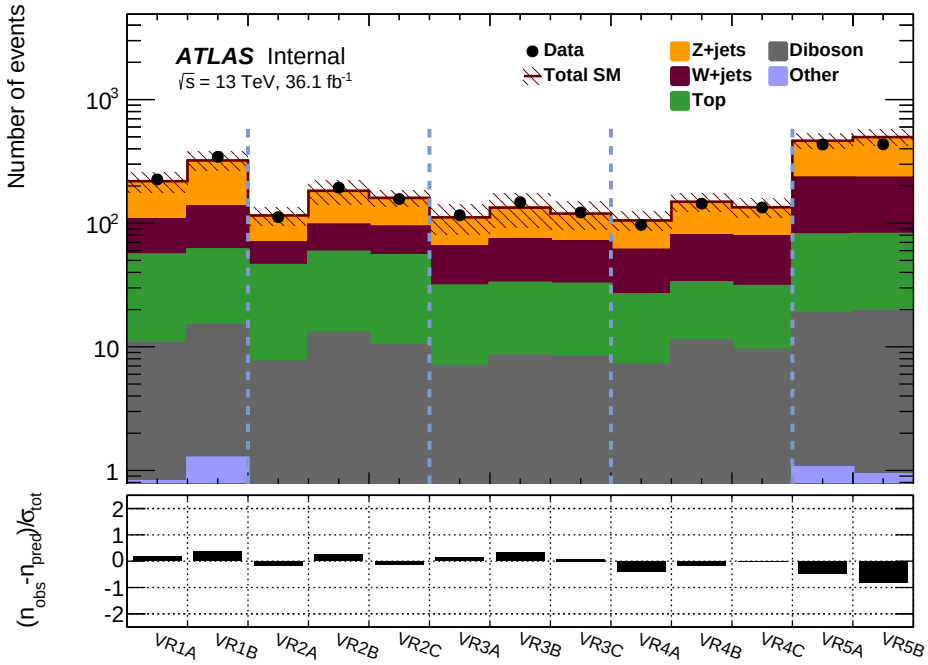

Figure 12.6: Observed data and post-fit background predictions in the validation regions.

[1] E.g. generator and showering systematics.

Uncertainty of channel	VR2 A	VR2 B	VR2 C	CR2 Z	CR2 W	CR2 Top
Total background expectation	115.50	182.84	160.15	65.02	140.93	69.00
Total statistical ($\sqrt{N_{\text{exp}}}$)	±10.75	±13.52	±12.66	±8.06	±11.87	±8.31
Total background systematic	±19.27 [16.69%]	±40.00 [21.88%]	±24.03 [15.00%]	±8.10 [12.46%]	±12.71 [9.02%]	±8.29 [12.01%]
mu_Top	±15.25 [13.2%]	±18.11 [9.9%]	±17.79 [11.1%]	±0.50 [0.78%]	±19.66 [13.9%]	±20.01 [29.0%]
alpha_Ttbar_Shower	±10.86 [9.4%]	±12.89 [7.0%]	±12.49 [7.8%]	±0.00 [0.00%]	±0.00 [0.00%]	±0.00 [0.00%]
alpha_FT_C	±9.47 [8.2%]	±15.87 [8.7%]	±14.38 [9.0%]	±5.33 [8.2%]	±12.10 [8.6%]	±5.15 [7.5%]
mu_Wc	±9.03 [7.8%]	±14.33 [7.8%]	±14.34 [9.0%]	±0.00 [0.00%]	±29.08 [20.6%]	±6.27 [9.1%]
mu_Z	±8.33 [7.2%]	±15.61 [8.5%]	±12.23 [7.6%]	±10.81 [16.6%]	±0.13 [0.09%]	±0.02 [0.03%]
alpha_VJets_PDFInt	±7.91 [6.8%]	±36.00 [19.7%]	±8.99 [5.6%]	±1.84 [2.8%]	±6.88 [4.9%]	±1.09 [1.6%]
alpha_V_RenormFac	±6.02 [5.2%]	±10.35 [5.7%]	±9.28 [5.8%]	±0.00 [0.00%]	±0.00 [0.00%]	±0.00 [0.00%]
gamma_stat_VR2A	±5.21 [4.5%]	±0.00 [0.00%]	±0.00 [0.00%]	±0.00 [0.00%]	±0.00 [0.00%]	±0.00 [0.00%]
alpha_VJets_qsf	±4.03 [3.5%]	±6.79 [3.7%]	±6.28 [3.9%]	±0.00 [0.00%]	±0.00 [0.00%]	±0.00 [0.00%]
alpha_single top_Theory	±3.94 [3.4%]	±4.73 [2.6%]	±5.19 [3.2%]	±0.00 [0.00%]	±0.00 [0.00%]	±0.00 [0.00%]
alpha_PRW	±3.36 [2.9%]	±1.85 [1.0%]	±3.71 [2.3%]	±0.80 [1.2%]	±0.34 [0.24%]	±4.17 [6.0%]
alpha_JES_NP1	±3.34 [2.9%]	±5.02 [2.7%]	±4.67 [2.9%]	±3.65 [5.6%]	±1.74 [1.2%]	±10.35 [15.0%]
alpha_FT_Light	±3.07 [2.7%]	±3.90 [2.1%]	±3.88 [2.4%]	±0.64 [0.99%]	±0.38 [0.27%]	±0.57 [0.83%]
alpha_VJets_ckkw	±2.90 [2.5%]	±5.25 [2.9%]	±4.34 [2.7%]	±0.00 [0.00%]	±0.00 [0.00%]	±0.00 [0.00%]
alpha_VV_renorm	±2.57 [2.2%]	±4.39 [2.4%]	±3.42 [2.1%]	±1.15 [1.8%]	±3.16 [2.2%]	±0.32 [0.46%]
alpha_Ttbar_Generator	±2.30 [2.0%]	±2.73 [1.5%]	±2.64 [1.6%]	±0.00 [0.00%]	±0.00 [0.00%]	±0.00 [0.00%]
alpha_VV_fac	±2.06 [1.8%]	±3.52 [1.9%]	±2.74 [1.7%]	±0.12 [0.19%]	±0.33 [0.23%]	±0.03 [0.05%]
alpha_JET_EtaCalib	±1.88 [1.6%]	±2.04 [1.1%]	±1.54 [0.96%]	±0.55 [0.85%]	±1.07 [0.76%]	±1.93 [2.8%]
alpha_JES_NP2	±1.56 [1.4%]	±4.29 [2.3%]	±2.05 [1.3%]	±0.86 [1.3%]	±1.18 [0.84%]	±3.34 [4.8%]
alpha_VV_qsf	±1.55 [1.3%]	±2.64 [1.4%]	±2.06 [1.3%]	±0.07 [0.11%]	±0.20 [0.14%]	±0.02 [0.03%]

Table 12.2: Breakdown of the systematic uncertainties in the control and validation regions of SR2 after the background-only fit (continued in table 12.3). Uncertainties can be correlated and do not necessarily add up in quadrature.

Uncertainty of channel	VR2 A	VR2 B	VR2 C	CR2 Z	CR2 W	CR2 Top
alpha_BGXSec	±1.10 [0.95%]	±2.00 [1.1%]	±1.50 [0.94%]	±0.67 [1.0%]	±1.93 [1.4%]	±0.29 [0.42%]
alpha_JES_NP3	±0.54 [0.47%]	±1.69 [0.93%]	±0.42 [0.27%]	±0.09 [0.13%]	±1.98 [1.4%]	±4.24 [6.1%]
alpha_Ttbar_Radiation	±0.36 [0.32%]	±0.43 [0.24%]	±0.42 [0.26%]	±0.00 [0.00%]	±0.00 [0.00%]	±0.00 [0.00%]
alpha_VJets_PDFSet	±0.33 [0.29%]	±0.49 [0.27%]	±0.46 [0.29%]	±0.15 [0.23%]	±0.42 [0.30%]	±0.05 [0.08%]
alpha_MET_Scale	±0.23 [0.20%]	±0.08 [0.05%]	±0.19 [0.12%]	±0.28 [0.44%]	±2.81 [2.0%]	±0.85 [1.2%]
alpha_FT_B	±0.23 [0.20%]	±0.18 [0.10%]	±0.27 [0.17%]	±0.02 [0.02%]	±1.53 [1.1%]	±0.92 [1.3%]
alpha_FT_Ex	±0.19 [0.17%]	±0.20 [0.11%]	±0.51 [0.32%]	±0.10 [0.15%]	±0.17 [0.12%]	±0.00 [0.00%]
alpha_VJets_AlphaS	±0.05 [0.04%]	±0.81 [0.44%]	±0.55 [0.34%]	±0.02 [0.02%]	±0.46 [0.33%]	±0.04 [0.05%]
alpha_JER	±0.01 [0.01%]	±0.07 [0.04%]	±0.08 [0.05%]	±0.02 [0.03%]	±0.03 [0.02%]	±0.10 [0.15%]
alpha_FT_ExC	±0.01 [0.01%]	±0.32 [0.18%]	±0.13 [0.08%]	±0.07 [0.11%]	±1.47 [1.0%]	±0.71 [1.0%]
alpha_JVT	±0.00 [0.00%]	±0.01 [0.01%]	±0.02 [0.01%]	±0.17 [0.26%]	±0.10 [0.07%]	±0.35 [0.50%]
gamma_stat_CR2 W	±0.00 [0.00%]	±0.00 [0.00%]	±0.00 [0.00%]	±0.00 [0.00%]	±7.69 [5.5%]	±0.00 [0.00%]
alpha_MET_ResoPerp	±0.00 [0.00%]	±0.00 [0.00%]	±0.00 [0.00%]	±0.00 [0.00%]	±0.00 [0.00%]	±0.00 [0.00%]
gamma_stat_VR2C	±0.00 [0.00%]	±0.00 [0.00%]	±5.79 [3.6%]	±0.00 [0.00%]	±0.00 [0.00%]	±0.00 [0.00%]
gamma_stat_VR2B	±0.00 [0.00%]	±6.91 [3.8%]	±0.00 [0.00%]	±0.00 [0.00%]	±0.00 [0.00%]	±0.00 [0.00%]
gamma_stat_SR	±0.00 [0.00%]	±0.00 [0.00%]	±0.00 [0.00%]	±0.00 [0.00%]	±0.00 [0.00%]	±0.00 [0.00%]
gamma_stat_CR2 Z	±0.00 [0.00%]	±0.00 [0.00%]	±0.00 [0.00%]	±2.27 [3.5%]	±0.00 [0.00%]	±0.00 [0.00%]
alpha_MET_ResoPara	±0.00 [0.00%]	±0.00 [0.00%]	±0.00 [0.00%]	±0.00 [0.00%]	±0.00 [0.00%]	±0.00 [0.00%]
gamma_stat_CR2 Top	±0.00 [0.00%]	±0.00 [0.00%]	±0.00 [0.00%]	±0.00 [0.00%]	±0.00 [0.00%]	±3.79 [5.5%]

Table 12.3: Breakdown of the systematic uncertainties in the control and validation regions of SR2 after the background-only fit (continuation of table 12.2). Uncertainties can be correlated and do not necessarily add up in quadrature.

Channels for SR1	CR1 Z	CR1 W	CR1 Top	VR1A	VR1B
Observed events	172	301	202	226	344
Fitted bkg events	172.07 ± 16.03	301.36 ± 30.90	202.04 ± 14.49	218.61 ± 40.62	321.79 ± 56.24
Fitted $Z \to \nu\nu$ events	0.00 ± 0.00	0.08 ± 0.03	0.04 ± 0.02	107.17 ± 23.51	183.55 ± 30.26
Fitted $W \to \tau\nu$ ISR events	0.00 ± 0.00	4.67 ± 1.41	1.06 ± 0.43	31.91 ± 14.53	47.13 ± 21.79
Fitted $W \to \tau\nu$ fake events	0.00 ± 0.00	0.16 ± 0.07	0.06 ± 0.03	4.44 ± 2.64	2.96 ± 2.51
Fitted $t\bar{t}$ events	0.29 ± 0.08	50.88 ± 17.41	112.74 ± 21.02	38.66 ± 14.73	40.43 ± 15.45
Fitted single top events	0.00 ± 0.00	16.32 ± 5.17	16.20 ± 3.52	$6.15^{+6.36}_{-6.15}$	$5.84^{+5.98}_{-5.84}$
Fitted Diboson events	7.77 ± 2.07	20.37 ± 6.00	5.78 ± 2.84	9.02 ± 2.82	12.29 ± 3.82
Fitted $Z \to ee$ events	88.07 ± 25.14	0.41 ± 0.24	0.30 ± 0.14	0.00 ± 0.00	0.00 ± 0.00
Fitted $Z \to \mu\mu$ events	75.93 ± 17.63	0.81 ± 0.33	0.05 ± 0.03	0.48 ± 0.17	0.78 ± 0.23
Fitted $W \to \mu\nu$ events	0.00 ± 0.00	104.59 ± 23.03	31.69 ± 10.96	11.51 ± 5.25	15.02 ± 7.10
Fitted $W \to e\nu$ events	0.00 ± 0.00	102.28 ± 21.52	32.47 ± 8.67	8.45 ± 3.85	12.54 ± 5.86
Fitted Other events	0.01 ± 0.01	0.80 ± 0.19	1.65 ± 0.31	0.82 ± 0.25	1.26 ± 0.30
MC exp. SM events	128.83	266.93	177.30	178.36	258.32
MC exp. $Z \to \nu\nu$ events	0.00	0.06	0.03	79.13	135.25
MC exp. $W \to \tau\nu$ ISR events	0.00	4.12	0.94	28.11	41.51
MC exp. $W \to \tau\nu$ fake events	0.00	0.16	0.06	4.44	2.96
MC exp. $t\bar{t}$ events	0.25	44.21	98.00	33.60	35.13
MC exp. single top events	0.00	14.18	14.08	5.35	5.07
MC exp. Diboson events	7.76	20.35	5.77	9.02	12.28
MC exp. $Z \to ee$ events	64.69	0.31	0.22	0.00	0.00
MC exp. $Z \to \mu\mu$ events	56.12	0.60	0.04	0.35	0.58
MC exp. $W \to \mu\nu$ events	0.00	92.07	27.91	10.11	13.23
MC exp. $W \to e\nu$ events	0.00	90.06	28.60	7.44	11.05
MC exp. Other events	0.01	0.80	1.65	0.81	1.26

Table 12.4: Event yields and their total systematic uncertainties in the control and validation regions of SR1 before and after the background-only fit.

Channels for SR2	CR2 Z	CR2 W	CR2 Top	VR2 A	VR2 B	VR2 C
Observed events	65	141	69	112	194	157
Fitted bkg events	65.02 ± 8.10	140.93 ± 12.71	69.00 ± 8.29	115.50 ± 19.27	182.84 ± 40.00	160.15 ± 24.03
Fitted $Z \to \nu\nu$ events	0.00 ± 0.00	0.02 ± 0.01	0.00 ± 0.00	45.60 ± 8.16	85.24 ± 32.41	66.87 ± 11.74
Fitted $W \to \tau\nu$ ISR events	0.00 ± 0.00	1.16 ± 0.44	0.25 ± 0.12	16.62 ± 8.12	26.31 ± 11.87	24.16 ± 11.28
Fitted $W \to \tau\nu$ fake events	0.00 ± 0.00	0.08 ± 0.04	0.02 ± 0.01	$0.09^{+0.10}_{-0.09}$	0.88 ± 0.65	0.26 ± 0.20
Fitted $t\bar{t}$ events	1.26 ± 0.50	37.87 ± 14.73	43.59 ± 11.26	34.21 ± 17.57	40.58 ± 20.61	39.32 ± 19.79
Fitted single top events	0.00 ± 0.00	11.34 ± 4.40	6.51 ± 2.02	$3.96^{+4.17}_{-3.96}$	$4.75^{+5.00}_{-4.75}$	$5.22^{+5.48}_{-5.22}$
Fitted Diboson events	4.43 ± 1.47	12.13 ± 4.98	1.22 ± 0.51	6.97 ± 3.90	11.92 ± 6.75	9.27 ± 5.19
Fitted $Z \to ee$ events	28.91 ± 4.16	0.44 ± 0.25	0.04 ± 0.01	0.00 ± 0.00	0.00 ± 0.00	0.00 ± 0.00
Fitted $Z \to \mu\mu$ events	30.41 ± 4.36	0.27 ± 0.17	0.07 ± 0.02	0.11 ± 0.08	0.42 ± 0.12	0.20 ± 0.08
Fitted $W \to \mu\nu$ events	0.00 ± 0.00	39.62 ± 12.17	9.17 ± 4.04	$3.70^{+4.28}_{-3.70}$	6.23 ± 3.13	6.73 ± 3.57
Fitted $W \to e\nu$ events	0.00 ± 0.00	37.36 ± 12.50	7.42 ± 3.87	3.96 ± 1.95	5.96 ± 2.62	7.63 ± 3.48
Fitted Other events	$0.01^{+0.01}_{-0.01}$	0.64 ± 0.19	0.71 ± 0.16	0.28 ± 0.08	0.55 ± 0.14	0.48 ± 0.13
MC exp. SM events	49.68	116.93	55.30	91.52	144.77	126.97
MC exp. $Z \to \nu\nu$ events	0.00	0.01	0.00	34.01	63.57	49.88
MC exp. $W \to \tau\nu$ ISR events	0.00	0.97	0.21	13.83	21.90	20.11
MC exp. $W \to \tau\nu$ fake events	0.00	0.08	0.02	0.09	0.88	0.26
MC exp. $t\bar{t}$ events	0.99	29.62	34.14	26.76	31.75	30.76
MC exp. single top events	0.00	8.87	5.10	3.10	3.72	4.09
MC exp. Diboson events	4.44	12.18	1.22	6.99	11.95	9.29
MC exp. $Z \to ee$ events	21.56	0.33	0.03	0.00	0.00	0.00
MC exp. $Z \to \mu\mu$ events	22.68	0.20	0.05	0.08	0.31	0.15
MC exp. $W \to \mu\nu$ events	0.00	32.95	7.64	3.07	5.19	5.60
MC exp. $W \to e\nu$ events	0.00	31.08	6.18	3.30	4.96	6.35
MC exp. Other events	0.01	0.64	0.71	0.28	0.55	0.48

Table 12.5: Event yields and their systematic uncertainties in the control and validation regions of SR2 before and after the background-only fit.

Channels for SR3	CR3 Z	CR3 W	CR3 Top	VR3A	VR3B	VR3C
Observed events	45	153	84	116	148	122
Fitted bkg events	45.00 ± 6.81	153.00 ± 12.29	84.00 ± 9.66	111.42 ± 29.97	133.69 ± 41.33	119.54 ± 29.94
Fitted $Z \to \nu\nu$ events	0.00 ± 0.00	$0.03^{+0.04}_{-0.03}$	0.01 ± 0.00	46.58 ± 10.70	59.08 ± 28.82	48.16 ± 11.00
Fitted $W \to \tau\nu$ ISR events	0.00 ± 0.00	2.37 ± 1.10	0.51 ± 0.13	22.65 ± 6.27	28.64 ± 6.94	24.87 ± 6.27
Fitted $W \to \tau\nu$ fake events	0.00 ± 0.00	0.11 ± 0.05	0.01 ± 0.01	0.00 ± 0.00	$0.56^{+0.59}_{-0.56}$	0.33 ± 0.21
Fitted $t\bar{t}$ events	0.43 ± 0.20	16.88 ± 6.12	39.20 ± 12.47	$21.41^{+26.82}_{-21.41}$	$21.79^{+27.29}_{-21.79}$	$21.23^{+26.58}_{-21.23}$
Fitted single top events	0.00 ± 0.00	8.33 ± 3.21	7.29 ± 2.50	$2.69^{+2.83}_{-2.69}$	$2.59^{+2.73}_{-2.59}$	$2.74^{+2.88}_{-2.74}$
Fitted Diboson events	3.55 ± 0.89	9.36 ± 2.69	2.90 ± 0.90	6.58 ± 1.78	7.71 ± 1.98	7.62 ± 2.07
Fitted $Z \to ee$ events	20.52 ± 3.50	0.50 ± 0.13	0.08 ± 0.03	0.00 ± 0.00	0.00 ± 0.00	0.00 ± 0.00
Fitted $Z \to \mu\mu$ events	20.48 ± 3.51	0.43 ± 0.11	0.04 ± 0.01	0.15 ± 0.09	0.41 ± 0.14	0.15 ± 0.08
Fitted $W \to \mu\nu$ events	0.00 ± 0.00	60.95 ± 9.40	11.67 ± 3.68	$4.98^{+5.60}_{-4.98}$	5.64 ± 3.01	6.00 ± 3.62
Fitted $W \to e\nu$ events	0.00 ± 0.00	53.04 ± 8.09	21.19 ± 5.31	6.19 ± 1.77	6.93 ± 1.86	8.16 ± 2.30
Fitted Other events	0.01 ± 0.01	0.99 ± 0.26	1.10 ± 0.25	0.19 ± 0.06	0.35 ± 0.08	0.28 ± 0.07
MC exp. SM events	37.64	108.76	77.59	92.81	109.75	98.48
MC exp. $Z \to \nu\nu$ events	0.00	0.02	0.01	38.14	48.36	39.43
MC exp. $W \to \tau\nu$ ISR events	0.00	1.39	0.30	13.30	16.81	14.60
MC exp. $W \to \tau\nu$ fake events	0.00	0.11	0.01	0.00	0.56	0.33
MC exp. $t\bar{t}$ events	0.49	19.56	45.43	24.81	25.25	24.60
MC exp. single top events	0.00	9.65	8.45	3.12	3.00	3.17
MC exp. Diboson events	3.55	9.36	2.90	6.58	7.71	7.62
MC exp. $Z \to ee$ events	16.81	0.41	0.07	0.00	0.00	0.00
MC exp. $Z \to \mu\mu$ events	16.77	0.35	0.03	0.13	0.33	0.13
MC exp. $W \to \mu\nu$ events	0.00	35.77	6.85	2.92	3.31	3.52
MC exp. $W \to e\nu$ events	0.00	31.13	12.43	3.63	4.07	4.79
MC exp. Other events	0.01	0.99	1.10	0.19	0.35	0.28

Table 12.6: Event yields and their systematic uncertainties in the control and validation regions of SR3 before and after the background-only fit.

Channels for SR4	CR4 Z	CR4 W	CR4 Top	VR4A	VR4B	VR4C
Observed events	54	179	71	97	144	134
Fitted bkg events	54.00 ± 7.66	179.01 ± 13.48	71.00 ± 8.43	105.22 ± 18.46	149.20 ± 24.63	134.45 ± 22.70
Fitted $Z \to \nu\nu$ events	0.00 ± 0.00	0.05 ± 0.01	0.01 ± 0.00	44.51 ± 9.21	68.29 ± 13.76	55.85 ± 11.30
Fitted $W \to \tau\nu$ ISR events	0.00 ± 0.00	2.10 ± 0.85	0.99 ± 0.30	22.22 ± 6.44	30.85 ± 8.63	29.65 ± 8.34
Fitted $W \to \tau\nu$ fake events	0.00 ± 0.00	0.03 ± 0.02	0.00 ± 0.00	0.25 ± 0.22	1.45 ± 0.73	0.71 ± 0.39
Fitted $t\bar{t}$ events	0.00 ± 0.00	17.03 ± 6.26	32.90 ± 10.64	17.43 ± 11.68	19.78 ± 13.26	19.35 ± 12.90
Fitted single top events	0.00 ± 0.00	9.30 ± 3.51	6.04 ± 2.00	$2.01^{+2.11}_{-2.01}$	$2.27^{+2.39}_{-2.27}$	$2.15^{+2.26}_{-2.15}$
Fitted Diboson events	3.74 ± 0.90	7.30 ± 2.50	2.50 ± 1.01	6.36 ± 2.50	10.10 ± 4.15	8.40 ± 3.30
Fitted $Z \to ee$ events	25.99 ± 4.09	0.88 ± 0.31	0.03 ± 0.03	0.00 ± 0.00	0.00 ± 0.00	0.00 ± 0.00
Fitted $Z \to \mu\mu$ events	24.26 ± 3.90	0.59 ± 0.19	0.03 ± 0.01	0.26 ± 0.09	0.26 ± 0.08	0.26 ± 0.08
Fitted $W \to \mu\nu$ events	0.00 ± 0.00	70.08 ± 9.45	8.71 ± 2.77	5.53 ± 2.95	7.18 ± 2.71	8.98 ± 3.91
Fitted $W \to e\nu$ events	0.00 ± 0.00	70.81 ± 9.30	18.69 ± 4.84	6.29 ± 1.81	8.50 ± 2.42	8.60 ± 2.42
Fitted Other events	0.01 ± 0.00	0.82 ± 0.21	1.10 ± 0.35	0.38 ± 0.13	0.51 ± 0.14	0.50 ± 0.14
MC exp. SM events	42.73	138.52	71.46	88.92	124.14	111.82
MC exp. $Z \to \nu\nu$ events	0.00	0.04	0.01	34.53	52.98	43.33
MC exp. $W \to \tau\nu$ ISR events	0.00	1.41	0.67	14.96	20.77	19.96
MC exp. $W \to \tau\nu$ fake events	0.00	0.03	0.00	0.25	1.45	0.71
MC exp. $t\bar{t}$ events	0.00	21.30	41.14	21.79	24.73	24.19
MC exp. single top events	0.00	11.63	7.55	2.51	2.84	2.69
MC exp. Diboson events	3.74	7.30	2.50	6.36	10.10	8.40
MC exp. $Z \to ee$ events	20.16	0.68	0.02	0.00	0.00	0.00
MC exp. $Z \to \mu\mu$ events	18.82	0.46	0.02	0.20	0.20	0.20
MC exp. $W \to \mu\nu$ events	0.00	47.17	5.87	3.72	4.83	6.04
MC exp. $W \to e\nu$ events	0.00	47.67	12.58	4.24	5.72	5.79
MC exp. Other events	0.01	0.82	1.10	0.38	0.51	0.50

Table 12.7: Event yields and their systematic uncertainties in the control and validation regions of SR4 before and after the background-only fit.

Channels for SR5	CR5 Z	CR5 W	CR5 Top	VR5A	VR5B
Observed events	55	192	60	433	435
Fitted bkg events	54.99 ± 7.97	192.00 ± 14.07	60.00 ± 8.42	464.58 ± 59.41	497.31 ± 67.44
Fitted $Z \to \nu\nu$ events	0.00 ± 0.00	0.08 ± 0.02	0.01 ± 0.00	223.61 ± 42.10	256.74 ± 49.54
Fitted $W \to \tau\nu$ ISR events	0.00 ± 0.00	1.91 ± 0.52	0.74 ± 0.32	93.87 ± 21.95	97.11 ± 23.56
Fitted $W \to \tau\nu$ fake events	0.00 ± 0.00	0.02 ± 0.01	0.00 ± 0.00	9.34 ± 4.03	9.27 ± 4.00
Fitted $t\bar{t}$ events	0.67 ± 0.26	18.50 ± 7.43	31.73 ± 9.05	52.96 ± 20.33	54.32 ± 20.87
Fitted single top events	0.00 ± 0.00	13.06 ± 5.16	7.98 ± 2.11	$9.03^{+9.51}_{-9.03}$	$7.83^{+8.28}_{-7.83}$
Fitted Diboson events	3.57 ± 1.20	6.37 ± 2.27	1.11 ± 0.40	16.42 ± 8.41	17.47 ± 9.09
Fitted $Z \to ee$ events	26.80 ± 4.34	0.80 ± 0.37	$0.04^{+0.04}_{-0.04}$	0.00 ± 0.00	0.00 ± 0.00
Fitted $Z \to \mu\mu$ events	23.95 ± 3.97	0.67 ± 0.22	0.11 ± 0.05	0.53 ± 0.21	0.47 ± 0.19
Fitted $W \to \mu\nu$ events	0.00 ± 0.00	64.55 ± 9.32	8.30 ± 2.37	32.19 ± 7.41	29.46 ± 7.46
Fitted $W \to e\nu$ events	0.00 ± 0.00	85.33 ± 11.07	9.17 ± 2.83	25.56 ± 5.72	23.71 ± 5.27
Fitted Other events	0.00 ± 0.00	0.70 ± 0.20	0.81 ± 0.23	1.06 ± 0.29	0.93 ± 0.27
MC exp. SM events	43.36	158.01	55.73	379.45	404.89
MC exp. $Z \to \nu\nu$ events	0.00	0.06	0.00	172.37	197.90
MC exp. $W \to \tau\nu$ ISR events	0.00	1.49	0.58	73.18	75.70
MC exp. $W \to \tau\nu$ fake events	0.00	0.02	0.00	9.34	9.27
MC exp. $t\bar{t}$ events	0.66	18.40	31.56	52.67	54.03
MC exp. single top events	0.00	12.99	7.93	8.98	7.79
MC exp. Diboson events	3.57	6.37	1.11	16.42	17.47
MC exp. $Z \to ee$ events	20.66	0.61	0.03	0.00	0.00
MC exp. $Z \to \mu\mu$ events	18.46	0.52	0.08	0.41	0.36
MC exp. $W \to \mu\nu$ events	0.00	50.32	6.47	25.09	22.97
MC exp. $W \to e\nu$ events	0.00	66.52	7.15	19.93	18.48
MC exp. Other events	0.00	0.70	0.81	1.06	0.93

Table 12.8: Event yields and their systematic uncertainties in the control and validation regions of SR5 before and after the background-only fit.

Similar to the control regions, the validation regions not only show agreement for the overall normalization, but also for all kinematic variables. Figure 12.7 focuses on distributions in VR2A, which are all consistent with the observed data within uncertainties. Figure 12.8 gives an overview of various validation regions, again showing good agreement. More VR distributions can be found in appendix F.4.

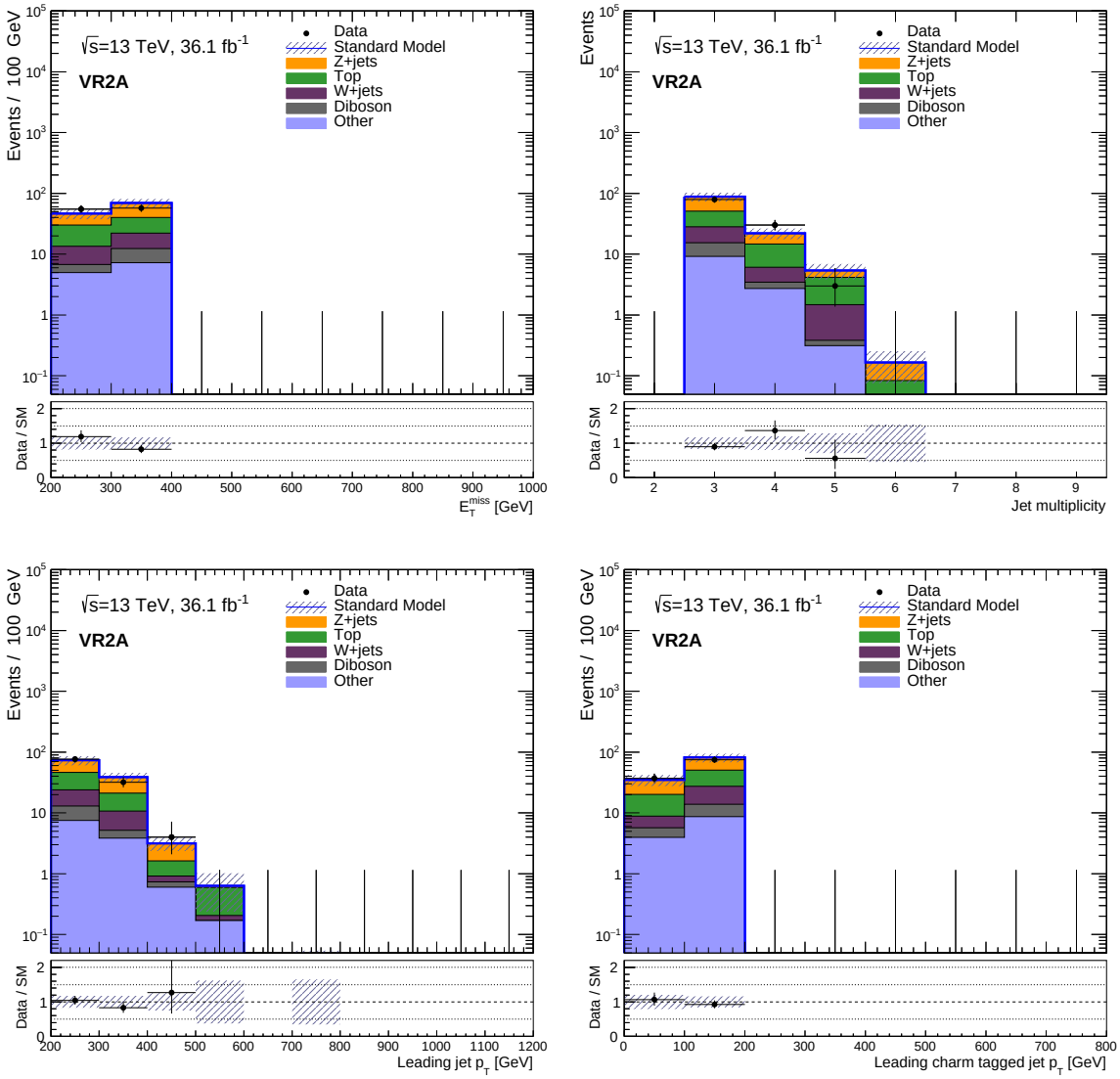

Figure 12.7: $E_{\mathrm{T}}^{\mathrm{miss}}$ (upper left), jet multiplicity (upper right), leading jet p_{T} (lower left) and leading charm tagged jet p_{T} (lower right) distributions in VR2A after the background-only fit. The shaded bands indicate the total uncertainty on the background prediction.

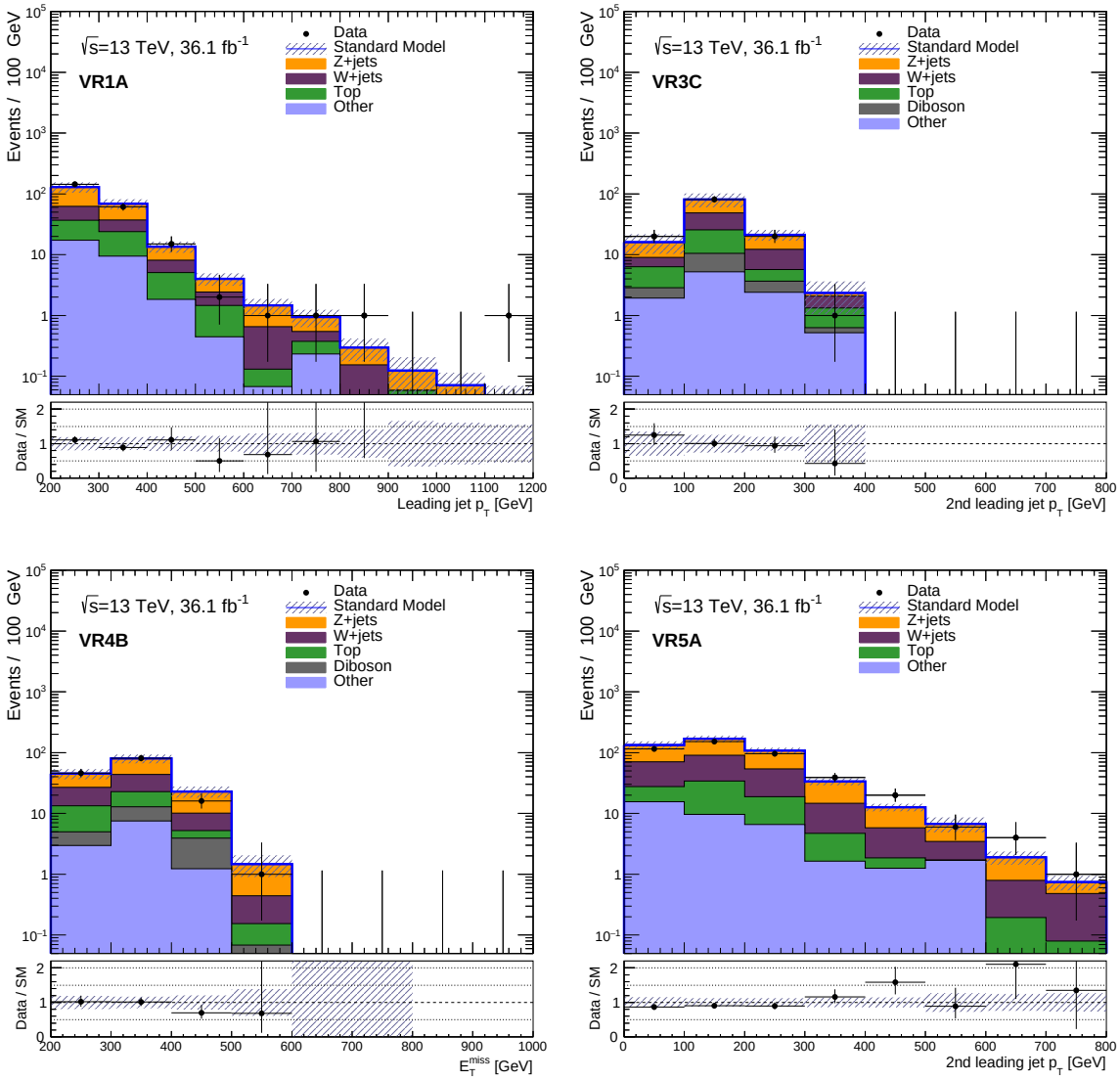

Figure 12.8: Various distributions of non-inverted variables in the validation regions after the background-only fit. The shaded bands indicate the total uncertainty on the background prediction.

12.2. Signal regions

As the background prediction method has been validated, the signal regions can be unblinded. Figure 12.9 shows the observed data and the post-fit background predictions in all signal regions, with the yields shown also in table 12.9. All observed values are consistent with the SM predictions, so no sign of any signal is apparent. Figures 12.10-12.11 show $E_{\mathrm{T}}^{\mathrm{miss}}$ and jet multiplicity variables in all signal regions after the fit, which also have good agreement.

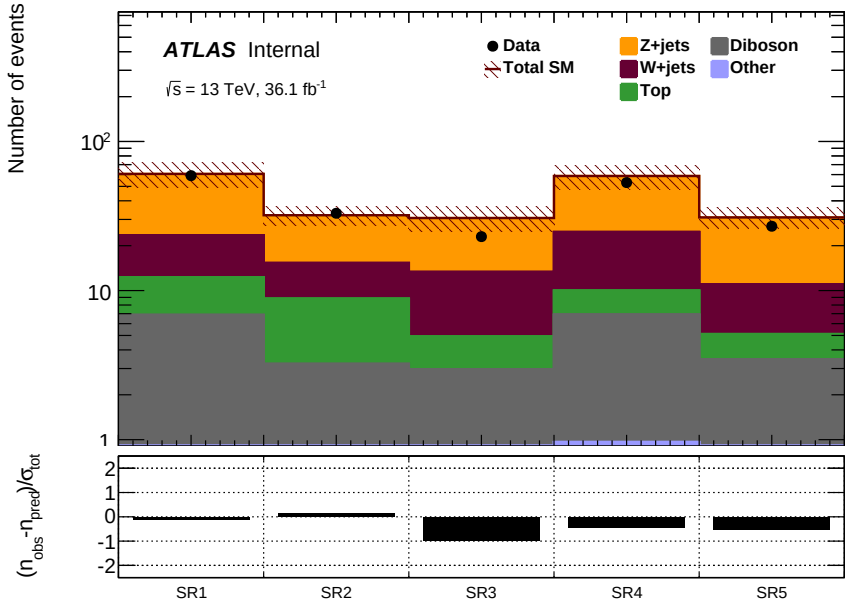

Figure 12.9: Post-fit yields and observed data in all signal regions after the background-only fit. The shaded bands indicate the total uncertainty on the background prediction.

The total systematic uncertainties are ~15-19% in all signal regions, a breakdown is shown in tables 12.10 and 12.11. The highest individual uncertainties vary between the regions, with `mu_Z`, charm tagging (FT_C), jet energy scale (JES_NP1) and the V+jets PDF, renormalization and factorization scales usually being among them. The influence of the high systematic uncertainties of $t\bar{t}$ (for example >100% in SR3) on the final result is small, as the background expectation is relatively low. It should be noted that the uncertainties can be correlated and do not necessarily add up quadratically.

The relatively low total uncertainty, for example compared to ~25% raw charm tagging uncertainty for each individual jet flavor, shows the success of the background estimation procedure. Most experimental uncertainties on the transfer factor cancel to a great extent because of the kinematic similarities between signal and control regions, as well as the matching jet flavor compositions. The remaining uncertainties are directly correlated to the differences between SRs and CRs: While the the experimental ones do not cancel completely (e.g. JES_NP1 is sensitive to the leading jet p_{T} requirement), the theory ones are defined via the extrapolation between the regions. The total systematic uncertainty could therefore be reduced by defining the control regions even closer to the signal regions. This is not possible at the moment due to the limited statistics, but could be done in future iterations of the analysis.

Channels	SR1	SR2	SR3	SR4	SR5
Observed events	59	33	23	53	27
Fitted bkg events	60.58 ± 11.15	32.01 ± 4.84	30.66 ± 5.76	58.67 ± 10.74	30.94 ± 4.84
Fitted $Z \to \nu\nu$	37.09 ± 7.75	16.71 ± 3.20	17.33 ± 4.74	33.98 ± 8.11	19.94 ± 4.09
Fitted $W \to \tau\nu$ ISR	6.62 ± 3.11	2.89 ± 1.21	5.38 ± 1.57	9.33 ± 2.72	3.57 ± 0.86
Fitted $W \to \tau\nu$ fake	1.72 ± 0.97	1.76 ± 0.85	0.80 ± 0.35	0.52 ± 0.24	0.03 ± 0.02
Fitted $t\bar{t}$	4.42 ± 1.57	5.49 ± 2.57	$1.67^{+2.06}_{-1.67}$	2.61 ± 1.68	1.19 ± 0.39
Fitted single top	$1.01^{+1.04}_{-1.01}$	$0.11^{+0.14}_{-0.11}$	$0.28^{+0.31}_{-0.28}$	$0.49^{+0.52}_{-0.49}$	$0.46^{+0.50}_{-0.46}$
Fitted Diboson	6.28 ± 2.09	2.73 ± 1.65	2.43 ± 0.74	5.93 ± 2.25	3.16 ± 1.59
Fitted $Z \to ee$	0.00 ± 0.00	0.00 ± 0.00	0.00 ± 0.00	0.00 ± 0.00	0.00 ± 0.00
Fitted $Z \to \mu\mu$	0.00 ± 0.00	0.00 ± 0.00	0.00 ± 0.00	0.00 ± 0.00	0.01 ± 0.00
Fitted $W \to \mu\nu$	2.08 ± 0.97	0.72 ± 0.38	1.16 ± 0.32	2.86 ± 1.62	0.93 ± 0.30
Fitted $W \to e\nu$	0.78 ± 0.56	1.10 ± 0.52	1.06 ± 0.24	1.99 ± 0.54	1.36 ± 0.32
Fitted Other	0.58 ± 0.11	0.49 ± 0.11	0.54 ± 0.12	0.96 ± 0.21	0.29 ± 0.06
MC exp. SM events	49.02	25.77	24.68	47.20	25.07
Exp. $Z \to \nu\nu$	37.09 ± 7.75	16.71 ± 3.20	17.33 ± 4.74	33.98 ± 8.11	19.94 ± 4.09
Exp. $W \to \tau\nu$ ISR	6.62 ± 3.11	2.89 ± 1.21	5.38 ± 1.57	9.33 ± 2.72	3.57 ± 0.86
Exp. $W \to \tau\nu$ fake	1.72 ± 0.97	1.76 ± 0.85	0.80 ± 0.35	0.52 ± 0.24	0.03 ± 0.02
Exp. $t\bar{t}$	4.42 ± 1.57	5.49 ± 2.57	$1.67^{+2.06}_{-1.67}$	2.61 ± 1.68	1.19 ± 0.39
Exp. single top	$1.01^{+1.04}_{-1.01}$	$0.11^{+0.14}_{-0.11}$	$0.28^{+0.31}_{-0.28}$	$0.49^{+0.52}_{-0.49}$	$0.46^{+0.50}_{-0.46}$
Exp. Diboson	6.28 ± 2.09	2.73 ± 1.65	2.43 ± 0.74	5.93 ± 2.25	3.16 ± 1.59
Exp. $Z \to ee$	0.00 ± 0.00	0.00 ± 0.00	0.00 ± 0.00	0.00 ± 0.00	0.00 ± 0.00
Exp. $Z \to \mu\mu$	0.00 ± 0.00	0.00 ± 0.00	0.00 ± 0.00	0.00 ± 0.00	0.01 ± 0.00
Exp. $W \to \mu\nu$	2.08 ± 0.97	0.72 ± 0.38	1.16 ± 0.32	2.86 ± 1.62	0.93 ± 0.30
Exp. $W \to e\nu$	0.78 ± 0.56	1.10 ± 0.52	1.06 ± 0.24	1.99 ± 0.54	1.36 ± 0.32
Exp. Other	0.58 ± 0.11	0.49 ± 0.11	0.54 ± 0.12	0.96 ± 0.21	0.29 ± 0.06

Table 12.9: Observed data and expected SM yields in the signal regions before and after the background-only fit.

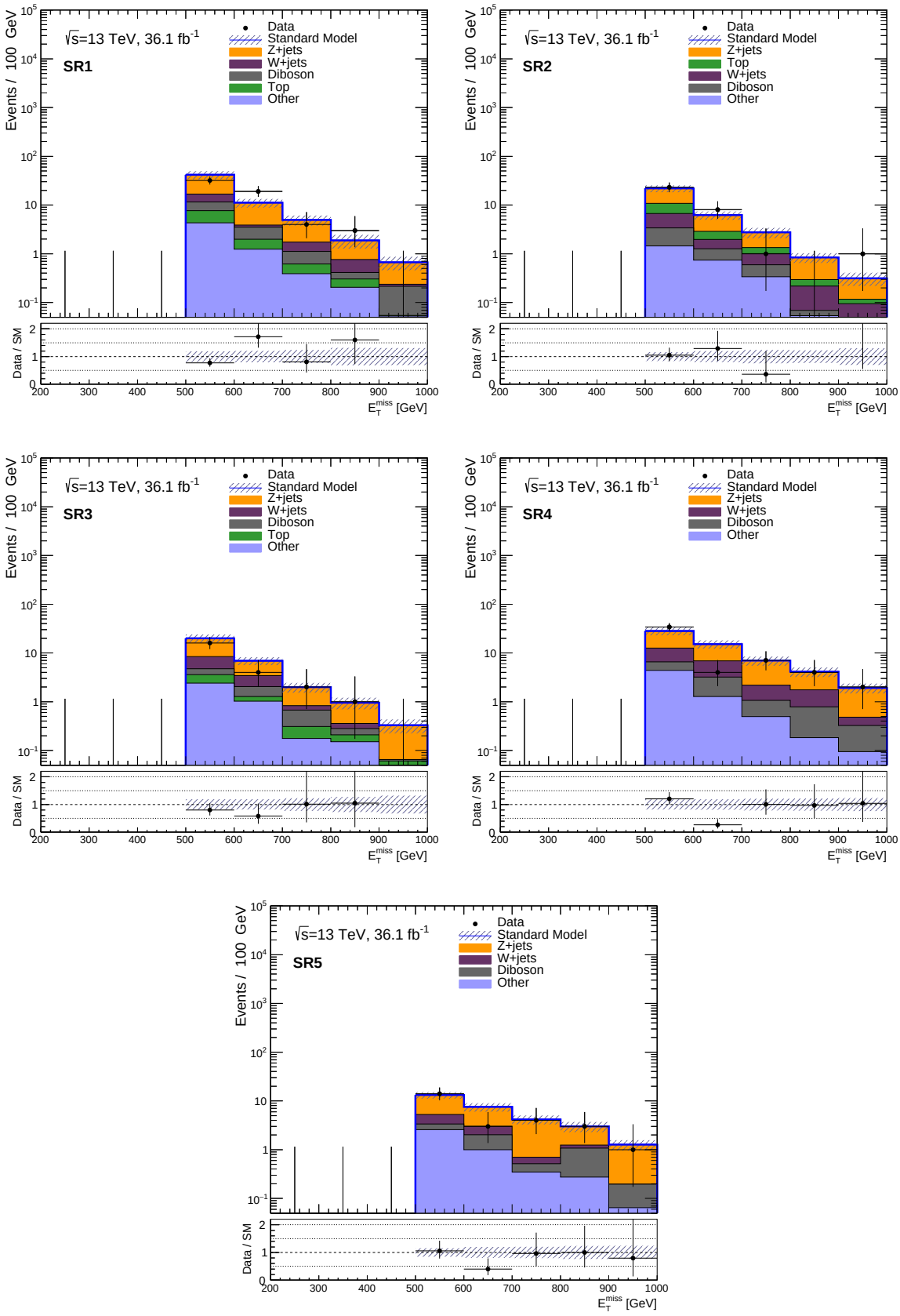

Figure 12.10: $E_{\mathrm{T}}^{\mathrm{miss}}$ distributions in all signal regions after the background-only fit. The shaded bands indicate the total uncertainty on the background prediction.

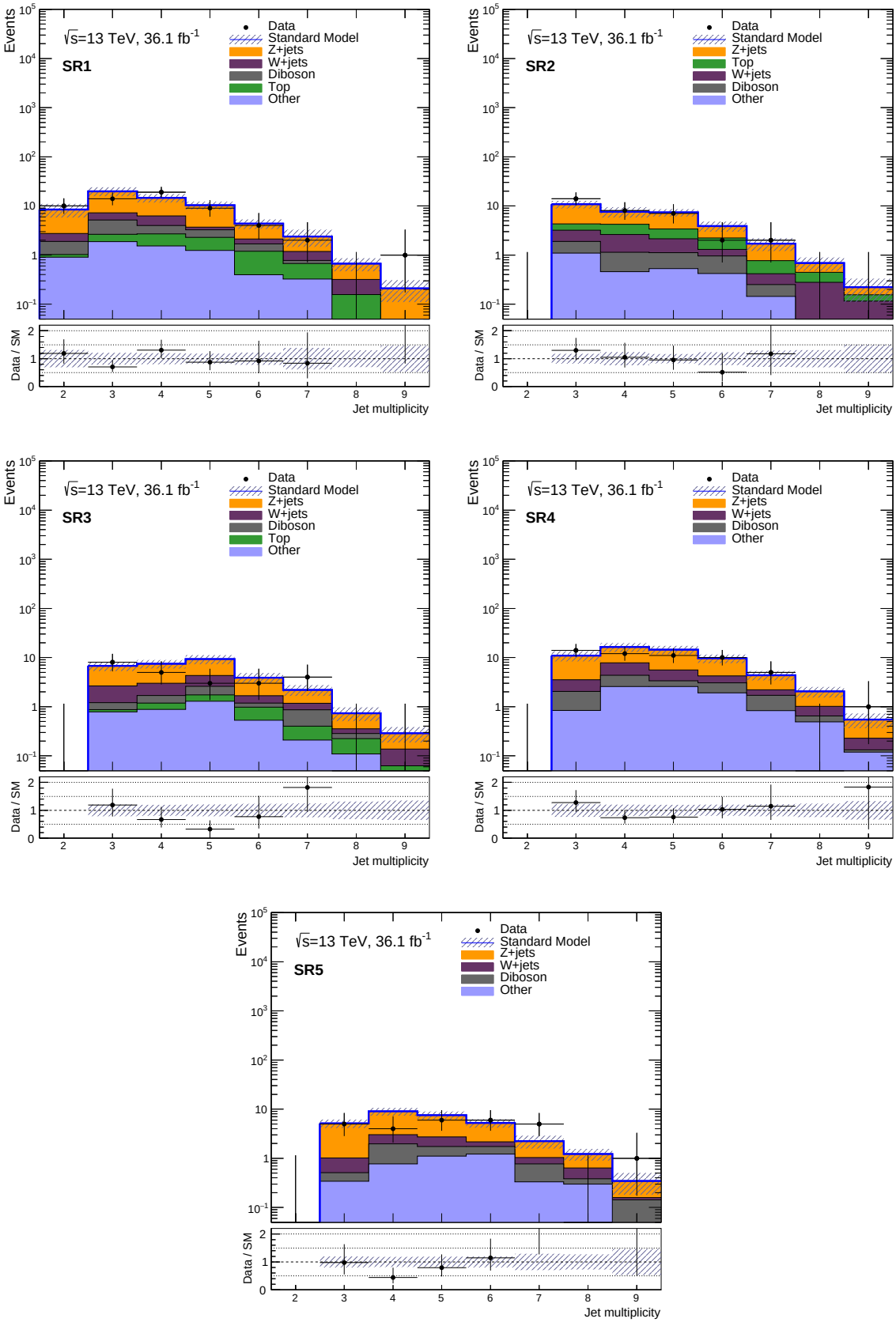

Figure 12.11: Jet multiplicity distributions in all signal regions after the background-only fit. The shaded bands indicate the total uncertainty on the background prediction.

Uncertainty of channels	SR1	SR2	SR3	SR4	SR5
Total background expectation	60.58	32.01	30.66	58.67	30.94
Total statistical ($\sqrt{N_{\text{exp}}}$)	±7.78	±5.66	±5.54	±7.66	±5.56
Total systematic uncertainty	±11.15 [18.41%]	±4.84 [15.11%]	±5.76 [18.79%]	±10.74 [18.30%]	±4.84 [15.64%]
mu_Z	±9.18 [15.2%]	±3.05 [9.5%]	±3.58 [11.7%]	±6.71 [11.4%]	±4.18 [13.5%]
alpha_V_RenormFac	±6.44 [10.6%]	±1.84 [5.8%]	±2.32 [7.6%]	±3.79 [6.5%]	±1.62 [5.2%]
alpha_JES_NP1	±4.76 [7.9%]	±1.60 [5.0%]	±2.09 [6.8%]	±3.05 [5.2%]	±1.72 [5.6%]
alpha_VJets_qsf	±4.74 [7.8%]	±1.18 [3.7%]	±0.77 [2.5%]	±3.26 [5.6%]	±0.21 [0.67%]
alpha_VJets_PDFInt	±4.67 [7.7%]	±2.28 [7.1%]	±4.13 [13.5%]	±8.61 [14.7%]	±2.82 [9.1%]
alpha_FT_C	±4.09 [6.7%]	±2.86 [8.9%]	±2.85 [9.3%]	±4.77 [8.1%]	±2.17 [7.0%]
gamma_stat_SR	±3.12 [5.2%]	±1.71 [5.3%]	±1.39 [4.5%]	±2.24 [3.8%]	±1.41 [4.6%]
mu_Wc	±2.63 [4.3%]	±1.76 [5.5%]	±1.93 [6.3%]	±3.29 [5.6%]	±1.34 [4.3%]
mu_$t\bar{t}$	±1.57 [2.6%]	±2.24 [7.0%]	±0.78 [2.5%]	±1.23 [2.1%]	±0.64 [2.1%]
alpha_FT_Light	±1.50 [2.5%]	±0.76 [2.4%]	±0.68 [2.2%]	±0.05 [0.09%]	±1.22 [3.9%]
alpha_VJets_ckkw	±1.36 [2.3%]	±0.99 [3.1%]	±1.77 [5.8%]	±3.75 [6.4%]	±1.36 [4.4%]
alpha_BGXSec	±1.29 [2.1%]	±0.75 [2.3%]	±0.57 [1.8%]	±1.11 [1.9%]	±0.52 [1.7%]
alpha_VV_renorm	±1.12 [1.8%]	±1.01 [3.1%]	±0.11 [0.35%]	±0.61 [1.0%]	±0.13 [0.43%]
alpha_VV_qsf	±1.03 [1.7%]	±0.61 [1.9%]	±0.33 [1.1%]	±1.57 [2.7%]	±1.46 [4.7%]
alpha_Ttbar_Shower	±1.01 [1.7%]	±1.74 [5.4%]	±1.05 [3.4%]	±1.25 [2.1%]	±0.08 [0.25%]

Table 12.10: Breakdown of the systematic uncertainties in the signal regions after the background-only fit. Uncertainties can be correlated and do not necessarily add up in quadrature. (Continued in table 12.11)

Uncertainty of channels	SR1	SR2	SR3	SR4	SR5
alpha_single top_Theory	±1.00 [1.7%]	±0.11 [0.36%]	±0.28 [0.92%]	±0.49 [0.83%]	±0.46 [1.5%]
alpha_PRW	±0.97 [1.6%]	±0.31 [0.95%]	±0.80 [2.6%]	±0.87 [1.5%]	±0.03 [0.11%]
alpha_MET_Scale	±0.82 [1.3%]	±0.08 [0.25%]	±0.41 [1.3%]	±0.12 [0.21%]	±0.09 [0.31%]
alpha_FT_ExC	±0.70 [1.2%]	±0.68 [2.1%]	±0.30 [0.97%]	±0.17 [0.29%]	±0.01 [0.04%]
alpha_Ttbar_Generator	±0.57 [0.95%]	±0.37 [1.2%]	±1.67 [5.4%]	±0.69 [1.2%]	±0.11 [0.37%]
alpha_JES_NP2	±0.40 [0.67%]	±0.95 [3.0%]	±0.90 [2.9%]	±1.66 [2.8%]	±1.07 [3.4%]
alpha_VV_fac	±0.39 [0.64%]	±0.81 [2.5%]	±0.20 [0.67%]	±1.04 [1.8%]	±0.17 [0.54%]
alpha_JET_EtaCalib	±0.32 [0.53%]	±0.06 [0.19%]	±0.20 [0.65%]	±0.12 [0.21%]	±0.47 [1.5%]
alpha_VJets_AlphaS	±0.27 [0.44%]	±0.09 [0.29%]	±0.15 [0.50%]	±0.19 [0.33%]	±0.05 [0.17%]
alpha_JVT	±0.18 [0.30%]	±0.05 [0.16%]	±0.03 [0.10%]	±0.06 [0.11%]	±0.05 [0.17%]
alpha_Ttbar_Radiation	±0.17 [0.28%]	±0.06 [0.18%]	±0.06 [0.18%]	±0.06 [0.10%]	±0.02 [0.05%]
alpha_VJets_PDFSet	±0.15 [0.25%]	±0.01 [0.04%]	±0.02 [0.06%]	±0.24 [0.40%]	±0.06 [0.19%]
alpha_FT_Ex	±0.06 [0.09%]	±0.05 [0.16%]	±0.07 [0.24%]	±0.38 [0.65%]	±0.38 [1.2%]
alpha_JES_NP3	±0.03 [0.04%]	±0.07 [0.22%]	±0.55 [1.8%]	±1.12 [1.9%]	±0.49 [1.6%]
alpha_FT_B	±0.02 [0.03%]	±0.13 [0.40%]	±0.03 [0.10%]	±0.05 [0.08%]	±0.09 [0.29%]
alpha_VJets_HF	±0.00 [0.00%]	±0.00 [0.00%]	±0.00 [0.00%]	±1.64 [2.8%]	±0.00 [0.00%]

Table 12.11: Breakdown of the systematic uncertainties in the signal regions after the background-only fit. Uncertainties can be correlated and do not necessarily add up in quadrature. (Continuation from table 12.10)

12.3. Interpretation

As no excess was observed in data, exclusion limits are set for the signal models. Exclusion fits are performed for each grid point and signal region as described in section 9.3 and the 95% confidence level exclusion limits are calculated using the CL_s method. The signal regions are not orthogonal, so the sensitivities can not be combined statistically. Instead, for each point the observed CL_s value is set to that of the region with the best *expected* sensitivity. This reduces the combined limit's dependence on fluctuations in data.

The observed combined limit is shown in figure 12.12, while the individual regions' exclusions are shown in figure 12.13. For high mass differences squark masses of up to ~845 GeV can be excluded, with the reach reducing for smaller mass differences. In the $\tilde{t}_1 \to c + \tilde{\chi}_1^0$ region the sensitivity reaches up to ~500 GeV and drops towards the Monojet area [27], leaving a gap. Because of the negative excesses in SR3-5, the observed limits are better than the expected ones, but are still in agreement.

The existing limits from the *Run1* ATLAS searches can be improved greatly in all directions. Yet, the shapes of the contours are different as the *Run1* limit is almost independent on the neutralino mass outside of the $\tilde{t}_1 \to c + \tilde{\chi}_1^0$ region. The huge loss in tagging efficiency for jets above $p_{\mathrm{T}} > 200$ GeV reduces the sensitivity greatly (see section 6.5). While it can be recovered partially for very high mass differences by further tightening the kinematic cuts, this is not possible for the intermediate region.

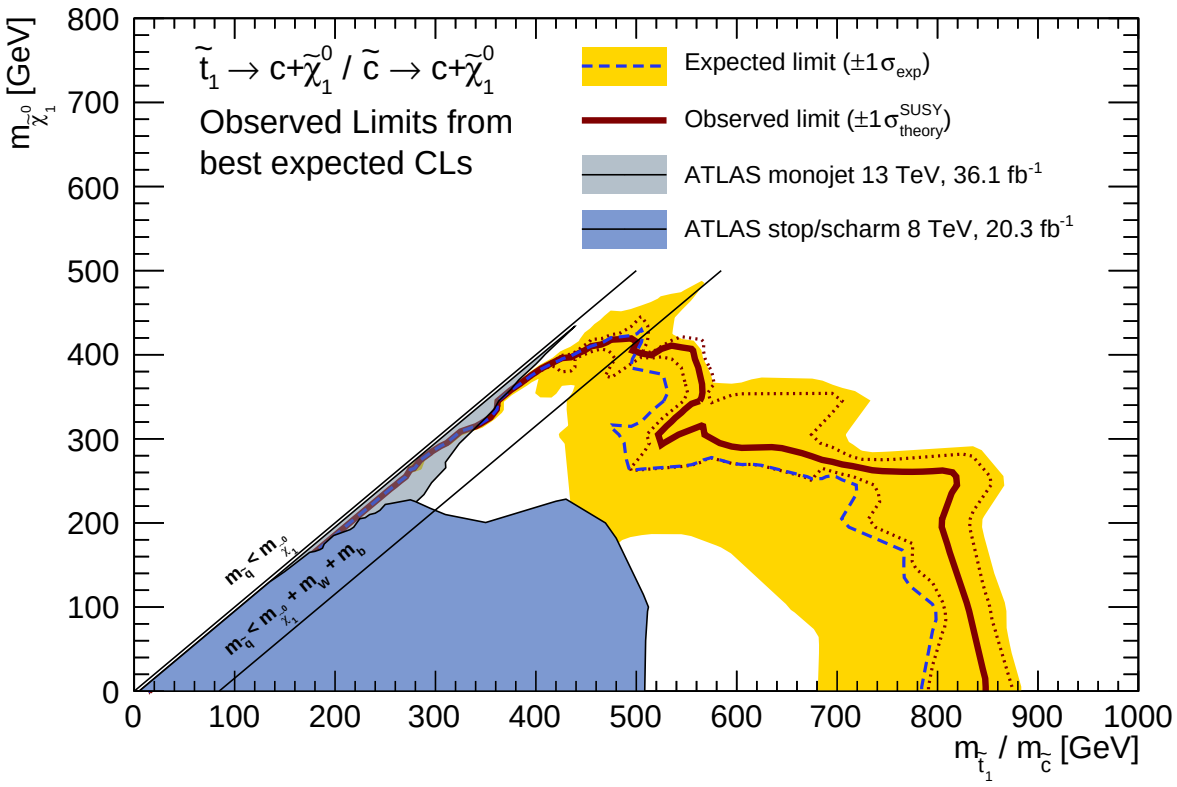

Figure 12.12: Observed and expected combined limit using the best expected CL_s method.

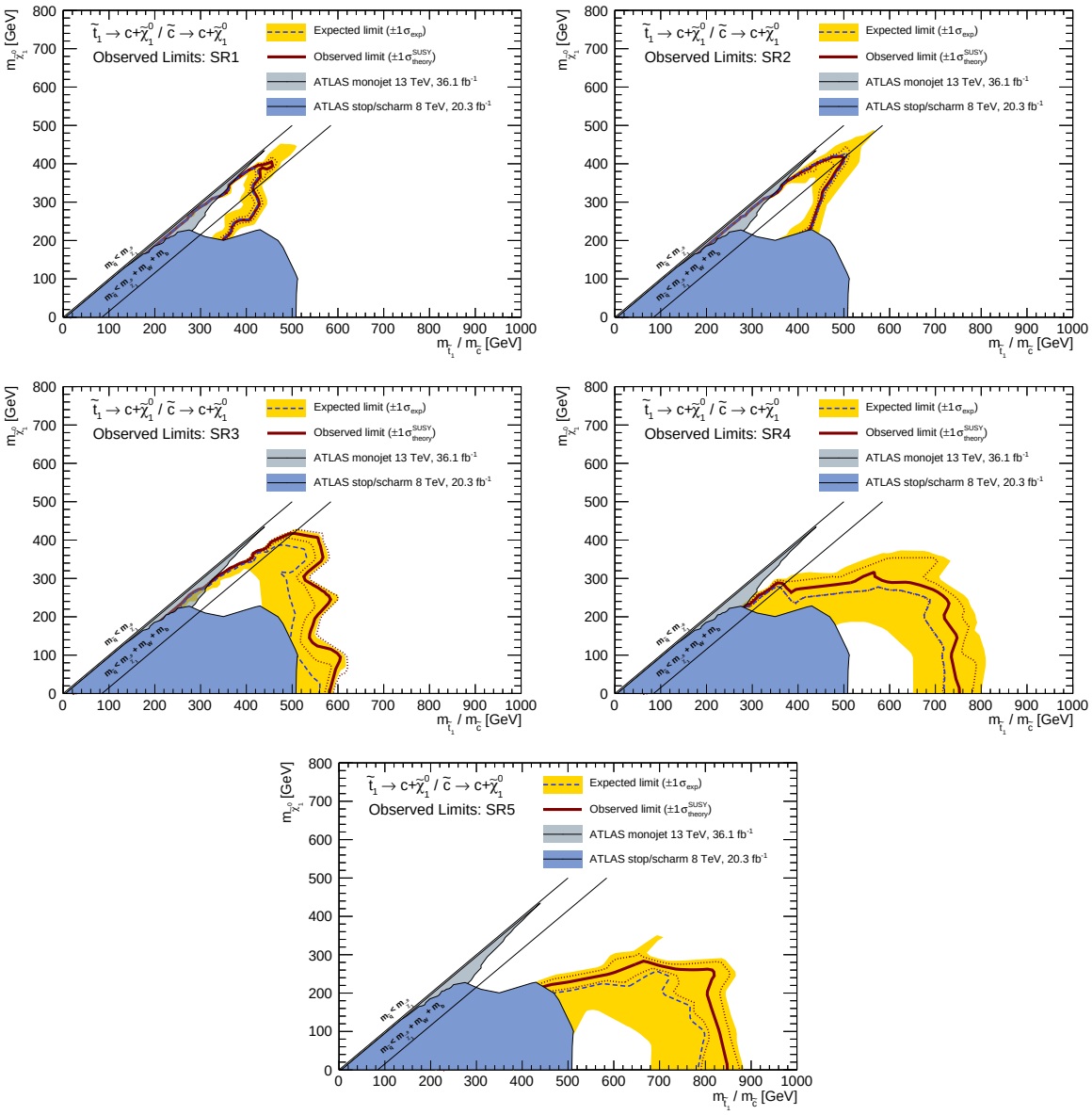

Figure 12.13: Observed and expected exclusion limits for the individual signal region at 95% confidence level.

Model-independent upper limits

As the limits discussed so far are only valid for very specific simplified models, model independent limits are calculated additionally. They allow for sensitivity checks with completely different models, or only slightly modified ones that assume for example a branching ratio of less than 100%.

The model-independent limits are calculated using the discovery fit configuration as described in section 9, in which the control regions are assumed to be signal free, so the numbers used are identical to the ones shown in tables 12.4-12.8. The results are shown in table 12.12. σ_{vis} and $S^{95}_{\text{obs/exp}}$ depend on the observed data, number of post-fit background events and total uncertainty in the signal region, so they vary for each signal region. The negative excesses in regions SR1, 3, 4 and 5 lead to slightly reduced values of S^{95}_{obs} as compared to S^{95}_{exp}, however they are in agreement within uncertainties. The probability for the background-only hypothesis, CL_b, is set to 0.5 in case of negative excesses, as the signal strength is defined to be positive.

	SR1	SR2	SR3	SR4	SR5
σ_{vis} [fb]	0.67	0.46	0.33	0.59	0.40
S^{95}_{obs}	24.2	16.6	11.9	21.3	14.3
S^{95}_{exp}	$24.4^{+13.2}_{-7.6}$	$16.0^{5.6}_{-4.4}$	$15.0^{5.2}_{-3.1}$	$24.9^{+9.6}_{-7.1}$	$15.3^{+6.8}_{-2.2}$
CL_b	0.5	0.41	0.5	0.5	0.5

Table 12.12: Model independent upper limits for all signal regions.

13. Summary

This thesis presented the search for Supersymmetry with charm jets and missing transverse momentum, using an integrated luminosity of 36.1 fb^{-1} of proton-proton collisions recorded with ATLAS experiment at a center of mass energy of $\sqrt{s} = 13$ TeV.

The reconstruction and identification of charm jets was a central piece, as the tagged jets can be used to define variables that strongly reduce standard model processes. However, charm tagging also introduced the necessity of a data-driven background estimation during the signal region optimization, as well as additional systematic uncertainties. Both were addressed with dedicated strategies for the main backgrounds, including replacements in the leptonic control regions. The similar jet flavor compositions and kinematic closeness between the signal and control regions lead to cancellations of most of the uncertainties and a reduction of the total value.

A special emphasis was also set on the signal's dependence of the mass difference between the squark and the neutralino, which strongly influences the event characteristics. Consequently, several signal regions needed to be defined, targeting different slices of $\Delta m = m_{\tilde{q}} - m_{\tilde{\chi}_1^0}$.

As no evidence for signal was observed, model independent limits were set on the visible cross section σ_{vis}, ranging from 0.33 to 0.67 fb. Additionally, limits for the simplified models $\tilde{t}_1 \to c + \tilde{\chi}_1^0$ and $\tilde{c} \to c + \tilde{\chi}_1^0$ were set. Squark masses are excluded up to 845 GeV for high mass differences and up to 500 GeV in the area at $\Delta m \approx 100$ GeV. The limits greatly increased the ATLAS *Run1* sensitivities and were added to the ATLAS stop overview plot (see figure 13.1).

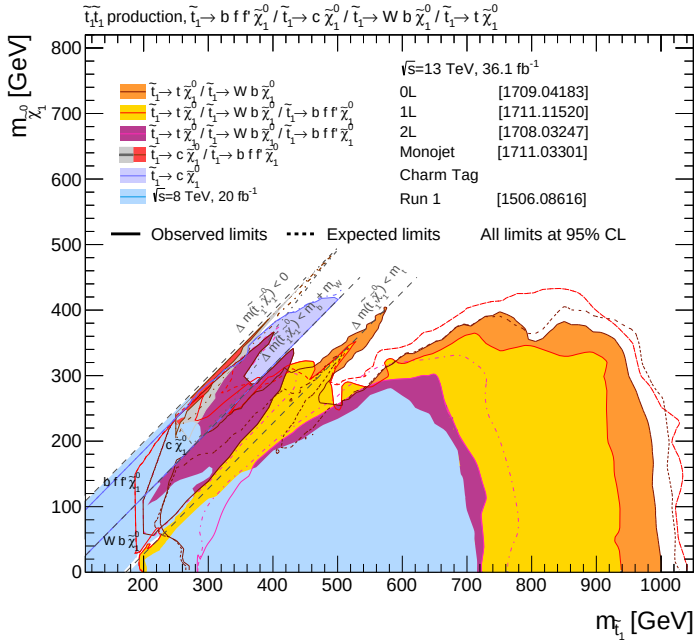

Figure 13.1: ATLAS overview plot of the current limits for various scalar top quark decay channels including this analysis' results (labelled *Charm Tag*).

14. Outlook

In 2017 the ATLAS experiment has recorded an integrated luminosity of 47.1 fb^{-1} of proton-proton data at $\sqrt{s} = 13$ TeV and the data taking will be continued in 2018. A total integrated luminosity of more than 120 fb^{-1} is expected. As this analysis struggles with low event yields in the control regions, a factor 3 increase in luminosity will reduce the systematic uncertainties on the main backgrounds.

The charm tagging algorithms are being improved for the next iteration, showing gains in both, signal efficiency and background rejection. As the current tagging efficiency drops rapidly for jets above $p_{\mathrm{T}} > 200$ GeV, a working point with fixed efficiency instead of fixed selections could be tested. In combination with the higher luminosity, the increased efficiencies could then allow for the definition of signal and control regions that require at least two charm tagged jets, which would drastically improve the signal sensitivity.

A new approach for the control region definitions using photons could be investigated (e.g. γ+jets to control the $Z \to \nu\nu$ background), which would also increase the control region statistics and could even open up the possibility of defining diboson control regions.

The search could also be extended to include additional production and decay modes that contain charm quarks in the final states (see figure 14.1). The first example is the direct pair production of gluinos, each decaying into two charm quarks and a neutralino. The second example assumes a slightly modified mass hierarchy, where the second lightest neutralino is close to, but below the squark mass (stop or scharm). The squark would first decay into a charm quark and the NLSP, which then decays into the LSP and a Z or Higgs boson. As the bosons decay further, their well known characteristics could be exploited to increase the sensitivity.

Many more analyses are carried out by ATLAS [30] and CMS [31], so far without any evidence of a supersymmetric signal. The increasingly tight exclusion limits, as well as the Higgs mass at 125 GeV, introduce problems for the naturalness arguments.

More general models like the phenomenological MSSM (pMSSM [109, 110]) have also been tested by scans through their 19 dimensional parameter space [111], resulting in the exclusion

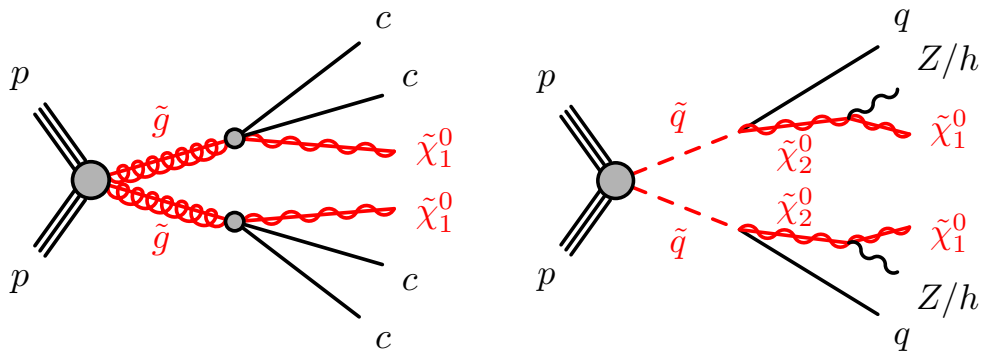

Figure 14.1: Supersymmetric final states that could be added to the analysis. [26]

of many models (see figure 14.2). However, this result also shows that exclusion limits in simplified models should be interpreted with care, as more general models can not always be constrained with the same strength. Many SUSY models with relatively low masses are not covered by the current searches and this number further increases when taking into account even more general approaches.

Further data will be recorded in the coming years at the LHC and its high luminosity upgrade (HL-LHC) and is projected to reach 3000 fb^{-1} during its run time, increasing the discovery potential for any kinds of physics beyond the Standard Model. There are also plans for the post-LHC era for example the International Linear Collider (ILC [112]) or the Future Circular Collider (FCC [113]) with 80-100 km length. While the ILC focuses on electron-positron collisions for high precision measurements at $\sqrt{s} = 500$ GeV, the FCC could be a direct successor of the LHC by significantly increasing the luminosity and center of mass energy for proton-proton collisions.

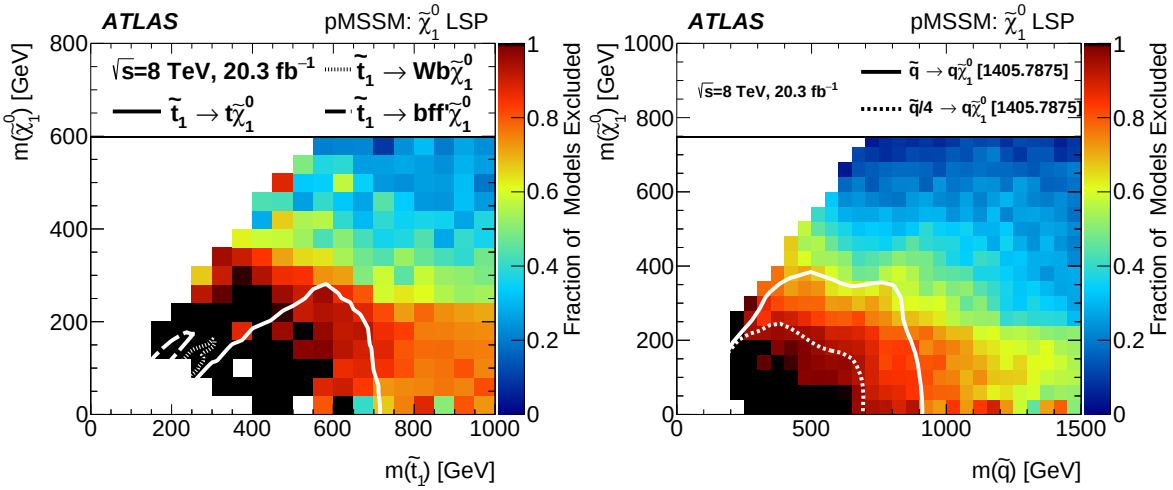

Figure 14.2: Fraction of pMSSM points excluded in the $\tilde{t}_1$-$\tilde{\chi}_1^0$ (left) and $\tilde{q}$-$\tilde{\chi}_1^0$ mass plane (right) after combining the results of 22 separate ATLAS *Run1* analyses [111]. The exclusion limits of several simplified models are shown for comparison. The $\tilde{q}/4$ line in the right plot corresponds to the scharm exclusion, however it uses both scharm states.

A. Comparison with CMS sensitivities

CMS has published limits for the $\tilde{t}_1 \to c + \tilde{\chi}_1^0$ and $\tilde{q} \to q + \tilde{\chi}_1^0$ (which can be interpreted as $\tilde{c} \to c + \tilde{\chi}_1^0$) channels [114, 115], reaching expected sensitivities of up to $m_{\tilde{c}} \approx 1000$ GeV for high mass differences[1] and $m_{\tilde{q}} \approx 450$ GeV for $\Delta m \lesssim 80$ GeV. While the latter is in line with the sensitivity that can be reached with this analysis, the former performs significantly better.

The CMS analysis mainly uses

$$H_{\mathrm{T}} = \sum_{j \in \mathrm{jets}} |\vec{p}_{\mathrm{T}}^{\,j}|,$$

as well as the extended transverse mass variable

$$m_{\mathrm{T2}} = \min_{\vec{q}_{\mathrm{T},1} + \vec{q}_{\mathrm{T},2} = \vec{p}_{\mathrm{T}}^{\,\mathrm{miss}}} \left[\max \left\{ m_{\mathrm{T}}^2(\vec{p}_{\mathrm{T},1}, \vec{q}_{\mathrm{T},1}), m_{\mathrm{T}}^2(\vec{p}_{\mathrm{T},2}, \vec{q}_{\mathrm{T},2}) \right\} \right]$$
$$\text{with } m_{\mathrm{T}}^2(\vec{p}_{\mathrm{T,i}}, \vec{q}_{\mathrm{T,i}}) = 2|\vec{p}_{\mathrm{T,i}}||\vec{q}_{\mathrm{T,i}}| \cdot (1 - \cos \Delta\phi(\vec{p}_{\mathrm{T,i}}, \vec{q}_{\mathrm{T,i}})).$$

The latter is optimized for particles that are produced in pairs and decay into a visible particle $\vec{p}_{\mathrm{T,i}}$ and an invisible particle $\vec{q}_{\mathrm{T,i}}$, each. As only the sum of the invisible particles' transverse momenta is known, all possible combinations of $\vec{q}_{\mathrm{T},1}$ and $\vec{q}_{\mathrm{T},2}$ are tested (for more information see [116]). $\vec{p}_{\mathrm{T,i}}$ are the transverse momenta of the leading two jets, as the targeted signal points have high mass differences and therefore high p_{T} jets from the squark decays.

The CMS analysis uses many finely binned signal regions in H_{T} and m_{T2}, however the main sensitivity is expected to yield from the high m_{T2} regions. The comparison with the binned regions is quite hard, so instead the so called *super signal regions* [115] will be tested here[2].

The loosest possible CMS-like selection that can be defined is roughly equivalent to the Preselection (see section 7.1) plus an additional requirement of $m_{\mathrm{T2}} > 250$ GeV. On top of this, a cut at $m_{\mathrm{T2}} > 1000$ GeV is applied, which results in the loss of almost all signal events (see figure A.1). While several kinematic requirements that are expected to further reduce the backgrounds have been dropped here, it is not expected that sensitivity can be reached with such low signal yields.

Since the CMS analysis still excludes the points, it is not clear where the sensitivity comes from. One possibility is the use of slightly different signal models with higher rates in this phase space (though the signal production diagram is the same). Another one is that the shape fit gains its sensitivity in the intermediate region $m_{\mathrm{T2}} \approx 750$ GeV, which shows a better signal over background ratio, and the super signal region has indeed no sensitivity.

[1] $\Delta m = m_{\tilde{q}} - m_{\tilde{\chi}_1^0}$

[2] Note that the super signal regions perform slightly worse than the finely binned ones.

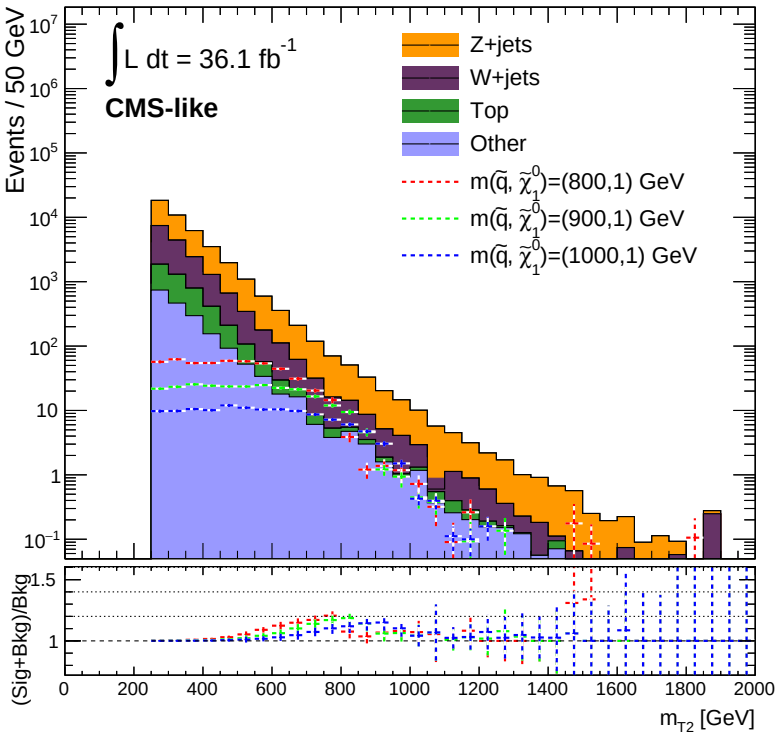

Figure A.1: m_{T2} distribution in an inclusive CMS-like region. No fit is performed and only statistical uncertainties are shown.

B. Z+jets control region distributions

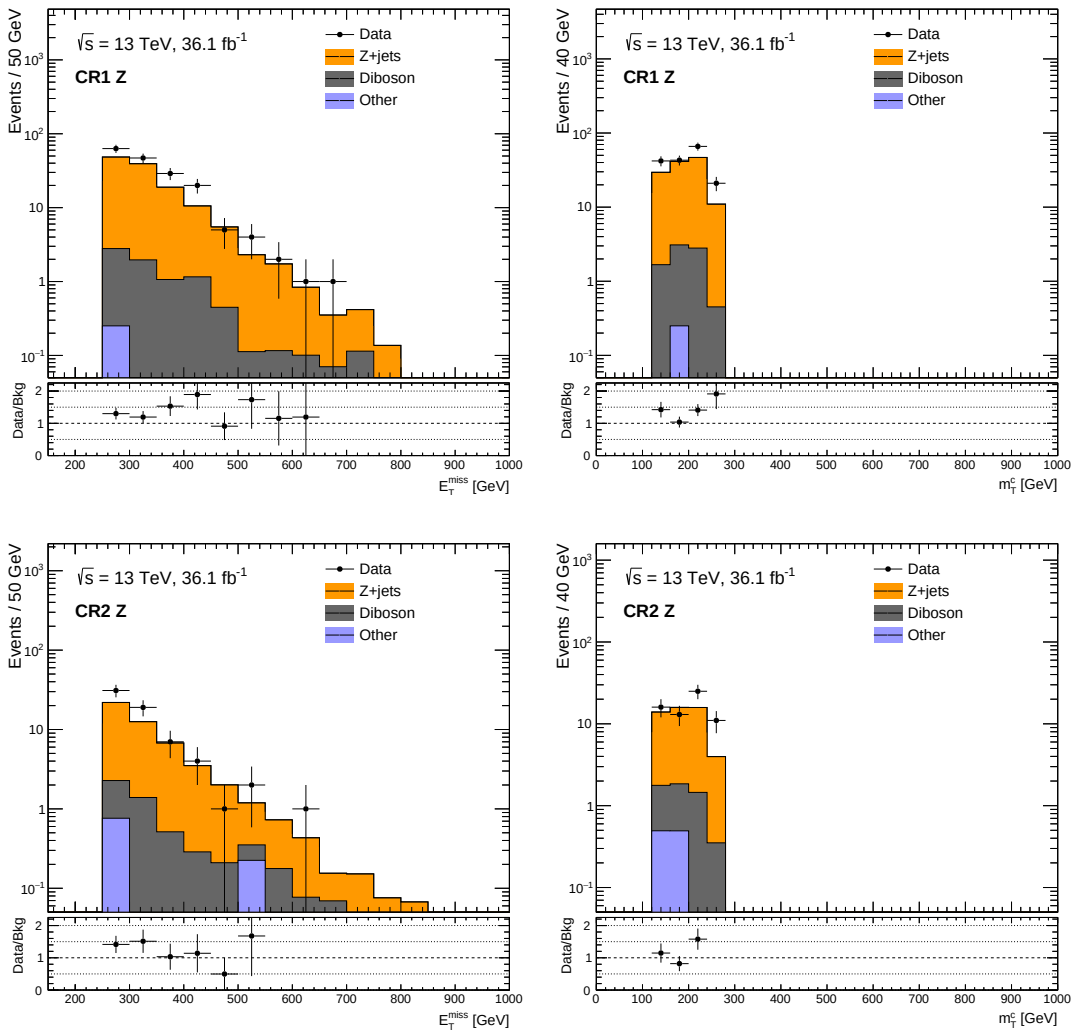

Figure B.1: $E_{\mathrm{T}}^{\mathrm{miss}}$(left) and m_{T}^{c} distributions (right) in in CRZ 1 and 2 before the fit. Only statistical uncertainties are shown.

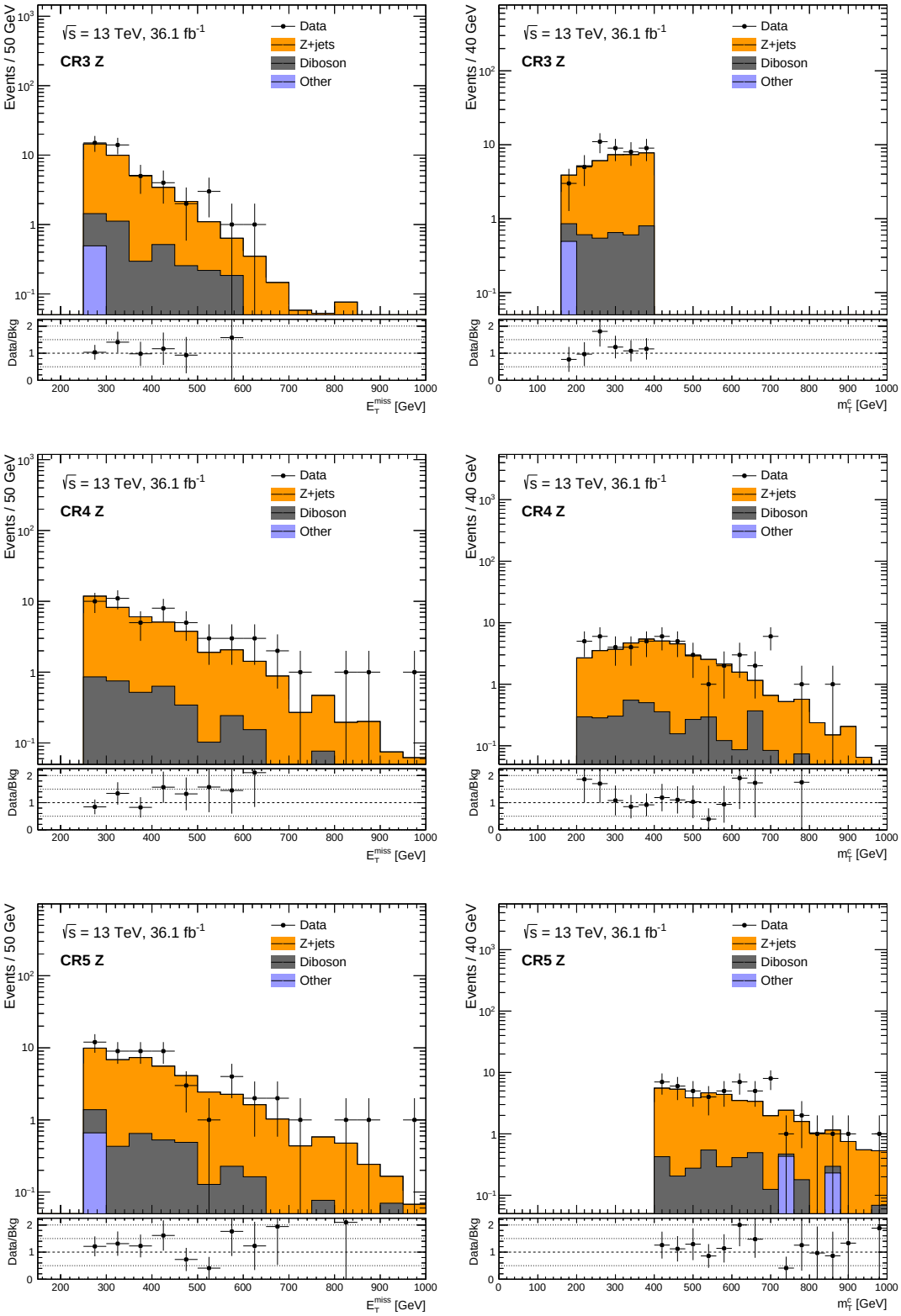

Figure B.2: $E_{\mathrm{T}}^{\mathrm{miss}}$(left) and m_{T}^{c} distributions (right) in in CRZ 3-5 before the fit. Only statistical uncertainties are shown.

C. W+jets control region distributions

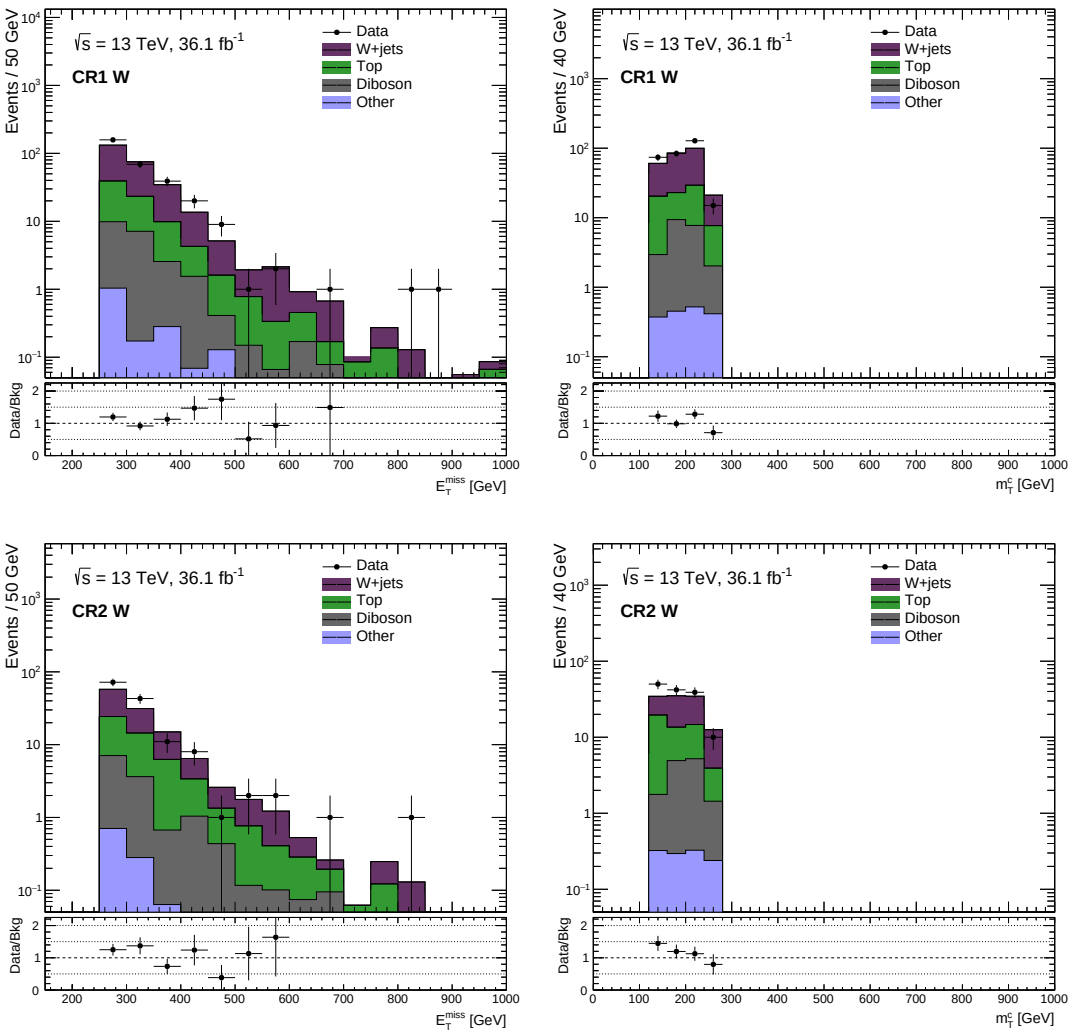

Figure C.1: $E_{\mathrm{T}}^{\mathrm{miss}}$(left) and m_{T}^{c} distributions (right) in in CRW 1 and 2 before the fit. Only statistical uncertainties are shown.

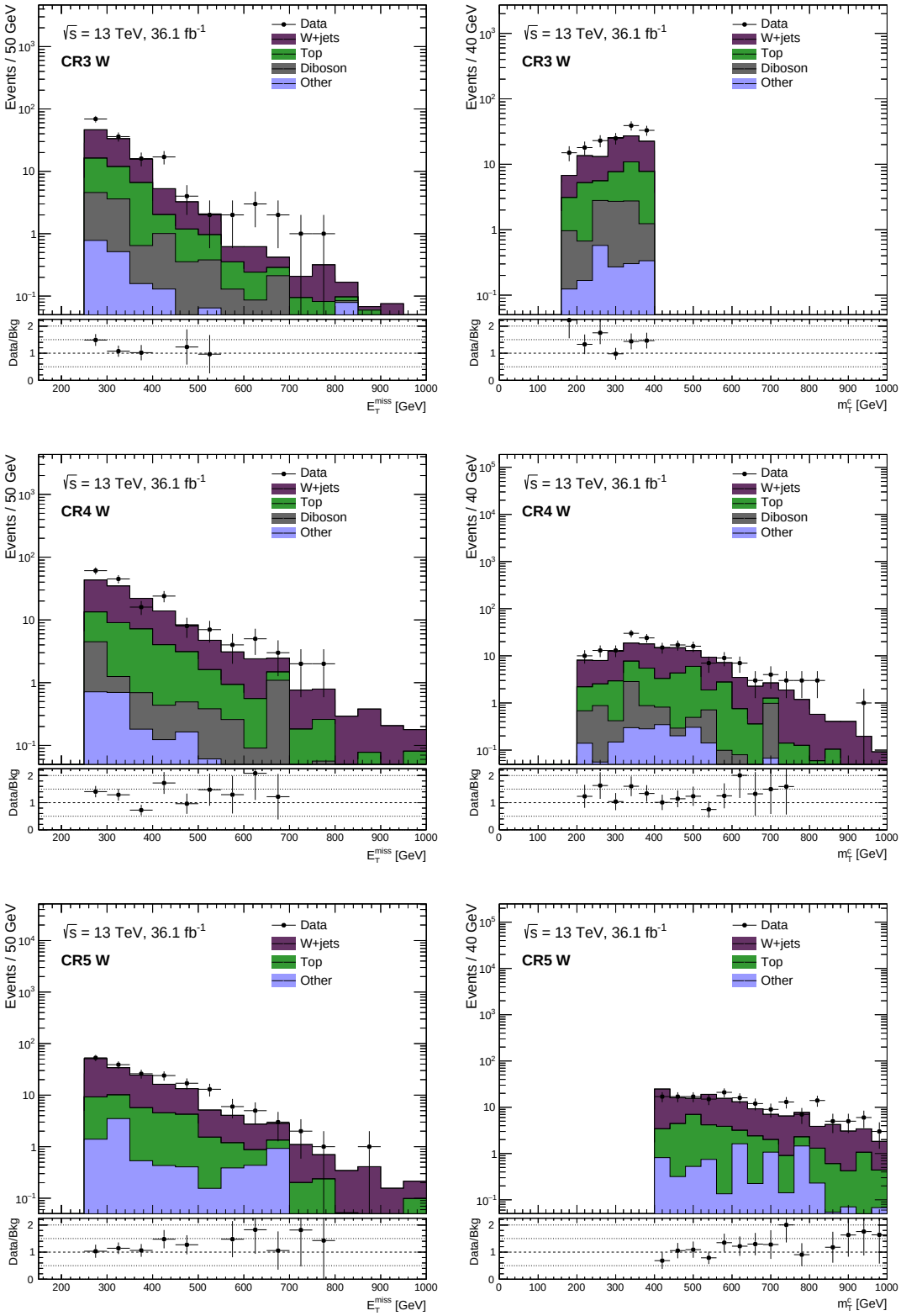

Figure C.2: $E_{\mathrm{T}}^{\mathrm{miss}}$(left) and m_{T}^{c} distributions (right) in in CRW 3-5 before the fit. Only statistical uncertainties are shown.

D. Top control region distributions

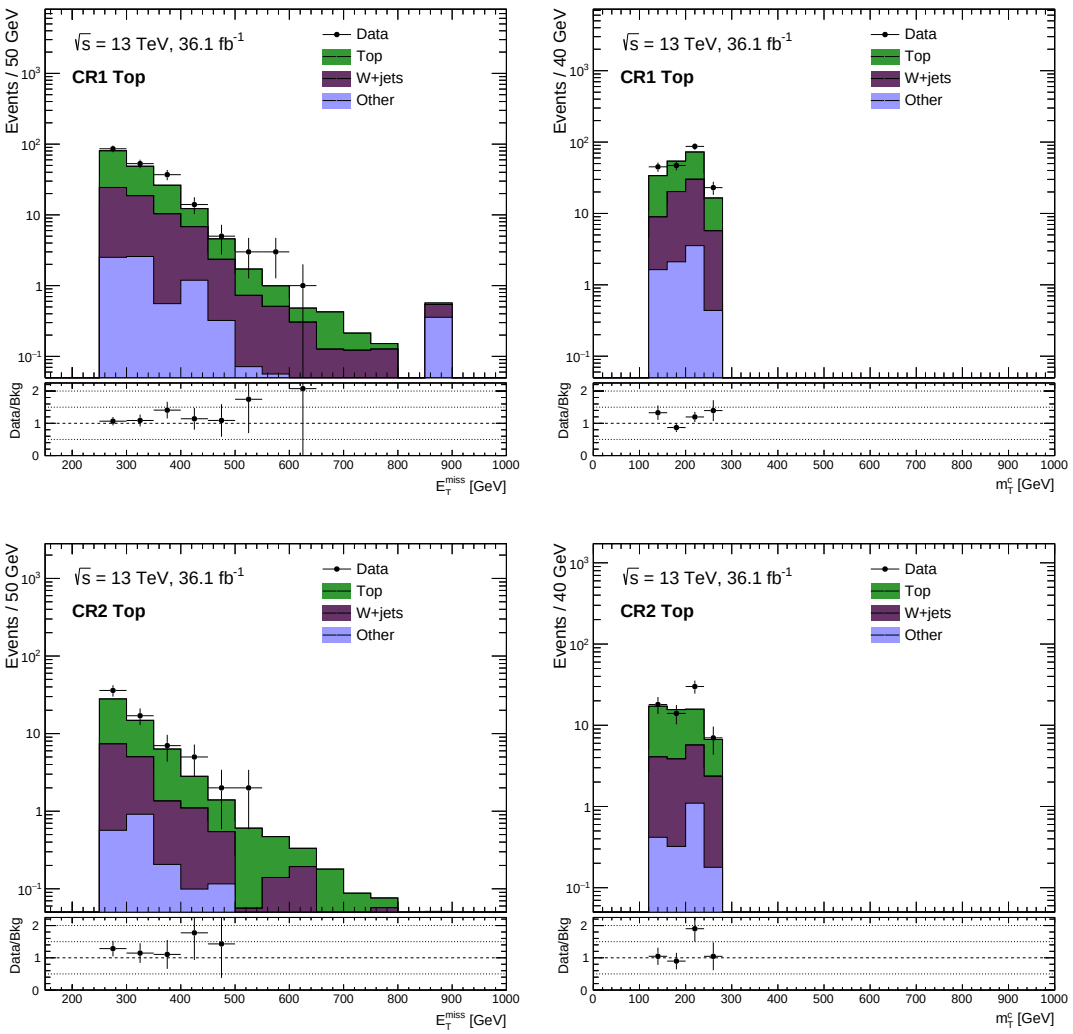

Figure D.1: $E_{\mathrm{T}}^{\mathrm{miss}}$(left) and m_{T}^{c} distributions (right) in in CRTop 1 and 2 before the fit. Only statistical uncertainties are shown.

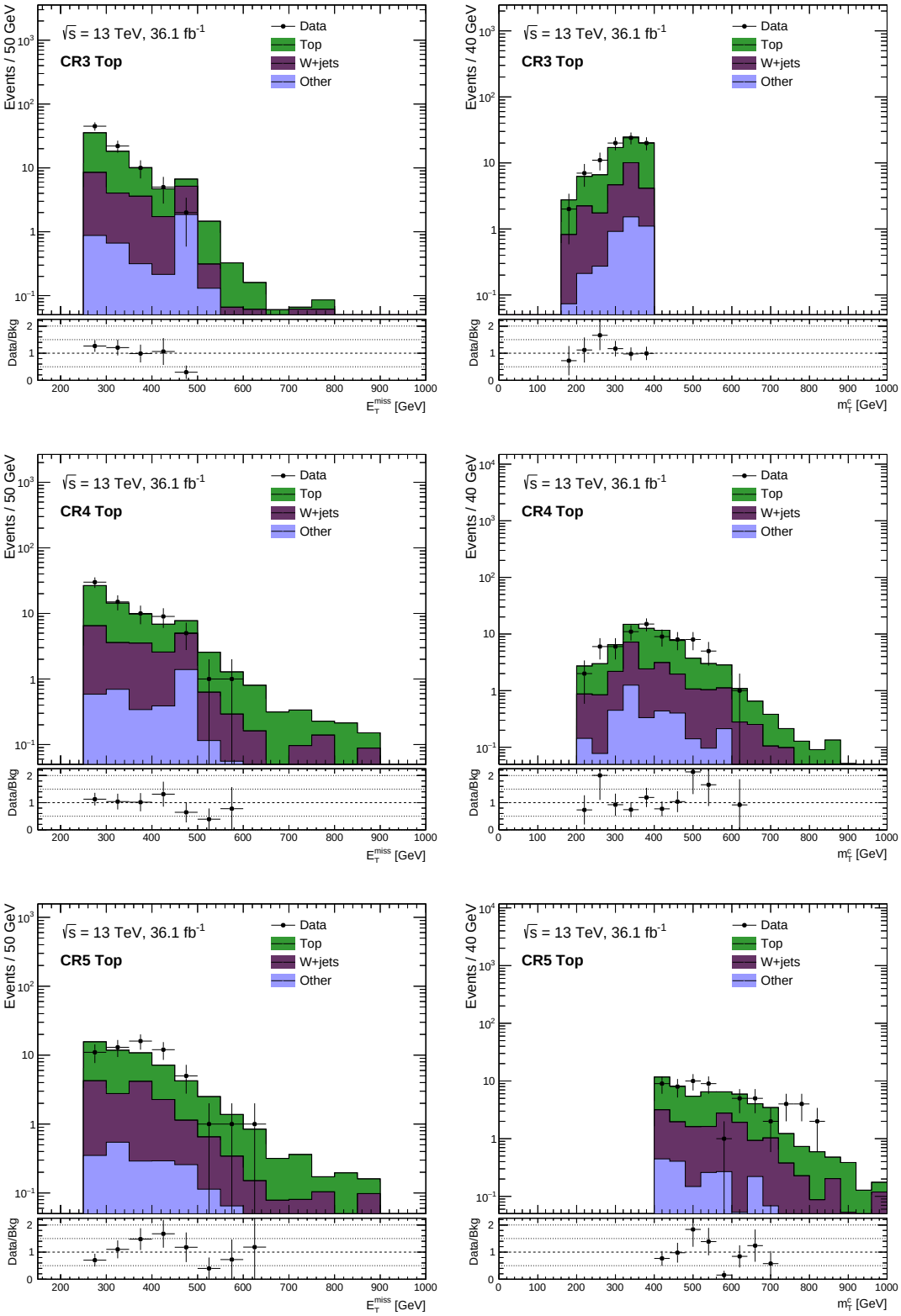

Figure D.2: $E_{\mathrm{T}}^{\mathrm{miss}}$(left) and m_{T}^{c} distributions (right) in in CRTop 3-5 before the fit. Only statistical uncertainties are shown.

E. Jet flavor compositions

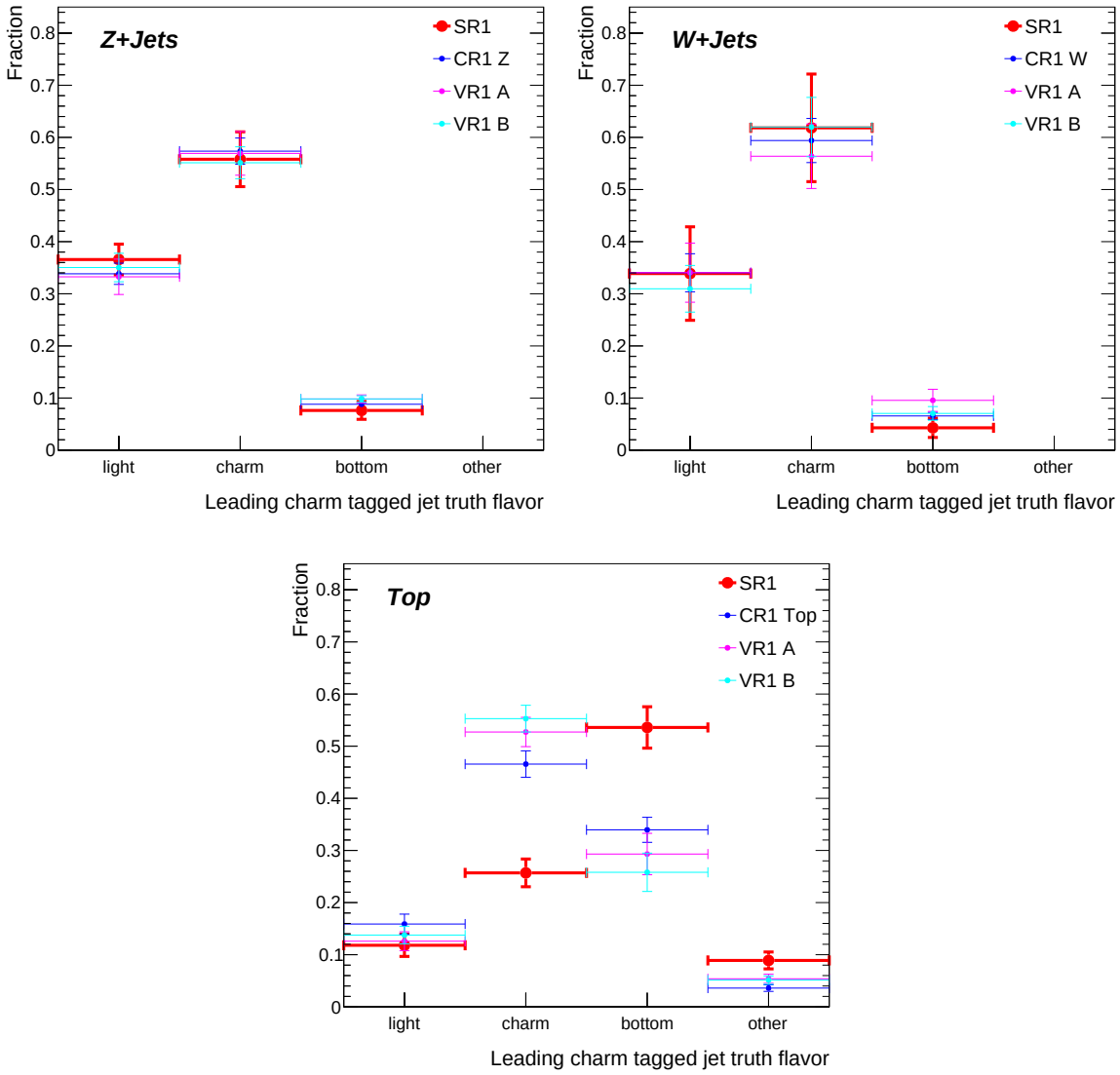

Figure E.1: Leading charm tagged jet flavor compositions in SR1 and the corresponding control and validation regions.

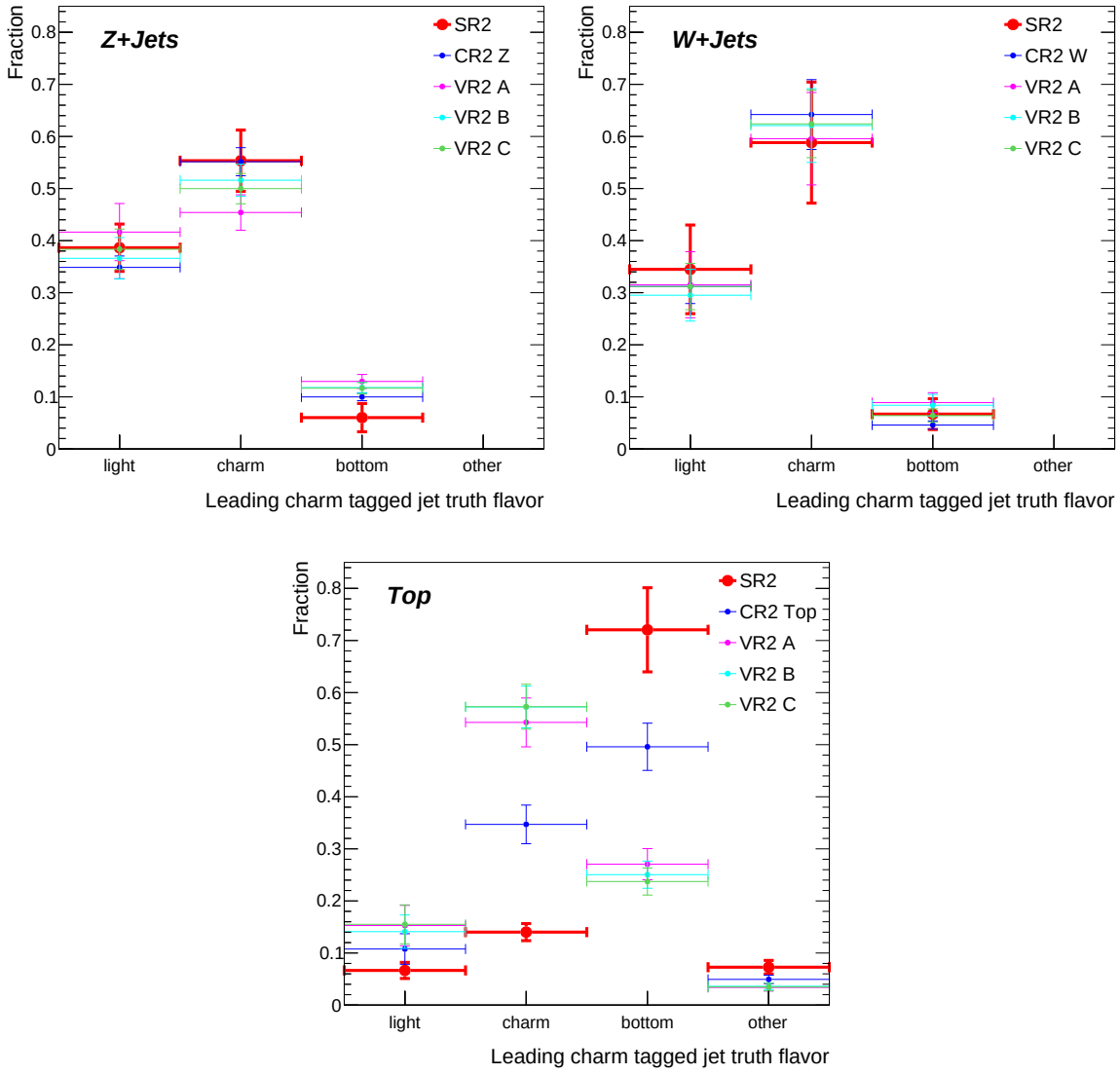

Figure E.2: Leading charm tagged jet flavor compositions in SR2 and the corresponding control and validation regions.

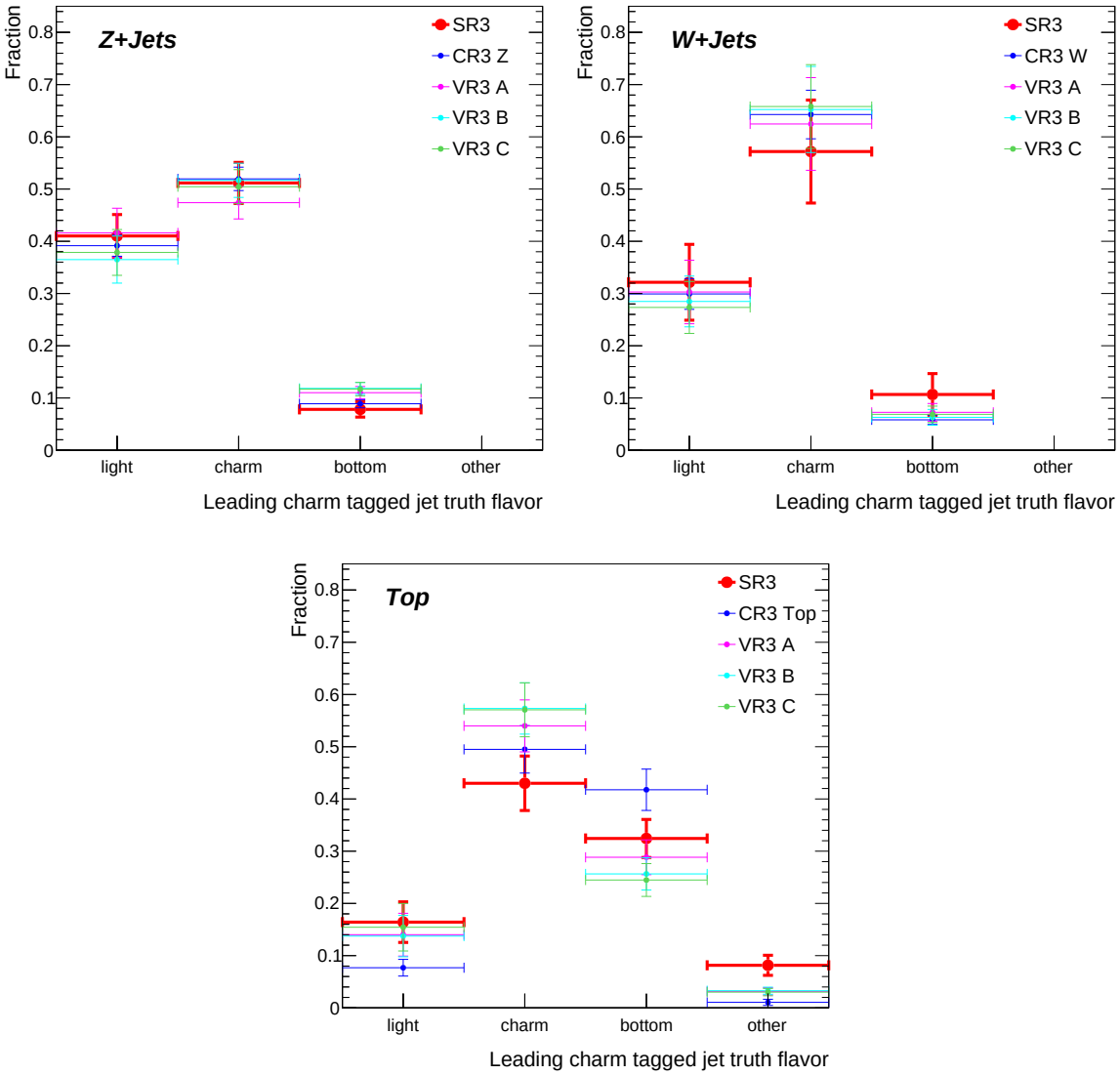

Figure E.3: Leading charm tagged jet flavor compositions in SR3 and the corresponding control and validation regions.

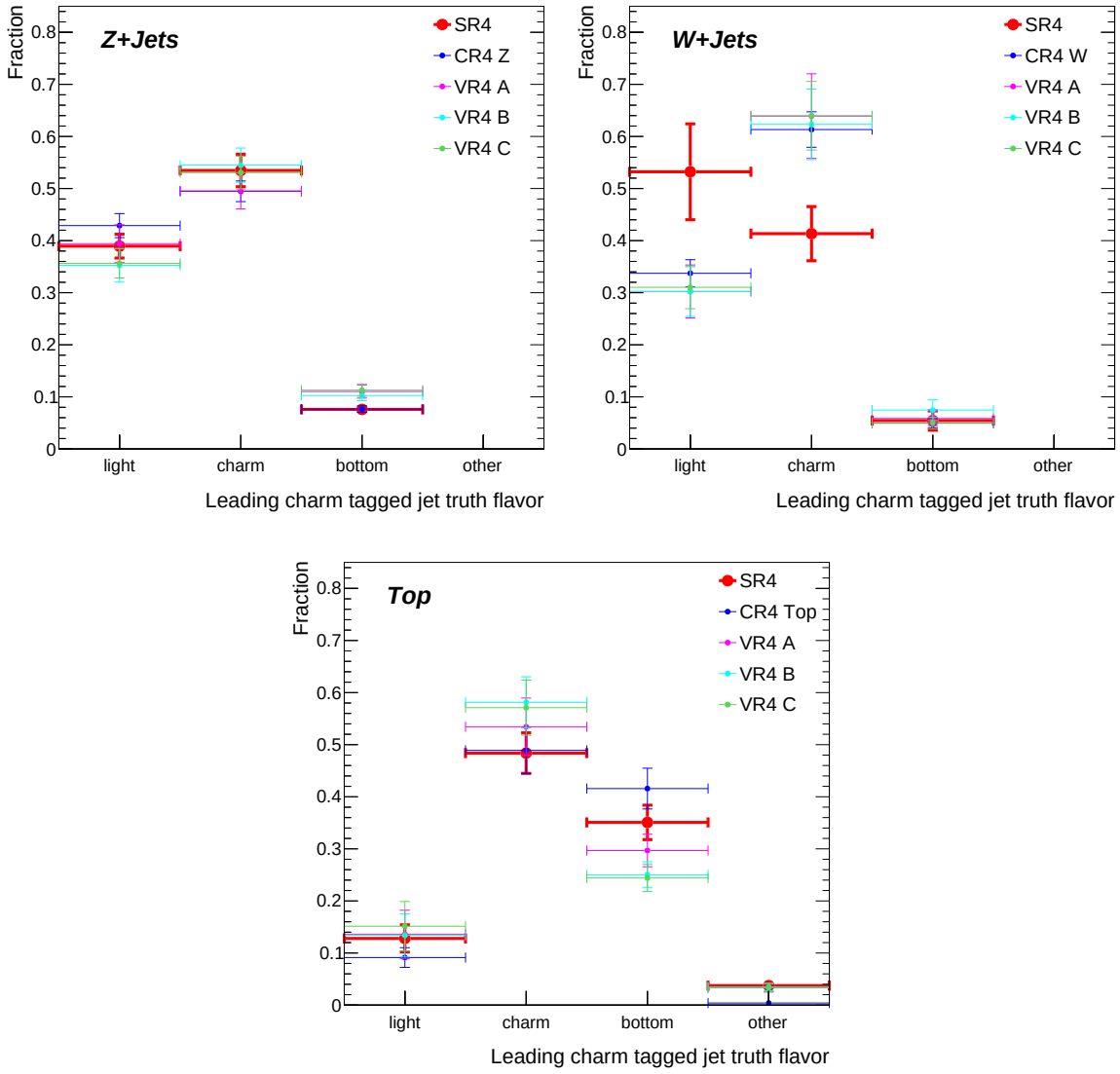

Figure E.4: Leading charm tagged jet flavor compositions in SR4 and the corresponding control and validation regions.

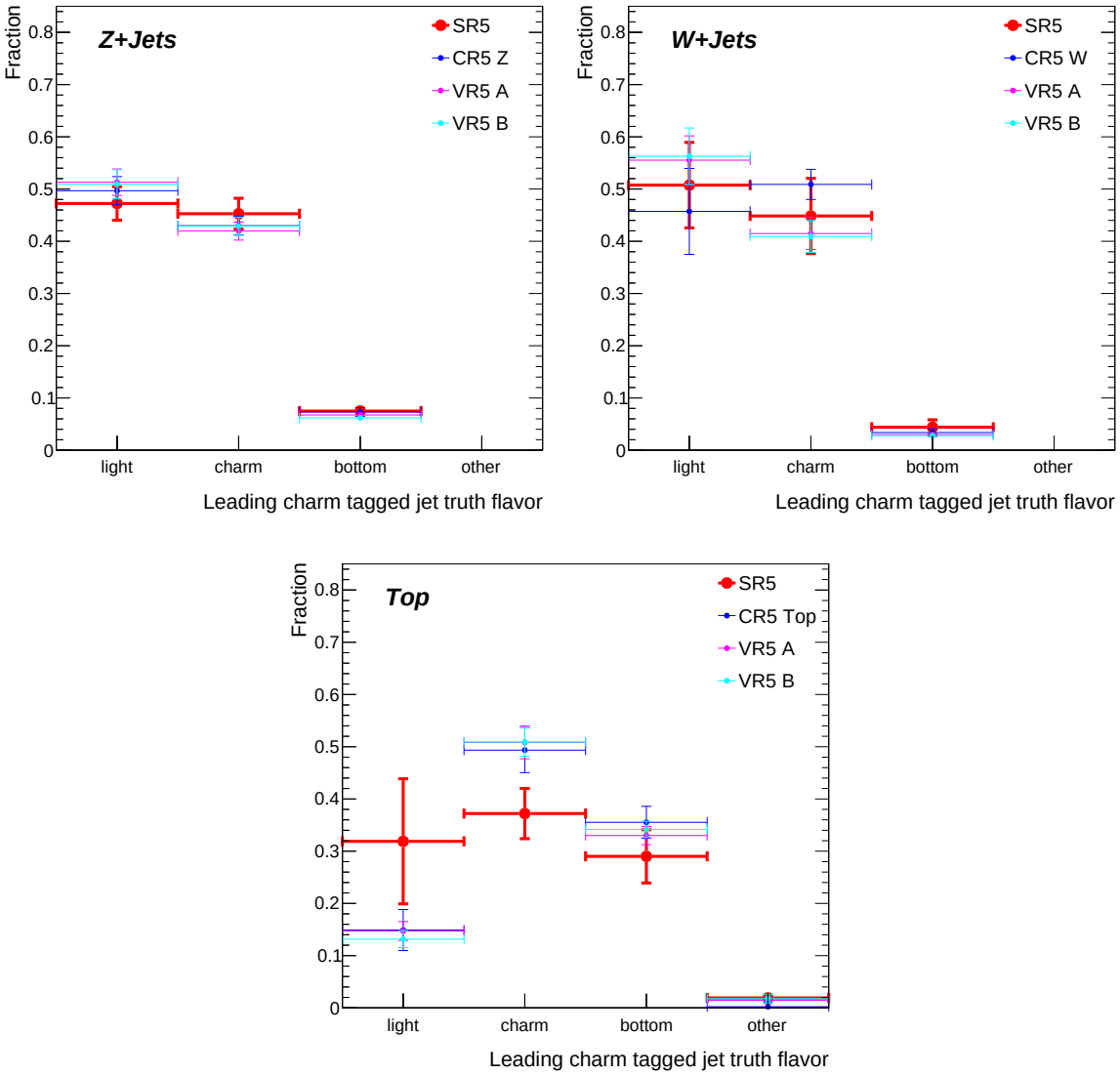

Figure E.5: Leading charm tagged jet flavor compositions in SR5 and the corresponding control and validation regions.

F. Results

F.1. Background-only fit correlation matrices

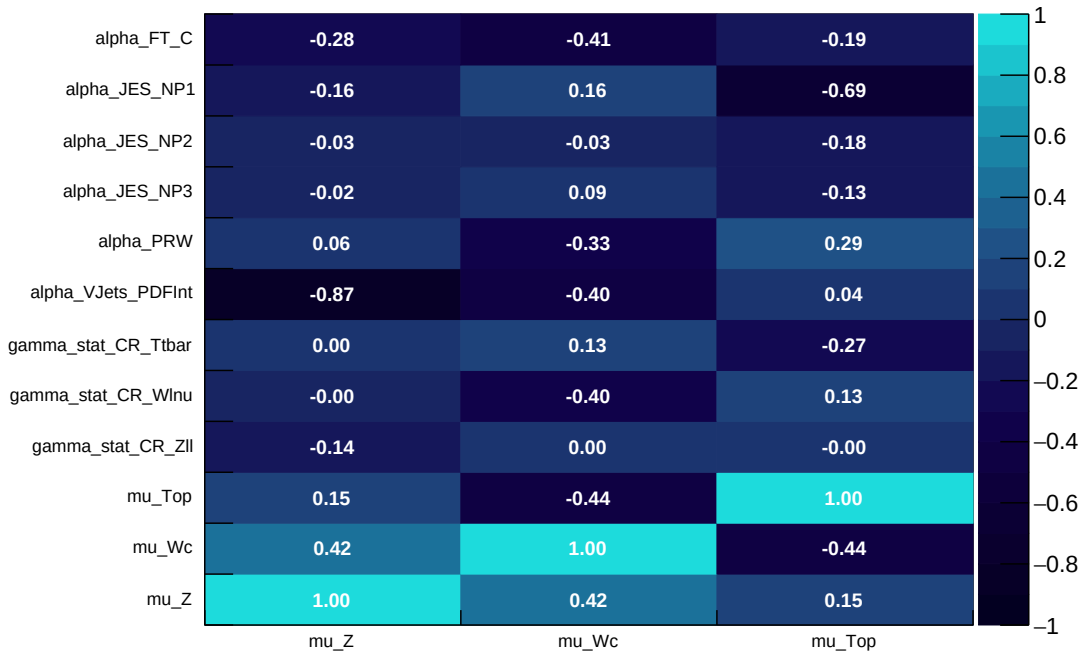

Figure F.1: Correlation matrix of the floating fit parameters in SR1. Only parameters that have at least one (anti-) correlation with an absolute value ≥ 0.1 are shown.

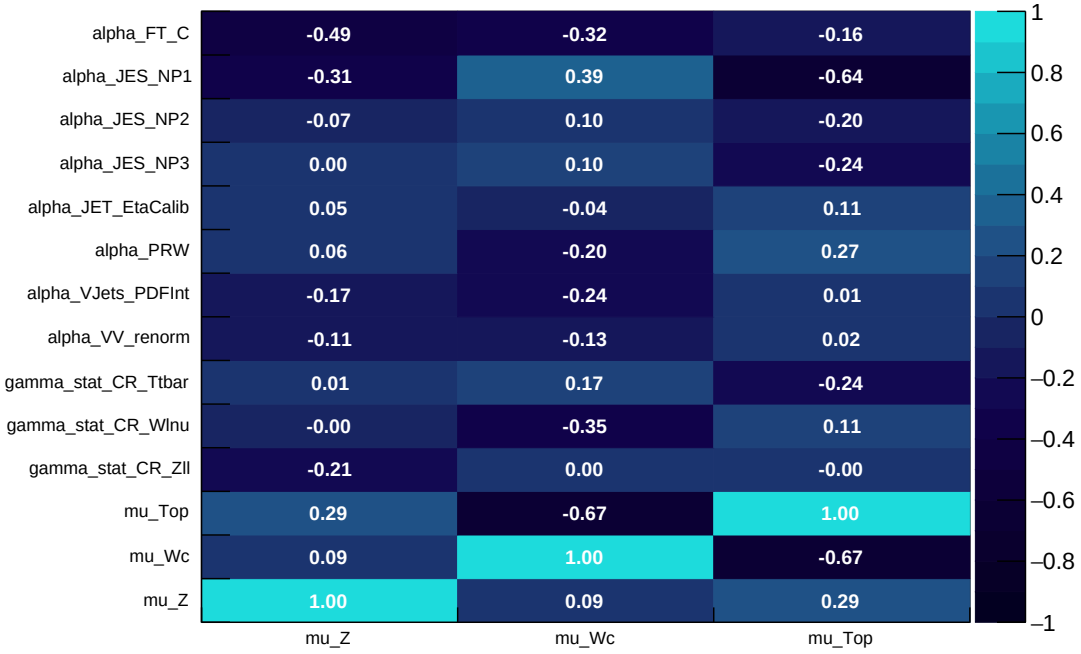

Figure F.2: Correlation matrix of the floating fit parameters in SR2. Only parameters that have at least one (anti-) correlation with an absolute value ≥ 0.1 are shown.

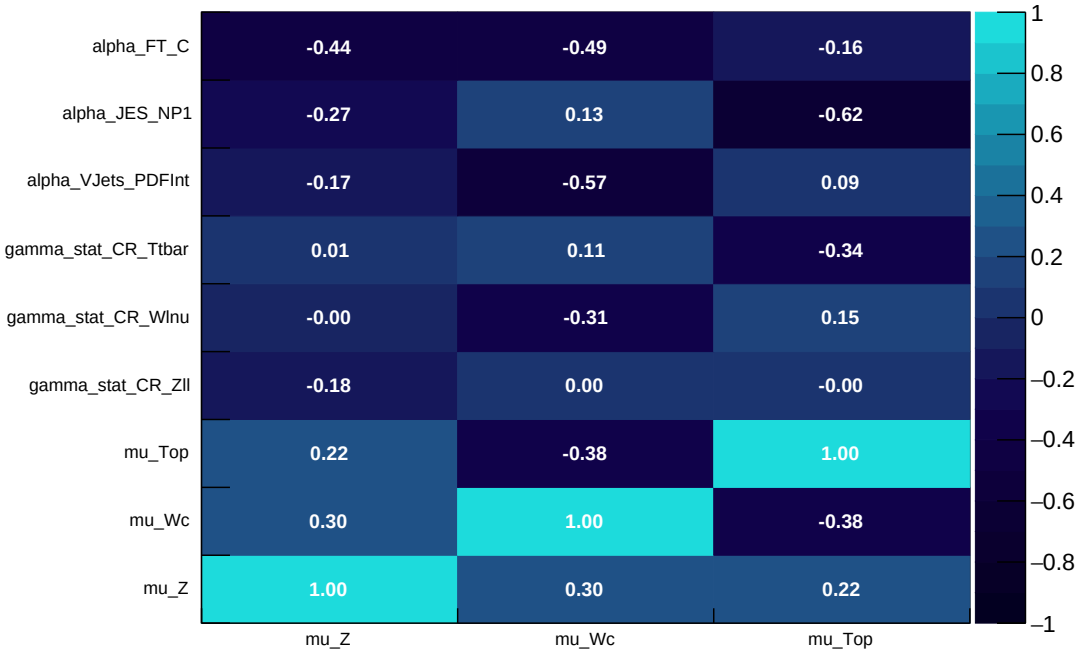

Figure F.3: Correlation matrix of the floating fit parameters in SR3. Only parameters that have at least one (anti-) correlation with an absolute value ≥ 0.1 are shown.

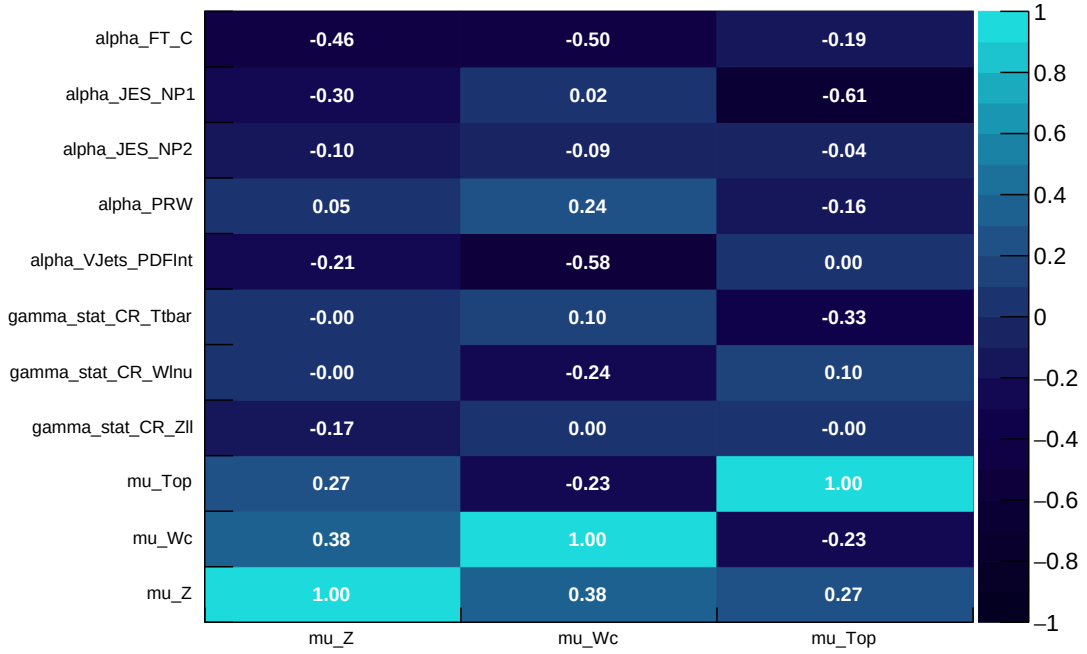

Figure F.4: Correlation matrix of the floating fit parameters in SR4. Only parameters that have at least one (anti-) correlation with an absolute value ≥ 0.1 are shown.

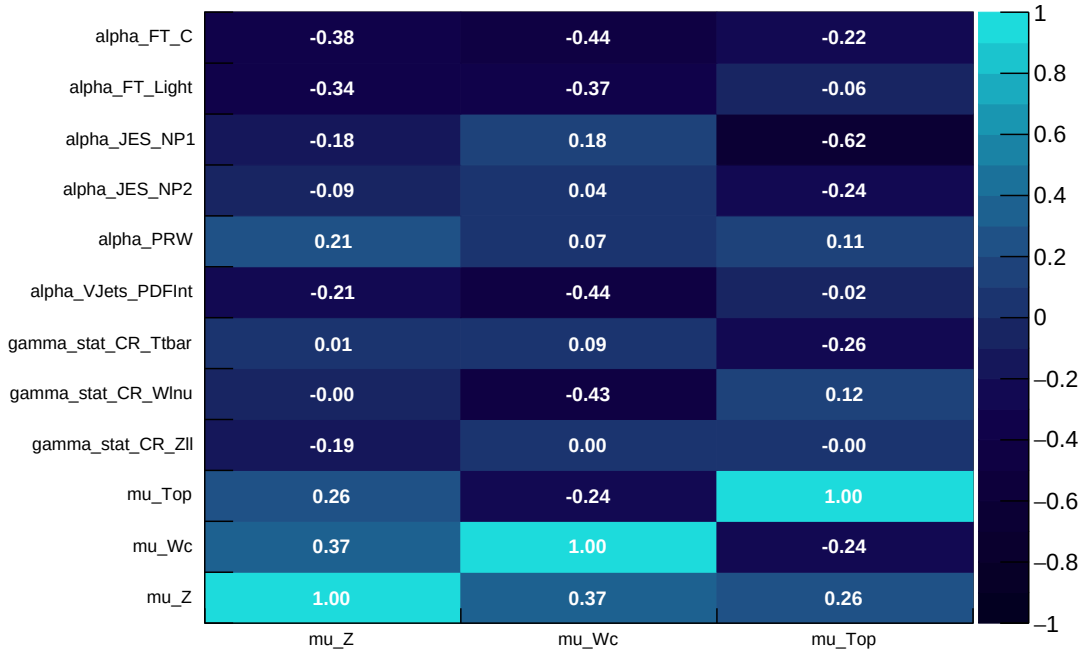

Figure F.5: Correlation matrix of the floating fit parameters in SR5. Only parameters that have at least one (anti-) correlation with an absolute value ≥ 0.1 are shown.

F.2. Background-only fit uncertainty tables

Uncertainty of channel	VR1 A	VR1 B	CR1 Z	CR1 W	CR1 Top
Total bkg systematic	±40.62 [18.58%]	±56.24 [17.48%]	±16.03 [9.31%]	±30.90 [10.25%]	±14.49 [7.17%]
mu_Z	±26.64 [12.2%]	±45.62 [14.2%]	±40.59 [23.6%]	±0.32 [0.11%]	±0.10 [0.05%]
alpha_V_RenormFac	±22.87 [10.5%]	±35.86 [11.1%]	±0.00 [0.00%]	±0.00 [0.00%]	±0.00 [0.00%]
alpha_VJets_qsf	±20.77 [9.5%]	±30.03 [9.3%]	±0.00 [0.00%]	±0.00 [0.00%]	±0.00 [0.00%]
alpha_FT_C	±16.79 [7.7%]	±23.78 [7.4%]	±10.35 [6.0%]	±19.82 [6.6%]	±11.66 [5.8%]
mu_Wc	±14.39 [6.6%]	±20.71 [6.4%]	±0.00 [0.00%]	±58.67 [19.5%]	±18.09 [9.0%]
mu_Top	±12.93 [5.9%]	±13.35 [4.1%]	±0.08 [0.05%]	±19.40 [6.4%]	±37.22 [18.4%]
alpha_VJets_PDFInt	±12.41 [5.7%]	±46.78 [14.5%]	±42.76 [24.9%]	±18.83 [6.2%]	±4.26 [2.1%]
alpha_Ttbar_Shower	±8.87 [4.1%]	±9.27 [2.9%]	±0.00 [0.00%]	±0.00 [0.00%]	±0.00 [0.00%]
alpha_JES_NP1	±8.68 [4.0%]	±16.88 [5.2%]	±6.04 [3.5%]	±6.67 [2.2%]	±22.98 [11.4%]
gamma_stat_VR1A	±8.12 [3.7%]	±0.00 [0.00%]	±0.00 [0.00%]	±0.00 [0.00%]	±0.00 [0.00%]
alpha_VJets_ckkw	±6.21 [2.8%]	±8.86 [2.8%]	±0.00 [0.00%]	±0.00 [0.00%]	±0.00 [0.00%]
alpha_single top_Theory	±6.12 [2.8%]	±5.81 [1.8%]	±0.00 [0.00%]	±0.00 [0.00%]	±0.00 [0.00%]
alpha_JES_NP2	±5.47 [2.5%]	±7.90 [2.5%]	±0.98 [0.57%]	±4.43 [1.5%]	±6.87 [3.4%]
alpha_PRW	±5.15 [2.4%]	±12.84 [4.0%]	±2.35 [1.4%]	±7.51 [2.5%]	±6.64 [3.3%]
alpha_Ttbar_Generator	±5.01 [2.3%]	±5.24 [1.6%]	±0.00 [0.00%]	±0.00 [0.00%]	±0.00 [0.00%]
alpha_JET_EtaCalib	±3.03 [1.4%]	±3.55 [1.1%]	±0.20 [0.12%]	±2.99 [0.99%]	±1.30 [0.65%]
alpha_FT_Light	±2.68 [1.2%]	±5.32 [1.7%]	±0.96 [0.56%]	±1.68 [0.56%]	±2.09 [1.0%]
alpha_BGXSec	±2.14 [0.98%]	±2.48 [0.77%]	±1.17 [0.68%]	±3.20 [1.1%]	±1.12 [0.56%]
alpha_VV_renorm	±1.61 [0.74%]	±2.19 [0.68%]	±1.46 [0.85%]	±3.82 [1.3%]	±1.08 [0.54%]
alpha_VV_qsf	±1.48 [0.67%]	±2.01 [0.62%]	±0.08 [0.05%]	±0.21 [0.07%]	±0.06 [0.03%]

Table F.1: Breakdown of the systematic uncertainties in the control and validation regions of SR1 after the background-only fit (continued in table F.2). Uncertainties can be correlated and do not necessarily add up in quadrature.

Uncertainty of channel	VR1 A	VR1 B	CR1 Z	CR1 W	CR1 Top
alpha_FT_ExC	±1.47 [0.67%]	±1.23 [0.38%]	±0.15 [0.09%]	±1.72 [0.57%]	±1.03 [0.51%]
alpha_Ttbar_Radiation	±1.46 [0.67%]	±1.52 [0.47%]	±0.00 [0.00%]	±0.00 [0.00%]	±0.00 [0.00%]
alpha_JES_NP3	±1.41 [0.64%]	±3.95 [1.2%]	±0.76 [0.44%]	±1.11 [0.37%]	±3.56 [1.8%]
alpha_MET_Scale	±0.87 [0.40%]	±1.03 [0.32%]	±0.87 [0.51%]	±1.92 [0.64%]	±0.53 [0.26%]
alpha_VJets_PDFSet	±0.66 [0.30%]	±0.76 [0.23%]	±0.15 [0.09%]	±0.29 [0.10%]	±0.03 [0.01%]
alpha_VV_fac	±0.56 [0.26%]	±0.76 [0.24%]	±0.07 [0.04%]	±0.19 [0.06%]	±0.05 [0.03%]
alpha_VJets_AlphaS	±0.51 [0.23%]	±1.49 [0.46%]	±0.53 [0.31%]	±1.67 [0.56%]	±0.14 [0.07%]
alpha_FT_Ex	±0.13 [0.06%]	±0.18 [0.05%]	±0.11 [0.06%]	±0.14 [0.05%]	±0.15 [0.07%]
alpha_FT_B	±0.05 [0.02%]	±0.01 [0.00%]	±0.07 [0.04%]	±1.65 [0.55%]	±1.72 [0.85%]
alpha_JVT	±0.02 [0.01%]	±0.10 [0.03%]	±0.65 [0.38%]	±0.31 [0.10%]	±1.40 [0.69%]
alpha_JER	±0.00 [0.00%]	±0.01 [0.00%]	±0.00 [0.00%]	±0.00 [0.00%]	±0.00 [0.00%]
alpha_MET_ResoPerp	±0.00 [0.00%]	±0.00 [0.00%]	±0.00 [0.00%]	±0.00 [0.00%]	±0.00 [0.00%]
alpha_MET_ResoPara	±0.00 [0.00%]	±0.00 [0.00%]	±0.00 [0.00%]	±0.00 [0.00%]	±0.00 [0.00%]
gamma_stat_CR1 W	±0.00 [0.00%]	±0.00 [0.00%]	±0.00 [0.00%]	±13.27 [4.4%]	±0.00 [0.00%]
gamma_stat_VR1B	±0.00 [0.00%]	±10.62 [3.3%]	±0.00 [0.00%]	±0.00 [0.00%]	±0.00 [0.00%]
gamma_stat_SR	±0.00 [0.00%]	±0.00 [0.00%]	±0.00 [0.00%]	±0.00 [0.00%]	±0.00 [0.00%]
gamma_stat_CR1 Z	±0.00 [0.00%]	±0.00 [0.00%]	±5.37 [3.1%]	±0.00 [0.00%]	±0.00 [0.00%]
gamma_stat_CR1 Top	±0.00 [0.00%]	±0.00 [0.00%]	±0.00 [0.00%]	±0.00 [0.00%]	±8.21 [4.1%]

Table F.2: Breakdown of the systematic uncertainties in the control and validation regions of SR1 after the background-only fit(continuation of table F.1). Uncertainties can be correlated and do not necessarily add up in quadrature.

Uncertainty of channel	VR2 A	VR2 B	VR2 C	CR2 Z	CR2 W	CR2 Top
Total background expectation	115.50	182.84	160.15	65.02	140.93	69.00
Total statistical ($\sqrt{N_{\text{exp}}}$)	±10.75	±13.52	±12.66	±8.06	±11.87	±8.31
Total background systematic	±19.27 [16.69%]	±40.00 [21.88%]	±24.03 [15.00%]	±8.10 [12.46%]	±12.71 [9.02%]	±8.29 [12.01%]
mu_Top	±15.25 [13.2%]	±18.11 [9.9%]	±17.79 [11.1%]	±0.50 [0.78%]	±19.66 [13.9%]	±20.01 [29.0%]
alpha_Ttbar_Shower	±10.86 [9.4%]	±12.89 [7.0%]	±12.49 [7.8%]	±0.00 [0.00%]	±0.00 [0.00%]	±0.00 [0.00%]
alpha_FT_C	±9.47 [8.2%]	±15.87 [8.7%]	±14.38 [9.0%]	±5.33 [8.2%]	±12.10 [8.6%]	±5.15 [7.5%]
mu_Wc	±9.03 [7.8%]	±14.33 [7.8%]	±14.34 [9.0%]	±0.00 [0.00%]	±29.08 [20.6%]	±6.27 [9.1%]
mu_Z	±8.33 [7.2%]	±15.61 [8.5%]	±12.23 [7.6%]	±10.81 [16.6%]	±0.13 [0.09%]	±0.02 [0.03%]
alpha_VJets_PDFInt	±7.91 [6.8%]	±36.00 [19.7%]	±8.99 [5.6%]	±1.84 [2.8%]	±6.88 [4.9%]	±1.09 [1.6%]
alpha_V_RenormFac	±6.02 [5.2%]	±10.35 [5.7%]	±9.28 [5.8%]	±0.00 [0.00%]	±0.00 [0.00%]	±0.00 [0.00%]
gamma_stat_VR2A	±5.21 [4.5%]	±0.00 [0.00%]	±0.00 [0.00%]	±0.00 [0.00%]	±0.00 [0.00%]	±0.00 [0.00%]
alpha_VJets_qsf	±4.03 [3.5%]	±6.79 [3.7%]	±6.28 [3.9%]	±0.00 [0.00%]	±0.00 [0.00%]	±0.00 [0.00%]
alpha_single top_Theory	±3.94 [3.4%]	±4.73 [2.6%]	±5.19 [3.2%]	±0.00 [0.00%]	±0.00 [0.00%]	±0.00 [0.00%]
alpha_PRW	±3.36 [2.9%]	±1.85 [1.0%]	±3.71 [2.3%]	±0.80 [1.2%]	±0.34 [0.24%]	±4.17 [6.0%]
alpha_JES_NP1	±3.34 [2.9%]	±5.02 [2.7%]	±4.67 [2.9%]	±3.65 [5.6%]	±1.74 [1.2%]	±10.35 [15.0%]
alpha_FT_Light	±3.07 [2.7%]	±3.90 [2.1%]	±3.88 [2.4%]	±0.64 [0.99%]	±0.38 [0.27%]	±0.57 [0.83%]
alpha_VJets_ckkw	±2.90 [2.5%]	±5.25 [2.9%]	±4.34 [2.7%]	±0.00 [0.00%]	±0.00 [0.00%]	±0.00 [0.00%]
alpha_VV_renorm	±2.57 [2.2%]	±4.39 [2.4%]	±3.42 [2.1%]	±1.15 [1.8%]	±3.16 [2.2%]	±0.32 [0.46%]
alpha_Ttbar_Generator	±2.30 [2.0%]	±2.73 [1.5%]	±2.64 [1.6%]	±0.00 [0.00%]	±0.00 [0.00%]	±0.00 [0.00%]
alpha_VV_fac	±2.06 [1.8%]	±3.52 [1.9%]	±2.74 [1.7%]	±0.12 [0.19%]	±0.33 [0.23%]	±0.03 [0.05%]
alpha_JET_EtaCalib	±1.88 [1.6%]	±2.04 [1.1%]	±1.54 [0.96%]	±0.55 [0.85%]	±1.07 [0.76%]	±1.93 [2.8%]
alpha_JES_NP2	±1.56 [1.4%]	±4.29 [2.3%]	±2.05 [1.3%]	±0.86 [1.3%]	±1.18 [0.84%]	±3.34 [4.8%]
alpha_VV_qsf	±1.55 [1.3%]	±2.64 [1.4%]	±2.06 [1.3%]	±0.07 [0.11%]	±0.20 [0.14%]	±0.02 [0.03%]

Table F.3: Breakdown of the systematic uncertainties in the control and validation regions of SR2 after the background-only fit (continued in table F.4). Uncertainties can be correlated and do not necessarily add up in quadrature.

Uncertainty of channel	VR2 A	VR2 B	VR2 C	CR2 Z	CR2 W	CR2 Top
alpha_BGXSec	±1.10 [0.95%]	±2.00 [1.1%]	±1.50 [0.94%]	±0.67 [1.0%]	±1.93 [1.4%]	±0.29 [0.42%]
alpha_JES_NP3	±0.54 [0.47%]	±1.69 [0.93%]	±0.42 [0.27%]	±0.09 [0.13%]	±1.98 [1.4%]	±4.24 [6.1%]
alpha_Ttbar_Radiation	±0.36 [0.32%]	±0.43 [0.24%]	±0.42 [0.26%]	±0.00 [0.00%]	±0.00 [0.00%]	±0.00 [0.00%]
alpha_VJets_PDFSet	±0.33 [0.29%]	±0.49 [0.27%]	±0.46 [0.29%]	±0.15 [0.23%]	±0.42 [0.30%]	±0.05 [0.08%]
alpha_MET_Scale	±0.23 [0.20%]	±0.08 [0.05%]	±0.19 [0.12%]	±0.28 [0.44%]	±2.81 [2.0%]	±0.85 [1.2%]
alpha_FT_B	±0.23 [0.20%]	±0.18 [0.10%]	±0.27 [0.17%]	±0.02 [0.02%]	±1.53 [1.1%]	±0.92 [1.3%]
alpha_FT_Ex	±0.19 [0.17%]	±0.20 [0.11%]	±0.51 [0.32%]	±0.10 [0.15%]	±0.17 [0.12%]	±0.00 [0.00%]
alpha_VJets_AlphaS	±0.05 [0.04%]	±0.81 [0.44%]	±0.55 [0.34%]	±0.02 [0.02%]	±0.46 [0.33%]	±0.04 [0.05%]
alpha_JER	±0.01 [0.01%]	±0.07 [0.04%]	±0.08 [0.05%]	±0.02 [0.03%]	±0.03 [0.02%]	±0.10 [0.15%]
alpha_FT_ExC	±0.01 [0.01%]	±0.32 [0.18%]	±0.13 [0.08%]	±0.07 [0.11%]	±1.47 [1.0%]	±0.71 [1.0%]
alpha_JVT	±0.00 [0.00%]	±0.01 [0.01%]	±0.02 [0.01%]	±0.17 [0.26%]	±0.10 [0.07%]	±0.35 [0.50%]
gamma_stat_CR2 W	±0.00 [0.00%]	±0.00 [0.00%]	±0.00 [0.00%]	±0.00 [0.00%]	±7.69 [5.5%]	±0.00 [0.00%]
alpha_MET_ResoPerp	±0.00 [0.00%]	±0.00 [0.00%]	±0.00 [0.00%]	±0.00 [0.00%]	±0.00 [0.00%]	±0.00 [0.00%]
gamma_stat_VR2C	±0.00 [0.00%]	±0.00 [0.00%]	±5.79 [3.6%]	±0.00 [0.00%]	±0.00 [0.00%]	±0.00 [0.00%]
gamma_stat_VR2B	±0.00 [0.00%]	±6.91 [3.8%]	±0.00 [0.00%]	±0.00 [0.00%]	±0.00 [0.00%]	±0.00 [0.00%]
gamma_stat_SR	±0.00 [0.00%]	±0.00 [0.00%]	±0.00 [0.00%]	±0.00 [0.00%]	±0.00 [0.00%]	±0.00 [0.00%]
gamma_stat_CR2 Z	±0.00 [0.00%]	±0.00 [0.00%]	±0.00 [0.00%]	±2.27 [3.5%]	±0.00 [0.00%]	±0.00 [0.00%]
alpha_MET_ResoPara	±0.00 [0.00%]	±0.00 [0.00%]	±0.00 [0.00%]	±0.00 [0.00%]	±0.00 [0.00%]	±0.00 [0.00%]
gamma_stat_CR2 Top	±0.00 [0.00%]	±0.00 [0.00%]	±0.00 [0.00%]	±0.00 [0.00%]	±0.00 [0.00%]	±3.79 [5.5%]

Table F.4: Breakdown of the systematic uncertainties in the control and validation regions of SR2 after the background-only fit(continuation of table F.3). Uncertainties can be correlated and do not necessarily add up in quadrature.

Uncertainty of channel	VR3 A	VR3 B	VR3 C	CR3 Z	CR3 W	CR3 Top
Total background expectation	111.42	133.69	119.54	45.00	153.00	84.00
Total statistical ($\sqrt{N_{\text{exp}}}$)	±10.56	±11.56	±10.93	±6.71	±12.37	±9.17
Total background systematic	±29.97 [26.90%]	±41.33 [30.91%]	±29.94 [25.04%]	±6.81 [15.13%]	±12.29 [8.03%]	±9.66 [11.50%]
alpha_Ttbar_Generator	±21.38 [19.2%]	±21.77 [16.3%]	±21.21 [17.7%]	±0.00 [0.00%]	±0.00 [0.00%]	±0.00 [0.00%]
alpha_Ttbar_Shower	±13.42 [12.0%]	±13.67 [10.2%]	±13.31 [11.1%]	±0.00 [0.00%]	±0.00 [0.00%]	±0.00 [0.00%]
alpha_VJets_PDFInt	±10.90 [9.8%]	±33.76 [25.3%]	±9.12 [7.6%]	±1.37 [3.1%]	±16.23 [10.6%]	±2.96 [3.5%]
mu_Z	±9.64 [8.7%]	±12.28 [9.2%]	±9.97 [8.3%]	±8.46 [18.8%]	±0.20 [0.13%]	±0.03 [0.03%]
mu_Top	±9.60 [8.6%]	±9.71 [7.3%]	±9.55 [8.0%]	±0.17 [0.38%]	±10.04 [6.6%]	±18.52 [22.0%]
alpha_FT_C	±9.23 [8.3%]	±11.68 [8.7%]	±10.74 [9.0%]	±3.71 [8.2%]	±16.12 [10.5%]	±6.93 [8.2%]
mu_Wc	±8.60 [7.7%]	±10.47 [7.8%]	±9.92 [8.3%]	±0.00 [0.00%]	±29.58 [19.3%]	±8.48 [10.1%]
alpha_V_RenormFac	±7.47 [6.7%]	±9.37 [7.0%]	±8.20 [6.9%]	±0.00 [0.00%]	±0.00 [0.00%]	±0.00 [0.00%]
gamma_stat_VR3A	±4.81 [4.3%]	±0.00 [0.00%]	±0.00 [0.00%]	±0.00 [0.00%]	±0.00 [0.00%]	±0.00 [0.00%]
alpha_VJets_ckkw	±4.79 [4.3%]	±6.09 [4.6%]	±4.95 [4.1%]	±0.00 [0.00%]	±0.00 [0.00%]	±0.00 [0.00%]
alpha_JES_NP1	±4.03 [3.6%]	±3.16 [2.4%]	±2.59 [2.2%]	±2.36 [5.2%]	±2.09 [1.4%]	±9.93 [11.8%]
alpha_PRW	±3.18 [2.9%]	±3.56 [2.7%]	±3.04 [2.5%]	±0.01 [0.03%]	±0.93 [0.61%]	±0.34 [0.40%]
alpha_FT_Light	±2.75 [2.5%]	±2.66 [2.0%]	±2.28 [1.9%]	±0.21 [0.46%]	±0.29 [0.19%]	±0.65 [0.77%]
alpha_single top_Theory	±2.68 [2.4%]	±2.58 [1.9%]	±2.72 [2.3%]	±0.00 [0.00%]	±0.00 [0.00%]	±0.00 [0.00%]
alpha_VJets_qsf	±2.21 [2.0%]	±2.80 [2.1%]	±2.34 [2.0%]	±0.00 [0.00%]	±0.00 [0.00%]	±0.00 [0.00%]
alpha_JES_NP2	±1.92 [1.7%]	±2.46 [1.8%]	±1.48 [1.2%]	±0.61 [1.4%]	±2.99 [2.0%]	±1.21 [1.4%]
alpha_BGXSec	±1.02 [0.91%]	±1.29 [0.97%]	±1.23 [1.0%]	±0.54 [1.2%]	±1.57 [1.0%]	±0.60 [0.72%]
alpha_JES_NP3	±0.90 [0.80%]	±0.84 [0.63%]	±0.98 [0.82%]	±0.72 [1.6%]	±1.88 [1.2%]	±1.01 [1.2%]
alpha_VV_qsf	±0.89 [0.80%]	±1.04 [0.78%]	±1.03 [0.86%]	±0.25 [0.54%]	±0.65 [0.42%]	±0.20 [0.24%]
alpha_Ttbar_Radiation	±0.71 [0.64%]	±0.73 [0.54%]	±0.71 [0.59%]	±0.00 [0.00%]	±0.00 [0.00%]	±0.00 [0.00%]

Table F.5: Breakdown of the systematic uncertainties in the control and validation regions of SR3 after the background-only fit (continued in table F.6). Uncertainties can be correlated and do not necessarily add up in quadrature.

Uncertainty of channel	VR3 A	VR3 B	VR3 C	CR3 Z	CR3 W	CR3 Top
alpha_VV_fac	±0.55 [0.50%]	±0.65 [0.48%]	±0.64 [0.54%]	±0.14 [0.32%]	±0.38 [0.25%]	±0.12 [0.14%]
alpha_VJets_PDFSet	±0.37 [0.33%]	±0.47 [0.35%]	±0.37 [0.31%]	±0.00 [0.01%]	±0.19 [0.12%]	±0.06 [0.08%]
alpha_JET_EtaCalib	±0.29 [0.26%]	±1.50 [1.1%]	±0.73 [0.61%]	±0.36 [0.79%]	±0.24 [0.16%]	±1.17 [1.4%]
alpha_MET_Scale	±0.29 [0.26%]	±0.10 [0.07%]	±0.16 [0.13%]	±0.05 [0.12%]	±0.56 [0.37%]	±0.05 [0.06%]
alpha_VV_renorm	±0.29 [0.26%]	±0.34 [0.25%]	±0.33 [0.28%]	±0.40 [0.88%]	±1.04 [0.68%]	±0.32 [0.38%]
alpha_FT_Ex	±0.22 [0.20%]	±0.22 [0.16%]	±0.31 [0.26%]	±0.12 [0.27%]	±0.41 [0.27%]	±0.05 [0.05%]
alpha_FT_ExC	±0.18 [0.16%]	±0.03 [0.02%]	±0.05 [0.04%]	±0.02 [0.05%]	±0.73 [0.48%]	±0.08 [0.09%]
alpha_FT_B	±0.13 [0.11%]	±0.09 [0.07%]	±0.11 [0.09%]	±0.05 [0.11%]	±0.52 [0.34%]	±0.61 [0.73%]
alpha_JVT	±0.02 [0.02%]	±0.03 [0.02%]	±0.02 [0.01%]	±0.07 [0.15%]	±0.17 [0.11%]	±0.41 [0.49%]
alpha_JER	±0.02 [0.01%]	±0.02 [0.01%]	±0.01 [0.01%]	±0.00 [0.00%]	±0.00 [0.00%]	±0.02 [0.02%]
alpha_VJets_AlphaS	±0.01 [0.01%]	±0.82 [0.61%]	±0.63 [0.53%]	±0.01 [0.03%]	±0.27 [0.18%]	±0.16 [0.19%]
alpha_MET_ResoPerp	±0.00 [0.00%]	±0.00 [0.00%]	±0.00 [0.00%]	±0.00 [0.00%]	±0.00 [0.00%]	±0.00 [0.00%]
alpha_MET_ResoPara	±0.00 [0.00%]	±0.00 [0.00%]	±0.00 [0.00%]	±0.00 [0.00%]	±0.00 [0.00%]	±0.00 [0.00%]
gamma_stat_CR3 W	±0.00 [0.00%]	±0.00 [0.00%]	±0.00 [0.00%]	±0.00 [0.00%]	±7.62 [5.0%]	±0.00 [0.00%]
gamma_stat_VR3C	±0.00 [0.00%]	±0.00 [0.00%]	±5.08 [4.2%]	±0.00 [0.00%]	±0.00 [0.00%]	±0.00 [0.00%]
gamma_stat_VR3B	±0.00 [0.00%]	±5.50 [4.1%]	±0.00 [0.00%]	±0.00 [0.00%]	±0.00 [0.00%]	±0.00 [0.00%]
gamma_stat_SR	±0.00 [0.00%]	±0.00 [0.00%]	±0.00 [0.00%]	±0.00 [0.00%]	±0.00 [0.00%]	±0.00 [0.00%]
gamma_stat_CR3 Z	±0.00 [0.00%]	±0.00 [0.00%]	±0.00 [0.00%]	±1.46 [3.2%]	±0.00 [0.00%]	±0.00 [0.00%]
gamma_stat_CR3 Top	±0.00 [0.00%]	±0.00 [0.00%]	±0.00 [0.00%]	±0.00 [0.00%]	±0.00 [0.00%]	±5.09 [6.1%]

Table F.6: Breakdown of the systematic uncertainties in the control and validation regions of SR3 after the background-only fit(continuation of table F.5). Uncertainties can be correlated and do not necessarily add up in quadrature.

Uncertainty of channel	VR4 A	VR4 B	VR4 C	CR4 Z	CR4 W	CR4 Top
Total background expectation	105.22	149.20	134.45	54.00	179.01	71.00
Total statistical ($\sqrt{N_{\text{exp}}}$)	±10.26	±12.21	±11.60	±7.35	±13.38	±8.43
Total background systematic	±18.46 [17.54%]	±24.63 [16.51%]	±22.70 [16.88%]	±7.66 [14.18%]	±13.48 [7.53%]	±8.43 [11.87%]
alpha_FT_C	±9.31 [8.8%]	±14.32 [9.6%]	±12.79 [9.5%]	±4.37 [8.1%]	±18.59 [10.4%]	±6.23 [8.8%]
mu_Z	±8.85 [8.4%]	±13.55 [9.1%]	±11.09 [8.2%]	±9.93 [18.4%]	±0.30 [0.17%]	±0.01 [0.02%]
alpha_Ttbar_Shower	±8.36 [7.9%]	±9.49 [6.4%]	±9.29 [6.9%]	±0.00 [0.00%]	±0.00 [0.00%]	±0.00 [0.00%]
mu_Wc	±7.89 [7.5%]	±10.79 [7.2%]	±10.95 [8.1%]	±0.00 [0.00%]	±33.15 [18.5%]	±6.58 [9.3%]
alpha_VJets_PDFInt	±7.69 [7.3%]	±9.23 [6.2%]	±10.05 [7.5%]	±1.89 [3.5%]	±19.21 [10.7%]	±3.51 [4.9%]
mu_Top	±7.68 [7.3%]	±8.72 [5.8%]	±8.50 [6.3%]	±0.00 [0.00%]	±10.42 [5.8%]	±15.40 [21.7%]
alpha_V_RenormFac	±6.48 [6.2%]	±9.48 [6.4%]	±8.62 [6.4%]	±0.00 [0.00%]	±0.00 [0.00%]	±0.00 [0.00%]
alpha_VJets_qsf	±6.30 [6.0%]	±9.04 [6.1%]	±8.57 [6.4%]	±0.00 [0.00%]	±0.00 [0.00%]	±0.00 [0.00%]
alpha_VJets_ckkw	±6.04 [5.7%]	±8.92 [6.0%]	±7.94 [5.9%]	±0.00 [0.00%]	±0.00 [0.00%]	±0.00 [0.00%]
alpha_Ttbar_Generator	±4.61 [4.4%]	±5.23 [3.5%]	±5.11 [3.8%]	±0.00 [0.00%]	±0.00 [0.00%]	±0.00 [0.00%]
gamma_stat_VR4A	±4.50 [4.3%]	±0.00 [0.00%]	±0.00 [0.00%]	±0.00 [0.00%]	±0.00 [0.00%]	±0.00 [0.00%]
alpha_VJets_HF	±3.95 [3.8%]	±5.40 [3.6%]	±5.48 [4.1%]	±0.00 [0.00%]	±0.00 [0.00%]	±0.00 [0.00%]
alpha_JES_NP1	±3.57 [3.4%]	±5.11 [3.4%]	±4.23 [3.1%]	±2.81 [5.2%]	±5.92 [3.3%]	±9.30 [13.1%]
alpha_PRW	±2.96 [2.8%]	±2.41 [1.6%]	±3.07 [2.3%]	±0.47 [0.87%]	±6.17 [3.4%]	±0.97 [1.4%]
alpha_FT_Light	±2.44 [2.3%]	±3.03 [2.0%]	±3.02 [2.2%]	±0.79 [1.5%]	±2.48 [1.4%]	±0.14 [0.20%]
alpha_single top_Theory	±2.00 [1.9%]	±2.26 [1.5%]	±2.14 [1.6%]	±0.00 [0.00%]	±0.00 [0.00%]	±0.00 [0.00%]
alpha_VV_qsf	±1.69 [1.6%]	±2.68 [1.8%]	±2.23 [1.7%]	±0.35 [0.65%]	±0.68 [0.38%]	±0.23 [0.33%]
alpha_JES_NP2	±1.34 [1.3%]	±2.34 [1.6%]	±1.44 [1.1%]	±0.99 [1.8%]	±3.24 [1.8%]	±1.16 [1.6%]
alpha_JES_NP3	±1.21 [1.2%]	±1.09 [0.73%]	±1.52 [1.1%]	±0.71 [1.3%]	±2.08 [1.2%]	±0.32 [0.45%]
alpha_VV_fac	±1.12 [1.1%]	±1.77 [1.2%]	±1.47 [1.1%]	±0.06 [0.12%]	±0.12 [0.07%]	±0.04 [0.06%]

Table F.7: Breakdown of the systematic uncertainties in the control and validation regions of SR4 after the background-only fit (continued in table F.8). Uncertainties can be correlated and do not necessarily add up in quadrature.

Uncertainty of channel	VR4 A	VR4 B	VR4 C	CR4 Z	CR4 W	CR4 Top
alpha_BGXSec	±1.05 [1.00%]	±1.81 [1.2%]	±1.44 [1.1%]	±0.56 [1.0%]	±1.22 [0.68%]	±0.54 [0.76%]
alpha_VV_renorm	±0.65 [0.62%]	±1.04 [0.70%]	±0.86 [0.64%]	±0.02 [0.04%]	±0.05 [0.03%]	±0.02 [0.02%]
alpha_VJets_AlphaS	±0.56 [0.54%]	±0.78 [0.52%]	±0.62 [0.46%]	±0.00 [0.01%]	±0.19 [0.11%]	±0.13 [0.19%]
alpha_Ttbar_Radiation	±0.39 [0.37%]	±0.45 [0.30%]	±0.44 [0.32%]	±0.00 [0.00%]	±0.00 [0.00%]	±0.00 [0.00%]
alpha_FT_Ex	±0.39 [0.37%]	±0.49 [0.33%]	±0.69 [0.51%]	±0.29 [0.54%]	±1.12 [0.62%]	±0.24 [0.34%]
alpha_JET_EtaCalib	±0.37 [0.35%]	±0.60 [0.40%]	±1.36 [1.0%]	±0.46 [0.86%]	±0.85 [0.48%]	±0.44 [0.61%]
alpha_VJets_PDFSet	±0.33 [0.31%]	±0.47 [0.31%]	±0.43 [0.32%]	±0.02 [0.04%]	±0.25 [0.14%]	±0.11 [0.16%]
alpha_MET_Scale	±0.20 [0.19%]	±0.00 [0.00%]	±0.51 [0.38%]	±0.39 [0.72%]	±0.61 [0.34%]	±0.22 [0.31%]
alpha_FT_B	±0.17 [0.17%]	±0.16 [0.11%]	±0.26 [0.20%]	±0.03 [0.06%]	±0.74 [0.41%]	±0.72 [1.0%]
alpha_FT_ExC	±0.16 [0.15%]	±0.21 [0.14%]	±0.02 [0.02%]	±0.02 [0.03%]	±0.37 [0.21%]	±0.01 [0.02%]
alpha_JVT	±0.02 [0.02%]	±0.05 [0.03%]	±0.00 [0.00%]	±0.08 [0.16%]	±0.18 [0.10%]	±0.32 [0.45%]
alpha_JER	±0.00 [0.00%]	±0.00 [0.00%]	±0.00 [0.00%]	±0.00 [0.00%]	±0.00 [0.00%]	±0.00 [0.00%]
alpha_MET_ResoPerp	±0.00 [0.00%]	±0.00 [0.00%]	±0.00 [0.00%]	±0.00 [0.00%]	±0.00 [0.00%]	±0.00 [0.00%]
alpha_MET_ResoPara	±0.00 [0.00%]	±0.00 [0.00%]	±0.00 [0.00%]	±0.00 [0.00%]	±0.00 [0.00%]	±0.00 [0.00%]
gamma_stat_CR4 W	±0.00 [0.00%]	±0.00 [0.00%]	±0.00 [0.00%]	±0.00 [0.00%]	±6.88 [3.8%]	±0.00 [0.00%]
gamma_stat_VR4C	±0.00 [0.00%]	±0.00 [0.00%]	±4.99 [3.7%]	±0.00 [0.00%]	±0.00 [0.00%]	±0.00 [0.00%]
gamma_stat_VR4B	±0.00 [0.00%]	±5.82 [3.9%]	±0.00 [0.00%]	±0.00 [0.00%]	±0.00 [0.00%]	±0.00 [0.00%]
gamma_stat_SR	±0.00 [0.00%]	±0.00 [0.00%]	±0.00 [0.00%]	±0.00 [0.00%]	±0.00 [0.00%]	±0.00 [0.00%]
gamma_stat_CR4 Z	±0.00 [0.00%]	±0.00 [0.00%]	±0.00 [0.00%]	±1.62 [3.0%]	±0.00 [0.00%]	±0.00 [0.00%]
gamma_stat_CR4 Top	±0.00 [0.00%]	±0.00 [0.00%]	±0.00 [0.00%]	±0.00 [0.00%]	±0.00 [0.00%]	±4.35 [6.1%]

Table F.8: Breakdown of the systematic uncertainties in the control and validation regions of SR4 after the background-only fit(continuation of table F.7). Uncertainties can be correlated and do not necessarily add up in quadrature.

Uncertainty of channel	VR5 A	VR5 B	CR5 Z	CR5 W	CR5 Top
Total background expectation	464.58	497.31	54.99	192.00	60.00
Total statistical ($\sqrt{N_{\text{exp}}}$)	±21.55	±22.30	±7.42	±13.86	±7.75
Total background systematic	±59.41 [12.79%]	±67.44 [13.56%]	±7.97 [14.49%]	±14.07 [7.33%]	±8.42 [14.04%]
alpha_FT_Light	±47.03 [10.1%]	±55.52 [11.2%]	±3.35 [6.1%]	±13.53 [7.0%]	±2.35 [3.9%]
mu_Z	±46.92 [10.1%]	±53.84 [10.8%]	±10.62 [19.3%]	±0.32 [0.17%]	±0.03 [0.05%]
mu_Wc	±34.75 [7.5%]	±34.45 [6.9%]	±0.00 [0.00%]	±34.79 [18.1%]	±4.17 [7.0%]
alpha_FT_C	±34.03 [7.3%]	±36.94 [7.4%]	±3.78 [6.9%]	±17.44 [9.1%]	±4.92 [8.2%]
alpha_V_RenormFac	±28.32 [6.1%]	±29.81 [6.0%]	±0.00 [0.00%]	±0.00 [0.00%]	±0.00 [0.00%]
alpha_VJets_PDFInt	±25.62 [5.5%]	±28.34 [5.7%]	±1.91 [3.5%]	±15.31 [8.0%]	±2.02 [3.4%]
mu_Top	±23.81 [5.1%]	±23.87 [4.8%]	±0.26 [0.47%]	±12.12 [6.3%]	±15.25 [25.4%]
alpha_VJets_ckkw	±20.52 [4.4%]	±22.14 [4.5%]	±0.00 [0.00%]	±0.00 [0.00%]	±0.00 [0.00%]
alpha_JES_NP1	±17.71 [3.8%]	±23.58 [4.7%]	±1.89 [3.4%]	±1.09 [0.57%]	±8.16 [13.6%]
gamma_stat_VR5A	±12.81 [2.8%]	±0.00 [0.00%]	±0.00 [0.00%]	±0.00 [0.00%]	±0.00 [0.00%]
alpha_PRW	±9.39 [2.0%]	±3.14 [0.63%]	±2.08 [3.8%]	±3.60 [1.9%]	±1.86 [3.1%]
alpha_JES_NP2	±9.24 [2.0%]	±13.13 [2.6%]	±0.94 [1.7%]	±1.44 [0.75%]	±3.26 [5.4%]
alpha_single top_Theory	±8.99 [1.9%]	±7.79 [1.6%]	±0.00 [0.00%]	±0.00 [0.00%]	±0.00 [0.00%]
alpha_VV_qsf	±7.59 [1.6%]	±8.08 [1.6%]	±0.87 [1.6%]	±1.55 [0.81%]	±0.27 [0.45%]
alpha_FT_Ex	±5.62 [1.2%]	±6.12 [1.2%]	±0.57 [1.0%]	±2.43 [1.3%]	±0.56 [0.93%]
alpha_JET_EtaCalib	±5.20 [1.1%]	±4.01 [0.81%]	±0.71 [1.3%]	±1.71 [0.89%]	±1.28 [2.1%]
alpha_Ttbar_Generator	±5.06 [1.1%]	±5.19 [1.0%]	±0.00 [0.00%]	±0.00 [0.00%]	±0.00 [0.00%]
alpha_FT_B	±4.21 [0.91%]	±4.58 [0.92%]	±0.21 [0.39%]	±1.47 [0.77%]	±1.31 [2.2%]
alpha_JES_NP3	±4.09 [0.88%]	±2.69 [0.54%]	±0.18 [0.33%]	±0.51 [0.27%]	±0.57 [0.95%]

Table F.9: Breakdown of the systematic uncertainties in the control and validation regions of SR5 after the background-only fit (continued in table F.10). Uncertainties can be correlated and do not necessarily add up in quadrature.

Uncertainty of channel	VR5 A	VR5 B	CR5 Z	CR5 W	CR5 Top
alpha_BGXSec	±4.02 [0.87%]	±4.15 [0.83%]	±0.54 [0.97%]	±1.06 [0.55%]	±0.29 [0.48%]
alpha_VJets_qsf	±3.80 [0.82%]	±3.97 [0.80%]	±0.00 [0.00%]	±0.00 [0.00%]	±0.00 [0.00%]
alpha_Ttbar_Shower	±3.38 [0.73%]	±3.46 [0.70%]	±0.00 [0.00%]	±0.00 [0.00%]	±0.00 [0.00%]
alpha_MET_Scale	±1.27 [0.27%]	±2.12 [0.43%]	±0.47 [0.85%]	±0.68 [0.35%]	±0.84 [1.4%]
alpha_VJets_AlphaS	±1.21 [0.26%]	±1.58 [0.32%]	±0.12 [0.21%]	±0.78 [0.41%]	±0.04 [0.06%]
alpha_VJets_PDFSet	±1.15 [0.25%]	±1.42 [0.29%]	±0.03 [0.05%]	±0.17 [0.09%]	±0.08 [0.13%]
alpha_FT_ExC	±1.14 [0.25%]	±1.22 [0.25%]	±0.01 [0.01%]	±0.22 [0.12%]	±0.00 [0.01%]
alpha_VV_fac	±0.87 [0.19%]	±0.93 [0.19%]	±0.36 [0.66%]	±0.64 [0.33%]	±0.11 [0.19%]
alpha_VV_renorm	±0.70 [0.15%]	±0.74 [0.15%]	±0.00 [0.01%]	±0.01 [0.00%]	±0.00 [0.00%]
alpha_Ttbar_Radiation	±0.70 [0.15%]	±0.71 [0.14%]	±0.00 [0.00%]	±0.00 [0.00%]	±0.00 [0.00%]
alpha_JVT	±0.36 [0.08%]	±0.66 [0.13%]	±0.09 [0.17%]	±0.13 [0.07%]	±0.19 [0.32%]
alpha_JER	±0.00 [0.00%]	±0.00 [0.00%]	±0.00 [0.00%]	±0.00 [0.00%]	±0.00 [0.00%]
alpha_MET_ResoPerp	±0.00 [0.00%]	±0.00 [0.00%]	±0.00 [0.00%]	±0.00 [0.00%]	±0.00 [0.00%]
alpha_MET_ResoPara	±0.00 [0.00%]	±0.00 [0.00%]	±0.00 [0.00%]	±0.00 [0.00%]	±0.00 [0.00%]
gamma_stat_CR5 W	±0.00 [0.00%]	±0.00 [0.00%]	±0.00 [0.00%]	±13.29 [6.9%]	±0.00 [0.00%]
gamma_stat_VR5B	±0.00 [0.00%]	±14.10 [2.8%]	±0.00 [0.00%]	±0.00 [0.00%]	±0.00 [0.00%]
gamma_stat_SR	±0.00 [0.00%]	±0.00 [0.00%]	±0.00 [0.00%]	±0.00 [0.00%]	±0.00 [0.00%]
gamma_stat_CR5 Z	±0.00 [0.00%]	±0.00 [0.00%]	±1.88 [3.4%]	±0.00 [0.00%]	±0.00 [0.00%]
gamma_stat_CR5 Top	±0.00 [0.00%]	±0.00 [0.00%]	±0.00 [0.00%]	±0.00 [0.00%]	±3.36 [5.6%]

Table F.10: Breakdown of the systematic uncertainties in the control and validation regions of SR5 after the background-only fit(continuation of table F.9). Uncertainties can be correlated and do not necessarily add up in quadrature.

F.3. Background-only fit control region distributions

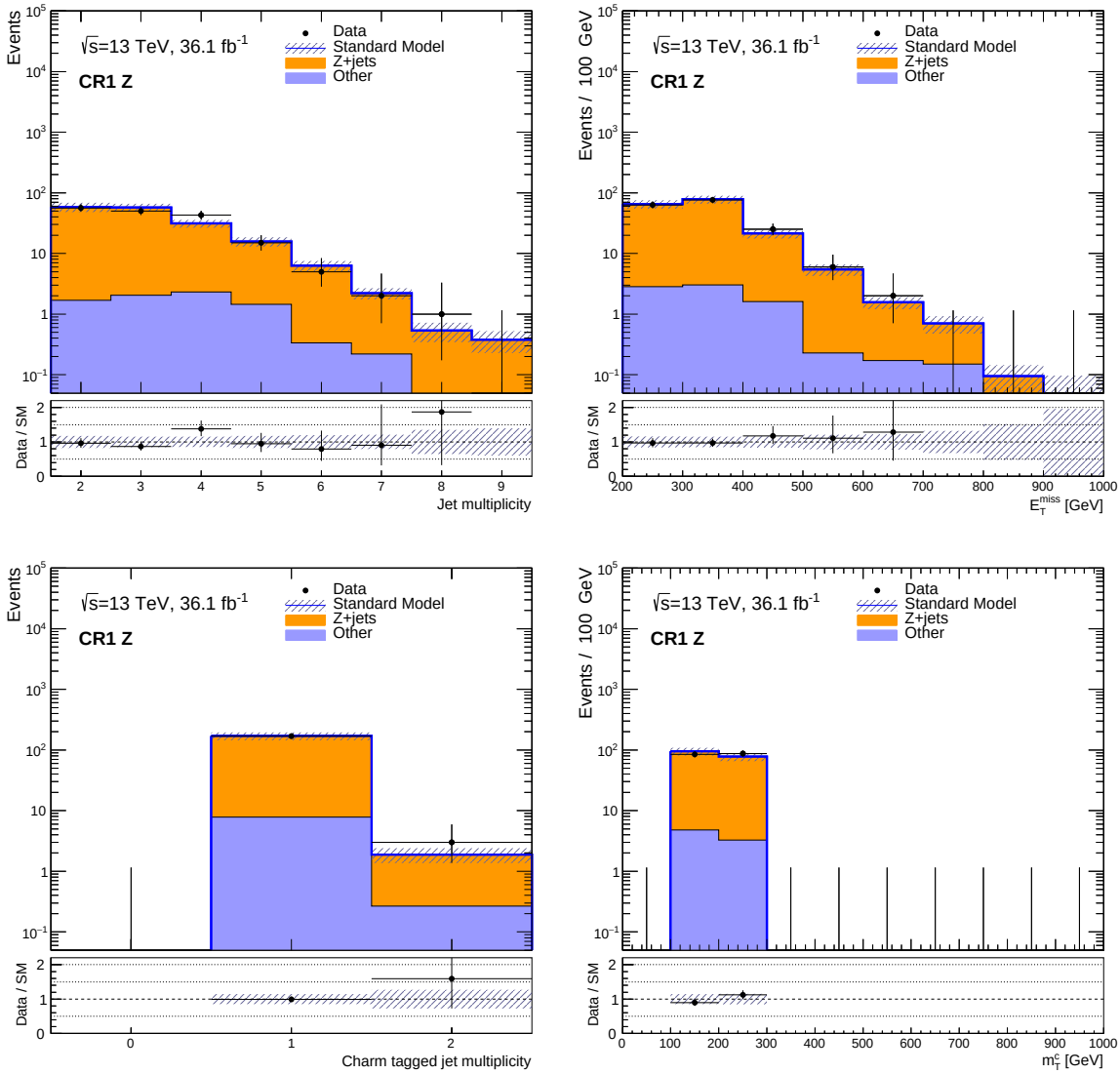

Figure F.6: Jet multiplicity (upper left), $E_{\mathrm{T}}^{\mathrm{miss}}$ (upper right), charm tagged jet multiplicity (lower left) and m_{T}^{c} (lower right) distributions in CR1 Z after the background-only fit. The shaded bands indicate the total uncertainty on the background prediction.

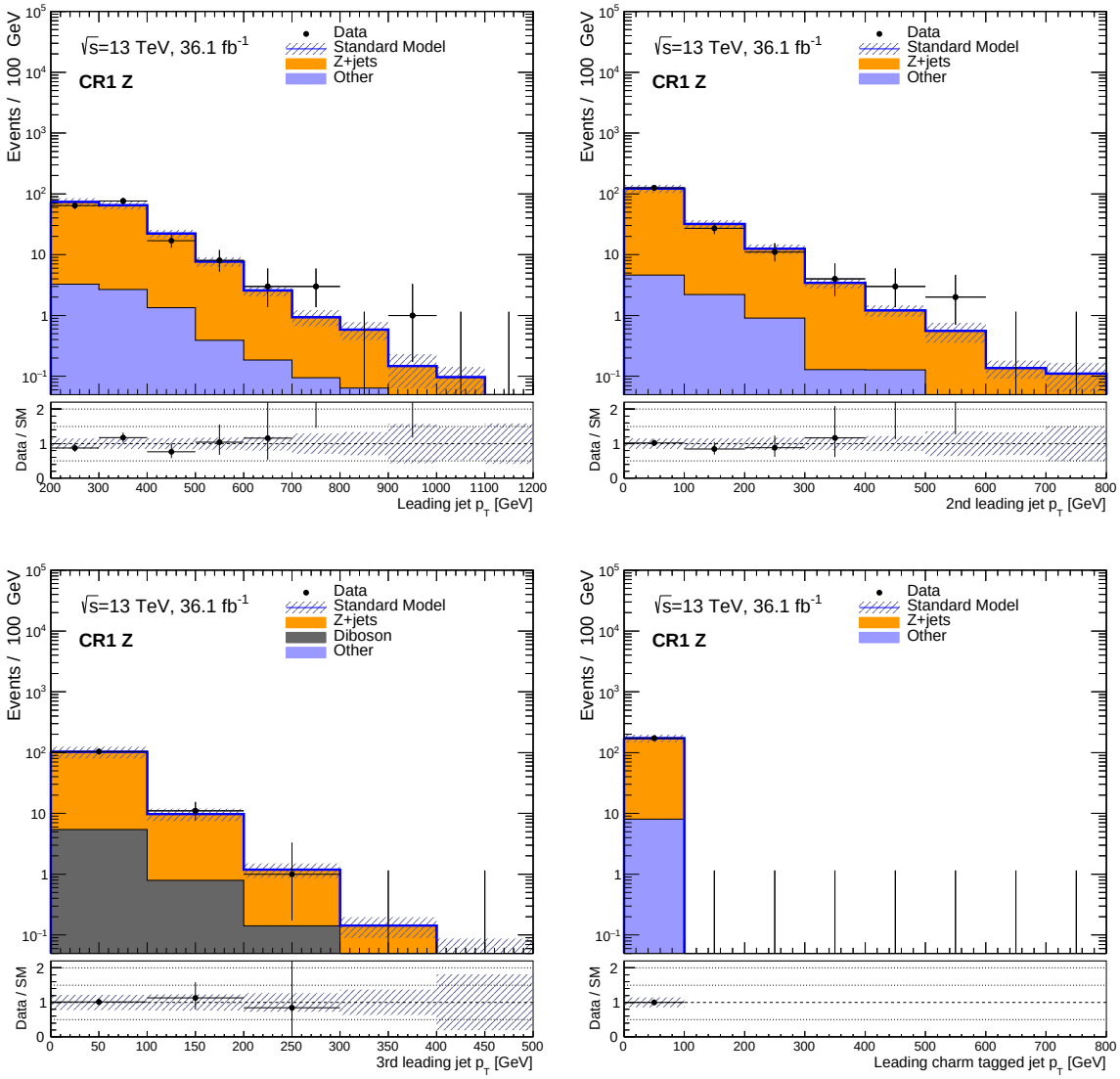

Figure F.7: Transverse momenta of the three leading jets (upper plots and lower left), and leading charm tagged jet p_{T} distributions in CR1 Z after the background-only fit. The shaded bands indicate the total uncertainty on the background prediction.

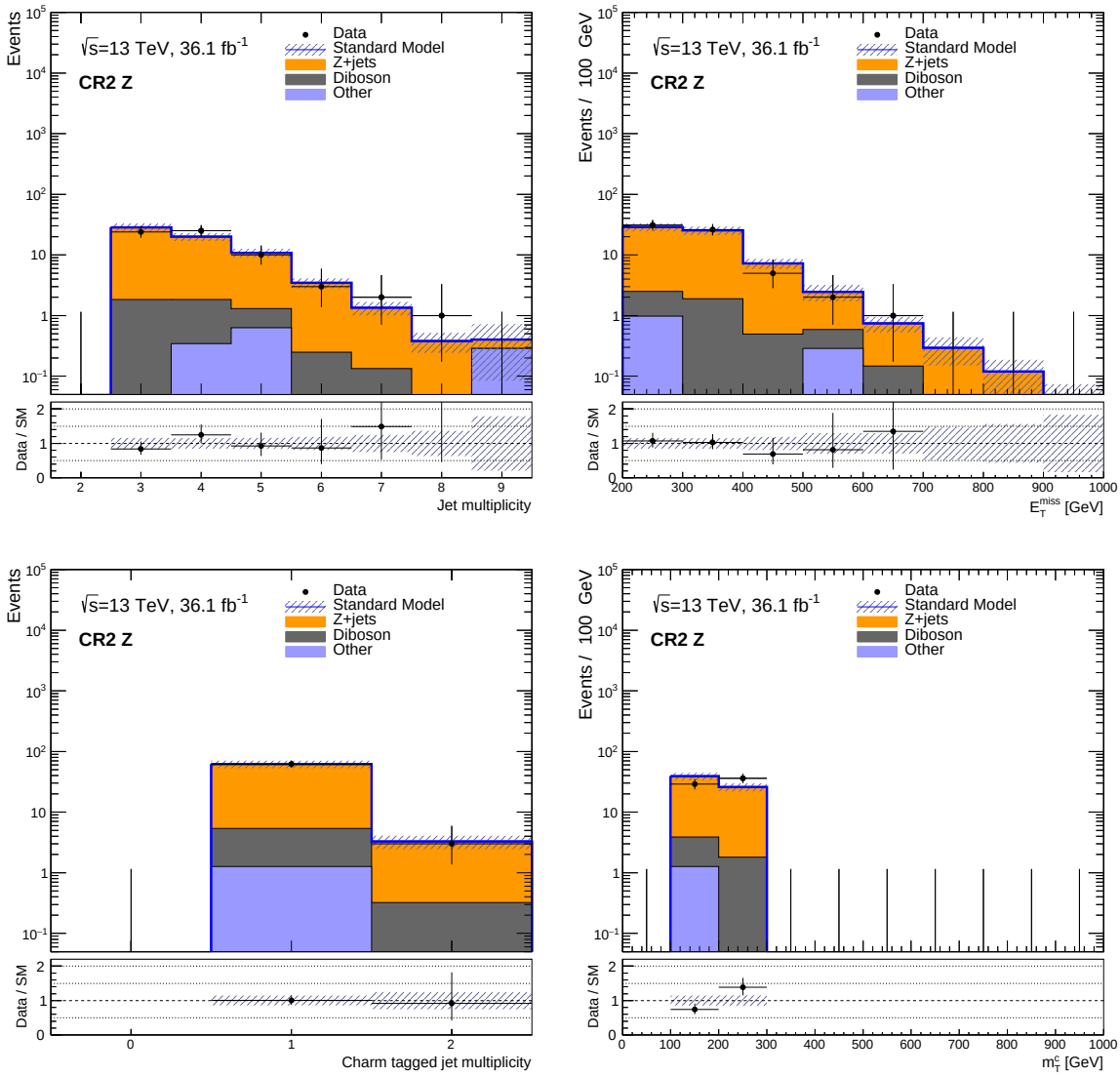

Figure F.8: Jet multiplicity (upper left), $E_{\mathrm{T}}^{\mathrm{miss}}$ (upper right), leading jet p_{T} (lower left) and m_{T}^{c} (lower right) distributions in CR2 Z after the background-only fit. The shaded bands indicate the total uncertainty on the background prediction.

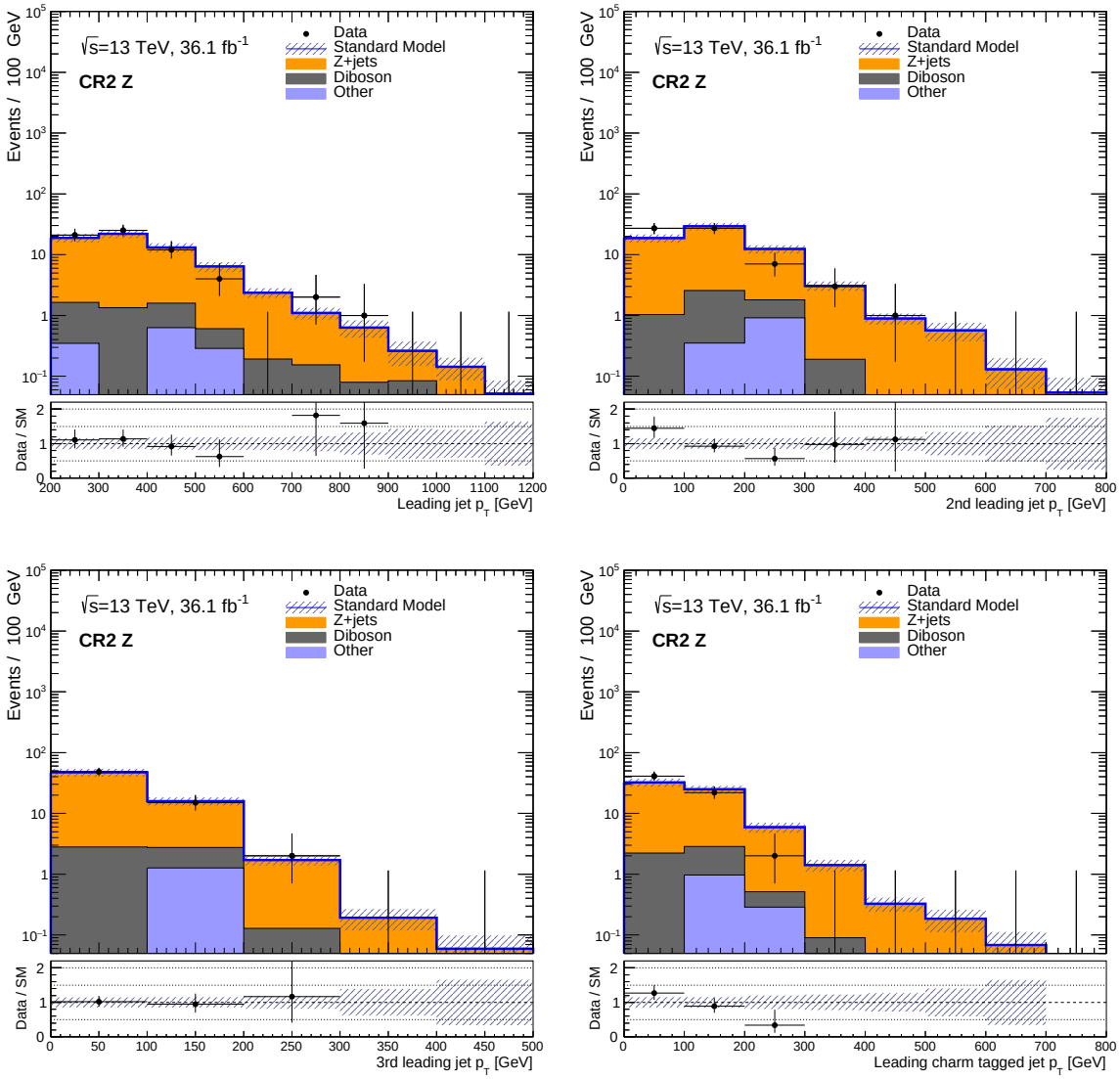

Figure F.9: Transverse momenta of the three leading jets (upper plots and lower left), and leading charm tagged jet p_{T} distributions in CR2 Z after the background-only fit. The shaded bands indicate the total uncertainty on the background prediction.

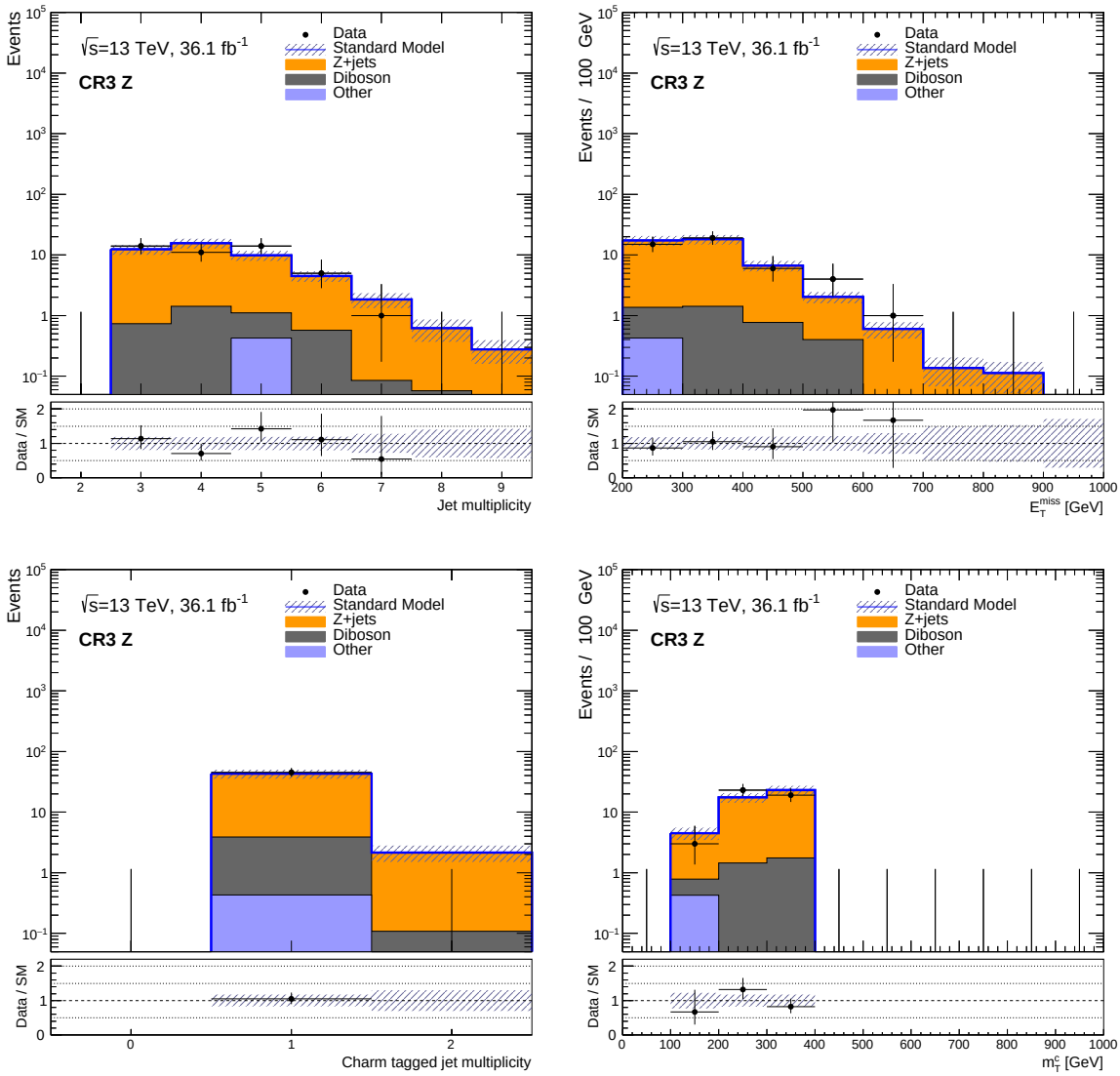

Figure F.10: Jet multiplicity (upper left), $E_{\mathrm{T}}^{\mathrm{miss}}$ (upper right), leading jet p_{T} (lower left) and m_{T}^{c} (lower right) distributions in CR3 Z after the background-only fit. The shaded bands indicate the total uncertainty on the background prediction.

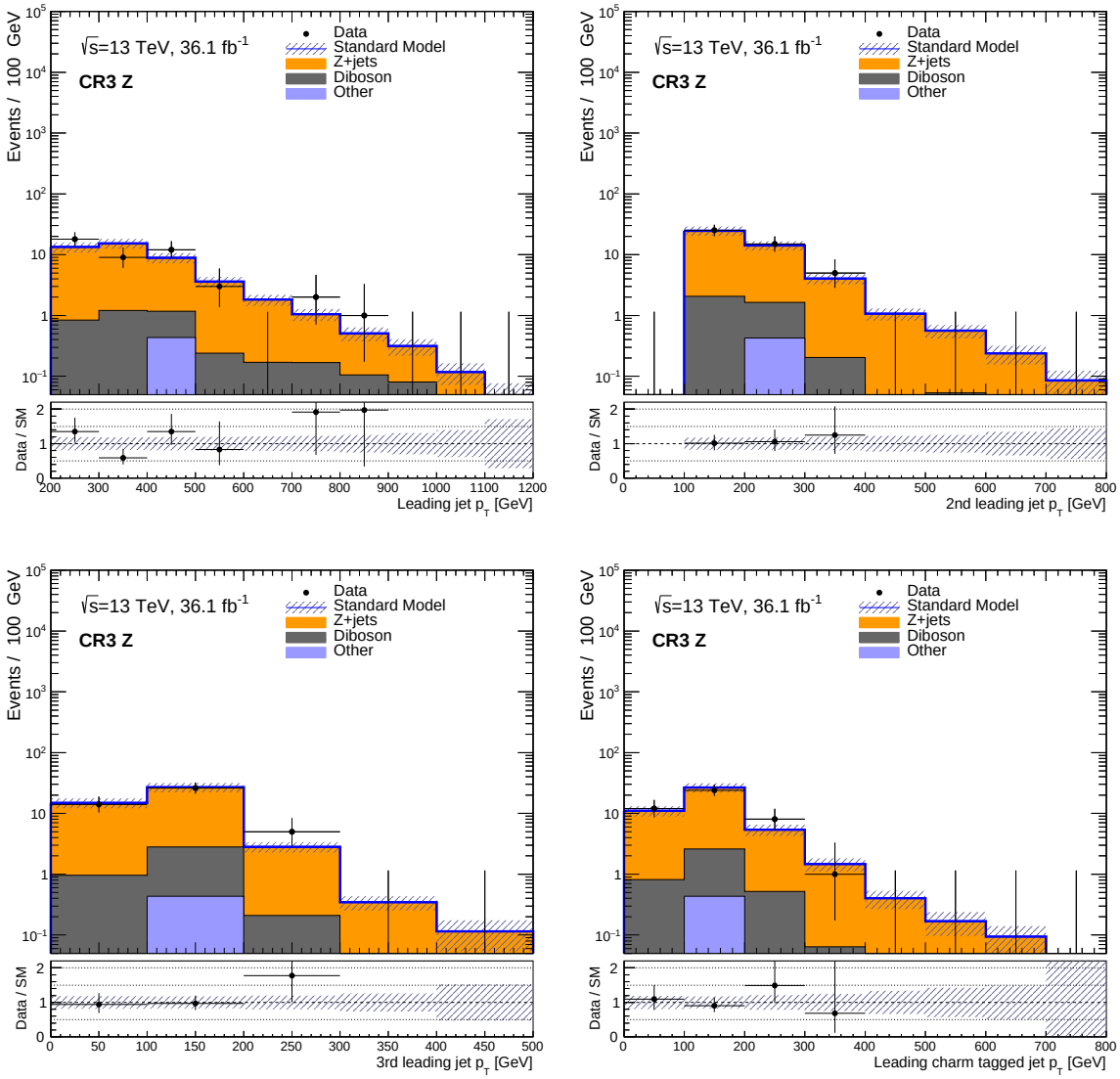

Figure F.11: Transverse momenta of the three leading jets (upper plots and lower left), and leading charm tagged jet p_{T} distributions in CR3 Z after the background-only fit. The shaded bands indicate the total uncertainty on the background prediction.

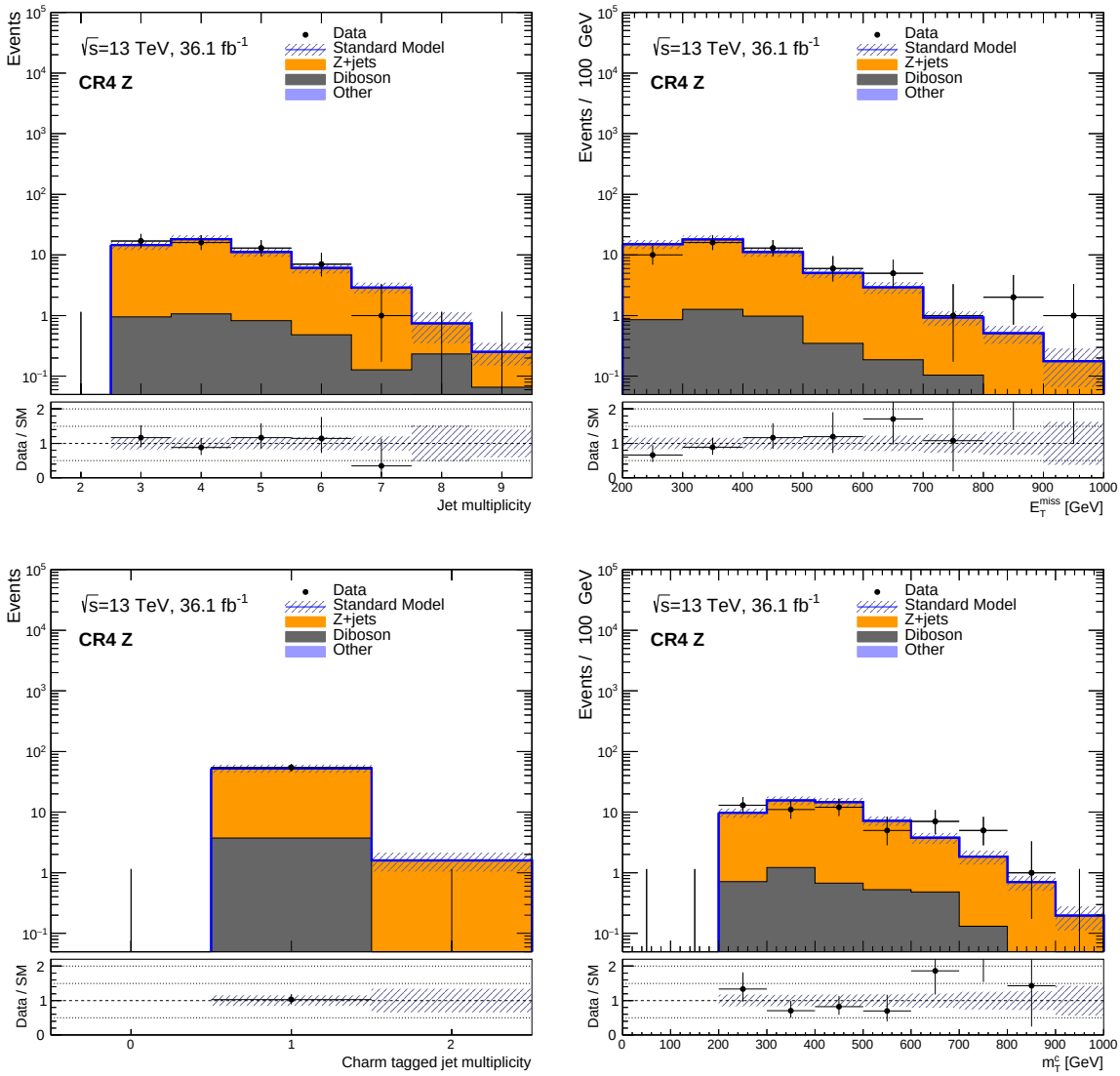

Figure F.12: Jet multiplicity (upper left), $E_{\mathrm{T}}^{\mathrm{miss}}$ (upper right), leading jet p_{T} (lower left) and m_{T}^{c} (lower right) distributions in CR4 Z after the background-only fit. The shaded bands indicate the total uncertainty on the background prediction.

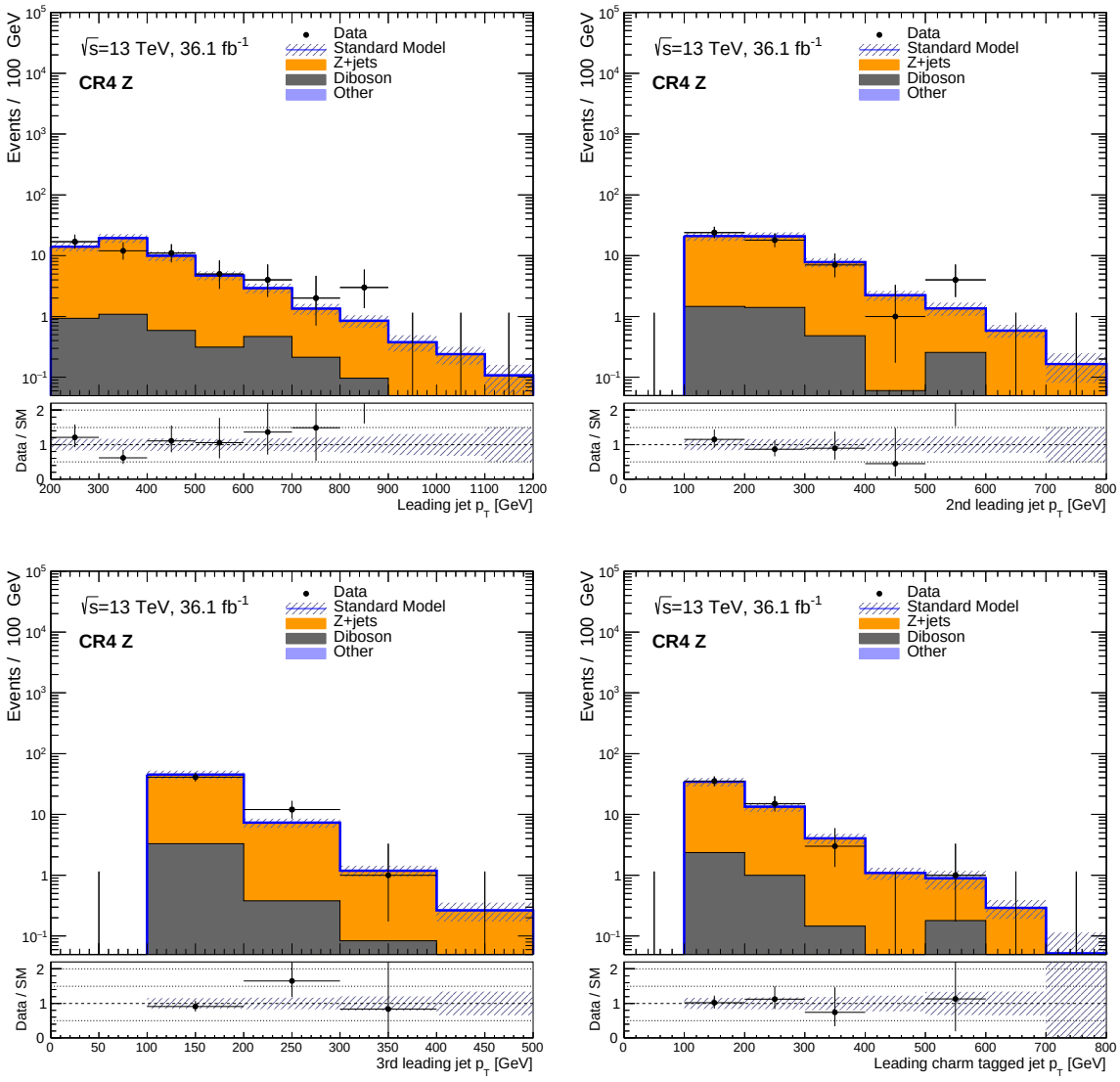

Figure F.13: Transverse momenta of the three leading jets (upper plots and lower left), and leading charm tagged jet p_{T} distributions in CR4 Z after the background-only fit. The shaded bands indicate the total uncertainty on the background prediction.

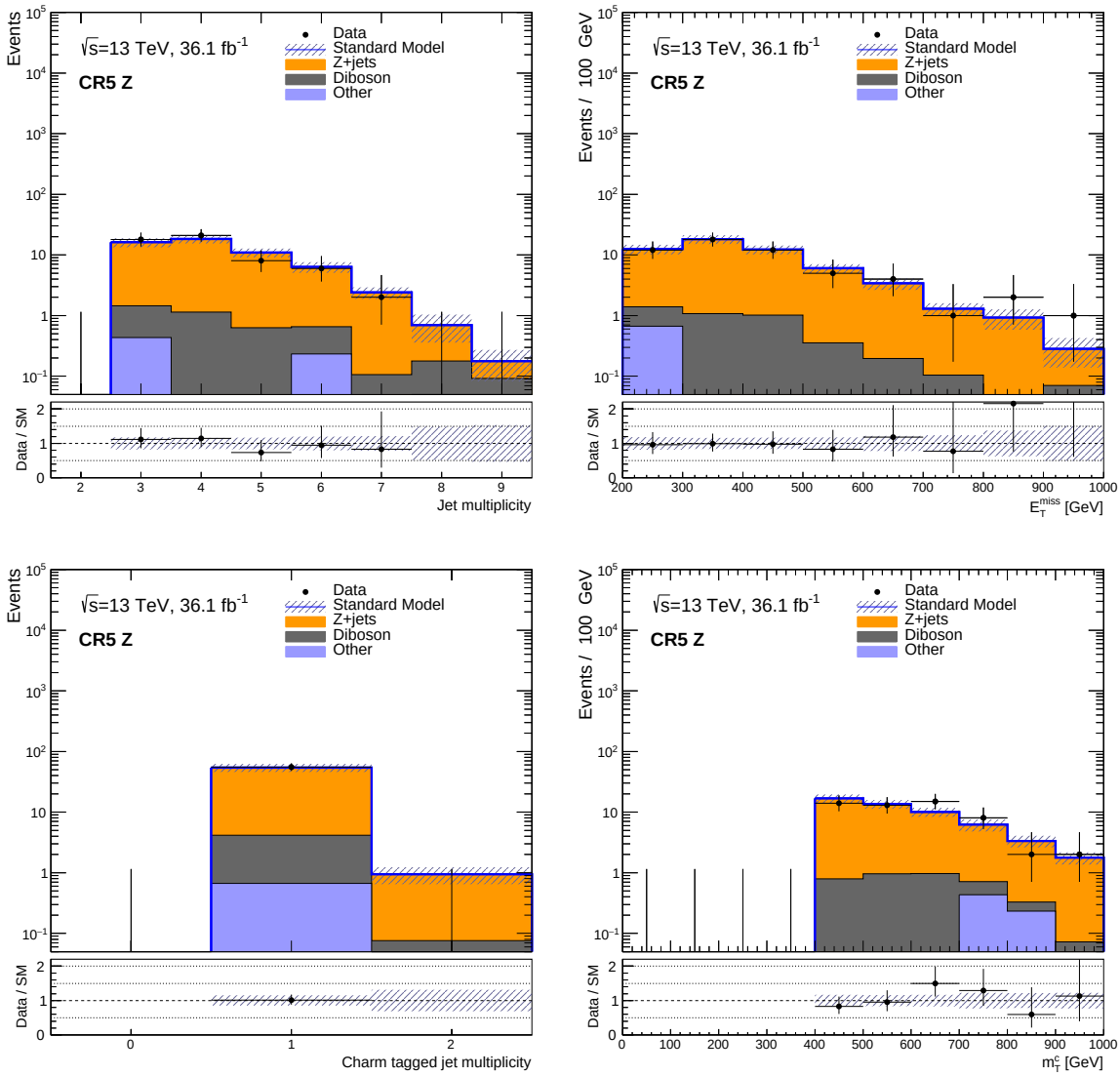

Figure F.14: Jet multiplicity (upper left), $E_{\mathrm{T}}^{\mathrm{miss}}$ (upper right), leading jet p_{T} (lower left) and m_{T}^{c} (lower right) distributions in CR5 Z after the background-only fit. The shaded bands indicate the total uncertainty on the background prediction.

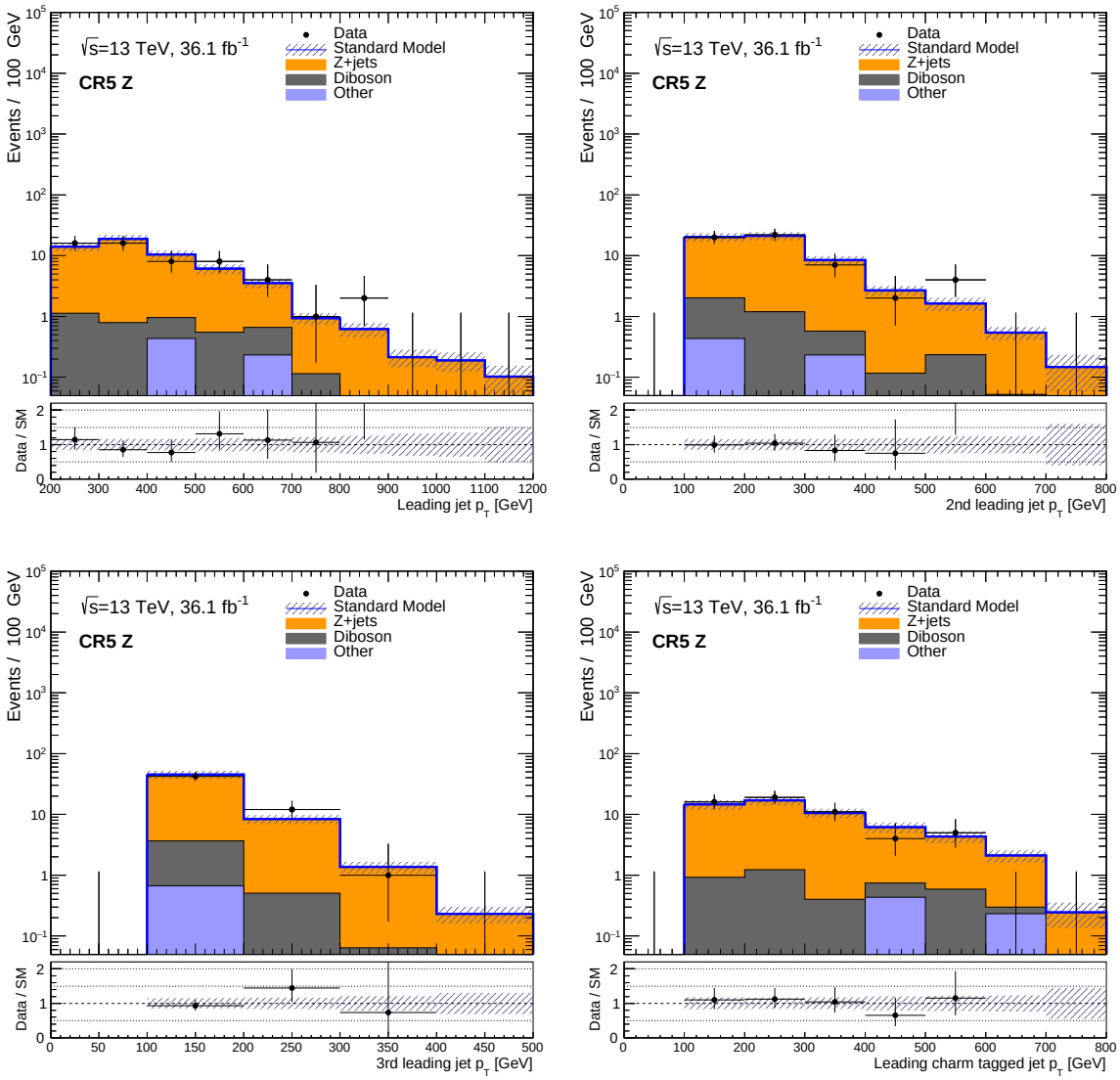

Figure F.15: Transverse momenta of the three leading jets (upper plots and lower left), and leading charm tagged jet p_{T} distributions in CR5 Z after the background-only fit. The shaded bands indicate the total uncertainty on the background prediction.

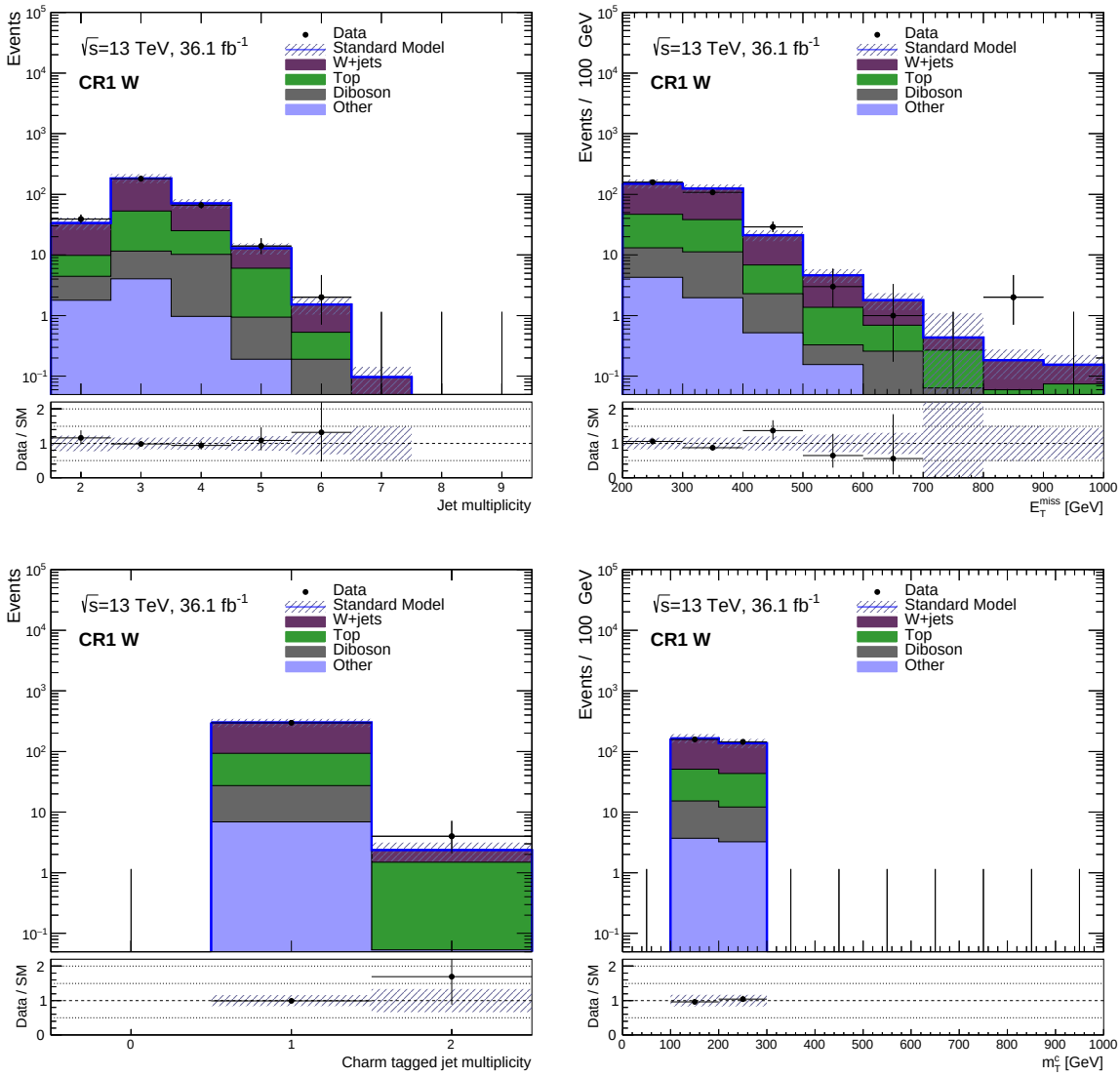

Figure F.16: Jet multiplicity (upper left), $E_{\mathrm{T}}^{\mathrm{miss}}$ (upper right), charm tagged jet multiplicity (lower left) and m_{T}^{c} (lower right) distributions in CR1 W after the background-only fit. The shaded bands indicate the total uncertainty on the background prediction.

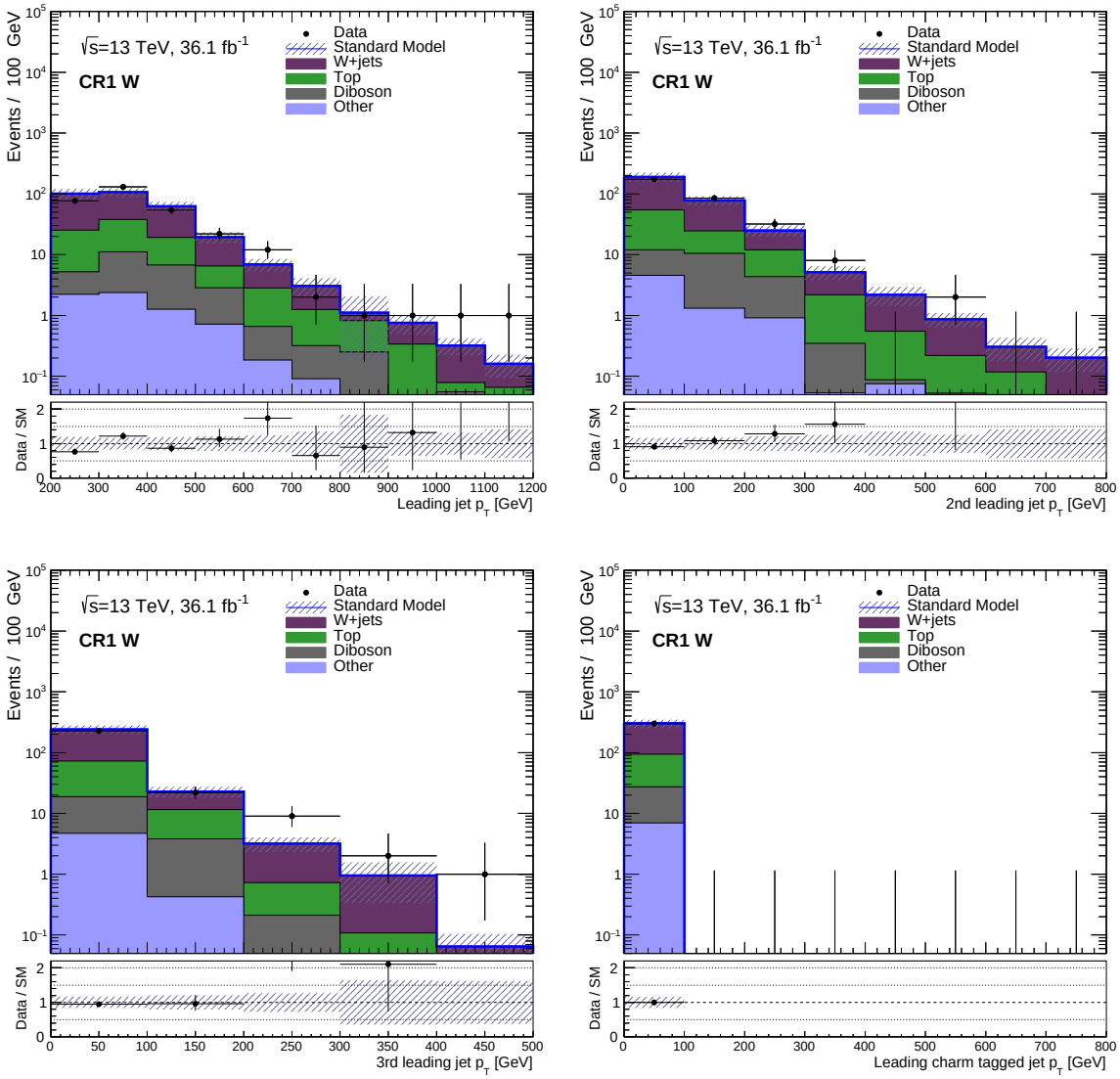

Figure F.17: Transverse momenta of the three leading jets (upper plots and lower left), and leading charm tagged jet p_{T} distributions in CR1 W after the background-only fit. The shaded bands indicate the total uncertainty on the background prediction.

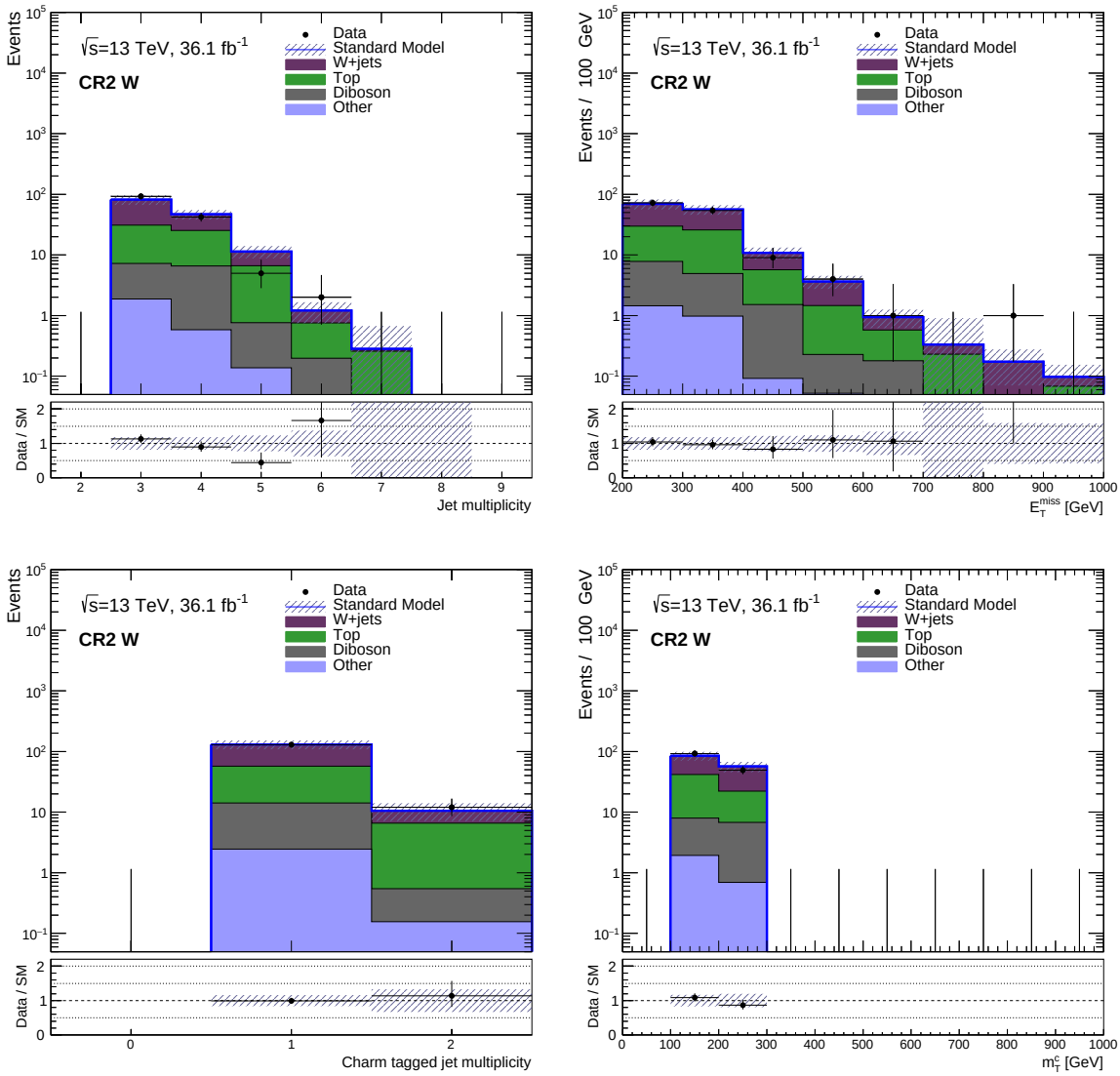

Figure F.18: Jet multiplicity (upper left), $E_{\mathrm{T}}^{\mathrm{miss}}$ (upper right), leading jet p_{T} (lower left) and m_{T}^{c} (lower right) distributions in CR2 W after the background-only fit. The shaded bands indicate the total uncertainty on the background prediction.

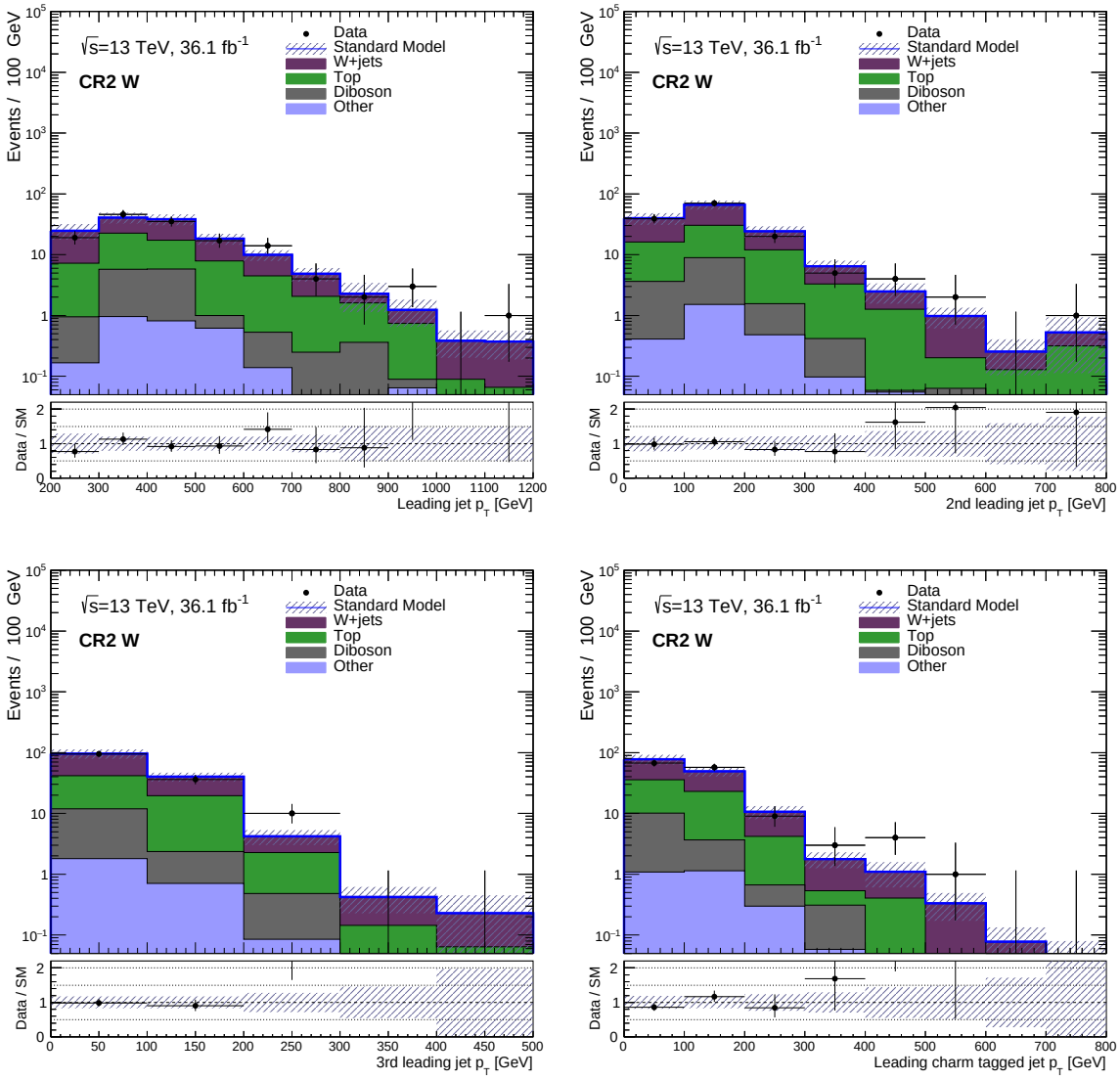

Figure F.19: Transverse momenta of the three leading jets (upper plots and lower left), and leading charm tagged jet p_{T} distributions in CR2 W after the background-only fit. The shaded bands indicate the total uncertainty on the background prediction.

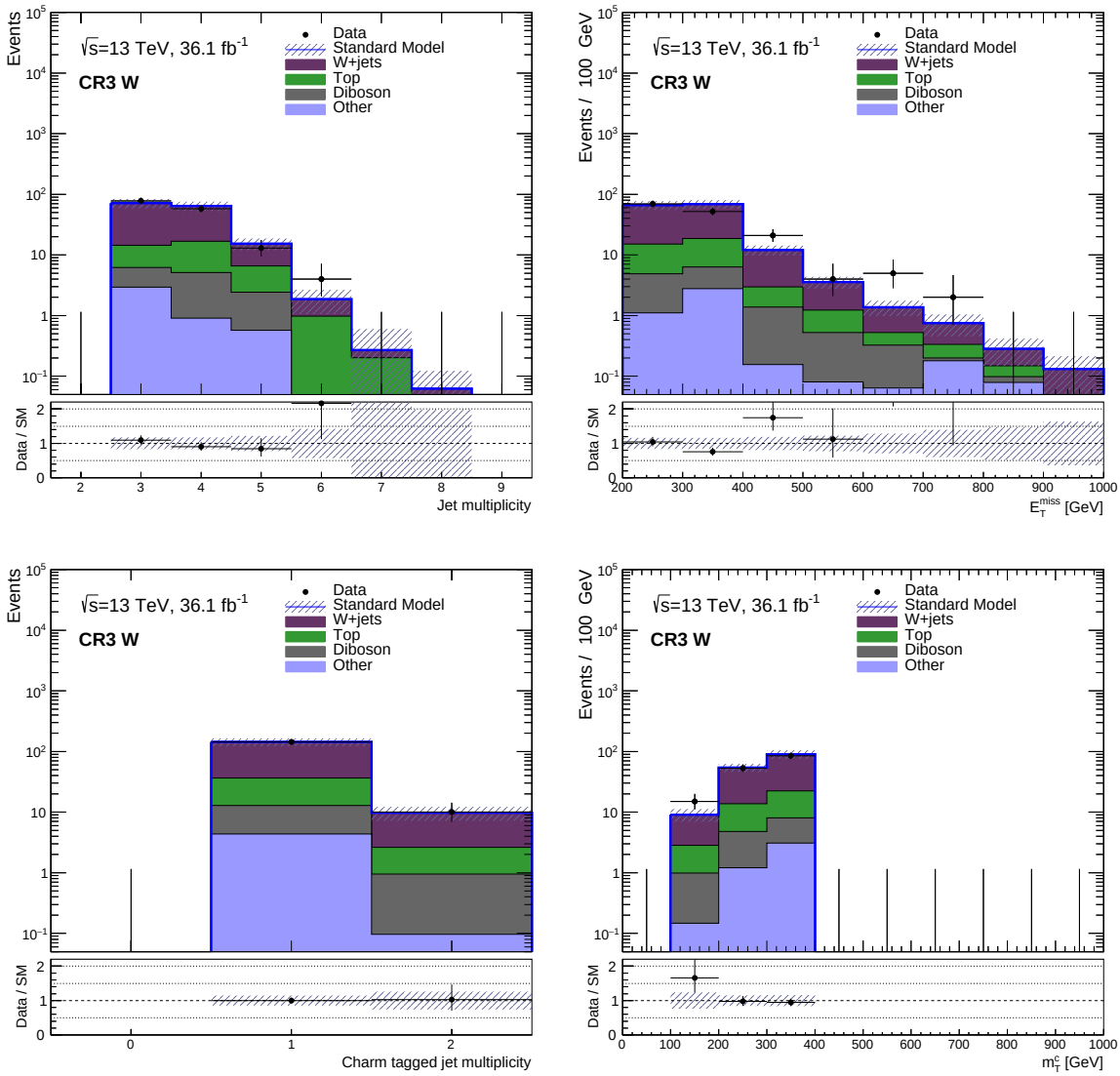

Figure F.20: Jet multiplicity (upper left), $E_{\mathrm{T}}^{\mathrm{miss}}$ (upper right), leading jet p_{T} (lower left) and m_{T}^{c} (lower right) distributions in CR3 W after the background-only fit. The shaded bands indicate the total uncertainty on the background prediction.

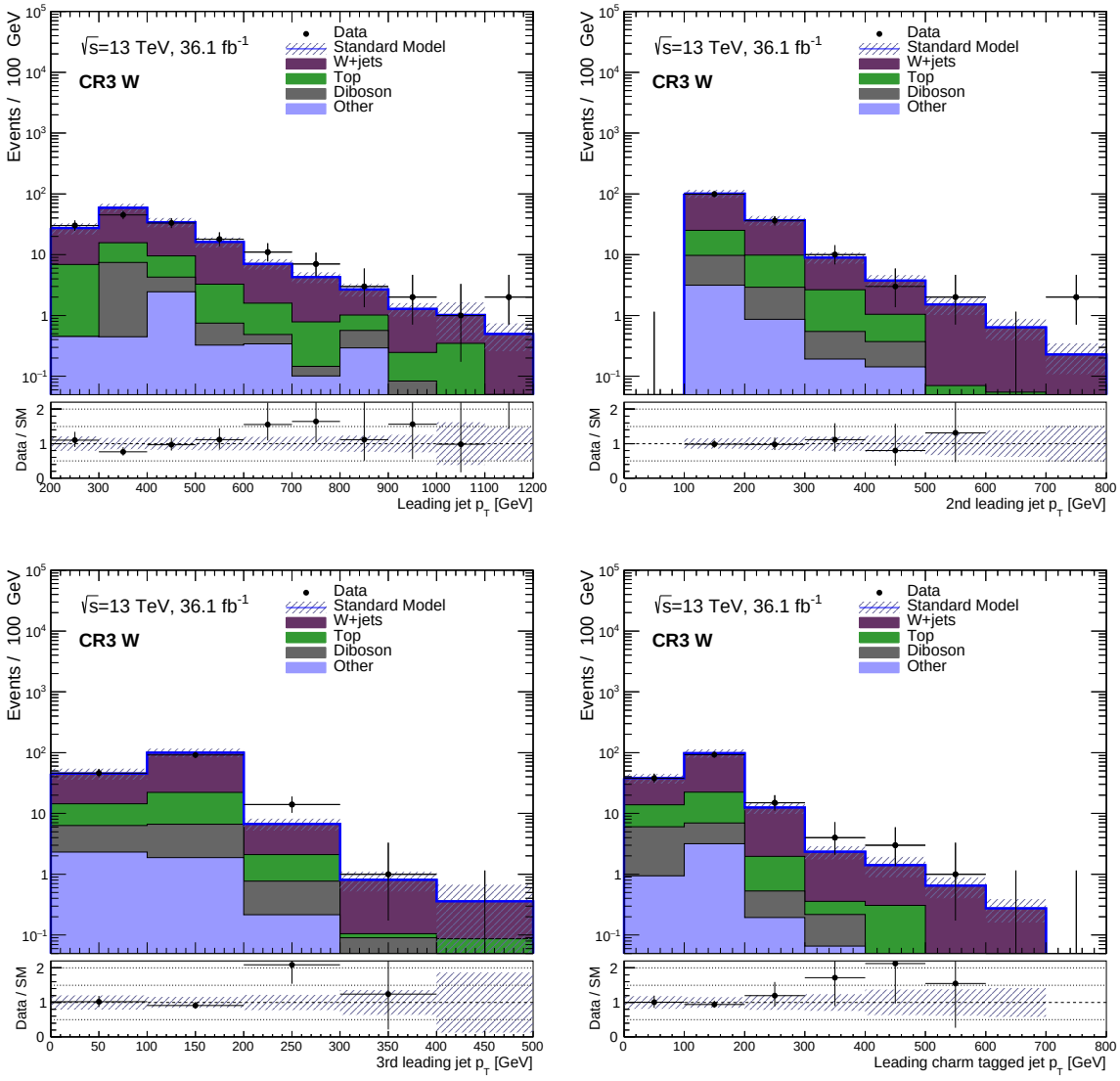

Figure F.21: Transverse momenta of the three leading jets (upper plots and lower left), and leading charm tagged jet p_{T} distributions in CR3 W after the background-only fit. The shaded bands indicate the total uncertainty on the background prediction.

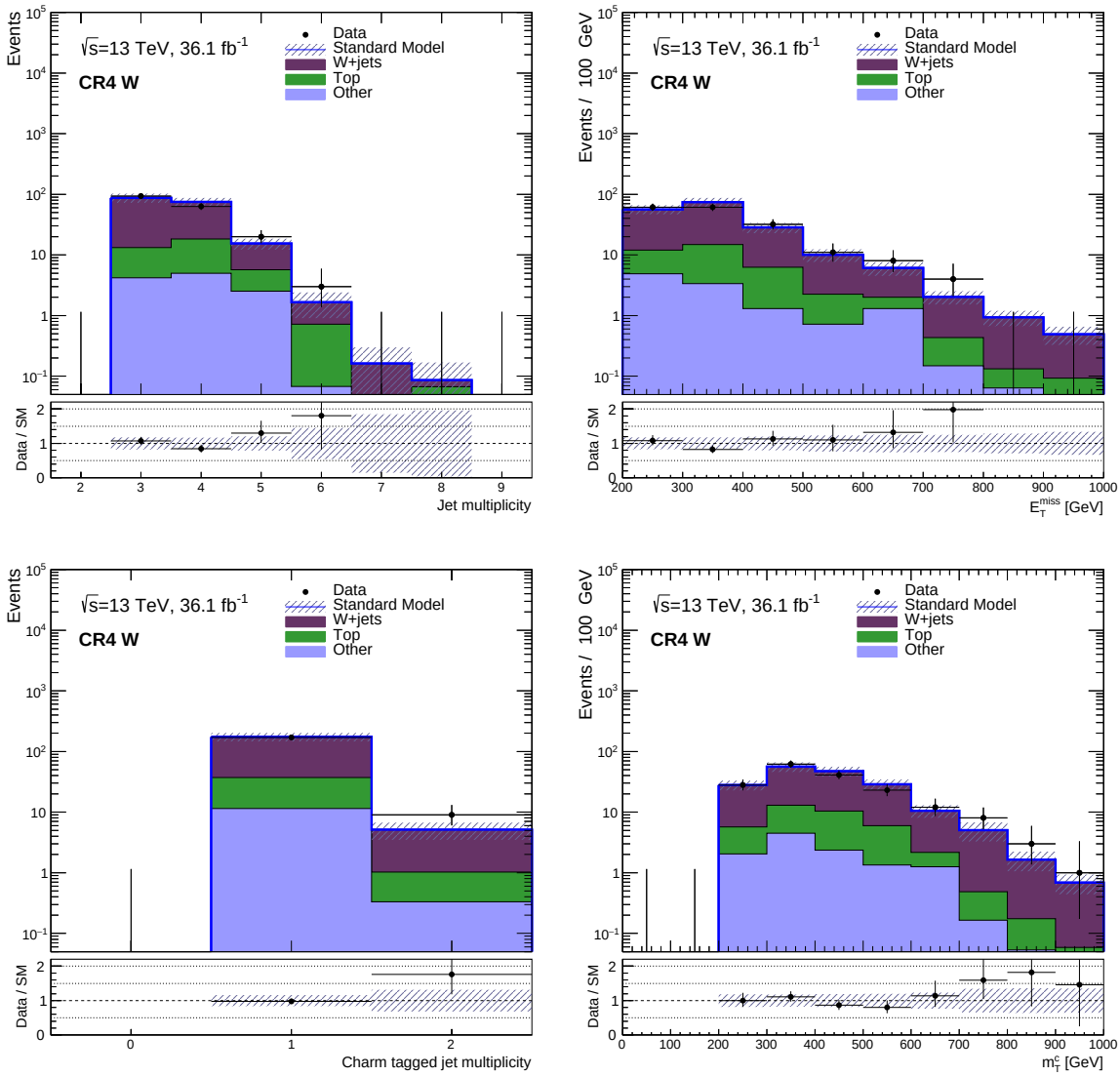

Figure F.22: Jet multiplicity (upper left), $E_{\mathrm{T}}^{\mathrm{miss}}$ (upper right), leading jet p_{T} (lower left) and m_{T}^{c} (lower right) distributions in CR4 W after the background-only fit. The shaded bands indicate the total uncertainty on the background prediction.

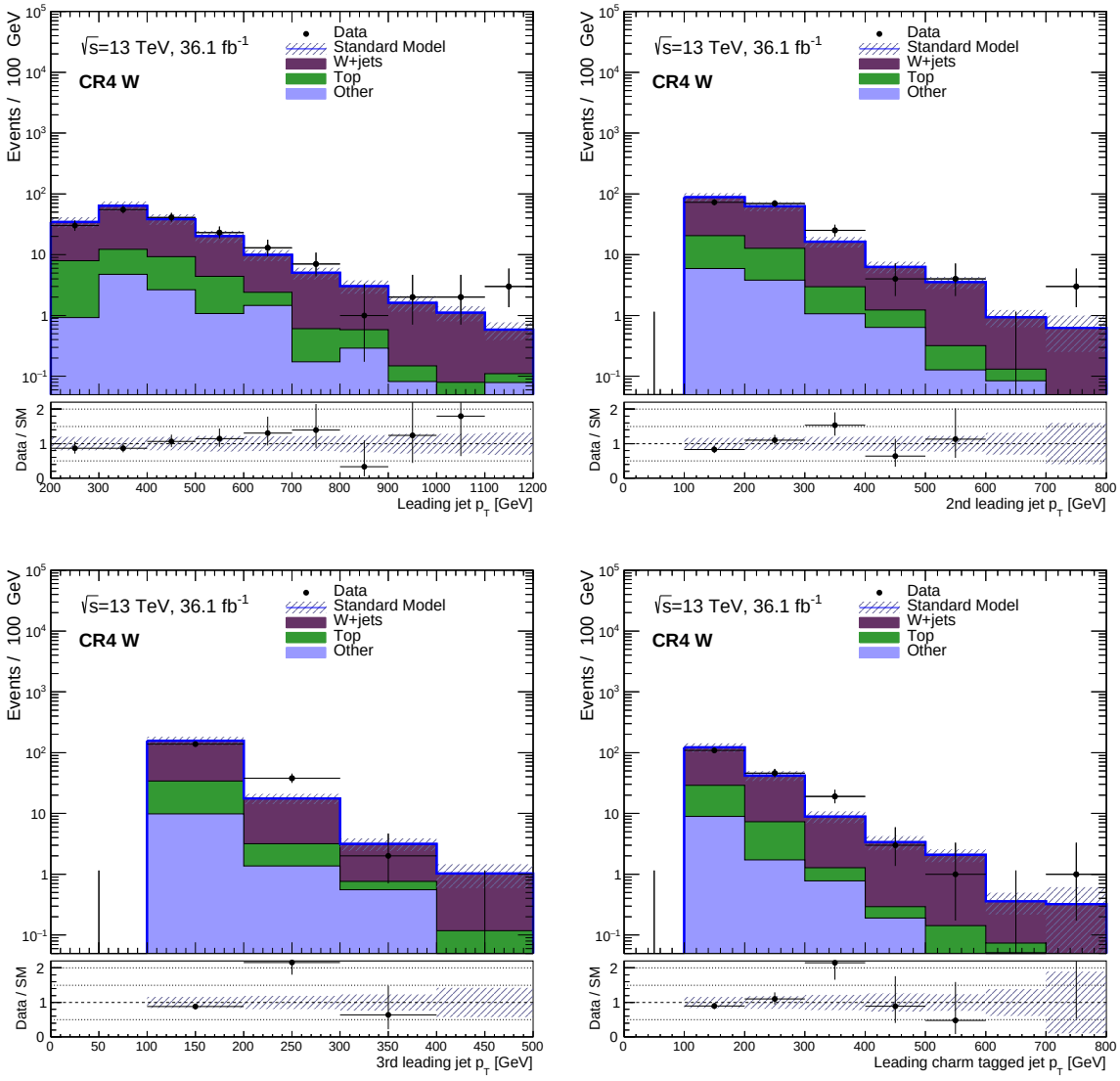

Figure F.23: Transverse momenta of the three leading jets (upper plots and lower left), and leading charm tagged jet p_{T} distributions in CR4 W after the background-only fit. The shaded bands indicate the total uncertainty on the background prediction.

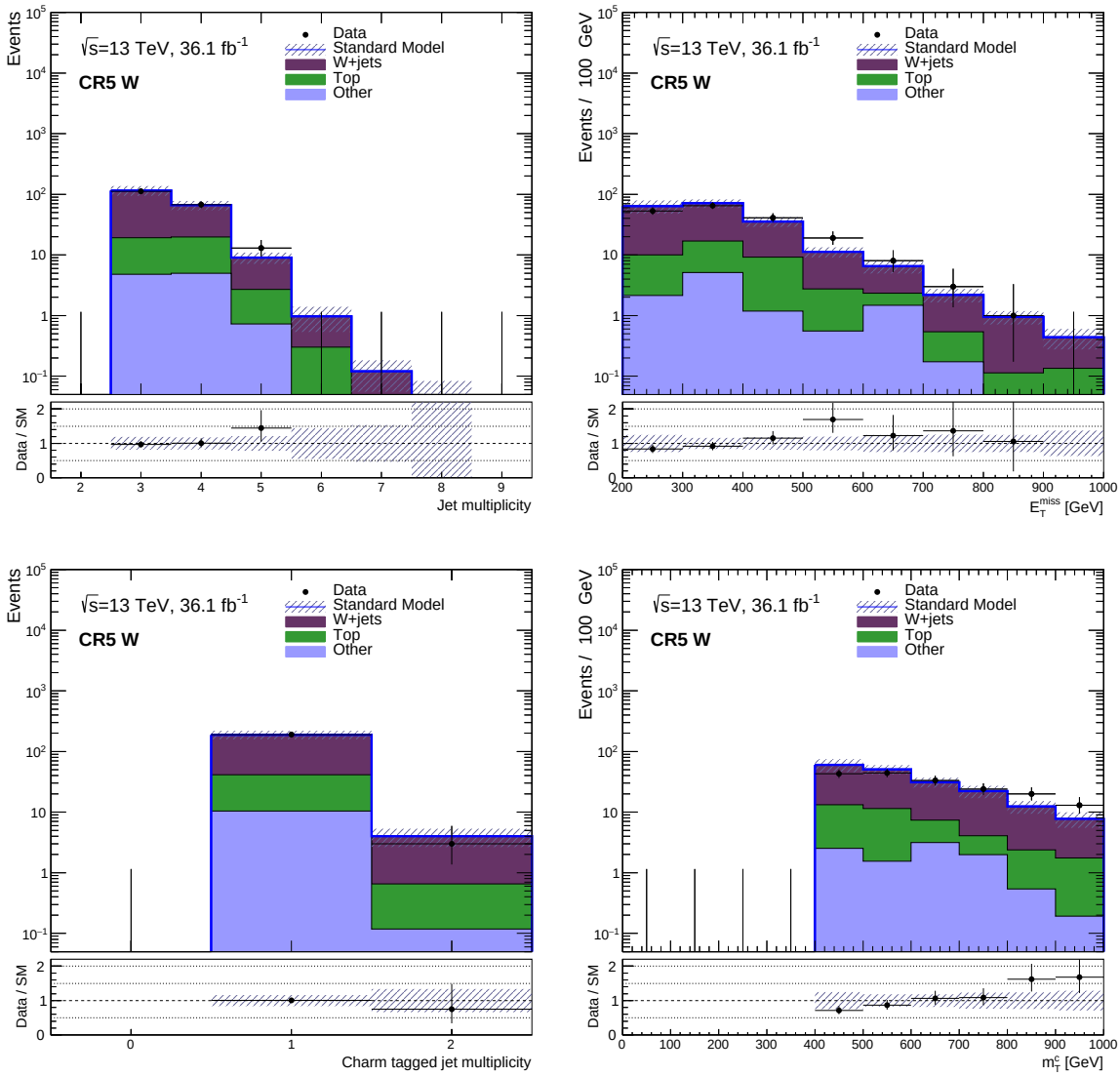

Figure F.24: Jet multiplicity (upper left), $E_{\mathrm{T}}^{\mathrm{miss}}$ (upper right), leading jet p_{T} (lower left) and m_{T}^{c} (lower right) distributions in CR5 W after the background-only fit. The shaded bands indicate the total uncertainty on the background prediction.

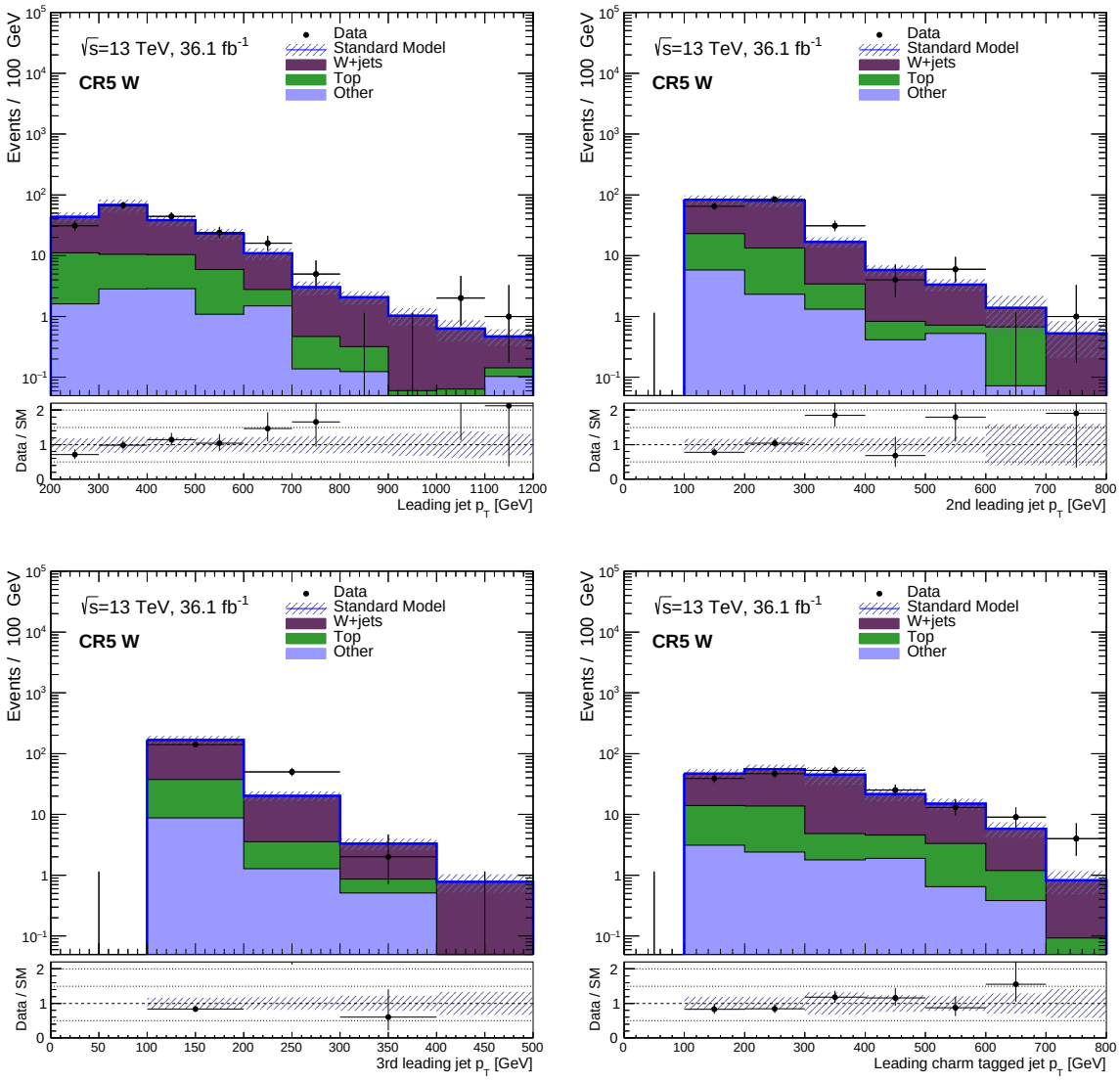

Figure F.25: Transverse momenta of the three leading jets (upper plots and lower left), and leading charm tagged jet p_{T} distributions in CR5 W after the background-only fit. The shaded bands indicate the total uncertainty on the background prediction.

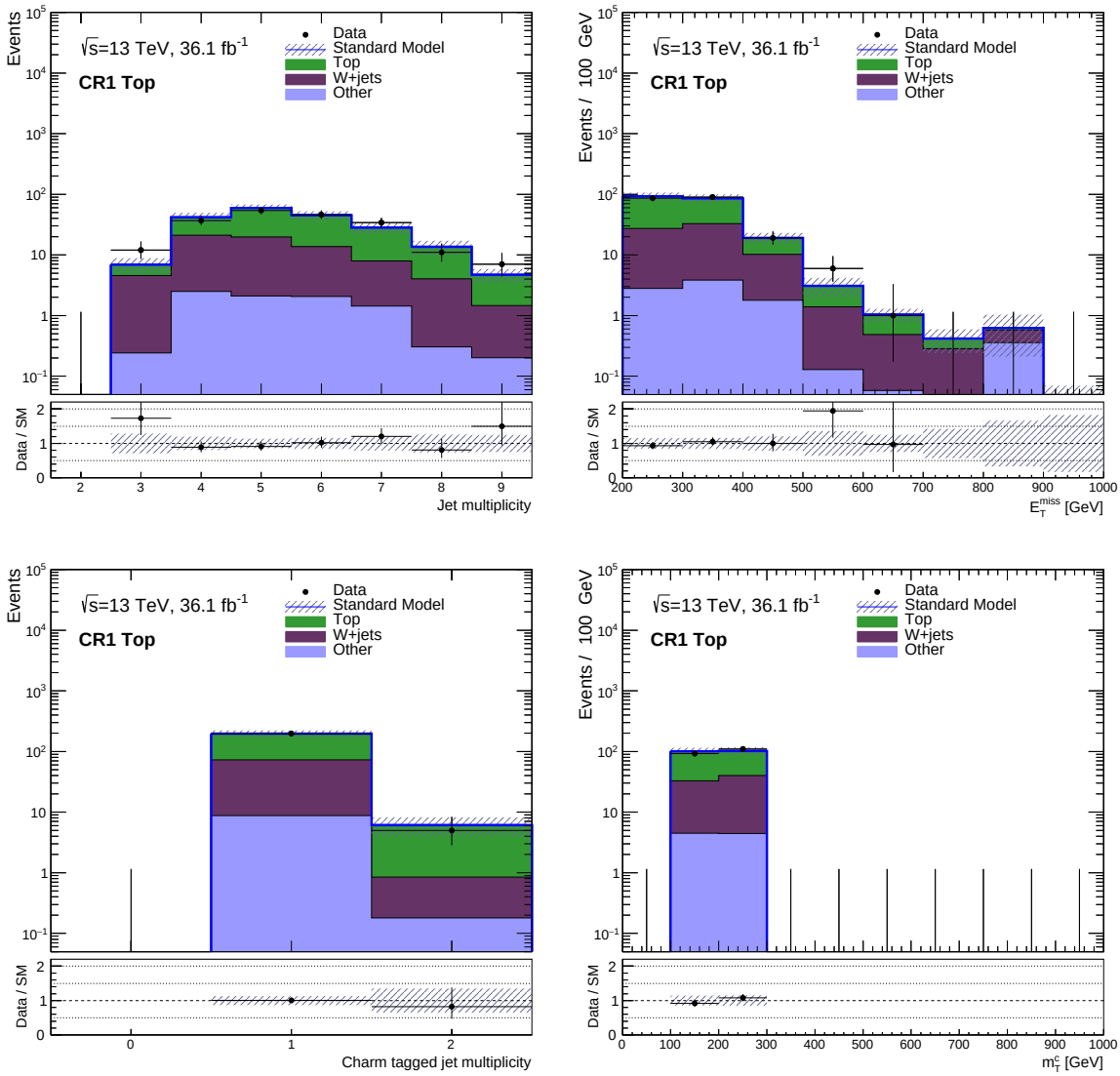

Figure F.26: Jet multiplicity (upper left), $E_{\mathrm{T}}^{\mathrm{miss}}$ (upper right), charm tagged jet multiplicity (lower left) and m_{T}^{c} (lower right) distributions in CR1 Top after the background-only fit. The shaded bands indicate the total uncertainty on the background prediction.

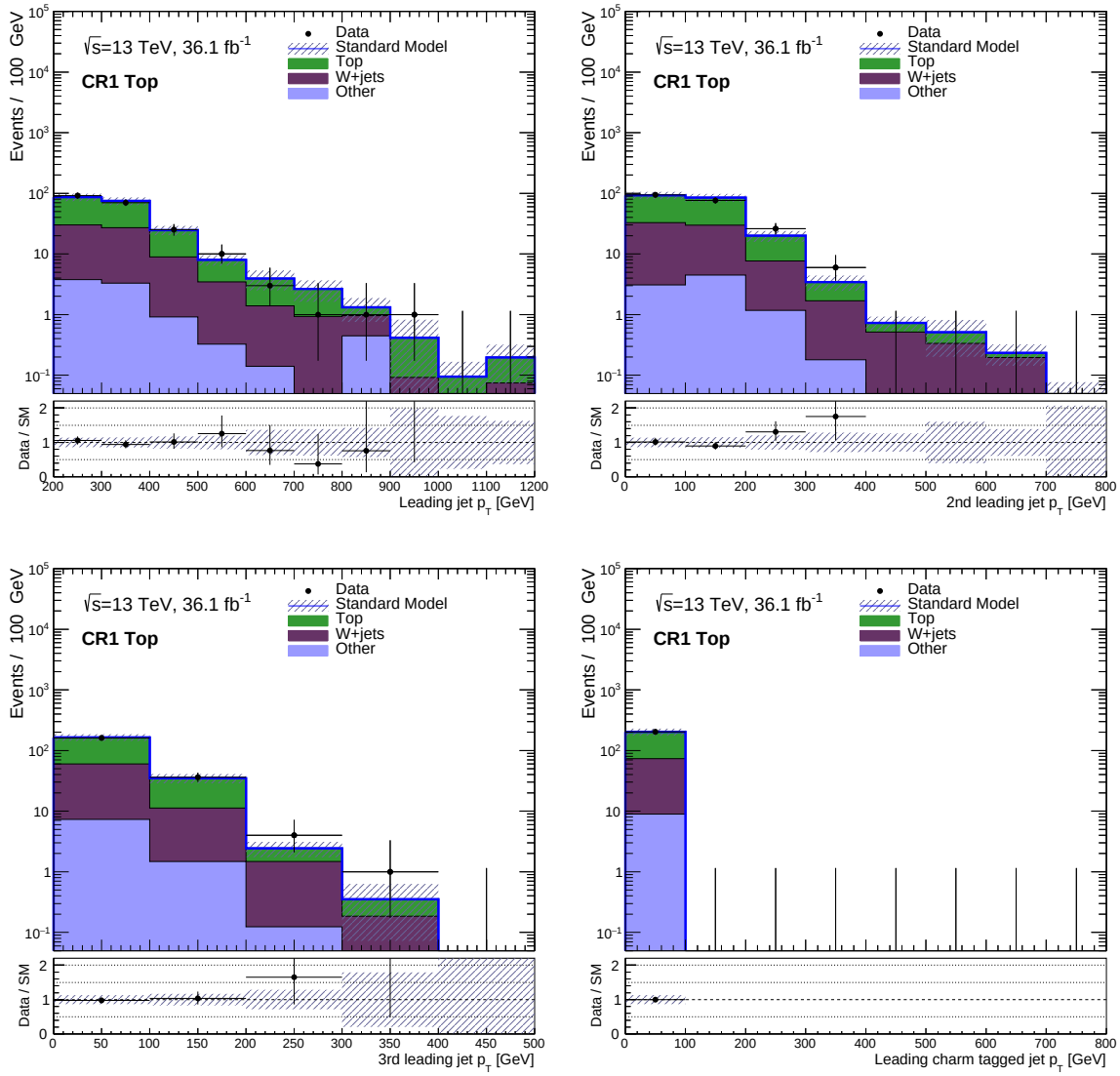

Figure F.27: Transverse momenta of the three leading jets (upper plots and lower left), and leading charm tagged jet p_{T} distributions in CR1 Top after the background-only fit. The shaded bands indicate the total uncertainty on the background prediction.

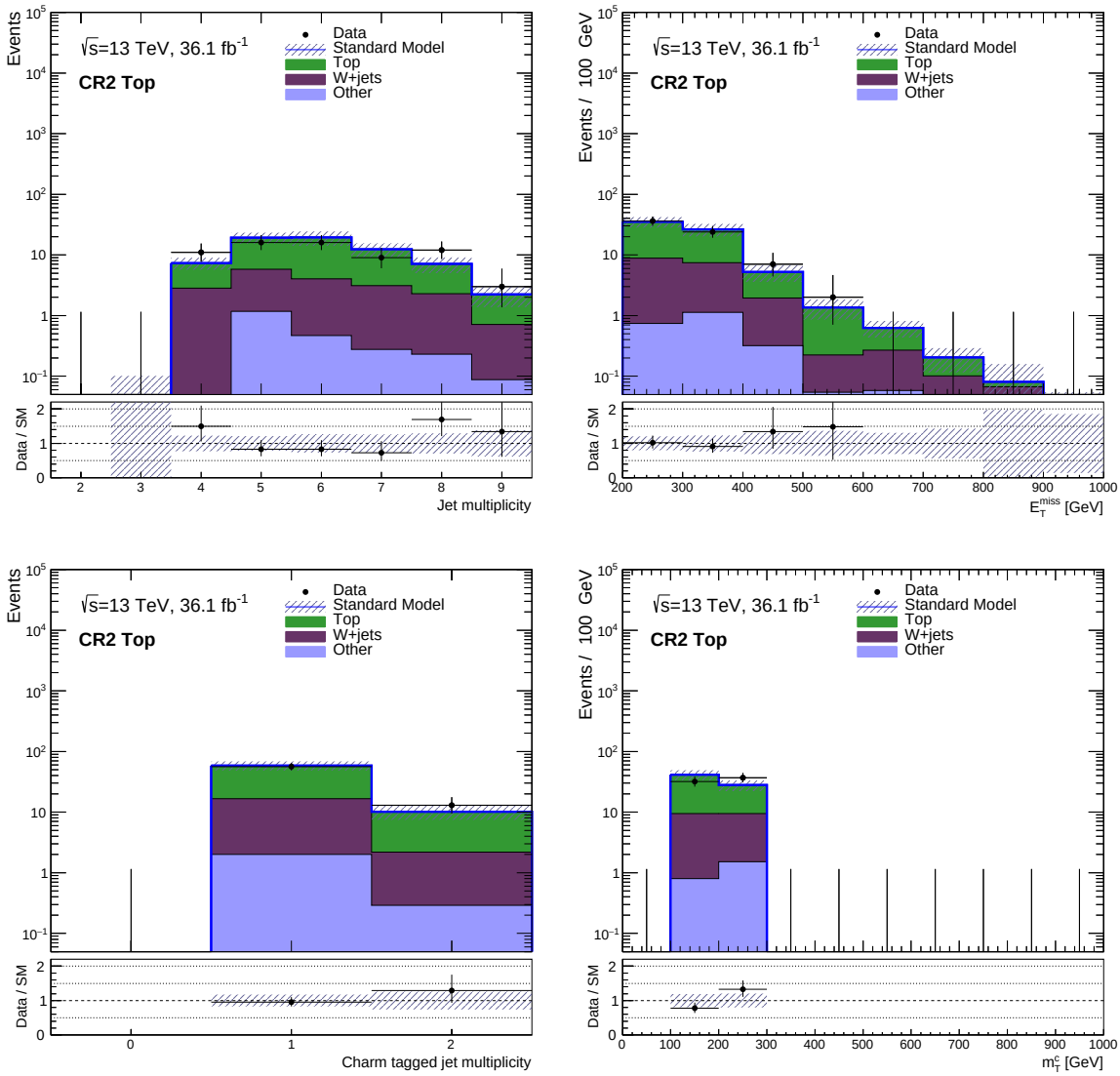

Figure F.28: Jet multiplicity (upper left), $E_{\mathrm{T}}^{\mathrm{miss}}$ (upper right), leading jet p_{T} (lower left) and m_{T}^{c} (lower right) distributions in CR2 Top after the background-only fit. The shaded bands indicate the total uncertainty on the background prediction.

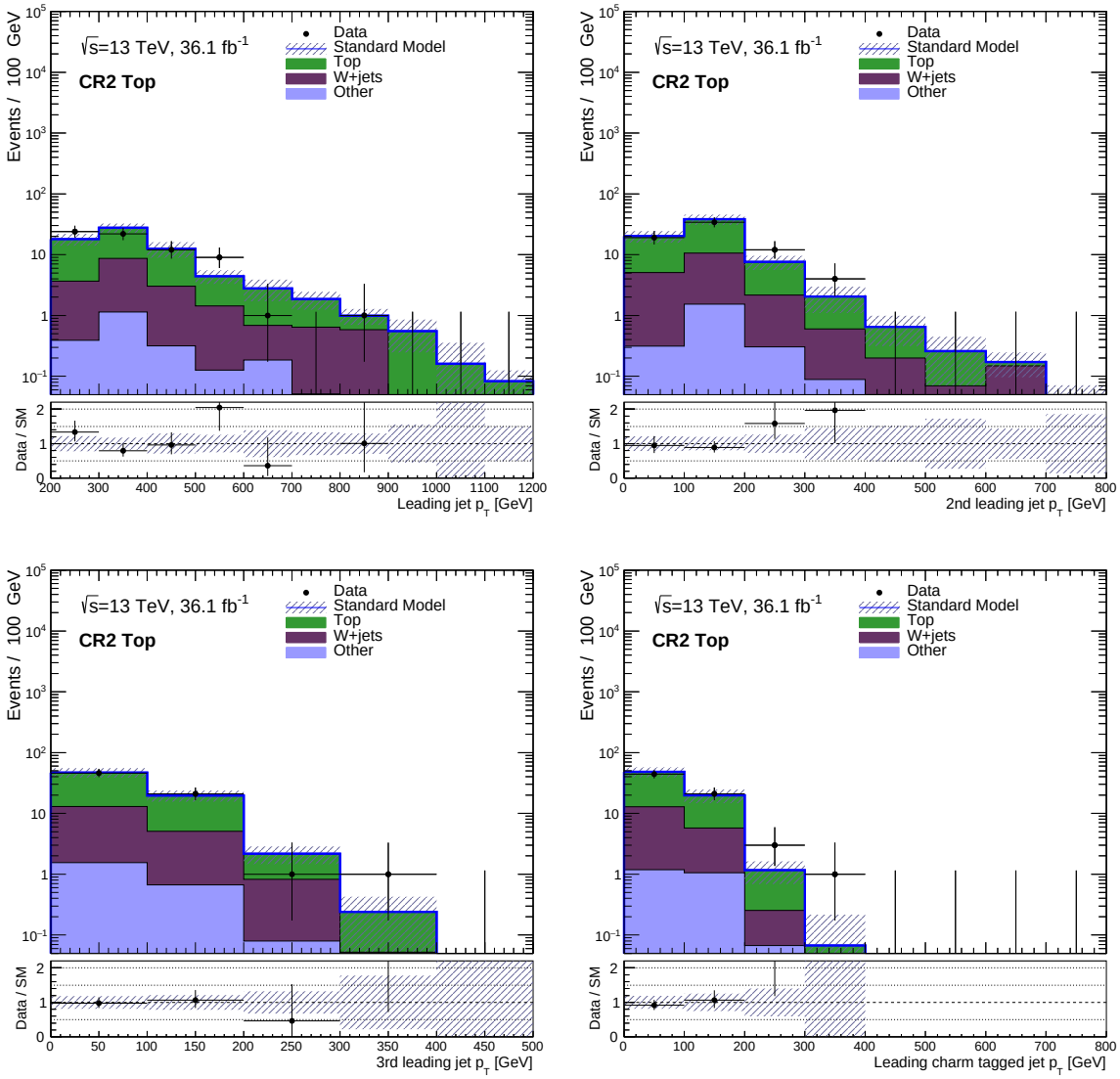

Figure F.29: Transverse momenta of the three leading jets (upper plots and lower left), and leading charm tagged jet p_{T} distributions in CR2 Top after the background-only fit. The shaded bands indicate the total uncertainty on the background prediction.

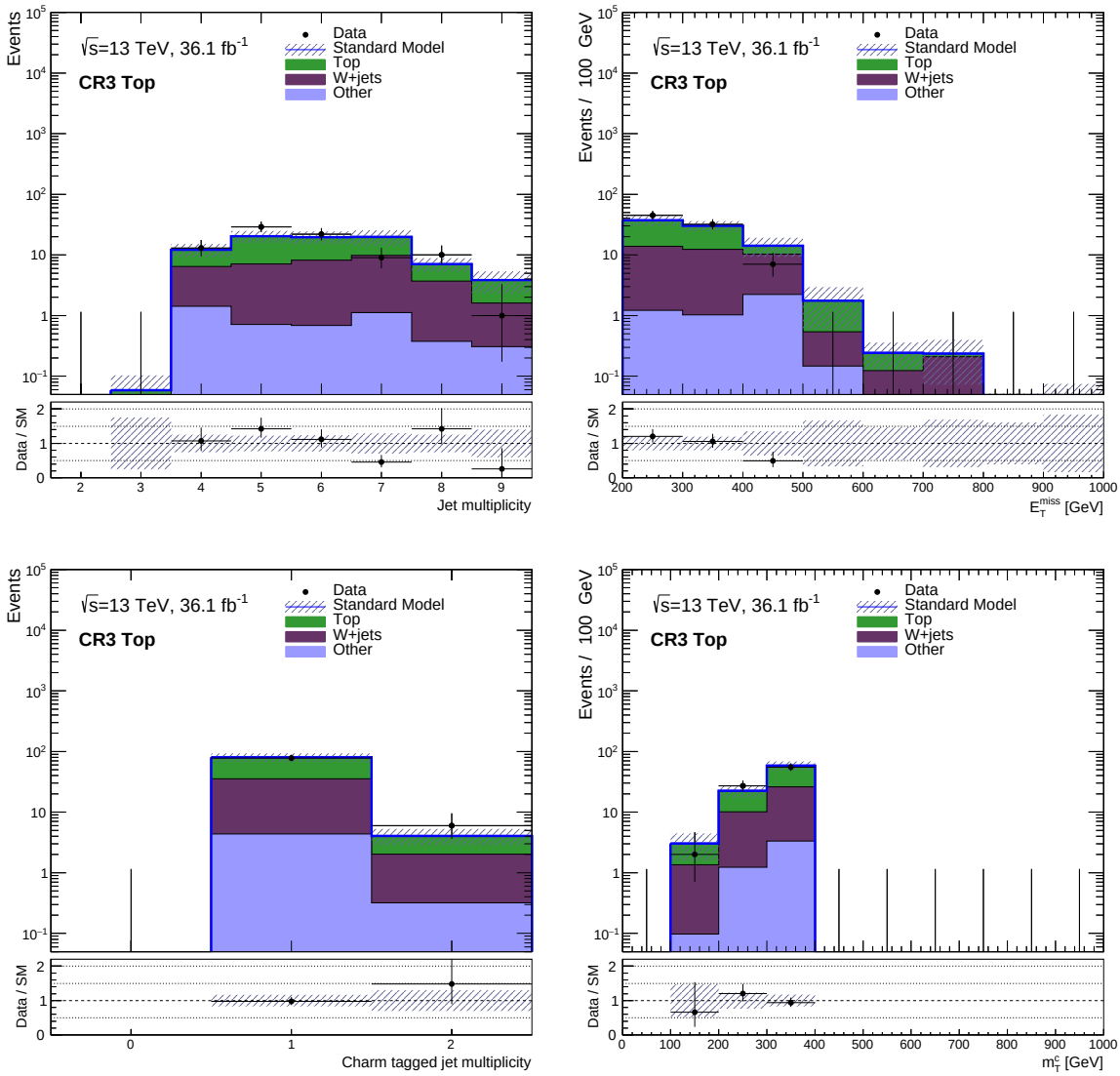

Figure F.30: Jet multiplicity (upper left), $E_{\mathrm{T}}^{\mathrm{miss}}$ (upper right), leading jet p_{T} (lower left) and m_{T}^{c} (lower right) distributions in CR3 Top after the background-only fit. The shaded bands indicate the total uncertainty on the background prediction.

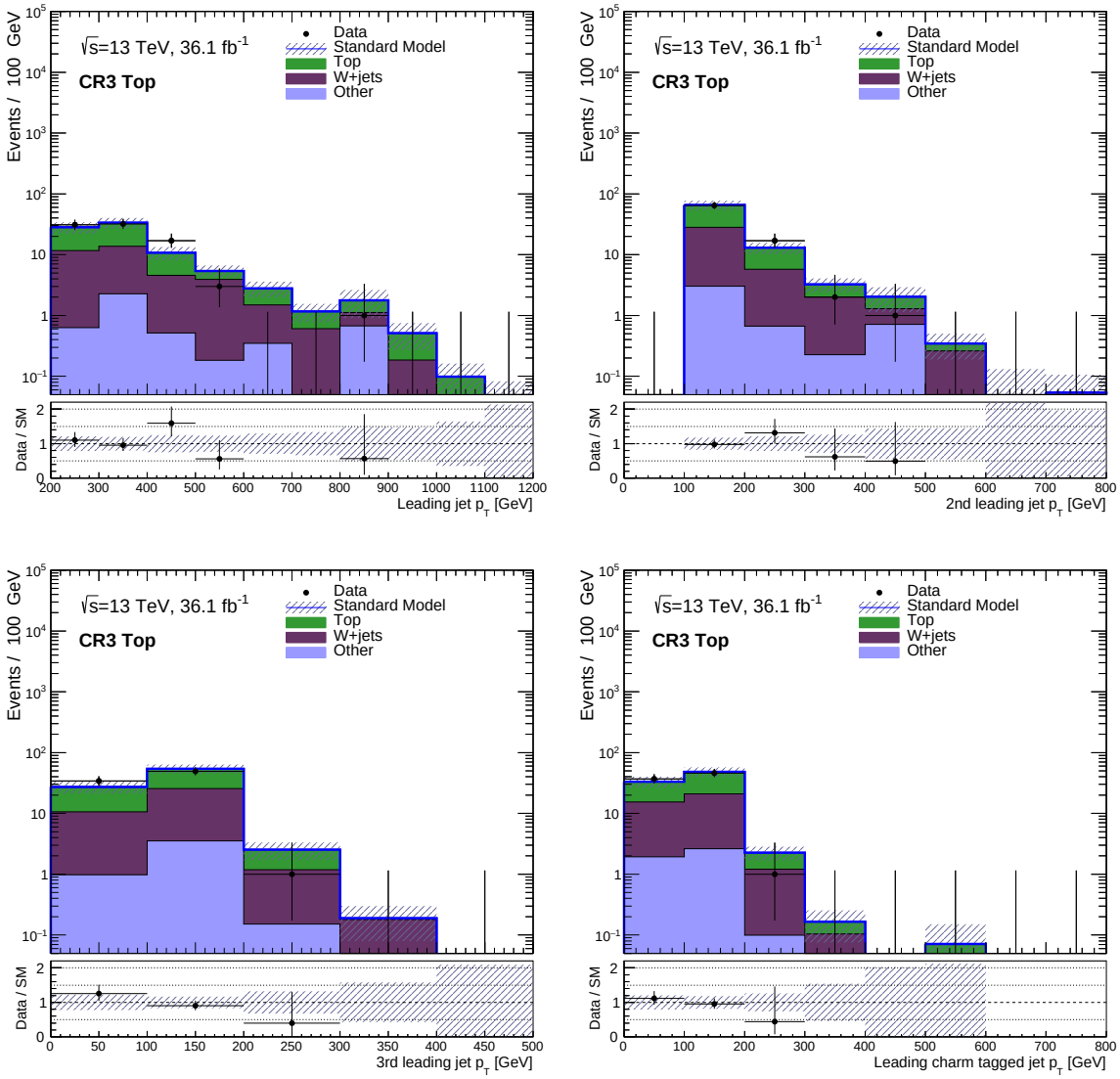

Figure F.31: Transverse momenta of the three leading jets (upper plots and lower left), and leading charm tagged jet p_{T} distributions in CR3 Top after the background-only fit. The shaded bands indicate the total uncertainty on the background prediction.

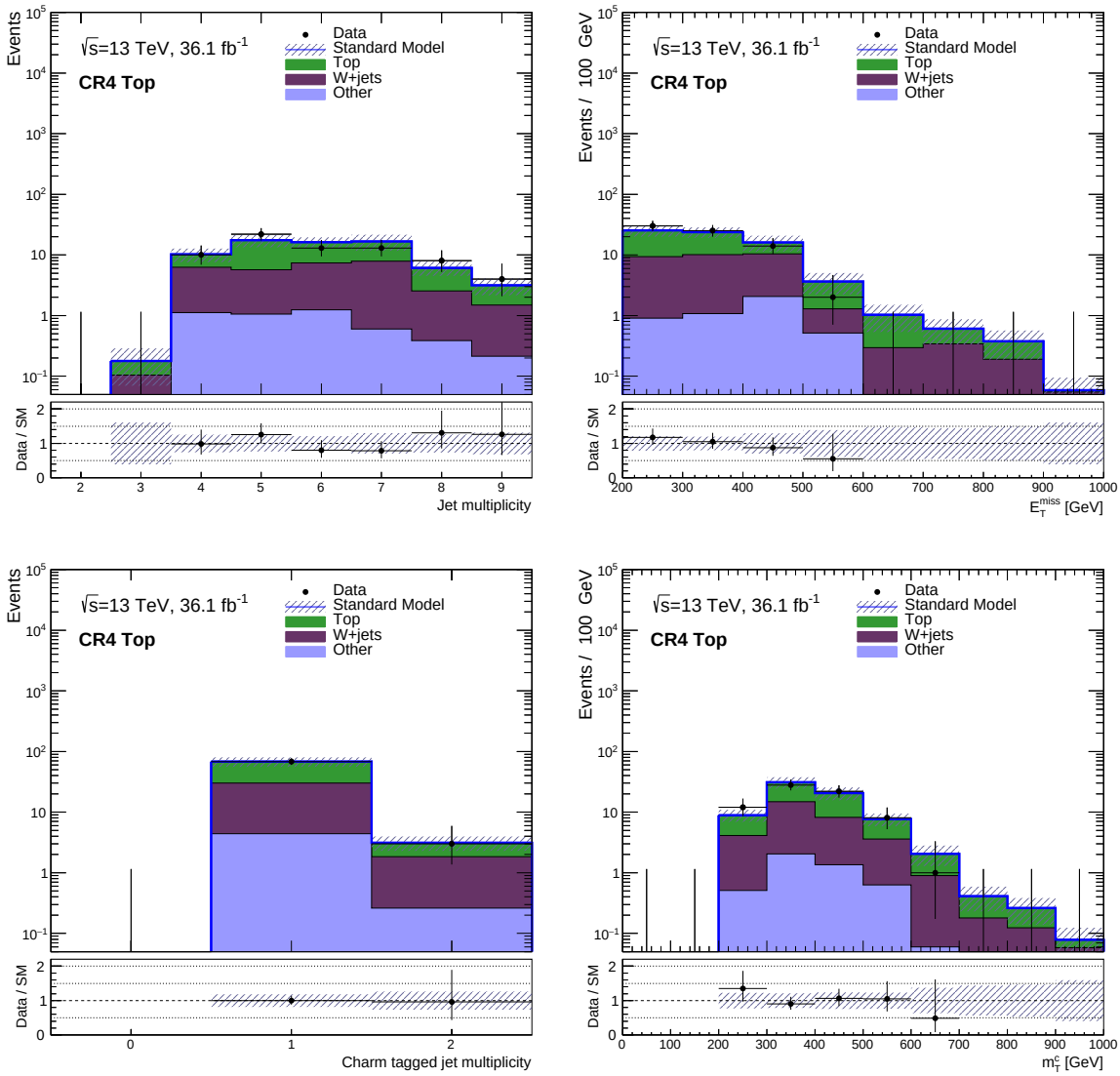

Figure F.32: Jet multiplicity (upper left), $E_{\mathrm{T}}^{\mathrm{miss}}$ (upper right), leading jet p_{T} (lower left) and m_{T}^{c} (lower right) distributions in CR4 Top after the background-only fit. The shaded bands indicate the total uncertainty on the background prediction.

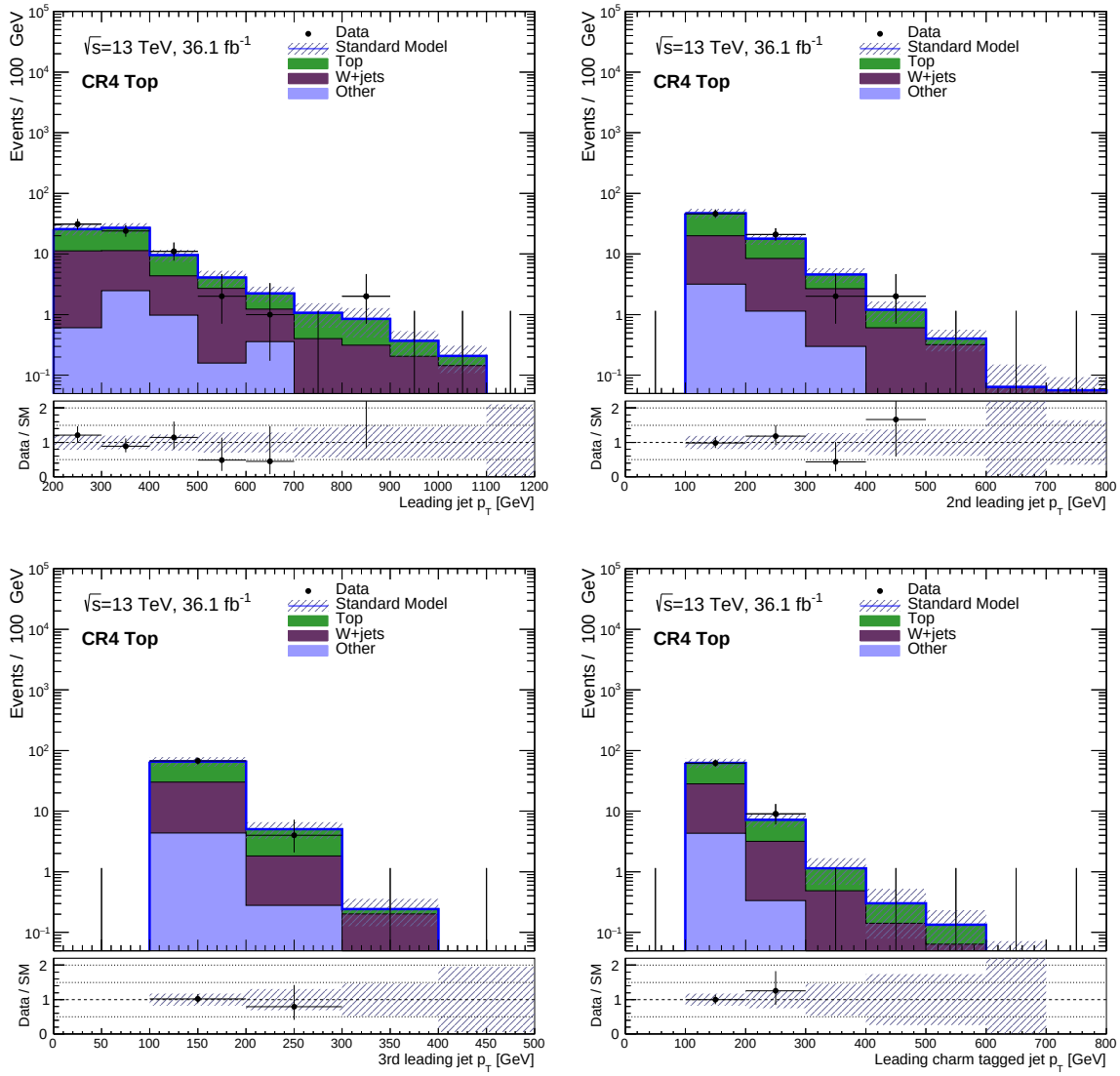

Figure F.33: Transverse momenta of the three leading jets (upper plots and lower left), and leading charm tagged jet p_{T} distributions in CR4 Top after the background-only fit. The shaded bands indicate the total uncertainty on the background prediction.

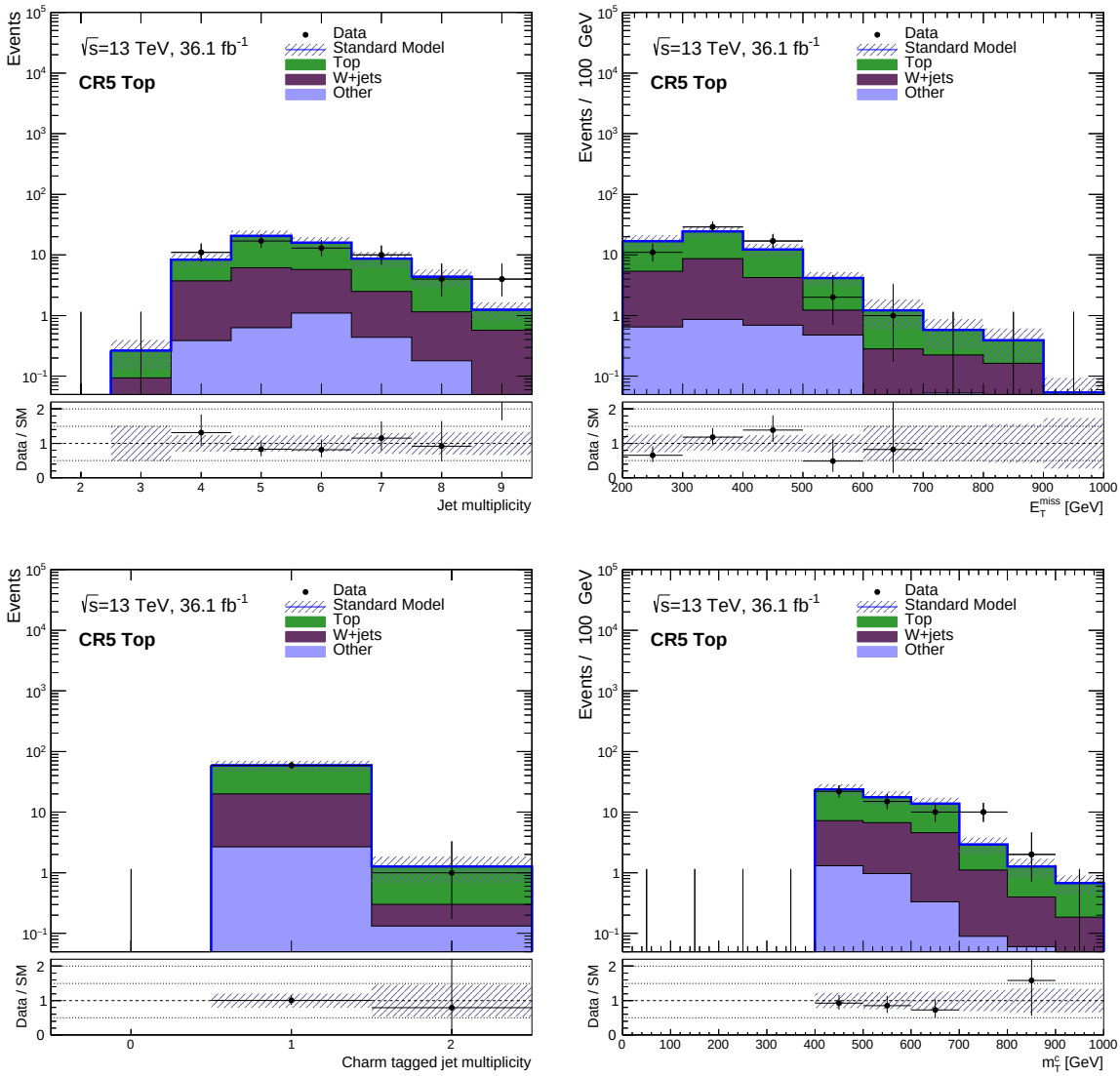

Figure F.34: Jet multiplicity (upper left), $E_{\mathrm{T}}^{\mathrm{miss}}$ (upper right), leading jet p_{T} (lower left) and m_{T}^{c} (lower right) distributions in CR5 Top after the background-only fit. The shaded bands indicate the total uncertainty on the background prediction.

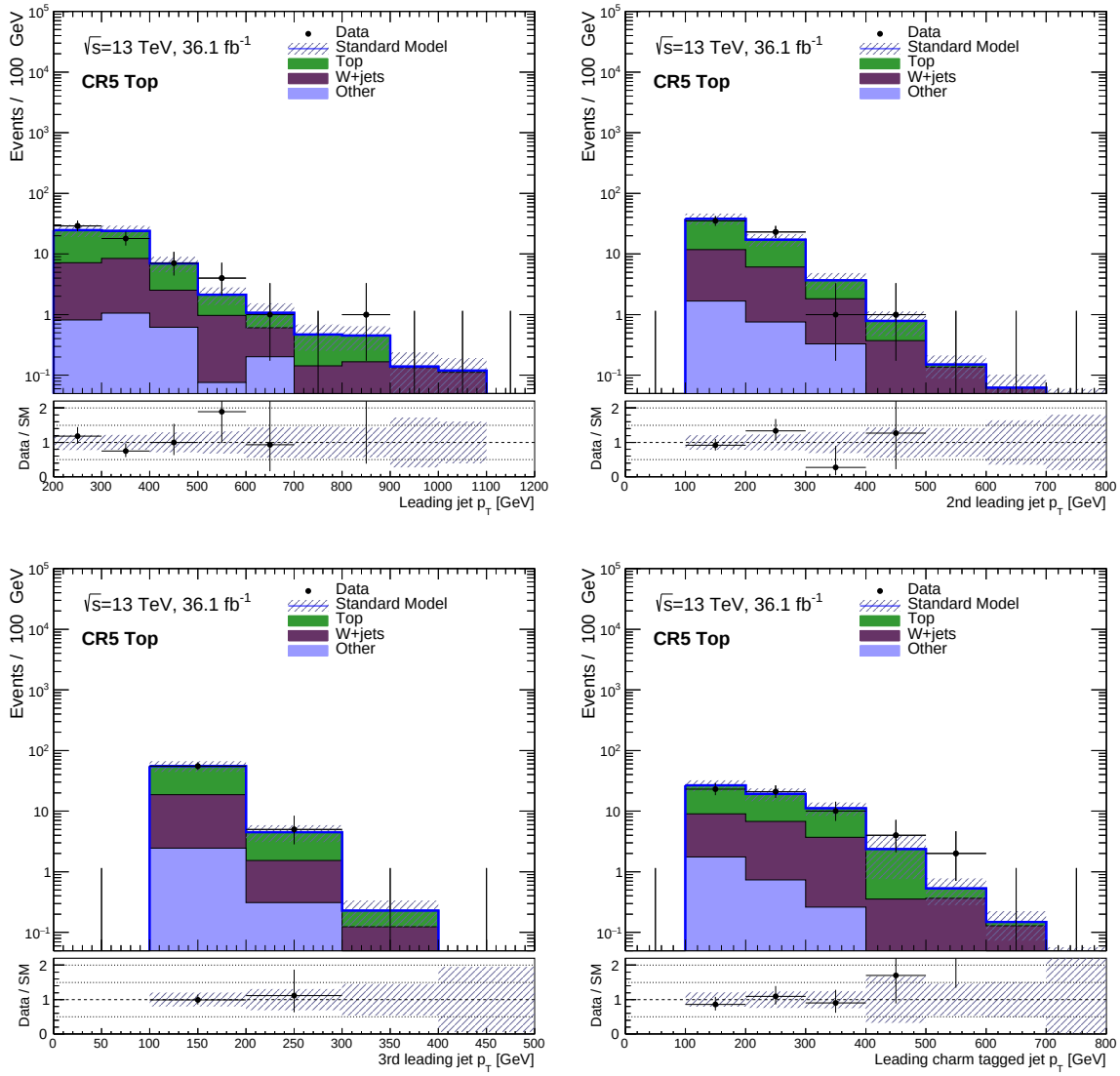

Figure F.35: Transverse momenta of the three leading jets (upper plots and lower left), and leading charm tagged jet p_{T} distributions in CR5 Top after the background-only fit. The shaded bands indicate the total uncertainty on the background prediction.

F.4. Background-only fit validation region distributions

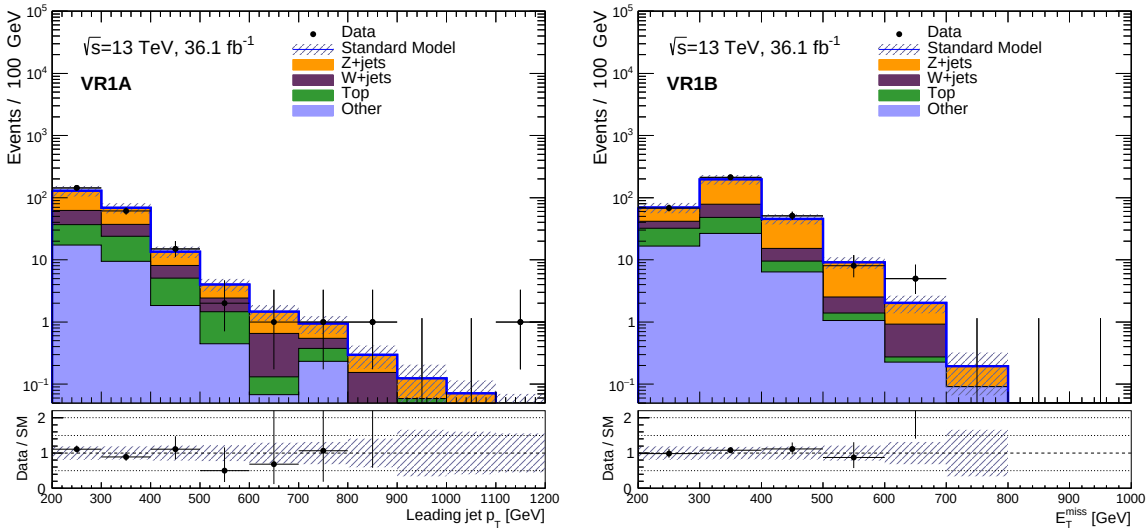

Figure F.36: Leading jet p_{T} in VR1A (left) and $E_{\mathrm{T}}^{\mathrm{miss}}$ in VR1B (right) after the background-only fit. The shaded bands indicate the total uncertainty on the background prediction.

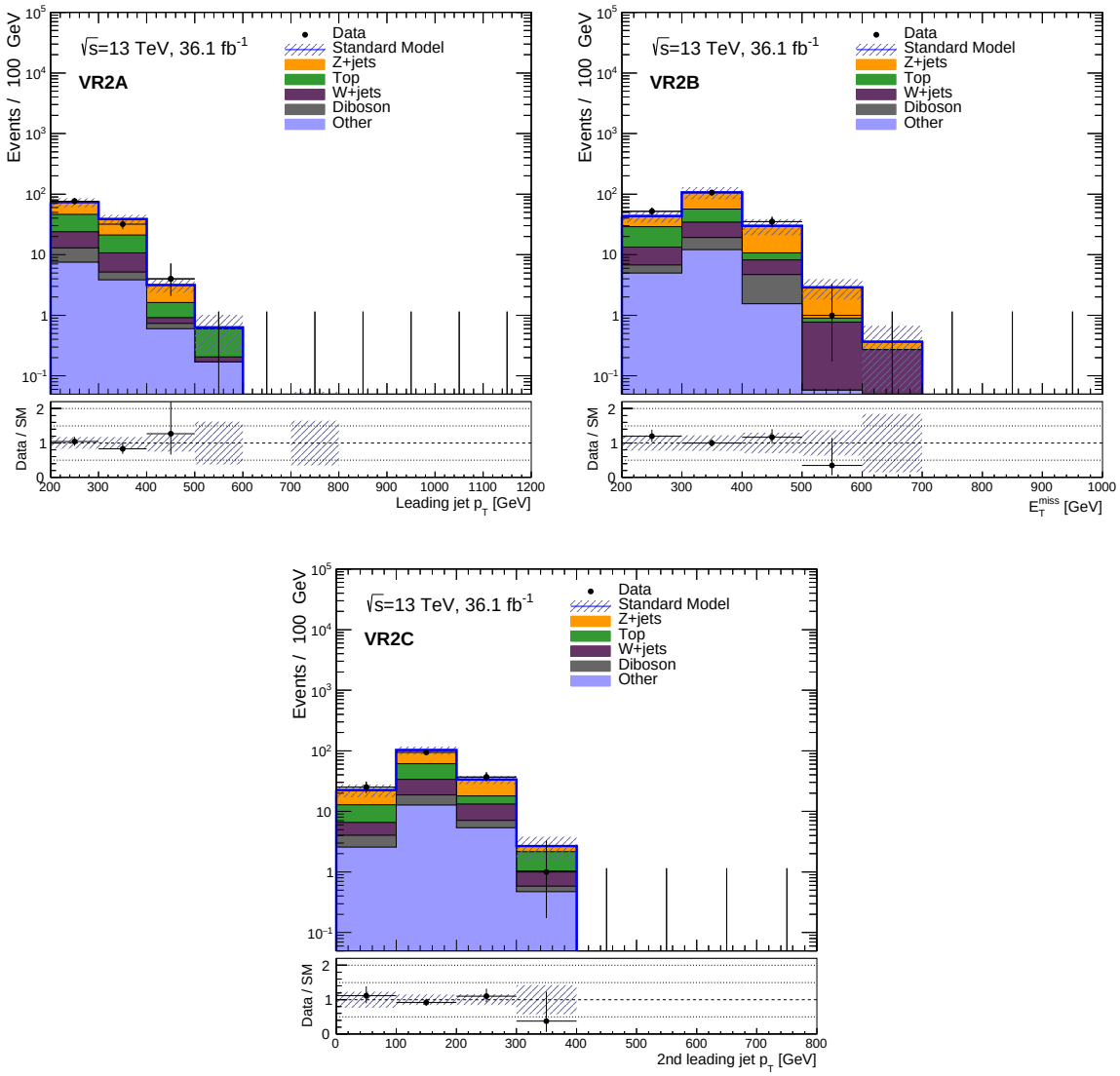

Figure F.37: Leading jet p_{T} in VR2A (upper left), $E_{\mathrm{T}}^{\mathrm{miss}}$ in VR2B (upper right) and the second leading jet p_{T}in VR2C (lower) after the background-only fit. The shaded bands indicate the total uncertainty on the background prediction.

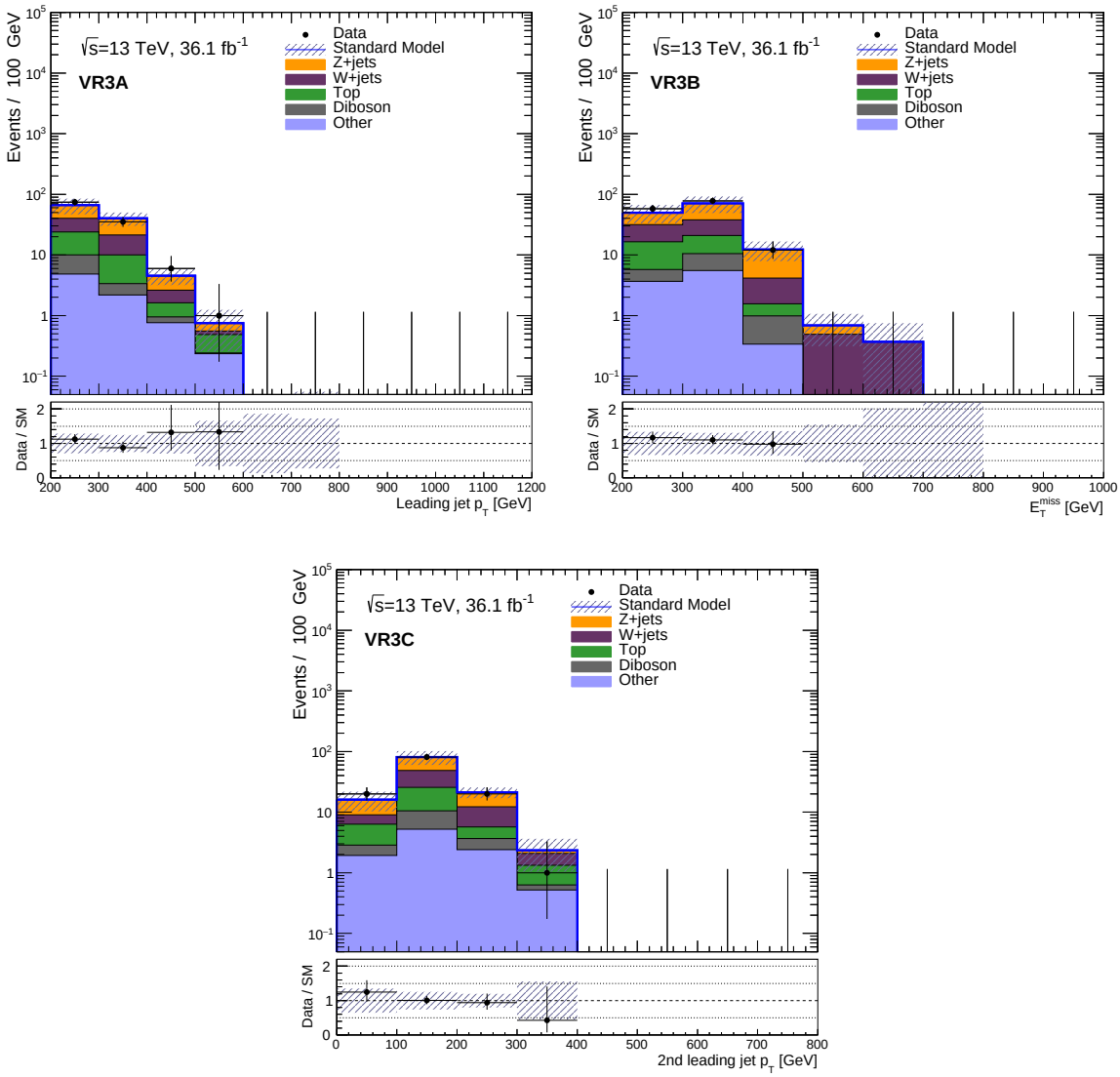

Figure F.38: Leading jet p_{T} in VR3A (upper left), $E_{\mathrm{T}}^{\mathrm{miss}}$ in VR3B (upper right) and the second leading jet p_{T}in VR3C (lower) after the background-only fit. The shaded bands indicate the total uncertainty on the background prediction.

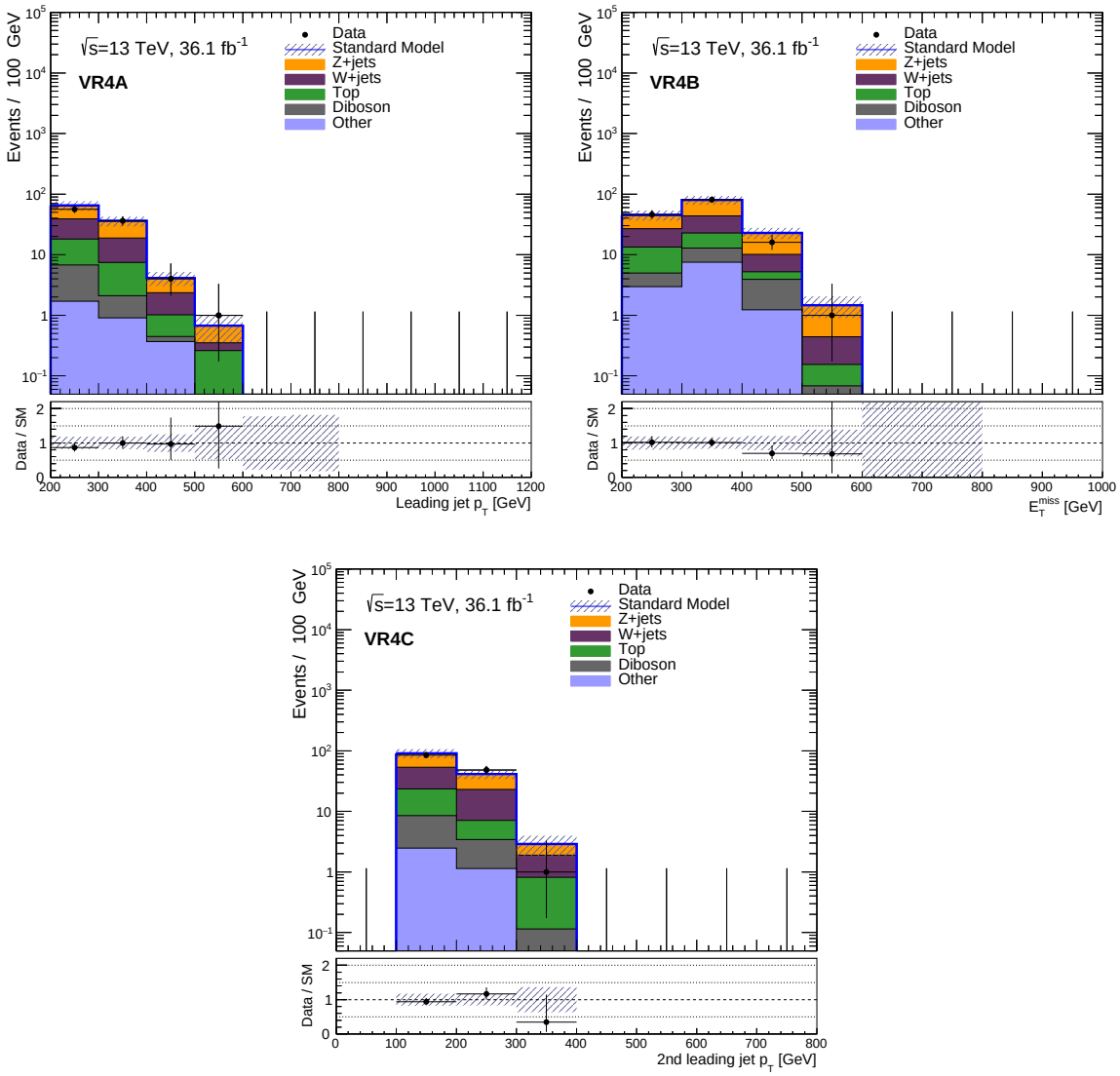

Figure F.39: Leading jet p_{T} in VR4A (upper left), $E_{\mathrm{T}}^{\mathrm{miss}}$ in VR4B (upper right) and the second leading jet p_{T}in VR4C (lower) after the background-only fit. The shaded bands indicate the total uncertainty on the background prediction.

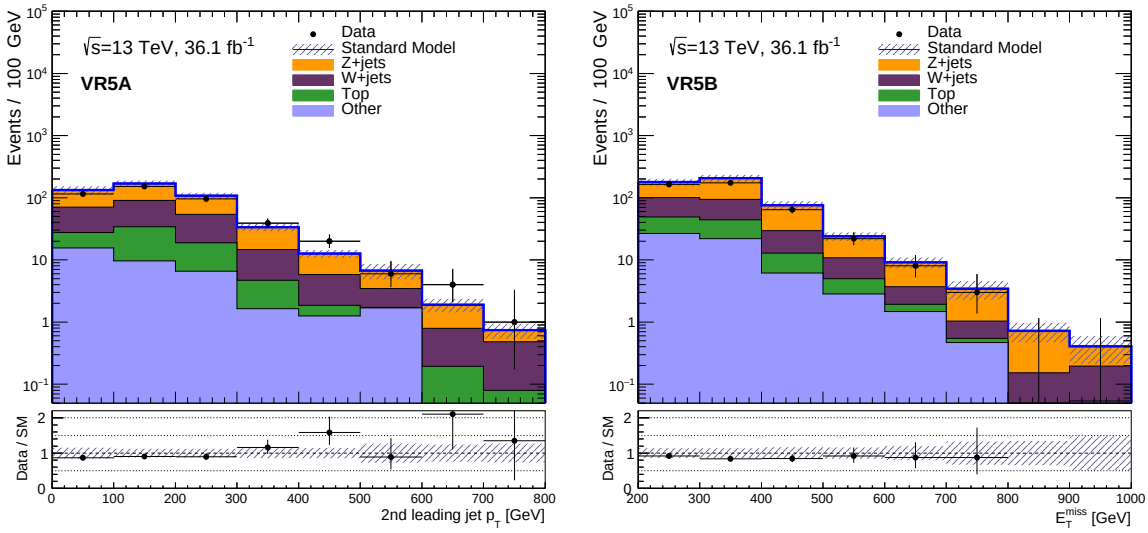

Figure F.40: Second leading jet p_{T} in VR5A (left) and $E_{\mathrm{T}}^{\mathrm{miss}}$ in VR5B (right) after the background-only fit. The shaded bands indicate the total uncertainty on the background prediction.

List of Figures

List of Tables

Bibliography

[1] G. Arnison et al. Experimental observation of isolated large transverse energy electrons with associated missing energy at s=540 GeV. *Physics Letters B*, 122(1):103 – 116, 1983. ISSN 0370-2693. doi: https://doi.org/10.1016/0370-2693(83)91177-2. URL http://www.sciencedirect.com/science/article/pii/0370269383911772.

[2] M. Banner et al. Observation of single isolated electrons of high transverse momentum in events with missing transverse energy at the CERN pp collider. *Physics Letters B*, 122 (5):476 – 485, 1983. ISSN 0370-2693. doi: https://doi.org/10.1016/0370-2693(83)91605-2. URL http://www.sciencedirect.com/science/article/pii/0370269383916052.

[3] F. Abe et al. Observation of top quark production in $\bar{p}p$ collisions. *Phys. Rev. Lett.*, 74: 2626–2631, 1995. doi: 10.1103/PhysRevLett.74.2626.

[4] S. Abachi et al. Observation of the top quark. *Phys. Rev. Lett.*, 74:2632–2637, 1995. doi: 10.1103/PhysRevLett.74.2632.

[5] ATLAS Collaboration. Observation of a new particle in the search for the Standard Model Higgs boson with the ATLAS detector at the LHC. *Phys. Lett.*, B716:1–29, 2012. URL http://dx.doi.org/10.1016/j.physletb.2012.08.020.

[6] The CMS Collaboration. Observation of a new boson at a mass of 125 GeV with the CMS experiment at the LHC. *Phys. Lett.*, B716:30–61, 2012. URL arXiv:1207.7235[hep-ex].

[7] 't Hooft and Veltman. Regularization and Renormalization of Gauge Fields. *Nucl. Phys.*, B44:189–213, 1972. URL http://dx.doi.org/10.1016/0550-3213(72)90279-9.

[8] Olive, K. A. and others. Review of Particle Physics. *Chin. Phys.*, C38:090001, 2014. doi: 10.1088/1674-1137/38/9/090001.

[9] A. Aguilar-Arevalo et al. Evidence for neutrino oscillations from the observation of anti-neutrino(electron) appearance in a anti-neutrino(muon) beam. *Phys. Rev.*, D64: 112007, 2001. doi: 10.1103/PhysRevD.64.112007.

[10] G. Bellini, L. Ludhova, G. Ranucci, and F. L. Villante. Neutrino oscillations. *Adv. High Energy Phys.*, 2014:191960, 2014. doi: 10.1155/2014/191960.

[11] Bogdan Povh, Klaus Rith, Christoph Scholz, Frank Zetsche, and Werner Rodejohann. *Teilchen und Kerne*. Springer Berlin Heidelberg, 2013.

[12] Sindey Coleman and Jeffrey Mandula. *All Possible Symmetries of the S Matrix*, pages 469–474. 2014. doi: 10.1142/9789814542319_0016. URL http://www.worldscientific.com/doi/abs/10.1142/9789814542319_0016.

[13] Rudolf Haag, Jan T. Lopuszanski, and Martin Sohnius. All Possible Generators of Supersymmetries of the s Matrix. *Nucl. Phys.*, B88:257, 1975. doi: 10.1016/0550-3213(75)90279-5.

[14] S. P. Martin. A Supersymmetry Primer. arXiv: hep-ph/9709356, 2016. URL `https://arxiv.org/abs/hep-ph/9709356`.

[15] D. I. Kazakov. Beyond the Standard Model (In Search of Supersymmetry), 2001. URL `http://arxiv.org/abs/hep-ph/0012288`. arXiv:hep-ph/0012288.

[16] H. et al. Nishino. Search for Proton Decay via $p \to e^+\pi^0$ and $p \to \mu^+\pi^0$ in a Large Water Cherenkov Detector. *Phys. Rev. Lett.*, 102:141801, Apr 2009. doi: 10.1103/PhysRevLett.102.141801. URL `https://link.aps.org/doi/10.1103/PhysRevLett.102.141801`.

[17] X-ray: NASA/CXC/CfA/M.Markevitch et al.; Optical: NASA/STScI; Magellan/U.Arizona/D.Clowe et al.; Lensing Map: NASA/STScI; ESO WFI; Magellan/U.Arizona/D.Clowe et al.

[18] Adrian Jenkins Volker Springel, Simon D. M. White. Simulations of the formation, evolution and clustering of galaxies and quasars, 2005. URL `http://www.nature.com/nature/journal/v435/n7042/abs/nature03597.html`.

[19] K. G. Begeman, A. H. Broeils, and R. H. Sanders. Extended rotation curves of spiral galaxies: dark haloes and modified dynamics. *Monthly Notices of the Royal Astronomical Society*, 249(3):523–537, 1991. doi: 10.1093/mnras/249.3.523. URL `http://dx.doi.org/10.1093/mnras/249.3.523`.

[20] C. L. et.al. Bennett. Nine-year Wilkinson Microwave Anisotropy Probe (WMAP) Observations: Final Maps and Results. *APJS*, 2012.

[21] Planck Collaboration. Planck 2015 results I. Overview of products and scientific results. 594:38, 2016. doi: https://doi.org/10.1051/0004-6361/201527101.

[22] S. Dimopoulos and S. Raby, Nucl. Phys. B 192, 353, (1981); E. Witten, Nucl. Phys. B 188, 513 (1981); M. Dine, W. Fischler and M. Srednicki, Nucl. Phys. B 189, 575 (1981); S. Dimopoulos and H. Georgi, Nucl. Phys. B 193, 150 (1981); N. Sakai, Z. Phys. C 11, 153 (1981); R.K. Kaul and P. Majumdar, Nucl. Phys. B 199, 36 (1982).

[23] S. Dimopoulos and D. Sutter. The Supersymmetric Flavor Problem. *Nucl. Phys.*, B 452:496, 1995. hep-ph/9504415.

[24] J. Alwall, P. Schuster und N. Toro. Simplified Models for a First Characterization of New Physics at the LHC. *Phys. Rev.*, D79, 2009. URL `http://dx.doi.org/10.1103/PhysRevD.79.075020`.

[25] LHC New Physics Working Group. Simplified Models for LHC New Physics Searches. *J. Phys.*, G39, 2012. URL `http://dx.doi.org/10.1088/0954-3899/39/10/105005`.

[26] ATLAS Collaboration. SUSY Feynman diagrams, 2017. URL `https://twiki.cern.ch/twiki/bin/view/AtlasProtected/SUSYFeynmanDiagrams`.

[27] ATLAS Collaboration. Search for dark matter and other new phenomena in events with an energetic jet and large missing transverse momentum using the ATLAS detector. 2017. URL `arXiv:1711.03301[hep-ex]`.

[28] ATLAS Public web page, 2017. URL `https://atlas.cern/`.

[29] CMS Public web page, 2017. URL `https://cms.cern/`.

[30] ATLAS Supersymmetry public results, 2017. URL `https://twiki.cern.ch/twiki/bin/view/AtlasPublic/SupersymmetryPublicResults`.

[31] CMS Supersymmetry public results, 2017. URL `https://twiki.cern.ch/twiki/bin/view/CMSPublic/PhysicsResultsSUS`.

[32] ATLAS Collaboration. Search for pair-produced third-generation squarks decaying via charm quarks or in compressed supersymmetric scenarios in pp collisions at $\sqrt{s} = 8$ TeV with the ATLAS detector. *Phys. Rev.*, D90(5):052008, 2014. doi: 10.1103/PhysRevD.90.052008.

[33] CMS Collaboration. Search for new phenomena with the MT2 variable in the all-hadronic final state produced in proton-proton collisions at $\sqrt{(s)} = 13$ TeV. 2017. URL `arXiv:1705.04650[hep-ex]`. CMS-SUS-16-036, CERN-EP-2017-084.

[34] ATLAS Collaboration. Search for Scalar Charm Quark Pair Production in pp Collisions at $\sqrt{s} = 8$ TeV with the ATLAS Detector. *Phys. Rev. Lett. 114, 161801*, 2015. doi: 10.1103/PhysRevLett.114.161801. URL `arXiv:1501.01325[hep-ex]`. CERN-PH-EP-2014-292.

[35] M Bajko, F Bertinelli, and et al. Report of the Task Force on the Incident of 19th September 2008 at the LHC. Technical Report LHC-PROJECT-Report-1168. CERN-LHC-PROJECT-Report-1168, CERN, Geneva, Mar 2009. URL `https://cds.cern.ch/record/1168025`.

[36] LHC timeline, 2017. URL `https://timeline.web.cern.ch/timelines/The-Large-Hadron-Collider`.

[37] Christiane Lefévre. The CERN accelerator complex, 2008. URL `http://cds.cern.ch/record/1260465`.

[38] Alice Collaboration. Public webpage, 2017. URL `http://aliceinfo.cern.ch/Public/Welcome.html`.

[39] LHCb Collaboration. Public webpage, 2017. URL `http://lhcb-public.web.cern.ch/lhcb-public/`.

[40] Number of Interactions per Crossing, 2017. URL `https://twiki.cern.ch/twiki/bin/view/AtlasPublic/LuminosityPublicResultsRun2`.

[41] ATLAS Collaboration. Luminosity determination in pp collisions at $\sqrt{s} = 8$ TeV using the ATLAS detector at the LHC. *The European Physical Journal C*, 76(12):653, Nov 2016. ISSN 1434-6052. doi: 10.1140/epjc/s10052-016-4466-1. URL `https://doi.org/10.1140/epjc/s10052-016-4466-1`.

[42] L. A. Harland-Lang, A. D. Martin, P. Motylinski, and R. S. Thorne. Parton distributions in the LHC era: MMHT 2014 PDFs. *Eur. Phys. J.*, C75(5):204, 2015. doi: 10.1140/epjc/s10052-015-3397-6.

[43] Richard D. Ball, , Valerio Bertone, Stefano Carrazza, Christopher S. Deans, Luigi Del Debbio, Stefano Forte, Alberto Guffanti, Nathan P. Hartland, José I. Latorre, Juan Rojo, and Maria Ubiali. Parton distributions for the LHC run II. *Journal of High Energy Physics*, 2015(4), apr 2015. doi: 10.1007/jhep04(2015)040. URL `http://nnpdf.mi.infn.it/nnpdf3-0qed/`.

[44] Jun Gao, Marco Guzzi, Joey Huston, Hung-Liang Lai, Zhao Li, Pavel Nadolsky, Jon Pumplin, Daniel Stump, and C.-P. Yuan. CT10 next-to-next-to-leading order global analysis of QCD. *Physical Review D*, 89(3), feb 2014. doi: 10.1103/physrevd.89.033009. URL `http://hep.pa.msu.edu/cteq/public/ct10.html`.

[45] ATLAS Collaboration. The ATLAS Experiment at the CERN Large Hadron Collider. *Journal of Instrumentation*, 3(08):S08003–S08003, aug 2008. doi: 10.1088/1748-0221/3/08/s08003. URL `http://atlas.cern/`.

[46] Joao Pequenao. Computer generated image of the whole ATLAS detector. Mar 2008. URL `https://cds.cern.ch/record/1095924`.

[47] Joao Pequenao. Computer generated image of the ATLAS inner detector. Mar 2008. URL `http://cds.cern.ch/record/1095926`.

[48] M Capeans, G Darbo, K Einsweiller, M Elsing, T Flick, M Garcia-Sciveres, C Gemme, H Pernegger, O Rohne, and R Vuillermet. ATLAS Insertable B-Layer Technical Design Report. Technical Report CERN-LHCC-2010-013. ATLAS-TDR-19, Sep 2010. URL `https://cds.cern.ch/record/1291633`.

[49] Joao Pequenao. Computer Generated image of the ATLAS calorimeter. Mar 2008. URL `https://cds.cern.ch/record/1095927`.

[50] C. Cojocaru and et al. Hadronic calibration of the ATLAS liquid argon end-cap calorimeter in the pseudorapidity region $1.6|\eta| < 1.8$ in beam tests. *Nuclear Instruments and Methods in Physics Research Section A: Accelerators, Spectrometers, Detectors and Associated Equipment*, 531(3):481–514, oct 2004. doi: 10.1016/j.nima.2004.05.133.

[51] ATLAS Collaboration. Jet energy measurement with the ATLAS detector in proton-proton collisions at $\sqrt{s} = 7$ TeV. *The European Physical Journal C*, 73(3), mar 2013. doi: 10.1140/epjc/s10052-013-2304-2.

[52] Monte Carlo Calibration and Combination of In-situ Measurements of Jet Energy Scale, Jet Energy Resolution and Jet Mass in ATLAS. Technical Report ATLAS-CONF-2015-037, CERN, Geneva, Aug 2015. URL `https://cds.cern.ch/record/2044941`.

[53] ATLAS Collaboration. Jet energy resolution in proton-proton collisions at $\sqrt{s} = 7$ TeV recorded in 2010 with the ATLAS detector. *Eur. Phys. J.*, C73(3):2306, 2013. doi: 10.1140/epjc/s10052-013-2306-0.

[54] Joao Pequenao. Computer generated image of the ATLAS Muons subsystem. Mar 2008. URL `https://cds.cern.ch/record/1095929`.

[55] URL `https://twiki.cern.ch/twiki/bin/viewauth/Atlas/TriggerForDummies`.

[56] Eduard Simioni. The Topological Processor for the future ATLAS Level-1 Trigger: from design to commissioning. 2014. URL `arXiv:1406.4316[physics.ins-det]`.

[57] ATLAS Collaboration. $E_{\mathrm{T}}^{\mathrm{miss}}$ trigger public results web page, 2016. URL `https://twiki.cern.ch/twiki/bin/view/AtlasPublic/MissingEtTriggerPublicResults#13_TeV_data_2016`.

[58] S. Abdel Khalek, B. Allongue, and F. Anghinolfi. The ALFA Roman Pot detectors of ATLAS. *Journal of Instrumentation*, 11(11):P11013, 2016. URL `http://stacks.iop.org/1748-0221/11/i=11/a=P11013`.

[59] V Cindro and D Dobos H Pernegger. The ATLAS Beam Conditions Monitor. *Journal of Instrumentation*, 3(02):P02004, 2008. URL `http://stacks.iop.org/1748-0221/3/i=02/a=P02004`.

[60] ATLAS Collaboration. Total Integrated Luminosity, 2015. URL `https://atlas.web.cern.ch/Atlas/GROUPS/DATAPREPARATION/DataSummary/2015/`.

[61] ATLAS Collaboration. Total Integrated Luminosity, 2016. URL `https://atlas.web.cern.ch/Atlas/GROUPS/DATAPREPARATION/DataSummary/2016/`.

[62] ATLAS Collaboration. Performance of the ATLAS trigger system in 2015. *The European Physical Journal C*, 77(5):317, May 2017. ISSN 1434-6052. doi: 10.1140/epjc/s10052-017-4852-3. URL `https://doi.org/10.1140/epjc/s10052-017-4852-3`.

[63] J. Alwall, R. Frederix, S. Frixione, V. Hirschi, F. Maltoni, O. Mattelaer, H. S. Shao, T. Stelzer, P. Torrielli, and M. Zaro. The automated computation of tree-level and next-to-leading order differential cross sections, and their matching to parton shower simulations. *JHEP*, 07:079, 2014. doi: 10.1007/JHEP07(2014)079.

[64] T. Gleisberg, Stefan. Hoeche, F. Krauss, M. Schonherr, S. Schumann, F. Siegert, and J. Winter. Event generation with SHERPA 1.1. *JHEP*, 02:007, 2009. doi: 10.1088/1126-6708/2009/02/007.

[65] Stefano Frixione, Paolo Nason, and Carlo Oleari. Matching NLO QCD computations with Parton Shower simulations: the POWHEG method. *JHEP*, 11:070, 2007. doi: 10.1088/1126-6708/2007/11/070.

[66] S. Agostinelli et al. GEANT4: A Simulation toolkit. *Nucl. Instrum. Meth.*, A506: 250–303, 2003. doi: 10.1016/S0168-9002(03)01368-8.

[67] ATLAS Collaboration. *ATLAS Computing: technical design report*. Technical Design Report ATLAS. CERN, Geneva, 2005. URL `https://cds.cern.ch/record/837738`.

[68] ATLAS Collaboration. The ATLAS Simulation Infrastructure. *Eur. Phys. J.*, C70: 823–874, 2010. doi: 10.1140/epjc/s10052-010-1429-9.

[69] Torbjorn Sjostrand, Stephen Mrenna, and Peter Z. Skands. PYTHIA 6.4 Physics and Manual. *JHEP*, 05:026, 2006. doi: 10.1088/1126-6708/2006/05/026.

[70] Torbjorn Sjostrand, Stephen Mrenna, and Peter Z. Skands. A Brief Introduction to PYTHIA 8.1. *Comput. Phys. Commun.*, 178:852–867, 2008. doi: 10.1016/j.cpc.2008.01.036.

[71] M. Bahr et al. Herwig++ Physics and Manual. *Eur. Phys. J.*, C58:639–707, 2008. doi: 10.1140/epjc/s10052-008-0798-9.

[72] Johannes Bellm et al. Herwig 7.0/Herwig++ 3.0 release note. *Eur. Phys. J.*, C76(4): 196, 2016. doi: 10.1140/epjc/s10052-016-4018-8.

[73] Michelangelo L. Mangano, Fulvio Piccinini, Antonio D. Polosa, Mauro Moretti, and Roberto Pittau. ALPGEN, a generator for hard multiparton processes in hadronic collisions. *Journal of High Energy Physics*, 2003(07):001, 2003. URL `http://stacks.iop.org/1126-6708/2003/i=07/a=001`.

[74] Simone Alioli, Paolo Nason, Carlo Oleari, and Emanuele Re. A general framework for implementing NLO calculations in shower Monte Carlo programs: the POWHEG BOX. *JHEP*, 06:043, 2010. doi: 10.1007/JHEP06(2010)043.

[75] Stop and sbottom cross sections and uncertainties. URL `https://twiki.cern.ch/twiki/bin/view/LHCPhysics/SUSYCrossSections13TeVstopsbottom`.

[76] W. Beenakker, M. Kramer, T. Plehn, M. Spira, and P. M. Zerwas. Stop production at hadron colliders. *Nucl. Phys.*, B515:3–14, 1998. doi: 10.1016/S0550-3213(98)00014-5.

[77] Wim Beenakker and et al. Squark and gluino hadroproduction. *International Journal of Modern Physics A*, 26(16):2637–2664, 2011. doi: 10.1142/S0217751X11053560. URL `http://www.worldscientific.com/doi/abs/10.1142/S0217751X11053560`.

[78] Wim Beenakker, Silja Brensing, Michael Kramer, Anna Kulesza, Eric Laenen, and Irene Niessen. Supersymmetric top and bottom squark production at hadron colliders. *JHEP*, 08:098, 2010. doi: 10.1007/JHEP08(2010)098.

[79] ATLAS Collaboration. Tracking Prerecommendations, Summer 2017. URL `https://twiki.cern.ch/twiki/bin/view/AtlasProtected/TrackingCPPreRecsSummer2017`.

[80] ATLAS Collaboration. Electron efficiency measurements with the ATLAS detector using the 2015 LHC proton-proton collision data. Technical Report ATLAS-CONF-2016-024, CERN, Geneva, Jun 2016. URL `https://cds.cern.ch/record/2157687`.

[81] W Lampl, S Laplace, D Lelas, P Loch, H Ma, S Menke, S Rajagopalan, D Rousseau, S Snyder, and G Unal. Calorimeter Clustering Algorithms: Description and Performance. Technical Report ATL-LARG-PUB-2008-002. ATL-COM-LARG-2008-003, CERN, Geneva, Apr 2008. URL `https://cds.cern.ch/record/1099735`.

[82] T Cornelissen, M Elsing, S Fleischmann, W Liebig, E Moyse, and A Salzburger. Concepts, Design and Implementation of the ATLAS New Tracking (NEWT). Technical Report ATL-SOFT-PUB-2007-007. ATL-COM-SOFT-2007-002, CERN, Geneva, Mar 2007. URL `https://cds.cern.ch/record/1020106`.

[83] ATLAS Collaboration. Muon reconstruction performance of the ATLAS detector in proton–proton collision data at $\sqrt{s} = 13$ TeV. *The European Physical Journal C*, 76(5):292, May 2016. ISSN 1434-6052. doi: 10.1140/epjc/s10052-016-4120-y. URL `https://doi.org/10.1140/epjc/s10052-016-4120-y`.

[84] ATLAS Collaboration. Measurement of the tau lepton reconstruction and identification performance in the ATLAS experiment using *pp* collisions at $\sqrt{s} = 13$ TeV. Technical Report ATLAS-CONF-2017-029, CERN, Geneva, May 2017. URL `http://cds.cern.ch/record/2261772`.

[85] Matteo Cacciari, Gavin P. Salam, and Gregory Soyez. The anti- k t jet clustering algorithm. *Journal of High Energy Physics*, 2008(04):063, 2008. URL `http://stacks.iop.org/1126-6708/2008/i=04/a=063`.

[86] Pile-up subtraction and suppression for jets in ATLAS. Technical Report ATLAS-CONF-2013-083, CERN, Geneva, Aug 2013. URL `https://cds.cern.ch/record/1570994`.

[87] Jet Calibration and Systematic Uncertainties for Jets Reconstructed in the ATLAS Detector at $\sqrt{s} = 13$ TeV. Technical Report ATL-PHYS-PUB-2015-015, CERN, Geneva, Jul 2015. URL `http://cds.cern.ch/record/2037613`.

[88] Matteo Cacciari and Gavin P. Salam. Pileup subtraction using jet areas. *Physics Letters B*, 659(1-2):119–126, jan 2008. doi: 10.1016/j.physletb.2007.09.077.

[89] Tagging and suppression of pileup jets with the ATLAS detector. Technical Report ATLAS-CONF-2014-018, CERN, Geneva, May 2014. URL `https://cds.cern.ch/record/1700870`.

[90] Selection of jets produced in 13TeV proton-proton collisions with the ATLAS detector. Technical Report ATLAS-CONF-2015-029, CERN, Geneva, Jul 2015. URL `https://cds.cern.ch/record/2037702`.

[91] ATLAS Collaboration. Expected performance of the ATLAS b-tagging algorithms in Run-2. Technical Report ATL-PHYS-PUB-2015-022, CERN, Geneva, Jul 2015. URL `https://cds.cern.ch/record/2037697`.

[92] ATLAS Collaboration. Commissioning of the ATLAS high-performance b-tagging algorithms in the 7 TeV collision data. Technical Report ATLAS-CONF-2011-102, CERN, Geneva, Jul 2011. URL `http://cds.cern.ch/record/1369219`.

[93] ATLAS Collaboration. *Expected performance of the ATLAS experiment: detector, trigger and physics*. CERN, Geneva, 2009. URL `https://cds.cern.ch/record/1125884`.

[94] G Piacquadio and C Weiser. A new inclusive secondary vertex algorithm for b-jet tagging in ATLAS. *Journal of Physics: Conference Series*, 119(3):032032, 2008. URL `http://stacks.iop.org/1742-6596/119/i=3/a=032032`.

[95] ATLAS Collaboration. Performance and Calibration of the JetFitterCharm Algorithm for c-Jet Identification. Technical Report ATL-PHYS-PUB-2015-001, CERN, Geneva, Jan 2015. URL `https://cds.cern.ch/record/1980463`.

[96] Valentina Cairo, Stefano Cali, Julian Glatzer, Emily Charlotte Graham, Kristian Gregersen, David Olivier Jamin, Krisztian Peters, Matthias Saimpert, Balthasar Maria Schachtner, Federico Sforza, and Jonathan Shlomi. Calibration of light-flavour jet b-tagging rates on ATLAS data at $\sqrt{s} = 13$ TeV. Technical Report ATL-COM-PHYS-2017-192, CERN, Geneva, Feb 2017. URL `https://cds.cern.ch/record/2253746`.

[97] Andrew Stuart Bell. Calibration of b-tagging using di-leptonic $t\bar{t}$ events produced in pp collisions at $\sqrt{s} = 13$ TeV and a combinatorial likelihood approach. Technical Report ATL-COM-PHYS-2016-1598, CERN, Geneva, Nov 2016. URL `https://cds.cern.ch/record/2231568`.

[98] Stefan Guindon, Valerio Dao, Snezana Nektarijevic, Giacinto Piacquadio, and Aaron Foley Webb. Measurement of c-jet tagging efficiency in $t\bar{t}$ events using a likelihood approach. Technical Report ATL-COM-PHYS-2017-073, CERN, Geneva, Feb 2017. URL `https://cds.cern.ch/record/2243764`.

[99] ATLAS Collaboration. Expected performance of missing transverse momentum reconstruction for the ATLAS detector at $\sqrt{s} = 13$ TeV. Technical Report ATL-PHYS-PUB-2015-023, CERN, Geneva, Jul 2015. URL `https://cds.cern.ch/record/2037700`.

[100] Jan Schäffer, Samuel David Jones, Kerim Suruliz, Katharina Bierwagen, and Rosa Simoniello. Search for $\tilde{t}_1 \to c\tilde{\chi}_1^0$ and $\tilde{c} \to c\tilde{\chi}_1^0$ with 35 fb^{-1} of ATLAS data. Technical Report ATL-COM-PHYS-2016-1698, CERN, Geneva, Nov 2016. URL `https://cds.cern.ch/record/2234856`.

[101] ATLAS Collaboration. Measurement of the cross-section for W boson production in association with b-jets in pp collisions at $\sqrt{s} = 7$ TeV with the ATLAS detector. *JHEP*, 06:084, 2013. doi: 10.1007/JHEP06(2013)084.

[102] ATLAS Collaboration. Measurement of differential production cross-sections for a Z boson in association with b-jets in 7 TeV proton-proton collisions with the ATLAS detector. *JHEP*, 10:141, 2014. doi: 10.1007/JHEP10(2014)141.

[103] M. Baak, G. J. Besjes, D. Côte, A. Koutsman, J. Lorenz, and D. Short. HistFitter software framework for statistical data analysis. *Eur. Phys. J.*, C75:153, 2015. doi: 10.1140/epjc/s10052-015-3327-7.

[104] Kyle Cranmer, George Lewis, Lorenzo Moneta, Akira Shibata, and Wouter Verkerke. HistFactory: A tool for creating statistical models for use with RooFit and RooStats. Technical Report CERN-OPEN-2012-016, New York U., New York, Jan 2012. URL `https://cds.cern.ch/record/1456844`.

[105] L. Moneta, K. Cranmer, G. Schott, and W. Verkerke. The RooStats project. 2010. URL `arXiv:1009.1003[physics.data-an]`.

[106] Glen Cowan, Kyle Cranmer, Eilam Gross, and Ofer Vitells. Asymptotic formulae for likelihood-based tests of new physics. *Eur. Phys. J.*, C71:1554, 2011. doi: 10.1140/epjc/s10052-011-1554-0,10.1140/epjc/s10052-013-2501-z. [Erratum: Eur. Phys. J.C73,2501(2013)].

[107] Sayipjamal Dulat, Tie-Jiun Hou, Jun Gao, Marco Guzzi, Joey Huston, Pavel Nadolsky, Jon Pumplin, Carl Schmidt, Daniel Stump, and C. P. Yuan. New parton distribution functions from a global analysis of quantum chromodynamics. *Phys. Rev.*, D93(3): 033006, 2016. doi: 10.1103/PhysRevD.93.033006.

[108] Andy Buckley, James Ferrando, Stephen Lloyd, Karl Nordström, Ben Page, Martin Rüfenacht, Marek Schönherr, and Graeme Watt. LHAPDF6: parton density access in the LHC precision era. *Eur. Phys. J.*, C75:132, 2015. doi: 10.1140/epjc/s10052-015-3318-8.

[109] Carola F. Berger, James S. Gainer, JoAnne L. Hewett, and Thomas G. Rizzo. Supersymmetry Without Prejudice. *JHEP*, 02:023, 2009. doi: 10.1088/1126-6708/2009/02/023.

[110] Matthew W. Cahill-Rowley, JoAnne L. Hewett, Stefan Hoeche, Ahmed Ismail, and Thomas G. Rizzo. The New Look pMSSM with Neutralino and Gravitino LSPs. *Eur. Phys. J.*, C72:2156, 2012. doi: 10.1140/epjc/s10052-012-2156-1.

[111] ATLAS Collaboration. Summary of the ATLAS experiment's sensitivity to supersymmetry after LHC Run 1 - interpreted in the phenomenological MSSM. *JHEP*, 10:134, 2015. doi: 10.1007/JHEP10(2015)134.

[112] ILC webpage. URL `http://www.linearcollider.org/`.

[113] FCC webpage. URL `https://fcc.web.cern.ch/Pages/default.aspx`.

[114] Albert M Sirunyan et al. Search for supersymmetry in multijet events with missing transverse momentum in proton-proton collisions at 13 TeV. *Phys. Rev.*, D96(3):032003, 2017. doi: 10.1103/PhysRevD.96.032003.

[115] CMS Collaboration. Search for new physics in the all-hadronic final state with the MT2 variable. 2017.

[116] Alan Barr, Christopher Lester, and P. Stephens. m_{T2}: The Truth behind the glamour. *J. Phys.*, G29:2343–2363, 2003. doi: 10.1088/0954-3899/29/10/304.